SEISMOELECTRIC IMAGING OF SHALLOW TARGETS

A DISSERTATION
SUBMITTED TO THE DEPARTMENT OF GEOPHYSICS
AND THE COMMITTEE ON GRADUATE STUDIES
OF STANFORD UNIVERSITY
IN PARTIAL FULFILLMENT OF THE REQUIREMENTS
FOR THE DEGREE OF
DOCTOR OF PHILOSOPHY

Seth Storey Haines
December 2004

printed as Stanford Exploration Project No. 119
by permission of the author

I certify that I have read this dissertation and that in my opinion it is fully adequate, in scope and quality, as a dissertation for the degree of Doctor of Philosophy.

Simon L. Klemperer
(Principal Adviser)

I certify that I have read this dissertation and that in my opinion it is fully adequate, in scope and quality, as a dissertation for the degree of Doctor of Philosophy.

Steven R. Pride

I certify that I have read this dissertation and that in my opinion it is fully adequate, in scope and quality, as a dissertation for the degree of Doctor of Philosophy.

Biondo L. Biondi

Approved for the University Committee on Graduate Studies:

Abstract

I have developed experimental methods in seismoelectrics in order to image targets in the shallow subsurface, motivated by theoretical predictions that the seismoelectric method (recording seismic-to-electric conversions) can provide useful, and otherwise unattainable, information about thin layers and permeability and chemical property contrasts. I approach this problem with a combination of field experimentation, data processing algorithm development, and numerical modeling.

My field experiments demonstrate the existence of a previously-undocumented seismoelectric phenomena which I term the "direct field". It is the electric field of an electric dipole created by the asymmetrical pressure field created at the location of an impact source (e.g. sledgehammer). I also document the Lorentz field created by the motion of a metal hammer plate in the Earth's magnetic field. Identification of these fields permits more accurate interpretation of seismoelectric records, and easier identification of the "interface response", which is the signal of interest. My field experiments with sources and receivers on opposite sides of two man-made trenches show the "coseismic field" carried within the seismic P-wave arriving at the receivers after the interface response from the trenches.

Seismoelectric data processing must extract the interface response from the recorded data. I use established methods to remove the 60 Hz power grid energy and to reduce cultural and atmospheric electrical noise. Beyond existing work, I use real and synthetic data examples to show that non-stationary prediction-error filters (PEF's) provide the most universally-effective option for separating the interface response from the coseismic noise. Linear radon transforms can also be quite effective if data are of adequate quality and include a sufficient number of

recording channels ($\sim$48).

I present the first-ever multichannel seismoelectric image supported by numerical modeling. Data were recorded with nine explosive shots recorded by 48 electrical channels. The image is produced by stacking the gathers from each shot, and is supported by a complementary image produced through numerical modeling. Further numerical models provide insight into the effectiveness of the seismoelectric method for imaging various targets and confirm that the seismoelectric method can provide useful new information about small targets and chemical property changes.

Preface

All of the figures in this thesis are marked with one of the three labels: [ER], [CR], and [NR]. These labels define to what degree the figure is reproducible from the data directory, source code and parameter files provided on the web version of this thesis [1].

ER denotes Easily Reproducible. The author claims that you can reproduce such a figure from the programs, parameters, and data included in the electronic document. We assume you have a UNIX workstation with Fortran, C, X-Window system, and the software on our CD-ROM at your disposal. Before the publication of the electronic document, someone other than the author tests the author's claim by destroying and rebuilding all ER figures.

CR denotes Conditional Reproducibility. The author certifies that the commands are in place to reproduce the figure if certain resources are available. SEP staff have not attempted to verify the author's certification. You may need a super computer, or you might simply need a large amount of time (20 minutes, or several months/years) on a workstation. This includes all of the numerical simulations, and some of the slower processing results.

NR denotes Non-Reproducible. This class of figure is considered non-reproducible. Figures in this class are scans and artists' drawings. Output of interactive processing are labeled NR.

[1] http://sepwww.stanford.edu/public/docs/sep119

Acknowledgements

My time at Stanford has been very productive and very pleasant, both of these in large part due to the many outstanding individuals who I've had the opportunity to interact with. First on this list is Simon Klemperer, who, as my adviser, has been more helpful and dedicated than a student could possibly ask. His door is truly always open, and I can not thank him enough for his support as this research project has taken him in a new scientific direction. He has taught me a great deal as dissertation adviser, and also as a research group leader in seminars and in the field. And he's made it enjoyable along the way. To Steve Pride I am also greatly indebted, for without him this project could not have been carried out. From the relaxed beer-by-the-pool-after-a-hard-day-of-trench-construction moments, to long hours working through equations (of which, thanks to him, I now have a much better understanding), Steve has played a huge role in the transition from my original (and unrealistic) conception of this project to the successful scientific endeavor that it has become. Biondo Biondi joined this project at a crucial time, when I was realizing that signal/noise separation would have to be a major component of the work. He provided the necessary guidance, and helped me to secure much-needed financial support. To Jerry Harris I am very grateful for guidance and support since the inception of this project. And with the 20:20 vision of hindsight, I can now see that his foresight at the beginning of this project correctly predicted nearly every difficulty that I faced along the way, not to mention the benefits of modeling the phenomena I was studying.

The field work component of this project was made possible by the generosity and good nature of Jim and Carolyn Pride. To agree to let an unknown graduate student dig up a meadow on their property, and to provide the necessary equipment and many dump trucks of sand, would be unthinkable to most people. But that's exactly what they did. And over the following

years they continued to be gracious hosts and generous benefactors. Jim Pride (1936-2004) was a great man, and I think of him with the utmost of respect. To both Jim and Carolyn I am very grateful.

Pride Mountain Vineyards is a beautiful and pleasant place to work, but the work itself was generally quite grueling. I enjoyed it, though, in part thanks to long-time employer Bob Browne (1943-2003) who helped me establish a respect for manual labor early in my life. And I enjoyed the work thanks to the help and camaraderie of the many friends who swung the sledgehammer (at the vineyard, or other sites). The list is long, and I sincerely hope that I have not left anyone out: Mike Beman, Stephan Bergbauer, Morgan Brown, Brian Ebel, Jonathan Ajo-Franklin, Antoine Guitton, Ashley Griffith, T.J. Kiczenski, Simon Klemperer, Jesse Lomask, Nick Martin, Jordan Muller, Adam Pidlisecky, Steve Pride, Phil Resor and Rob Sanders. It's amazing the work you can get a person to do for a steak and a few beers. I am also grateful to Rufus Catchings and Tom Burdette of the USGS who made possible the use of the explosive sources that proved to be a key part of completing this dissertation.

Virtually everyone who has set foot in the Mitchell Building in the last several years helped with this project in one way or another, but some deserve specific thanks. Antoine Guitton provided a great deal of help (and coding expertise) for data processing. Bob Clapp, Morgan Brown, Brad Artman, Bill Curry, and many others have helped with my use of SEPlib and the SEP computer system. Adam Pidlisecky has been my go-to guy for my many questions involving electric fields in the earth and how to model them, with Kamini Singha and Dave Alumbaugh also providing a lot of help. Jim Berryman provided much valuable input on the modeling algorithm, and Chunling Wu provided the Biot code that I used. I also am grateful to the other members of the Crustal Group and of SEP for their help with science and just having fun. The SEP seminar group (Jon, Biondo, Bob, and all the students) provided countless tid-bits that added to this work in many ways. I'm also very grateful to the Geophysics Department staff, without whom I never would have gotten through the bureaucratic hurdles that stood between me and paychecks and degree-attainment.

Although his direct role in this project was indistinct, I am very glad to have had the opportunity to interact with George Thompson during the last six and a half years. I think he's got it all pretty much figured out. I haven't, but he gives me something to aspire to. I've

learned a huge amount just from being around him. I am also grateful to George and Anita for the use of their tree farm as a test site for my work, as well as the occasional relaxing day in the redwoods.

Finding funding for this project was not an easy task. I am grateful to the many organizations who have provided funding, and the many individuals who have helped me to acquire this funding. Acknowledgment is made to the Donors of the American Chemical Society Petroleum Research Fund for support of this research. Additional funding was provided by the Achievement Rewards for College Scientists Foundation, the Stanford School of Earth Sciences McGee Fund, the American Association of Petroleum Geologists student research grants program, the Geological Society of America student research grants program, the Colorado Geological Survey and the sponsors of the Stanford Exploration Project. And thankfully the Geophysics Department provided funding at various points in the last several years when other sources fell through. I am fortunate to have been part of a department where it was possible to pursue a research project outside of existing research areas.

This list grows long, but the people at the end are every bit as important as those at the beginning. In particular, I want to thank my parents and the rest of my family for their love and support throughout the many many years of my education. And I also want to acknowledge the countless friends who've made this experience so enjoyable. I can't possibly list them all, but I'm sure I'll see them again across a BBQ grill, or flying through fresh-fallen snow, or hiking on rocky peaks. These are the people who've kept me happy and sane. Without my family and friends, this dissertation could not possibly ever have come to exist.

Contents

Chapter 1

Introduction

MOTIVATION

Geophysical techniques offer an affordable means to determine useful information about the subsurface without digging holes or drilling wells. We can image major interfaces in acoustic and electromagnetic impedance and we can map changes in electrical conductivity using well-established methods. The resolution of these methods depends on many factors, but typically we can hope to image features with dimensions on the order of $\sim$1 m in the upper few tens of meters, the region of interest in environmental studies. In this sort of study, a variety of information is often desired but hydraulic permeability is frequently one of the most critical material properties. Although existing geophysical techniques can provide a wealth of subsurface information, they can provide very little information about hydraulic permeability. A thin ($\sim$1 cm) impermeable layer has a major impact on ground water flow, and is of great interest in environmental studies, but is virtually invisible to conventional geophysical methods. A thin highly-permeable fracture is similarly of great interest, but is equally difficult to image. These examples relate to the shallow subsurface, as that is the realm considered in this thesis. However, information regarding these sorts of targets is equally important in deeper studies conducted in hydrocarbon exploration. The seismoelectric method can potentially provide new information about subsurface permeability contrasts, including very thin layers, and so it

has been the focus of my doctoral research. The work presented in this thesis represents significant progress toward the goal of developing seismoelectric experimental methods so that the technique can be reliably used in shallow geophysical surveys.

SEISMOELECTRIC BACKGROUND

The first reported observation of seismoelectric phenomena appeared in the first issue of Geophysics (Thompson, 1936), and was closely followed by Ivanov (1939) in the Russian literature. Thompson (1936, 1939) reported changes in electrical conductivity caused by a passing seismic wave, whereas Ivanov observed the electric field localized within a compressional seismic wave. Together with theoretical work by Frenkel (1944), these contributions initiated the study of effects related to the interaction of mechanical energy (sound) and electromagnetic fields.

The five decades that followed these initial publications saw only sporadic interest in seismoelectric phenomena. Russell et al. (1997) identifies four distinct effects representing the inter-relation between seismic and electrical energy: (1) the change in electrical conductivity caused by the pressure changes within a seismic wave (Thompson, 1939; Long and Rivers, 1975), (2) piezoelectric effects in quartz grains (Maxwell et al., 1992), (3) the poorly-understood electric signals produced by massive sulfide bodies (Kepic et al., 1995) (radio-frequency signals possibly created by micro-fractures resulting from the seismic wave), and (4) electric signal caused by electrokinetic effects related to the motion of pore fluid relative to the grain matrix. This thesis focuses on effects of the fourth type (electrokinetic effects), and in particular on the use of these phenomena in shallow geophysical site characterization. While the words "electroseismic" and "seismoelectric" could be used with regard to any effect linking seismic and electrical energy, I use the words to identify only those effects that are electrokinetic in origin. These electrokinetic effects include electric-to-seismic conversions, but I focus exclusively on electric signals created by seismic energy. It is these seismic-to-electric conversions, caused by electrokinetic effects, that I refer to with the term "seismoelectric" throughout the remainder of this dissertation. In keeping with English language standards, and scientific practice, I reserve the word "electroseismic" for electric-to-seismic conversions.

Martner and Sparks (1959) were the first to report independently propagating electromagnetic disturbances (now referred to as the "interface response") created at a subsurface interface by seismic energy. They interpret the interface in their experiments to be the base of the weathering layer, but it is co-located with the water table so either could be responsible for the observed signals. Broding et al. (1963) report observations of the electric field localized within seismic waves (now termed the "coseismic" field), at a distance from large quarry blasts and also in laboratory experiments. On-going laboratory and field experiments by Parkhomenko (1971a) and Migunov and Kokorev (1977) provided further insight into the relation between seismoelectric phenomena and material properties. These publications, along with field studies by Murty (1985) and others, represent a first phase of seismoelectric studies marked by isolated experimental observations and lacking a thorough understanding of the underlying physics.

The second phase of seismoelectric studies is marked by the greatly increased frequency of seismoelectric publications in the last fifteen years, and an improvement in the presented data and interpretations. Improvements in data quality are in part due to the widespread availability of high-quality digital recording instruments with 24 or more channels. This second phase began with the theoretical contribution of Neev and Yeatts (1989), but it was the presentation of experimental work by Thompson and Gist (1993) that brought seismoelectric research into the spotlight. Thompson and Gist (1993) present a seismoelectric image of subsurface interfaces along with associated theoretical modeling, the first study of its kind. These experimental advances were matched by the development of much-needed seismoelectric theory. In an important series of publications, Pride (1994), Pride and Haartsen (1996), and Haartsen and Pride (1997) derive a complete understanding seismoelectric phenomena for fluid-saturated materials based on the combination of Biot theory (Biot, 1956a,b) and Maxwell's equations. These contributions provide a theoretical framework within which to interpret the many field observations of seismoelectric phenomena, and encouraged an increase in experimental complexity.

At the University of British Columbia, Butler et al. (1996) observed the interface response from the base of a layer of organic fill overlying glacial till using sledgehammer and explosive sources, and Russell et al. (1997) presented results from seismoelectric, piezoelectric and sulfide studies. At MIT, a series of laboratory experiments (Zhu et al., 1999; Zhu and Toksoz,

2003) and field experiments (Mikhailov et al., 1997, 2000) demonstrated interface response signals in bore hole studies and surface surveys of layered and fractured materials. These observations were supported by numerical modeling based on the recently-developed theoretical understanding (Haartsen and Pride, 1997). Meanwhile at the University of Grenoble, France, Garambois and Dietrich (2001, 2002) conducted field studies and numerical analysis further proving the existence of the seismoelectric phenomena and adding to our understanding of the exact relation between the coseismic field and the associated seismic wave. Field and theoretical seismoelectric studies at Wright State University, Ohio, (Wolfe et al., 1996; Strachan and Wolfe, 2001; Gershenzon and Bambakidis, 2001), along with some experimental work by Beamish and Peart (1998) rounded out the past decade as one of great progress in seismoelectric research. The existence of observable seismoelectric phenomena was finally well-established, and rigorous theory provided an explanation of the observations.

SEISMOELECTRIC THEORY

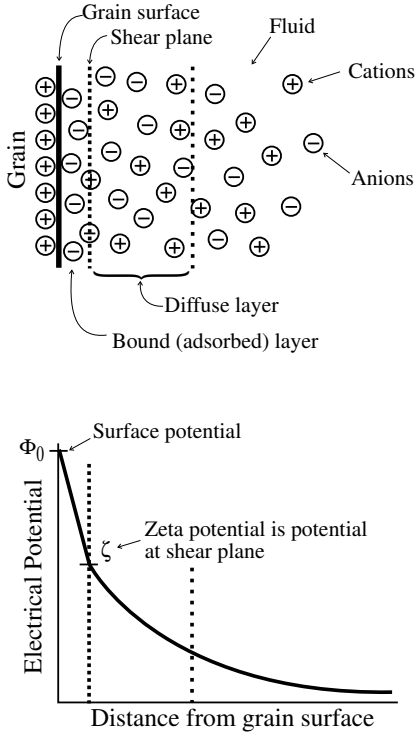

Figure 1.1: Schematic representation of the electric double layer (EDL), with a plot of electric potential versus distance from the grain boundary, after Shaw (1992). Charge at the grain surface attracts oppositely-charged ions in the fluid. The EDL is made up of two parts- the adsorbed layer and the diffuse layer. The first layer of charge is adsorbed to the grain surface and is essentially immobile. The diffuse layer is made up of mobile ions carrying a net charge relative to the grain, and it is this charge separation (measured as ζ) that makes possible the seismoelectric effects described in this dissertation. intro-EDL [NR]

Biot (1956a,b) predicts that a seismic wave passing through a fluid-saturated porous material will cause a small amount of relative motion between the pore fluid and the grain matrix. There exists an electric potential between the grains and the fluid (called the zeta potential, ζ) at the grain-fluid interface. The so-called "electric double layer" (Shaw, 1992) is a micro-scale (a few molecules thick) region of interaction between the charged outer surface of the grain and ions in the pore fluid (Figure 1.1), but the zeta potential is essential to the macro-scale seismoelectric phenomena that we observe. The charge separation of the electric double layer causes the pore fluid to carry with it a small amount of electric charge when it flows in response to the pressure gradients within a seismic wave. Maxwell's equations predict the electric and magnetic fields that result from this flow of charge. Pride (1994) presents the following governing equations that describe the seismoelectric phenomena in a porous continuum, assuming $e^{-i\omega t}$ time dependence of all fields and displacements:

$$\nabla \times \mathbf{E} = i\omega\mathbf{B}, \tag{1.1}$$

$$\nabla \times \mathbf{H} = -i\omega\mathbf{D} + \mathbf{J}, \tag{1.2}$$

$$\nabla \cdot \tau = -\omega^2\left[\rho\mathbf{u} + \rho_f\mathbf{w}\right], \tag{1.3}$$

$$\mathbf{J} = \sigma\mathbf{E} + L\left[-\nabla p_f + \omega^2\rho_f\mathbf{u}\right], \tag{1.4}$$

$$-i\omega\mathbf{w} = L\mathbf{E} + \frac{k}{\eta}\left[-\nabla p_f + \omega^2\rho_f\mathbf{u}\right], \tag{1.5}$$

$$\mathbf{D} = \epsilon\mathbf{E}, \tag{1.6}$$

$$\mathbf{B} = \mu\mathbf{H}, \tag{1.7}$$

$$\tau = [K_U\nabla \cdot \mathbf{u} + C\nabla \cdot \mathbf{w}]\mathbf{I} + G\left[\nabla\mathbf{u} + \nabla\mathbf{u}^T - \frac{2}{3}\nabla \cdot \mathbf{u}\mathbf{I}\right], \tag{1.8}$$

$$-p_f = C\nabla \cdot \mathbf{u} + M\nabla \cdot \mathbf{w}. \tag{1.9}$$

These equations relate the electric field **E**, the magnetic field **H**, the dielectric displacement **D**, the magnetic flux density **B**, and the electric current density **J** to the particle displacement **u** and the relative grain/fluid displacement **w**. The mechanical response is also characterized by the fluid pressure p_f and stresses described by the bulk stress tensor τ. Other terms in the equations are G the grain framework shear modulus, **I** the identity matrix, ρ the bulk

density, ρ_f the pore fluid density, ω the angular frequency, σ the electrical conductivity, ϵ the electrical permittivity, μ the magnetic permeability, η the fluid viscosity, and k the hydraulic permeability. The electrokinetic coupling coefficient L is a key component of these equations, as it describes the relation between grain/fluid motion and electric fields. If L is set to zero, these equations decouple into Biot's and Maxwell's equations.

The undrained bulk modulus K_U (also known as Gassmann's modulus), and the other coefficients C and M, can be expressed in terms of the bulk moduli of the solid and fluid phases (K_s and K_f) and the bulk modulus of the drained framework K_{fr} as follows:

$$K_U = \frac{K_{fr} + \phi K_f + (1+\phi) K_s D}{1+D}, \tag{1.10}$$

$$C = \frac{K_f + K_s D}{1+D}, \tag{1.11}$$

$$M = \frac{1}{\phi} \frac{K_f}{1+D}, \tag{1.12}$$

with

$$D = \frac{K_f}{\phi K_s^2} \left[(1+\phi) K_s - K_{fr} \right]. \tag{1.13}$$

From a seismoelectric standpoint, the most interesting (or at least the most relevant) of these relations are Equations (1.4) and (1.5) since they are the transport equations that link the electromagnetic and mechanical effects. Equation (1.5) is essentially Darcy's law for water flow caused by a hydraulic head difference (fluid pressure gradient), but it also includes the term $L\mathbf{E}$ which describes how an electric field can cause grain/fluid displacement. The fluid pressure gradient ∇P tends to dominate this equation, however, and it is primarily the pressure gradient that causes the grain/fluid displacement at the heart of seismoelectric phenomena. Equation (1.4) provides an expression of the streaming electric currents (with density $\mathbf{J}$) that form in response to the fluid pressure gradient of the seismic wave. The current $L \nabla P$ caused by the pressure-induced fluid flow is countered by an equal and opposite current ($\sigma \mathbf{E}$) that flows in response to the electric field of the charge separation. For the case of a seismic P-wave, this electric field is the "*coseismic field*" associated with that wave.

A second electric field is predicted by the seismoelectric theory to occur when the coseismic field is disrupted by an interface encountered by the propagating seismic wave. An interface in mechanical or electrical properties causes asymmetrical charge build-up centered at the first Fresnel zone, and results in what can be approximated as an oscillating electric dipole. The associated electromagnetic disturbance propagates with the velocity V_{EM}, corresponding with an electromagnetic wave. In the seismic frequency range, however, an electromagnetic wave has a wavelength on the order of 10^4 or 10^5 m, so the region of interest (up to several tens of meters from the source) is within the diffusive realm and the electromagnetic energy can not be thought of as truly "propagating". We refer to this field as the "*interface response*".

A third electric field predicted by Pride and Haartsen (1996) is created at the location of a directed point source (i.e. a sledgehammer impact). Like the interface response, it propagates/diffuses with velocity V_{EM}. The electromagnetic disturbance created at the directed point source is measured almost immediately by nearby electrodes, and is what we refer to as the "*direct field*". It was first reported by Haines et al. (2004), and is analyzed in Chapter 2 of this dissertation.

DISSERTATION RESEARCH GOALS

Even after the extensive progress made during the last sixty years, and particularly during the last decade, the seismoelectric method was not yet ready for use in solving real geophysical problems. The seismoelectric theory outlined in the previous section suggests that the method could provide useful new information about subsurface interfaces and flow property variations, but the development of field methods lagged behind the theory. While many publications showed evidence of the seismoelectric interface response, none showed more than one or two examples of such. Most published signals were the result of a fortuitous choice of field site rather than a well-thought out experimental design with specific targets in mind. Very few publications showed data from more than a single day of field work, and fewer still showed data from more than one site or experimental set-up. The development of a set of field methods for seismoelectric data collection remained an elusive goal, and an extensive set of field experiments testing various data collection options was yet to be conducted. Additionally,

very little thought had been put into the serious issue of seismoelectric data processing. The interface response signal is extremely weak, such that observation of the signal from layers deeper than a few meters requires major improvements in the signal-to-noise ratio. In addition to these data collection and data processing needs, improvements in data interpretation were an obvious necessity. In order to advance the science, it was necessary to better understand the observed signals, and the sorts of targets that might be imaged with the seismoelectric method. This is the starting point from which my dissertation research began.

This dissertation is a presentation of seismoelectric research designed to fill the primary voids just described. Beginning where other authors left off, I began a research program involving extensive field experimentation centered around a unique experimental geometry. These field experiments included the testing of many different seismic sources and data collection options. In the process I identified a previously undocumented seismoelectric phenomenon, the direct field, and gained a thorough understanding of exactly what happens when soil is struck with a sledgehammer. These field experiments were accompanied by the development of data processing methods specifically designed to solve the problem of seismoelectric signal/noise separation. The data processing methods were tested on real data from the field experiments as well as synthetic seismoelectric data. This dissertation presents results from a new numerical algorithm for simulation of seismoelectric phenomena in media of arbitrary two-dimensional heterogeneity. These models help us to better understand the sorts of situations where the seismoelectric method will be most likely to provide useful new subsurface information and allow me to simulate many surveys that my budget does not allow me to conduct.

This thesis has three main chapters. Chapter 2 describes experimental methods and field observations. It includes results from seismic source comparisons and different receiver options. It includes a presentation of the direct field as well. The bulk of the material in Chapter 2 is included in the paper “Field methods for seismoelectric surveys and identification of three distinct seismoelectric phenomena”, which will be submitted to the journal Geophysics and authored by S. Haines, S. Pride, S. Klemperer, and B. Biondi. Chapter 3 presents a comparison of several different signal/noise separation techniques, and other essential aspects of seismoelectric data processing. These processing techniques are tested on synthetic and real data

examples. The bulk of the material in Chapter 3 makes up a paper ("Seismoelectric data processing") that will be submitted to the journal Geophysics, authored by S. Haines, A. Guitton, and B. Biondi. Chapter 4 presents a "grand finale" seismoelectric image of the two vertical targets in the shallow subsurface and numerical simulations of the same experiment. Additional models are used to examine the applications where the seismoelectric method holds promise, and the limitations that exist on these applications. This work makes up a paper titled "Seismoelectric imaging of shallow targets: real and synthetic examples" that will be submitted to Geophysics and authored by S. Haines, S. Pride, and S. Klemperer.

In addition, this dissertation has two appendices. Appendix A describes the numerical algorithm used in the modeling that produced the synthetic simulations presented. Appendix B describes the design, construction, and testing, of an electromagnetic vibrator source that proved ineffective for seismoelectric work, but does hold promise for high-resolution seismic surveys. I describe this work in the paper "Design and application, of an electromagnetic vibrator seismic source" that will be submitted to the Journal of Environmental and Engineering Geophysics, authored by S. Haines.

The combined results of this research project provide a stepping stone on which further method development may be based. I conclude that the seismoelectric method can be used to image shallow layers, but that certain constraints must be kept in mind. The method will not solve all problems in all places, but it can provide information not available with any other method. The most successful applications of the seismoelectric method will likely be those that employ survey geometries that separate the signals of interest, such as by the use of bore hole geometries.

Chapter 2

Field Methods

INTRODUCTION

The breadth and resolution of information that can be gained from geophysical studies is generally exceeded by the expectations and needs of those who use the information. In particular, geophysical surveys are limited in their ability to image thin layers and to adequately characterize permeability variation, often leading to large uncertainties in fluid-flow models. Electrokinetic phenomena represent the inter-relation between mechanical energy, fluid flow, and electrical energy, and promise to provide otherwise unattainable subsurface information. Two distinct types of seismoelectric phenomena have been observed in the field, beginning with the initial experiments conducted by Thompson (1936) and continuing with experiments by Martner and Sparks (1959), Long and Rivers (1975), Thompson and Gist (1993), Butler et al. (1996), Garambois and Dietrich (2001), and our group (Haines et al., 2004), among others. Development of the relevant seismoelectric theory by Neev and Yeatts (1989), Pride (1994), Pride and Haartsen (1996), and Haartsen and Pride (1997) affords us a clearer understanding of the physics behind the observed phenomena and suggests that the seismoelectric method could provide useful new information about thin layers and flow properties.

A compressional wave traveling through a fluid-saturated porous material creates a fluid pressure gradient that induces pore fluid flow. Due to the electric double layer (Shaw, 1992)

that exists at the grain-fluid boundary, the pore fluid movement transports a small (but consequential) amount of electric charge relative to the fixed charge on the adjacent grains (Figure 2.1. The strength and polarity of the electric double layer varies with grain composition and fluid chemistry, but often (such as for quartz grains) the grain surface charge is negative and the fluid positive. The net flow of charge relative to the grains is a streaming electrical current that creates a charge separation within a compressional wave, at the scale of the seismic wavelet. This charge separation has an associated electric field which we refer to as the "coseismic" field that is co-located with a compressional (P) wave (Pride, 1994) (Figure 2.2a). This is the most commonly and most easily observed seismoelectric phenomenon. It differs from the horizontal component of ground acceleration only by a frequency-independent scalar because of the close relation between grain/fluid acceleration and the coseismic field.

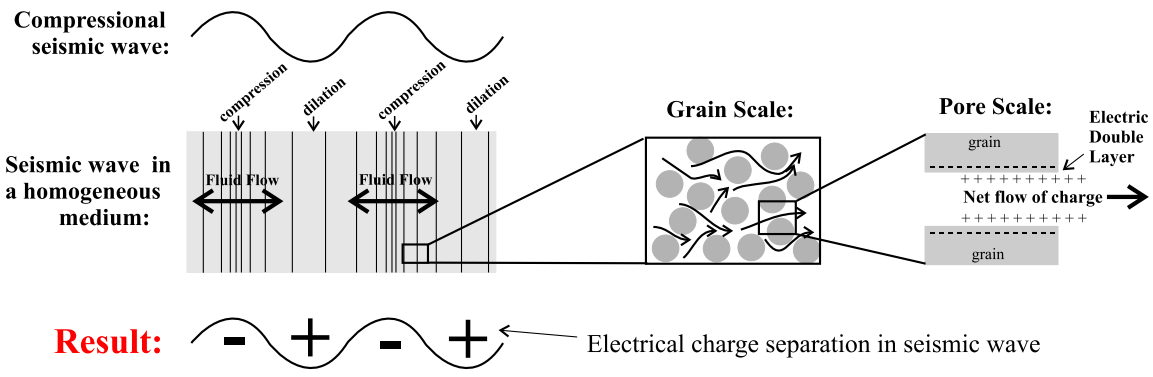

Figure 2.1: Seismoelectric phenomena depend on the charge separation created by streaming currents that flow in response to the pressure gradient of a seismic wave. The electric double layer is responsible for streaming currents at the grain scale. field-esbasics [NR]

The second recognized seismoelectric phenomenon occurs when the P-wave encounters an interface in material properties (elastic, chemical, flow-related, etc). The charge separation in the wave is disturbed (Figure 2.2b), causing asymmetry in the charge distribution, and resulting in what can be approximated as an oscillating electric dipole with its dominant contribution coming from the first seismic Fresnel zone (Thompson and Gist, 1993; Haartsen and Pride, 1997). Essentially, the entire region of the first Fresnel zone acts as a disk of vertical electric dipoles. Since the electromagnetic wavelengths at seismic frequencies are typically enormous compared to the depth of the interface, induction effects can be neglected, and the

electric fields generated at the interface can be modeled as being quasi-static. The resulting electric potential distribution is that of a quasi-static dipole. If q is the magnitude of the seismically-induced charge that is separated across the interface by distance d, and if the earth is approximated as being uniform, then a crude estimate of the potential distribution is simply (Landau and Lifshitz, 1984)

$$\Phi(x,z) = \frac{qd}{4\pi\epsilon}\left[\frac{z-h}{(x^2+(z-h)^2)^{3/2}} - \frac{z+h}{(x^2+(z+h)^2)^{3/2}}\right], \tag{2.1}$$

where x is the lateral offset, z is the depth, h is the depth of the interface, and ϵ is the electrical permittivity. This field (Figure 2.2b), called the "interface response," can be measured almost immediately at the Earth's surface since the travel-time of electromagnetic radiation is negligible compared with that of seismic waves ($V_{EM} \approx 10^5 V_P$). Unlike the coseismic field, which contains information only about the material immediately surrounding the receiver dipole, the interface response can provide useful new subsurface information. In particular, the interface response occurs even for very thin layers (e.g. 10^{-2} m), such as thin fractures in otherwise solid rock, or a thin impermeable layer in an aquifer or reservoir.

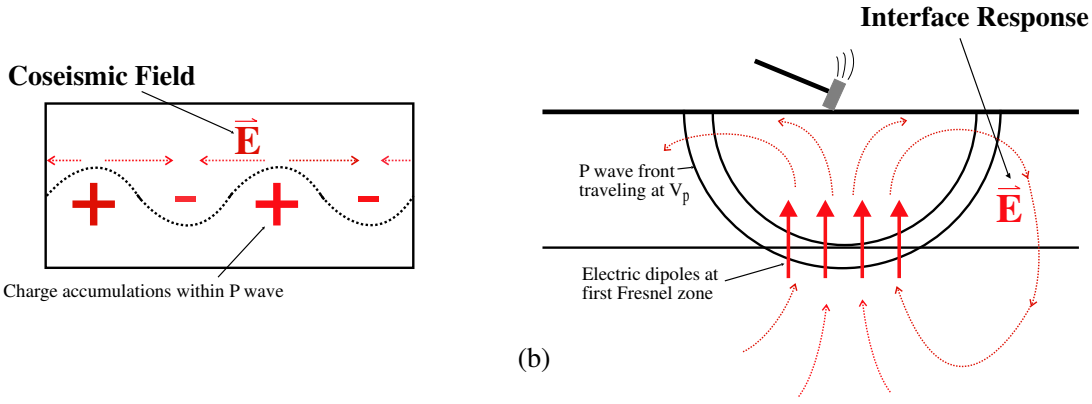

Figure 2.2: Two types of seismoelectric phenomena commonly measured in the field: (a) the coseismic field of a P-wave (due to the charge accumulations "+" and "-"), and (b) the interface response created when the P-wave hits an interface at depth. field-2effects [NR]

A third type of seismoelectric phenomenon is predicted by Pride and Haartsen (1996) and its observation was first reported by Haines et al. (2004). We term this the "direct field", as it can be thought of as analogous to the seismic direct wave. A directed point source (e.g. a

sledgehammer impact, as opposed to an isotropic explosion) creates an enhanced fluid pressure on one side of the impact point (beneath the hammer strike plate) and a decreased pressure on the other. The fluid-pressure distribution equilibrates, which results in a charge separation due to the electrokinetic mechanism previously discussed. The charge separation at a vertical impact point will have a strong vertical dipole component and the associated electric field emanating from the region of impact is what we call the "direct field"(Figure 2.3). Similar to the interface response, the direct field shows the amplitude pattern of a dipole (Equation 2.1) and reversed polarity on opposite sides of the shot point. It occurs at the time of the source impulse, and continues until the soil has relaxed to its original state.

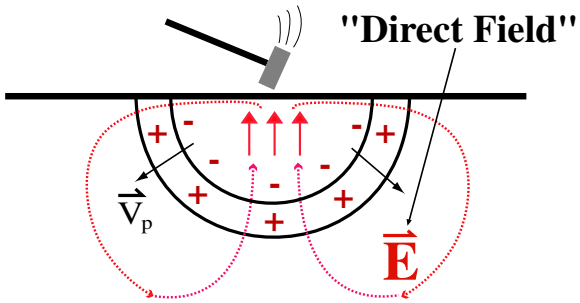

Figure 2.3: Schematic representation of the seismoelectric direct field. The pressure wave from the source creates an asymmetrical charge distribution that acts as an oscillating electric dipole. field-direct_field [NR]

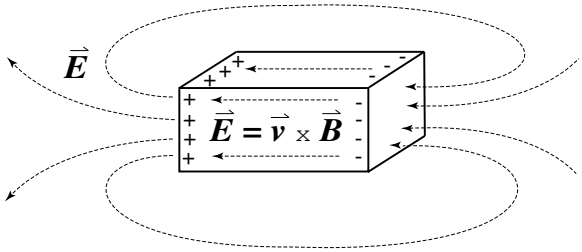

Figure 2.4: Schematic representation of the Lorentz field. An electric field **E** results from the motion **v** of the metal hammer plate in the Earth's magnetic field **B**. field-lorentz [NR]

If the source is a hammer impacting a metal plate, seismoelectric data may also demonstrate the existence of a similar-looking, but entirely unrelated, electric field. This is the field created by moving a conductor (the metal plate) with velocity **v** within the Earth's magnetic field **B**, described by the Lorentz equation (Landau and Lifshitz, 1984):

$$\mathbf{E} = \mathbf{v} \times \mathbf{B}. \tag{2.2}$$

Because shallow seismoelectric experiments are frequently carried out with a sledgehammer source (Butler et al., 1996; Garambois and Dietrich, 2001; Haines et al., 2003), it is essential that we consider the possibility of this field as we interpret our data.

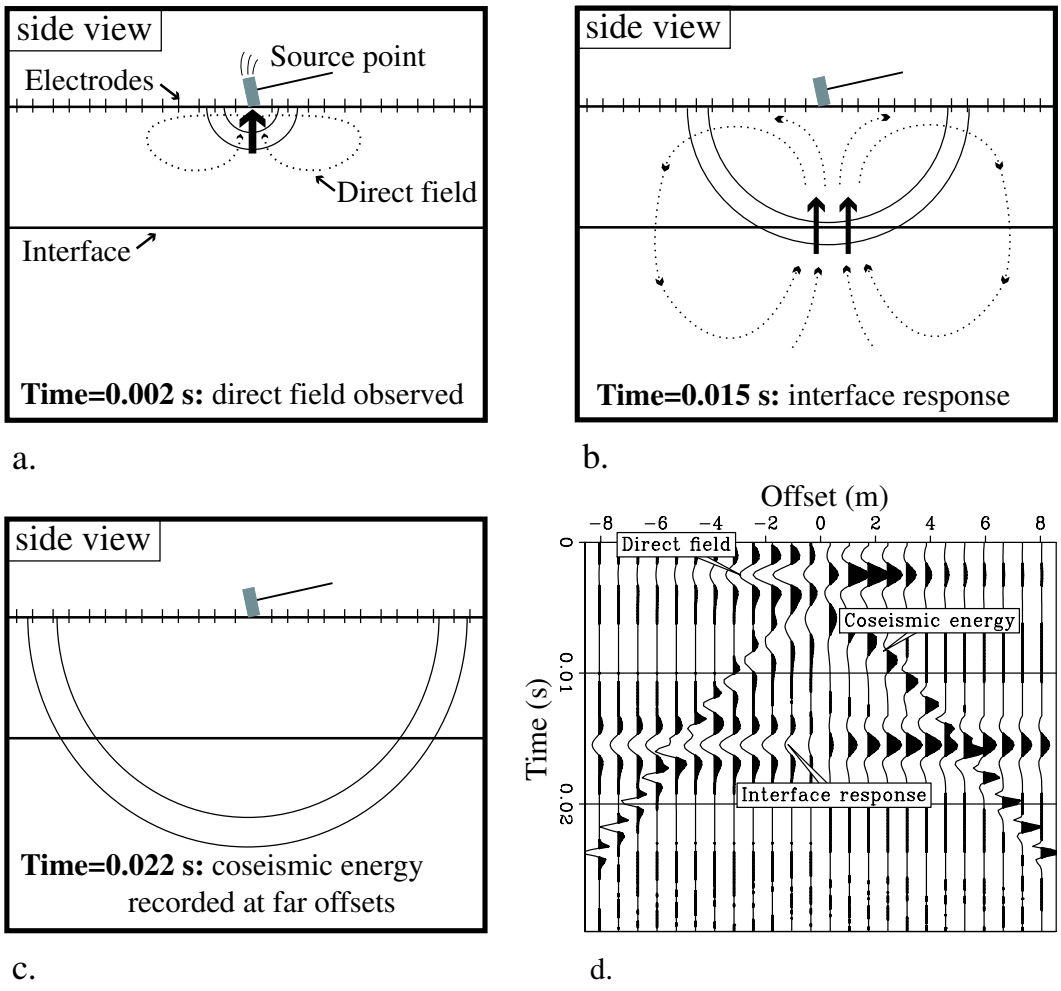

Figure 2.5: Cartoon schematic of a "standard" in-line geometry seismoelectric survey and simplified synthetic data. The three cartoons are side-view sketches of the same location, but at different points in time. The source point is in the center of a line of electrodes at the surface, above a single subsurface interface. a) The hammer strikes the soil at time=0, and creates the direct field which we observe during the next several milliseconds. b) At time=0.015 s, the seismic wave is propagating through the interface, and creates the interface response at the first Fresnel zone. c) The coseismic field continues to move along the electrode array at the velocity of the seismic wave that carries it. Note that the reflected seismic wave from the interface has been neglected for simplicity. d) Synthetic seismoelectric data corresponding with the cartoon sketches, with direct field, interface response, and coseismic energy labeled. field-cartoon_inline [NR]

The seismoelectric method can potentially provide valuable information about important subsurface targets that can not be imaged using other geophysical methods, including information about changes in flow properties. The seismoelectric interface response is created at changes in flow properties, even for layers too thin to be imaged seismically. The interface response is sensitive to other properties as well (e.g. electric double-layer strength, rigidity, etc.), and is generally a very weak signal. Seismoelectric data (when collected with a geometry similar to conventional surface seismic data) include simultaneous recordings of the interface response from subsurface layers and unwanted coseismic fields (Figure 2.5b and d). The direct field (and perhaps also the Lorentz field) may also be recorded along with the other two forms of seismoelectric response, but these occur only for a brief period after time zero so do not present a problem in surveys targeting layers deeper than a few meters (Figure 2.5a and d). The coseismic and interface fields are of comparable magnitude when the recording antennas are within a seismic wavelength of the interface. However, since the interface response field is essentially a dipole, it falls off as the distance cubed for receivers removed from the interface and can thus be many orders of magnitude smaller than the coseismic fields, especially as target depth increases. Coseismic energy therefore represents a formidable form of coherent source-generated noise that can obscure large parts of the seismoelectric record. So although the seismoelectric method has great promise, we must better understand seismoelectric effects and data collection before the method will be viable. We present here a novel experimental design that enables us to separately record and identify the three seismoelectric fields described above. Such highly-controlled field experiments help us to refine field experimental methods and provide insight into the seismoelectric phenomena themselves.

We begin by describing our field methods, then describe our specific experimental designs and explore the effects of varying various experimental variables (seismic sources, electrode receivers, etc). We provide a careful interpretation of our field data and discuss data examples. We carefully examine the direct and Lorentz fields as well as the observed interface response.

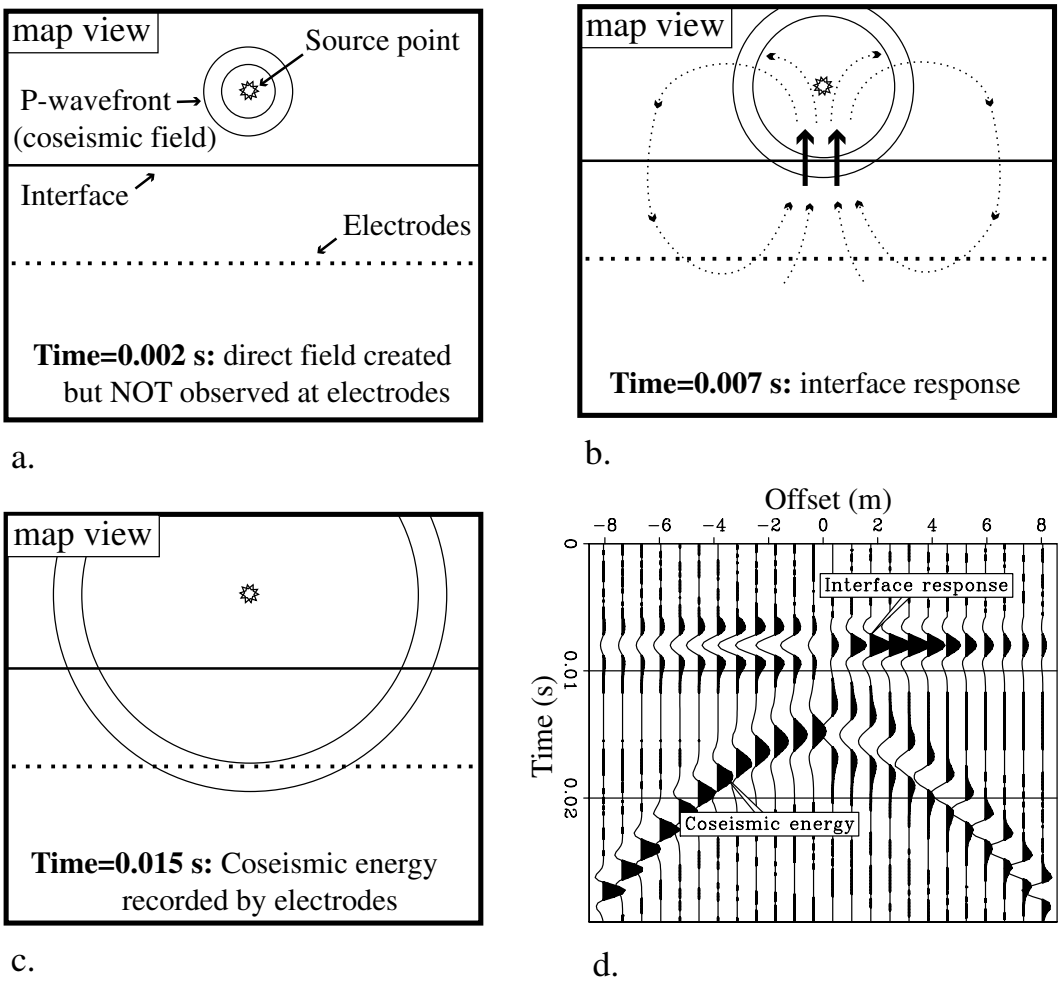

Figure 2.6: Cartoon schematic of a fan-geometry seismoelectric survey along with simplified synthetic data. The three cartoons are map-view sketches of the same location, but at different points in time. The source and receivers are on opposite sides of a vertical interface. a) The hammer strikes the soil at time=0, and creates the direct field. We do not observe the direct field at the electrodes, however, because it is the field of a vertical dipole at the source point, which is far from the electrodes. Also, the horizontal part of the field is radial, and so roughly orthogonal to the electrode dipoles. b) At time=0.007 s, the seismic wave is propagating through the interface, and creates the interface response at the first Fresnel zone. c) The coseismic field continues to propagate outward, and we observe it at the electrodes at time=0.015 s. d) Synthetic seismoelectric data corresponding with the cartoon sketches, with interface response, and coseismic energy labeled. field-cartoon_fan [NR]

FIELD SITES

Site I: The Trench experiment

By placing source and receivers on opposite sides of a vertical interface it is possible to record the interface response before the coseismic energy. The seismic wave encounters the interface and creates the interface response before the seismic wave (and associated coseismic field) reaches the receiver electrodes (Figure 2.6d). In order to achieve this geometry, we constructed a trench ∼0.6 m wide, ∼2 m deep, and ∼18 m long, lined with plastic, and filled with wet sand, at a site with relatively homogeneous clayey soil to at least 4 m depth (Figures 2.7 and 2.8). The site is a small meadow at the Pride Mountain Vineyards on the ridge between Napa and Sonoma Valleys in St. Helena, CA.

Figure 2.7: Site construction. The first trench is 18 meters long, two meters deep, and about 0.6 m wide. It is dug in relatively homogeneous clayey soil. field-digging_crop [NR]

After successfully observing the interface response with the one-trench geometry (Figures 2.9 and 2.10), we constructed a second trench (Figure 2.11) two meters from the first, in order to increase the experiment complexity. It is deeper (∼3 m deep in the center), narrower (∼0.5 m wide), and lacks the plastic sheeting that lines the first trench.

The geometry of this field site provides a great deal of versatility in recording geometry. We can place sources and receivers on opposite sides of the trenches in order to record the interface response before the coseismic energy, simulating a cross-well type geometry ("Fan-geometry source point", in Figure 2.11). To simulate a "typical" surface survey of subsurface

Figure 2.8: The first trench was lined with plastic and filled with sand and water. The second trench was not lined with plastic. field-fill_1 [NR]

Figure 2.9: Data acquisition prior to construction of second trench, using "fan" geometry. Source point in this photo is one meter from one side of the trench, and receiver line is one meter from the opposite side of the trench. Shooter is standing in the trench, with PVC piezometers on either side of him that are used to measure water level in the trench. field-steve2 [NR]

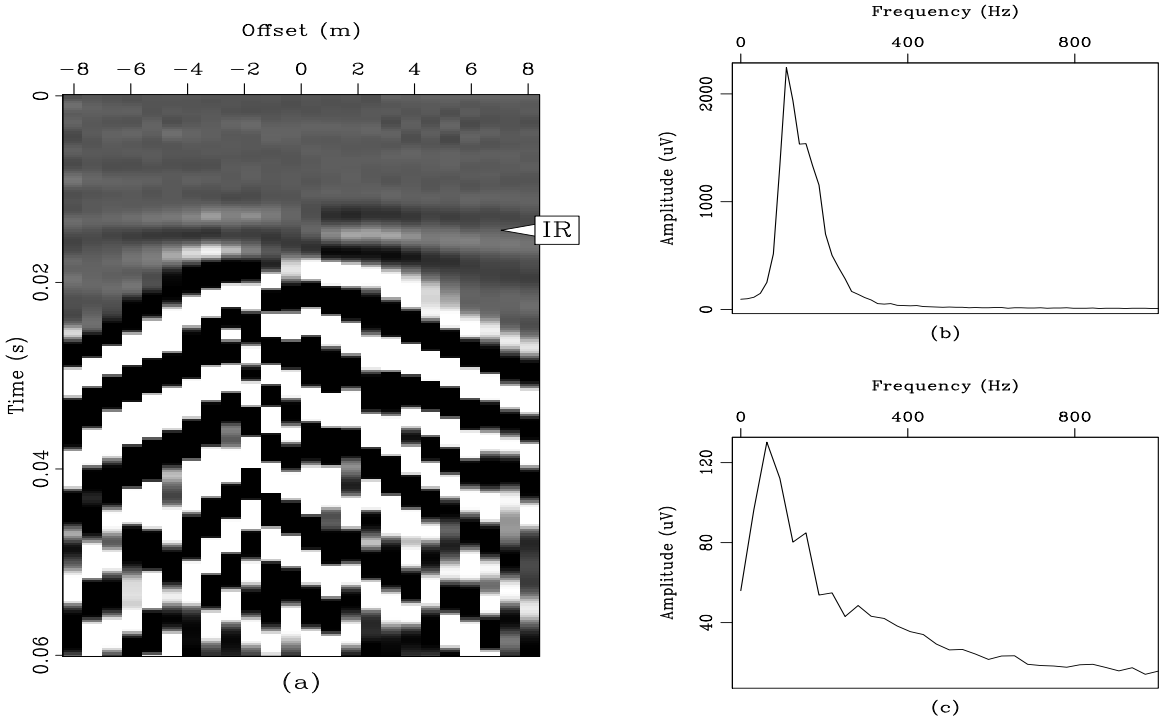

Figure 2.10: Electric field recordings: a)"Fan" geometry shot record recorded with source and receivers two meters from opposite sides of the first trench (before construction of the second trench). Record is the result of stacking 50 hammer strikes and is shown with 60 Hz energy removed and bandpass filter (120-500 Hz) applied. Note horizontal interface response event at 0.015 seconds, marked "IR". b) Mean spectrum of window of data shown in part a, from 0.012 s to 0.06 s. c) Mean spectrum of background noise of data in part a, spectrum is calculated from window of data from -0.01 s (pre-trigger) to 0.01 s, and has not been frequency-filtered. field-basic526 [ER]

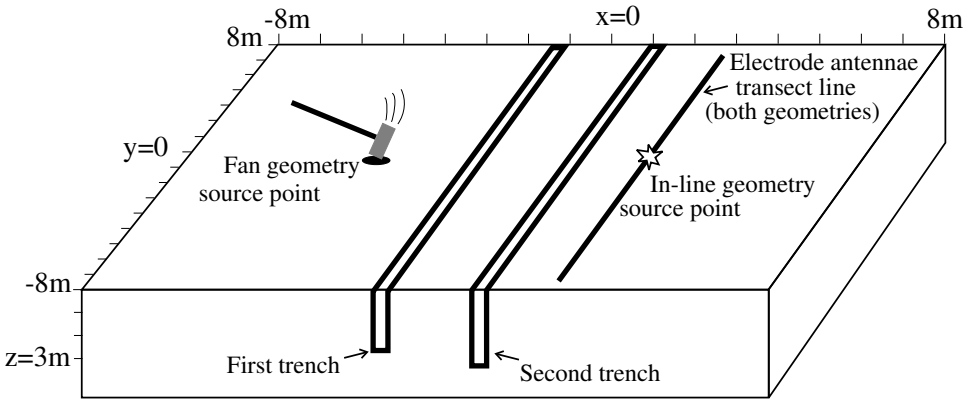

Figure 2.11: Layout of vineyard field site after construction of second trench. Seismoelectric data were acquired with both recording geometries, as shown. The fan-profile geometry features the source point opposite the electrodes, while the in-line geometry features the source point in the center of the electrode array. field-new_layout [NR]

targets (the geometry generally used in surface seismic, and shown in Figure 2.2b) we also collect data with the source located on the same side of the trench as the receivers ("In-line source point", in Figure 2.11). In this case the coseismic energy and interface response are recorded simultaneously. In addition, we conducted surveys in the same meadow with the "in-line" geometry, ∼20 m from the trenches, for control purposes. We also conducted one experiment with seismic sources in the center of a circular array of electrode receivers; this is described later in more detail.

Site II: Thompson Tree Farm

We conducted additional experiments at the Thompson redwood tree farm in the Santa Cruz Mountains on the San Francisco peninsula. This site is far removed from cultural noise, including the power grid, so is ideal for collecting quiet electrical data. The site itself is a small level clearing with clayey soil. Seismic and geologic data suggest that bedrock is a few meters deep, and that the soil/bedrock contact is very diffuse (George Thompson, personal communication).

We use this site to test basic field methodologies and to test site-related variables. We

have not recorded, and do not expect to record, strong interface response energy at this site. Using the in-line geometry we conducted a series of experiments with different types of impact source in order to better understand the effects of source composition (e.g. wood, plastic, and metal), as well as the triggering circuitry.

SEISMOELECTRIC DATA COLLECTION

We collect seismoelectric data using a standard engineering seismograph, in our case a Geometrics 24-channel Geode, sometimes augmented with a second 24-channel Geode. The geophone cables are outfitted with electrode pairs rather than geophones. Thus each channel of the seismograph records the voltage difference across a given pair of electrodes (essentially acting as a 24-channel voltmeter). Our electrodes are 0.95-cm (3/8-inch) stainless steel rods that are ~ 0.7 m long with sharpened tips, pounded almost completely into the ground. We typically use a spacing of $\sim$1 m between the two electrodes in a given pair, and overlap electrode pairs if necessary to achieve station spacing smaller than dipole width. In order to eliminate the resonant electrical noise caused by the lightning protection circuitry in the seismograph, we insulate each channel of the instrument from the electrodes with a 5:1 step-up transformer (Art Thompson, personal communication September 2001). This approach also provides a signal of increased voltage to the recording instrument, which is a benefit as we try to record signals that are close to its sensitivity level. The use of pre-amplifiers would also fulfill both of these objectives, but at greater cost. We find that grounding the seismograph (attaching a wire from the grounding jack on the Geode to a dedicated electrode) helps to maintain data consistency and avoid spurious instrument-related noise.

We have collected well over 300 seismoelectric shot gathers, the vast majority of which employed stacked sledgehammer impacts as the seismic source. Because of the time-variable nature of electrical noise we prefer to perform the final stack in the office after manually removing individual noisy shots. We have tested various hammer plates, including plastic and different metals, to determine strike-to-strike repeatability and to identify any associated electrical noise related to the hammer plate. We generally record 25 or 50 impacts, and stack the 10 to 40 that remain after removal of noisy records. We have also tested various seismic

sources including shotgun, an electromagnetic vibrational source (Appendix B), and chemical explosives. We present comparisons between the resulting data in a later section.

Nearly all of the data presented here are collected using a linear array of electrodes with the source in one of the two previously-mentioned geometries (see Figure 2.11):

- *"in-line" geometry*: Source location is in the center of electrode receiver array, similar to a standard split-spread seismic deployment (Figure 2.5).

- *"fan" geometry*: Source location is a distance away from the center of the receiver array, in a direction perpendicular to the center of the array, similar to a seismic fan deployment (Figure 2.6).

We generally record one-second records at a sample rate of 4000 Hz, including a half-second of pre-trigger recording for noise estimation. Typical signal measurements are on the order of 0.1 mV for the coseismic energy, and 0.001 mV for the interface response in stacked records. Noise levels are typically $\sim$0.01 mV for noise from the electric power grid (at 60 Hz and its harmonics), and $\sim$0.001 mV for other background electrical noise at our vineyard field site. At the tree farm site we find 60 Hz noise levels of $\sim$0.001 mV and background electrical noise at $\sim$0.0002 mV for stacked records.

The development of seismoelectric data collection in some ways mirrors the development of seismic methods many decades ago. Many of the same issues exist- source choice, receiver choice, etc. We have explored many of these options (sources, receiver geometries, electrode dipole widths, etc.) but do not present any results from the use of receiver groups or arrays. While it is possible that receiver groups could be used to enhance our high- (electromagnetic) velocity signal and diminish the low- (seismic) velocity noise, a couple of crude tests did not encourage further experimentation. The primary limitation in our case is budgetary (e.g., with 48 electrodes we can collect 24 channels of non-grouped data, or 6 channels of data from groups of 4 electrode pairs).

Data pre-processing

Raw seismoelectric data are dominated by energy from the power grid at harmonics of 60 Hz. We remove this noise using the sinusoid subtraction technique of Butler and Russell (1993) for all harmonics of 60 Hz up to the Nyquist frequency. For particularly troublesome shot gathers, we achieve better results with a more rigorous, but more computationally intensive, approach described by Butler and Russell (2003). This technique begins with an inversion for the exact frequency of the noise, rather than the assumption that the noise is at 60.00 Hz and its harmonics. This is a particularly important consideration at sites closer to local sources of electrical energy (pumps, generators, etc.) that may not be as precisely 60 Hz as the power grid and also for non-stacked shot gathers (explosives, etc., as opposed to hammer stacking) which do not average out small temporal variations in the 60 Hz field.

Coseismic fields are generally lower in frequency than the interface response due to attenuation resulting from a greater distance of travel as a seismic wave, so we use a low-cut filter ($\sim$120 Hz) to begin the process of noise removal. Because the electromagnetic wavelength and skin depth associated with the interface response is on the order of one kilometer, our experiments are within the electrostatic nearfield, and so attenuation of the electromagnetic energy is negligible.) We employ a high-cut filter ($\sim$500 Hz) to minimize background noise that can obscure weaker arrivals. Figure 2.10 shows a typical shot gather after these processing steps. We do not find any evidence of data contamination by AM radio broadcasts, a problem encountered using similar instrumentation at other sites (Karl Butler, personal communication, 2003). This problem is likely site-dependent, and seems not to be present at our sites.

Data interpretation

In order to present a comprehensive discussion of seismoelectric data collection options, we must first provide the reader with our interpretations of the different types of electric fields observed in field data gathers. Support for these interpretations is provided in a later section.

Figure 2.12 shows a 24-channel seismoelectric shot gather collected with sledgehammer impacts on a metal hammer plate located in the center of the electrode array. The coseismic

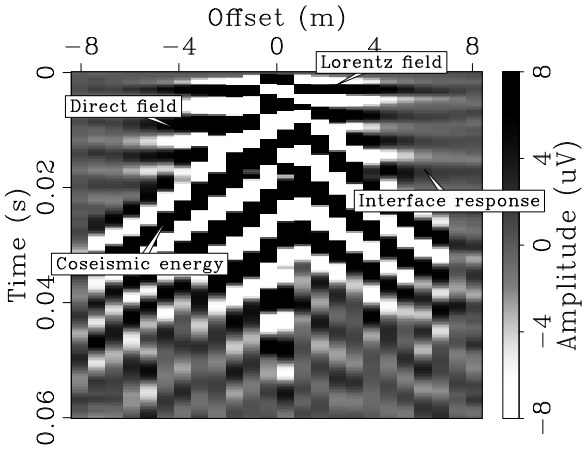

Figure 2.12: Seismoelectric in-line geometry shot gather with interpreted arrivals marked. Justification for these interpretations is provided later in this paper. field-interp [ER]

electric field, propagating at ∼400 m/s, is clearly visible, along with the direct field (flat events in the upper ∼15 ms, showing a polarity reversal on opposite sides of the shot point). The Lorentz field is also a flat arrival in the first part of the shot record, but may be distinguished from the direct field because it does not show the polarity reversal. An interface response event is also identified; it too shows a polarity reversal and no moveout (flat arrival), and is identified on the basis of travel time (corresponding to when the seismic wave first hits the trench).

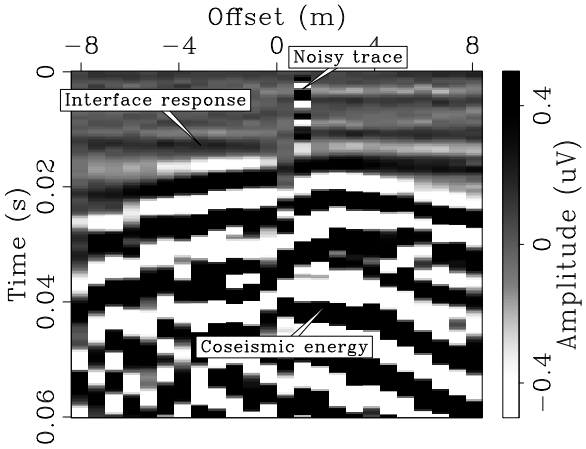

Figure 2.13: Seismoelectric fan-profile shot gather with interpreted arrivals marked. Justification for these interpretations is provided later in this article. field-fan_interp [ER]

Figure 2.13 shows a 24-channel seismoelectric fan-profile shot gather collected with sledge-hammer impacts on a metal hammer plate located across the trenches from the center of the electrode array. The coseismic energy is labeled, as is an interface response arrival from the trenches; the direct and Lorentz fields are not observed because the receivers are distant from the shot location.

Electrode coupling

When the ground is dry, we improve electrode coupling by wetting each electrode hole thoroughly with water. Each electrode is pounded nearly all the way into the soil, pulled out, and the hole thoroughly soaked with water before the electrode is pounded fully into the soil. We find that the addition of conductive agents such as salts or bentonite clay offers only minimal improvement over tap water for our generally clay-rich field areas. We qualitatively estimate coupling quality by measuring the resistance across a given pair of electrodes using a low-cost DC ohmmeter. Because the measured resistance is highly impacted by local ion effects at the electrode/soil contact, the measured resistance varies with time as the DC current from the ohmmeter passes between the electrodes. For this reason we measure the resistance in both directions, and prefer to find an average resistance of less than about 100 ohms. The use of an AC Ohmmeter would be preferable, and would provide a more reliable measure of resistance.

Electrode dipole width

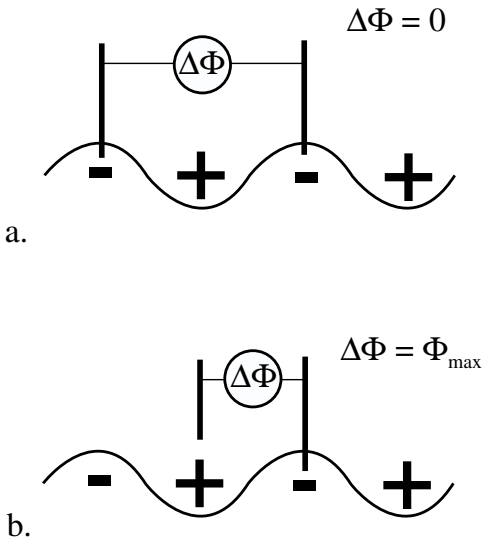

Figure 2.14: Schematic showing the relation between electrode spacing, wavelength, and the measured coseismic electric field. a) The dipole width is the same as the seismic wavelength, so no signal is measured. b) The dipole width is half the wavelength, so the maximum signal is measured. field-widths [NR]

Simple geometric relations suggest that the width of the electrode dipole used to record seismoelectric energy will have an impact on the recorded amplitude of various (apparent) wavelengths in very much the same way that geophone groups are used to suppress certain

Table 2.1: Expected positions of zeros in amplitude spectra

Electrode dipole width	f_{zero}'s
1.05 m	381, 762, 1143... Hz
2.45 m	163, 327, 489... Hz
3.85 m	104, 208, 311, 415... Hz
5.25 m	76, 152, 229, 304... Hz

apparent wavelengths in seismic surveys. Figure 2.14 shows the basic concept. When the electrode dipole width is the same as the apparent wavelength, the recorded signal will be zero (as in Figure 2.14a), but when the electrode dipole width is half the apparent wavelength, the recorded signal will be maximum. It is more realistic to consider this effect as a function of frequency f. Zeros in the frequency response (f_{zero}), corresponding with a given electrode dipole width w, should occur at

$$f_{zero} = \frac{n\,V_{app}}{w}, \quad \text{where } n = 1,2,3... \tag{2.3}$$

for a seismic wave traveling with an apparent velocity V_{app}. We can quickly see that for direct field or interface response fields arriving at V_{EM} ($\sim 10^3$ V_p), the zeros will occur at very high frequencies and dipole width will not impact frequency spectrum of the recorded signal. However, for arrivals at seismic velocities (the coseismic field), we do expect to see a relation between the frequency spectra of recorded signals, and the electrode width used for measurement. Because this effect could provide a means for eliminating certain frequencies (such as part of the coseismic energy), we investigate it by comparing data collected with differing electrode dipole spacings.

We collected a series of shot gathers at the vineyard site with an off-end sledgehammer source and electrode dipole widths ranging from 1.05 to 5.25 m (Figure 2.15). Spectra for each dipole width are shown at right. The spectra are calculated after a 50 Hz low-cut filter and the data are plotted with a bandpass filter of 100 to 500 Hz. The displayed spectra are the result of stacking spectra from 6 traces of offsets of 4 to 8 meters, selected to avoid the high-amplitude near-offset traces, and the predominantly low-frequency longer-offset traces.

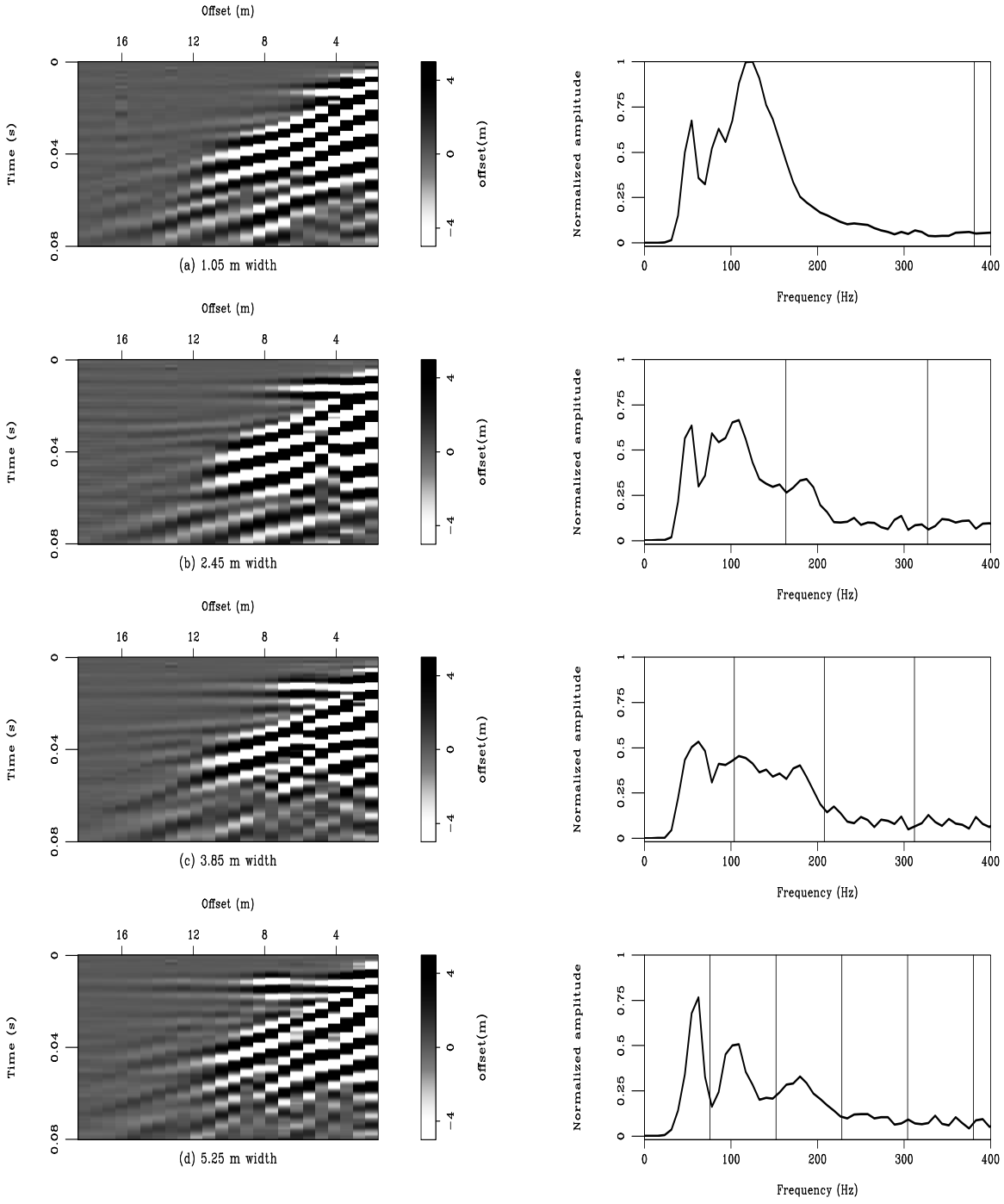

Figure 2.15: Seismoelectric data collected with varied dipole width on the left, with corresponding spectra at right. Vertical lines in the spectra plots show the locations of expected zeros based on a velocity of 400 m/s. field-width_data [ER,M]

We use the time window of 0.02 to 0.1 s for the spectra to avoid the direct field energy in the upper 0.02 s of the records. An exponential gain of (frequency)$^{1.7}$ has been applied to the spectra so that the strong low frequencies do not entirely dominate the displays. We assume a velocity of V=400m/s for the targeted coseismic energy, and calculate expected positions of zeros in the frequency spectra for each electrode dipole width (Table 2.1, and plotted as black lines on spectra in Figure 2.15).

For a dipole spacing of 1.05 m, we do not expect to see any zeros in the frequency range generally observed for the hammer (the first f_{zero} occurs at 381 Hz). So the data for this width (Figure 2.15a) are used as a reference against which other data may be compared. For w = 2.45 m, we expect to see an f_{zero} at 163 Hz, and we do observe a significant reduction of frequencies around 163 Hz when comparing the spectra of Figure 2.15b with that in Figure 2.15a. For w = 3.85 m, we expect f_{zero}'s at 104 and 208 Hz, and indeed we do observe a relative lack of ∼100 Hz energy in the data shown in Figure 2.15c. For w = 5.25 m we expect f_{zero}'s at 76 and 152 Hz, and again observe that these frequencies are nearly absent in Figure 2.15d. We also observe that the amplitude of the recorded direct field energy (flat events in the upper ∼20 ms) increases with dipole width, as is expected for such an electric field. Fit to the predictions of Equation (2.3) is far from perfect, but the general trends are honored (particularly for the wider electrode pairs). We attribute the misfit to the simplicity assumed in our prediction (we do not take into account surface waves, soil inhomogeneities, etc).

Our experiments confirm that electrode dipole width impacts the frequency response of the recorded data, and that for our site, a width of 5.25 m most increases the amplitude of the flat direct field energy relative to the coseismic energy. While this is valuable in that the direct field is similar to the sought-after interface response, we also note that by eliminating certain frequencies of the coseismic energy we have disrupted the character of the wave form. Our ultimate goal is to produce a seismoelectric record showing only interface response energy after signal processing. Because the coseismic energy in Figure 2.15a is the most predictable (regular), it will be the most easily removed, and so we consider smaller electrode dipole widths (∼1 m) to be preferable, although they do result in a lower signal-to-noise ratio in the raw shot gathers.

Geophone/electrode interaction

As noted previously, particle acceleration is closely related to the coseismic field within the passing seismic wave. Thus the collection of horizontal geophone data (oriented parallel to the electrode dipole) may be advantageous for data verification and/or for use in the removal of coseismic energy from the seismoelectric record. Because seismic sources are seldom perfectly repeatable, it is preferable to record these data simultaneously. However, this practice raises the concern that the moving geophone magnet may create an electric field that corrupts the electrode data.

We address this problem by comparing seismoelectric gathers collected with and without geophones present. Figure 2.16a and d show data recorded in the standard fashion, with the source point off-end and in-line, without geophones anywhere nearby. Figure 2.16b and e show data recorded a few minutes later by the same electrode array, but with actively-recording horizontal geophones (Mark Products L-28) in the centers of the electrode dipoles. The associated geophone data are shown in Figure 2.16 c and f. Figure 2.16 a and b are virtually indistinguishable, as are the data in Figure 2.16 d and e, so we conclude that the simultaneous recording of geophone data with seismoelectric data does not present a problem.

Garambois and Dietrich (2001) demonstrate that for a P-wave the horizontal component of the coseismic field (E_x) and horizontal particle acceleration (a_x) should differ only in amplitude and a small phase adjustment, and show field data confirming this close relation. We compare our own geophone and electrical data (same data as Figure 2.16b and c) in Figure 2.17, displayed with a bandpass filter of 90 to 190 Hz. The electric field E_x is plotted as a dashed line and is plotted a_x as a solid line for each offset. At the nearer offsets we see a reasonable fit of E_x to a_x, but this fit is lost at the longer offsets. It should be noted also that the goodness of fit displayed in Figure 2.17 was achieved in part by careful choice of the included frequencies. Inclusion of a broader frequency band shows that the frequency response of our geophones is considerably different from that of our electrode array, as can also be seen by visual inspection of the data in Figure 2.16. In particular, the electrical data tend to contain more low-frequency energy, while our geophones show generally more high-frequency energy and seem to show some resonance later in the time window (0.08 to 0.12 s, for the geophone

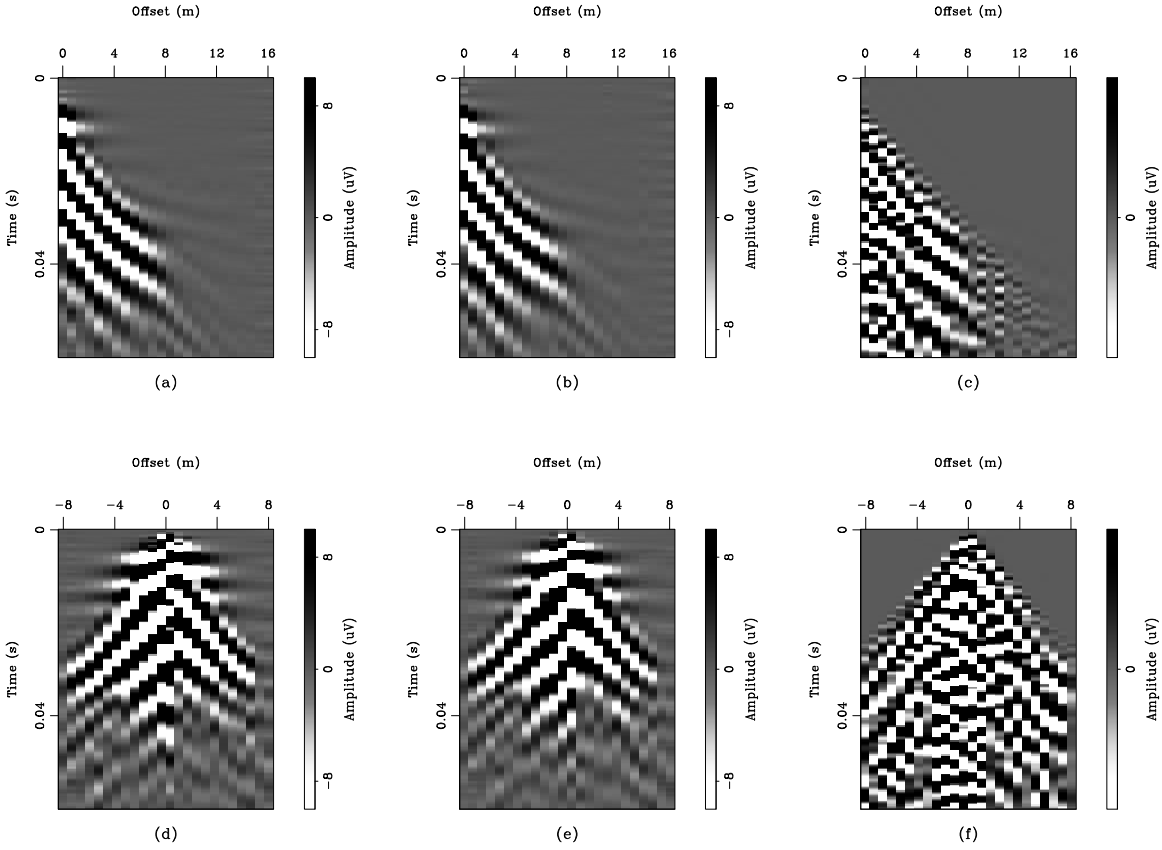

Figure 2.16: Off-end recording (source 2 m from center of first electrode pair with a) just electrodes b) horizontal geophones in the centers of each electrode pair and c) the corresponding horizontal geophone data. In-line (center source) recording with d) just electrodes e) horizontal geophones in the centers of each electrode pair and f) the corresponding horizontal geophone data. Note that data shown in a and b are indistinguishable, as are data in d and e. field-phone_comp [ER,M]

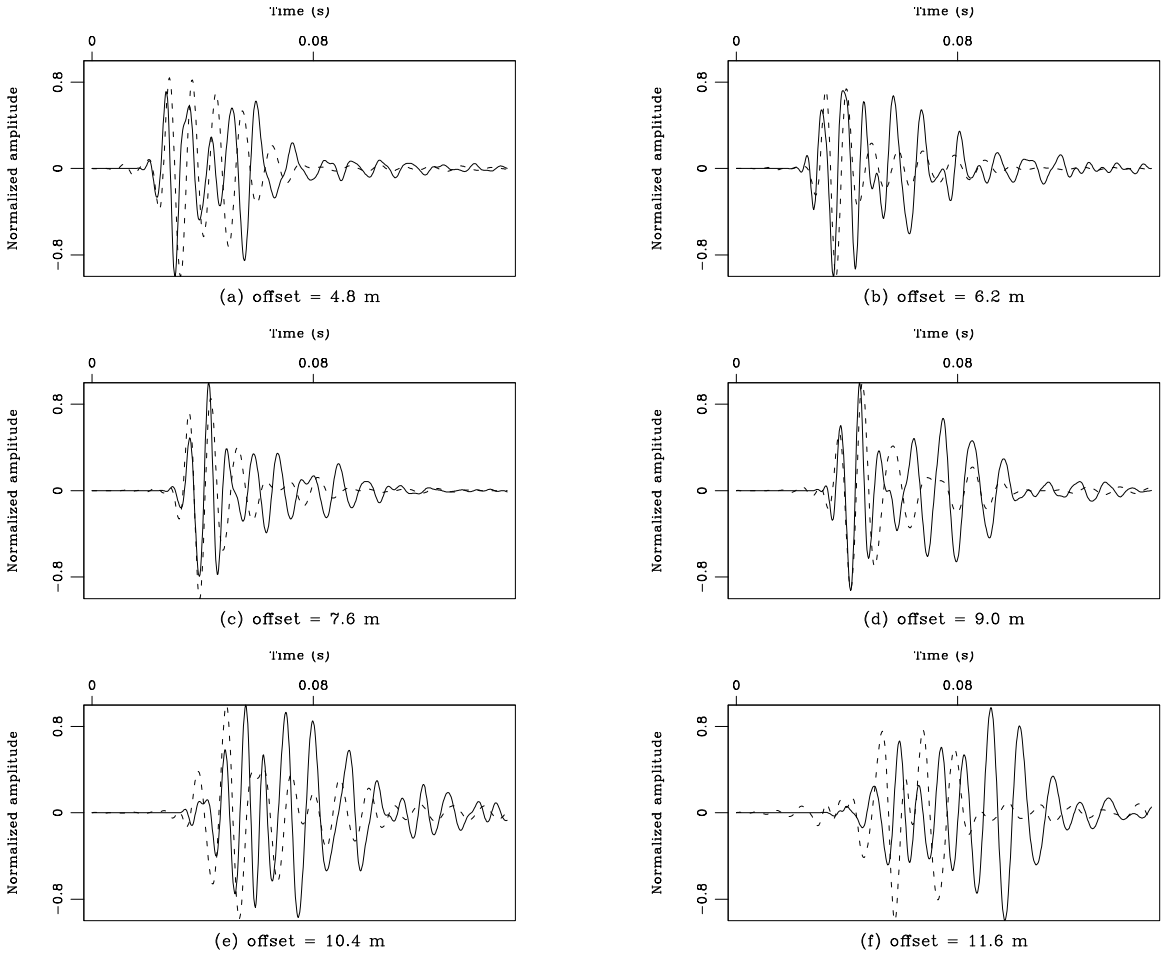

Figure 2.17: Horizontal particle acceleration (solid lines) and horizontal electric field (dashed lines) for traces at various offsets, as marked. Note goodness of fit, particularly for shorter offsets, and earlier in the arrival. Data are the same as shown in Figure 2.16b and c), with 90 to 190-Hz bandpass filter applied. field-traces_accel [ER,M]

at 11.6 m shown in Figure 2.17f).

We do not find that our E_x and a_x data compare as favorably as the similar comparison of Garambois and Dietrich (2001). We do however see close fit in some cases (such as shown in Figure 2.17b, c, d, and e) for the earlier parts of the waveform (likely before the arrival of surface waves). We attribute the misfit to two factors. First, the frequency responses of our geophone and electrode arrays are clearly different, likely due to the fact that the geophone data were collected using rented phones which are old and no longer fitting the manufacturer's specifications (Don Pierce, Geometrics Corp., personal communication, April 2004). And second, the expected relation between E_x and a_x is valid for P-waves only, and a large part of our recorded energy is due to Rayleigh waves.

Seismic source comparison

As with conventional seismic data collection, the choice of seismic source is an important consideration in seismoelectric work. Because the seismoelectric signal is so weak, the source characteristics are particularly important. We have tested a number of different sources at our vineyard test site and compare the resulting data. Although the site is the same, the conditions are not; some data were collected during the dry summer months while others were collected during the rainy winter. Soil water saturation plays an important role in electrode coupling and shallow seismic wave propagation, so the source-comparison data can not always be independently compared. For this reason we show corresponding sledgehammer data for comparison with data for each source when possible, as the sledgehammer was used during nearly every field campaign.

Sledgehammer source

A 12-pound (5.4 kg) sledgehammer has been our primary seismic source throughout this project. As noted previously, we individually record between 25 and 50 hammer impacts, manually remove those that show excess electrical noise, and stack the remaining records to

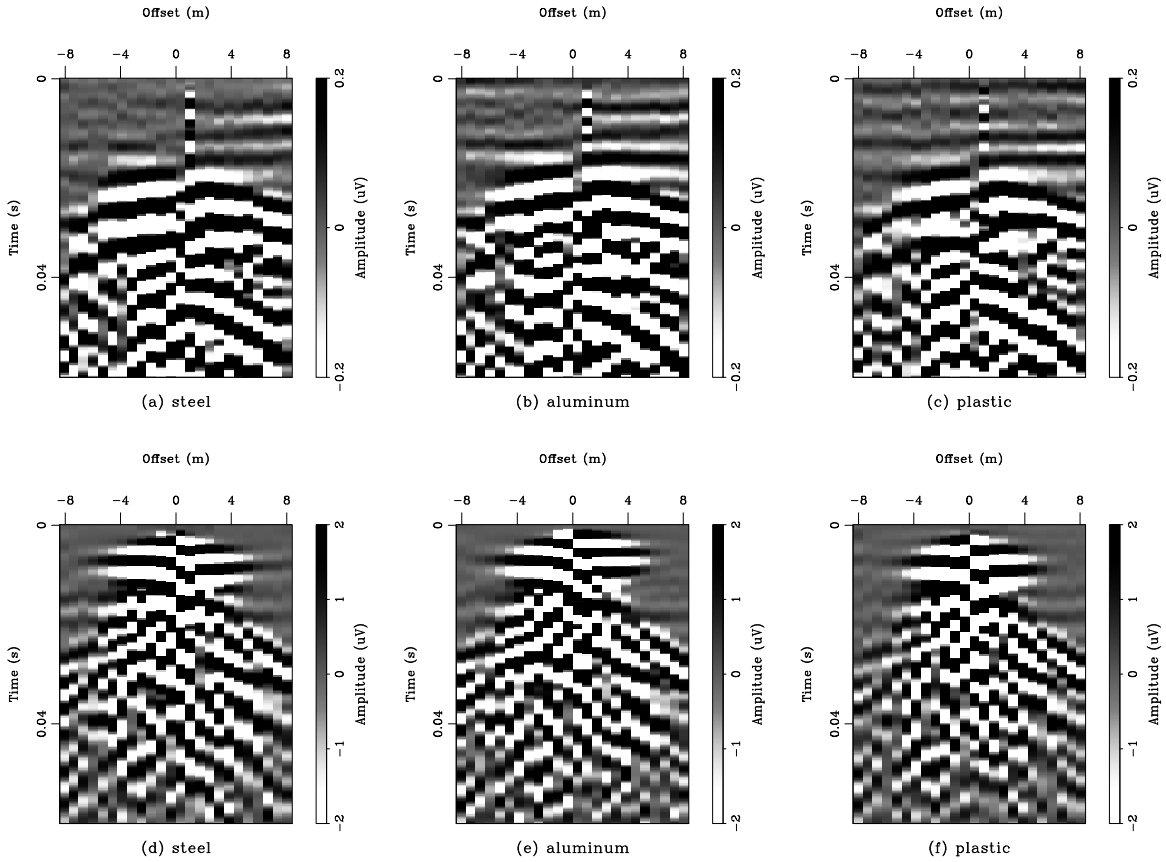

Figure 2.18: Seismoelectric data collected using steel, aluminum, and plastic hammer plates. Fan-profile data with a) steel plate, b) cylindrical aluminum "plate", and c) polycarbonate plastic plate. In-line data collected simultaneously, with d) steel plate, e) cylindrical aluminum "plate", and f) polycarbonate plastic plate. Note that high-amplitude trace at offset ∼+1 m in fan data is noisy. field-hammer_plates [ER]

produce a single shot gather. The hammer is struck on a hammer plate that is partially embedded in the soil. We trigger the seismograph with a standard mechanical (contact closure) hammer switch. We have tested various hammer-plate options and compare the resulting data in Figure 2.18. These data were recorded by 48 seismoelectric channels recorded simultaneously, with half of the receivers on each side of the two vineyard trenches. Electrode pairs are 1.05 m wide, spaced at 0.7 m intervals, and located 1.5 m from the near edge of the nearer trench. The source is located in the center of one line of electrodes, such that we record in-line data and fan profile data at once. These data were collected in the month of August, with very dry soil. The data in Figure 2.18 are shown with the 60-Hz noise removed, and with a 150 to 300 Hz bandpass filter applied.

The first plate (Figure 2.18 a and d) is a 12.9-kg steel plate with dimensions 38.5 cm by 16 cm by 2.5 cm. The second plate (Figure 2.18 b and e) is an 8.5-kg aluminum cylinder of radius 7 cm and length 20 cm. It is oriented with the axis horizontal, and perpendicular to the direction that the hammer-swinger is facing. The third plate (data shown in Figure 2.18 c and f) is a 3.4-kg polycarbonate plastic plate with dimensions 31 cm by 17 cm by 5 cm thick. All plates are placed in a shallow indentation dug in the soil to fit the plate and minimize its movement. At first glance all three plates seem to produce similar results. When we look at individual hammer strikes, however, we notice that the aluminum plate shows greater strike-to-strike repeatability. This can likely be attributed to both the shape and the material. The plastic plate offers the advantage of being non-metal, allowing us to easily avoid creating any Lorentz field. We therefore prefer to use the aluminum and plastic plates, but do not find them to be substantially superior to the steel plate. It should be noted that none of these gathers (or the un-stacked shot records) show any Lorentz energy, despite the use of metal plates, due to the very dry soil. Similar data collected with wet soil show Lorentz energy when metal hammer plates are used; this finding is elaborated upon in a later section.

Shotgun source

We next show data (Figure 2.19) collected with a Betsy seis-gun, firing blank 400-grain 8-gauge shells. The 24 channels of electrodes (1.05-m dipoles at a spacing of 0.7 m) were

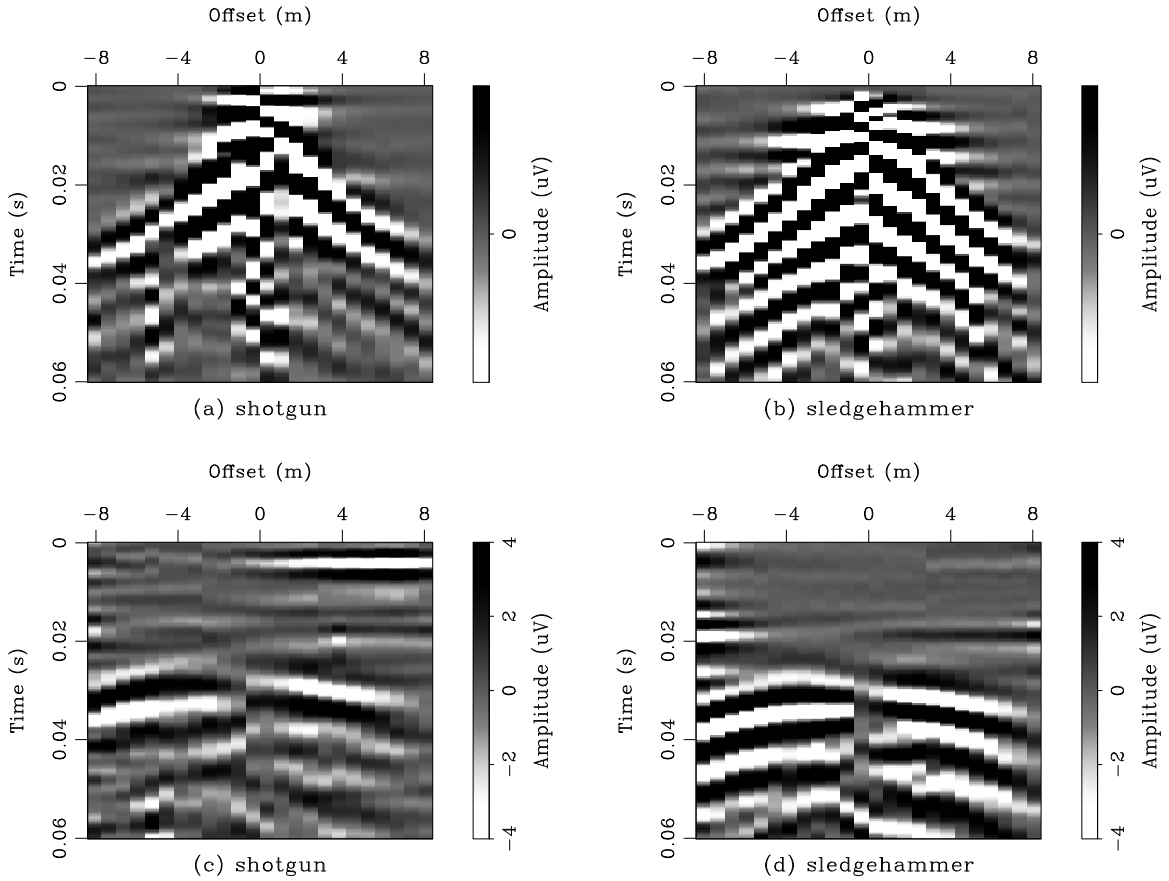

Figure 2.19: Comparison between shotgun source and sledgehammer data collected during the same field campaign. a) In-line source shotgun data, b) in-line source sledgehammer data, c) fan profile shotgun data, d) fan-profile sledgehammer data. field-gun_data [ER]

located 2 m from the second trench, with sources located in the center of this array (in-line source point) or on the other side of the trenches (fan geometry). The gun was triggered using a contact-closure mechanism between the gun itself and the small hammer used to fire it. We found that the closure of the circuit created a large electric field until we insulated the trigger circuitry from the body of the gun. The data shown here were collected with the gun insulated from the trigger circuitry. Data were collected in May, so the soil was moderately saturated, but not recently rained on. Data are displayed after 60-Hz removal and a 120 to 300 Hz bandpass filter.

Figure 2.19a shows an in-line shotgun blast, with the gun angled $\sim 50^\circ$ from vertical, toward the trenches. A comparable sledgehammer gather (25 strikes stacked in the field, without manual strike-by-strike selection) is shown in Figure 2.19b. A shotgun-source fan shot (gun angled $\sim 50^\circ$ from vertical, toward the trenches, at 1 m from the first trench) is shown in Figure 2.19c, with a comparable sledgehammer gather (25 strikes 2 m from the first trench) in Figure 2.19d. For both geometries we see that the stacked hammer strikes produce greater energy and a superior signal-to-noise ratio than the gun. This is particularly evident for the fan-profile plots, where even the coseismic energy is obscured by background electrical noise in the shotgun record.

Explosive sources

We conducted a series of experiments with chemical explosives at the vineyard site using a variety of in-line and fan geometries. Because of the large amount of source energy, we were able to successfully use greater source-receiver offsets than are practical with the sledgehammer, hence we did not attempt to collect comparable hammer data. Data shown in Figure 2.20 were recorded by electrodes located 2 m from the second trench during the month of March, with wet soil conditions. Timing information was provided by an up-hole geophone, but since the source-electrode offsets are similar in scale to the source-geophone distance, the establishment of a time zero is imprecise. Shots were located at a depth of ~ 1.5 m in augered shot holes and were detonated using a small battery to fire a blasting cap which, in turn, detonated the main charge. Displayed data (Figure 2.20) are shown after 60 Hz removal and bandpass

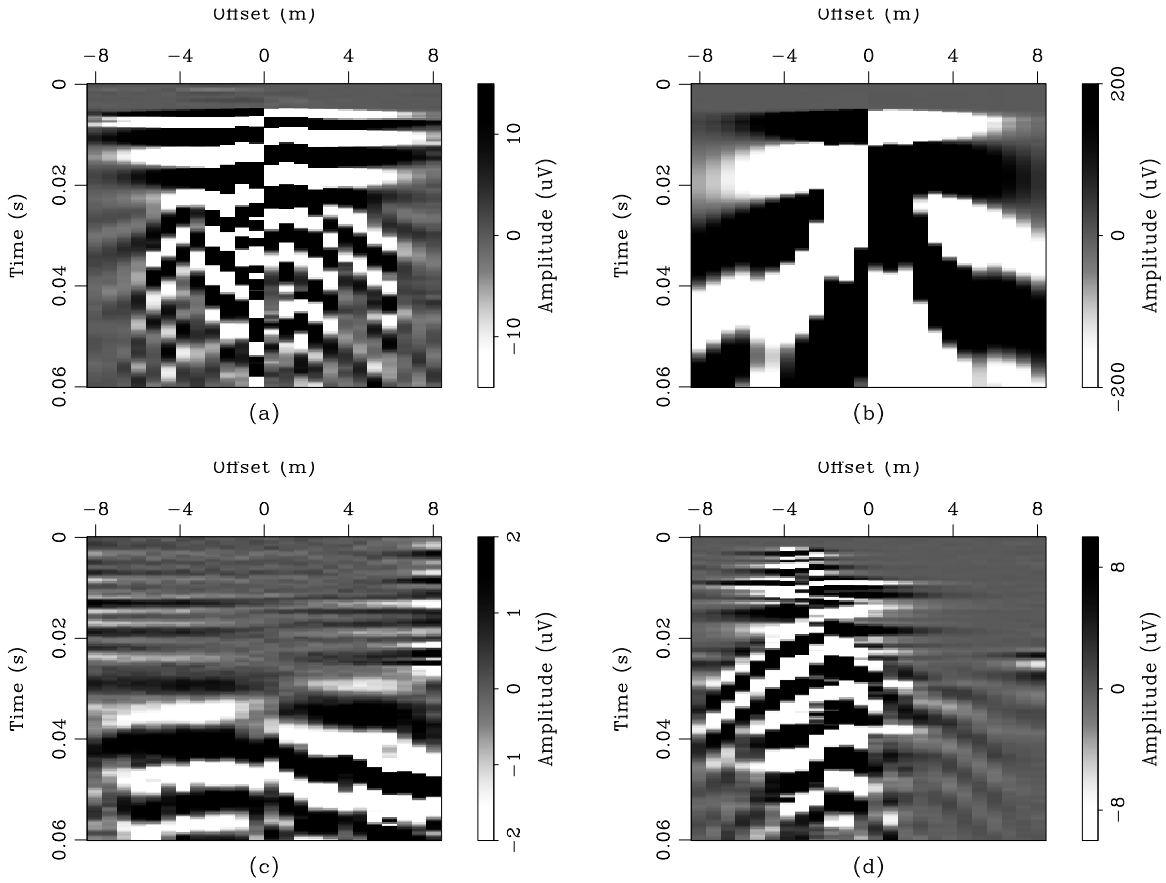

Figure 2.20: Comparison of various chemical explosive source shot gathers as recorded by an electrode array 2 m from the second trench. a) In-line source explosive (0.15 kg of explosive) and b) same data as in (a), but including frequencies as low as 10 Hz, showing that the several flat events in the upper ∼10 ms appear as a single flat event at low frequency. c) Fan-profile data, with 0.45 kg of explosive at 6 m from the nearer trench. d) In-line data recorded with 5 400-grain shotgun shells fired by a blasting cap. Note the presence of several flat events in the upper ∼15 ms. All data bandpass filtered 120 to 800 Hz, except part (b) filtered 10 to 800 Hz. field-boom_data [ER]

filtering (120 to 800 Hz, except where noted).

The in-line geometry gather shown in Figure 2.20a (120 to 800 Hz) and b (including low frequencies, pass band is 10 to 800 Hz) was collected using a 0.15 kg (1/3 lb) explosive charge located about one meter from the receiver electrodes ($\sim$3 m from the near trench). The 5 ms delay before the first arrivals is likely due to the travel time to the up-hole phone used for timing. We interpret the strong flat energy in the upper $\sim$15 ms as direct-field energy, despite the fact that explosives are not an impact source. This is because an explosive detonated in a shallow hole is far from isotropic; energy propagates preferentially upward to the free surface, and creates an asymmetrical pressure (and charge) distribution that is essentially the same as the direct field observed with hammer impacts on the surface. The lower-frequency display of the same data Figure 2.20b confirms that the flat energy is basically one or two events, as is expected for a surge of energy upward followed by the relaxation of the earth to its original state. The fan-profile gather shown in Figure 2.20c was collected with 0.45 kg (1 lb) of explosive located 6 m from the first trench. At this offset, a sledgehammer gather would show very little coseismic energy, let alone the flat events in the upper $\sim$25 ms which we interpret as interface response energy from the trench. The fact that we are able to observe these events in the data without any processing beyond simple frequency filtering indicates that explosives are a substantial improvement over the sledgehammer. Figure 2.20d shows a shot gather recorded using 5 400-grain shotgun shells that were electrically fired down-hole, using an in-line geometry. The gather is encouraging in that the frequency content is higher than for the other explosive shots, and it shows many flat events. However amplitude analysis of these events suggests that they are all created very near to the source point, perhaps some variation on direct fields.

Vibrator source

We have also tested an electromagnetic source developed in-house, and described in Appendix B. It is built around a “tactile transducer”, a device designed to shake stationary objects such as amusement-park rides and home-theater seating. The device is considered by its manufacturer (Clark Synthesis, Littleton, CO) to be effective from 5 to 800 Hz. We mount the device in a

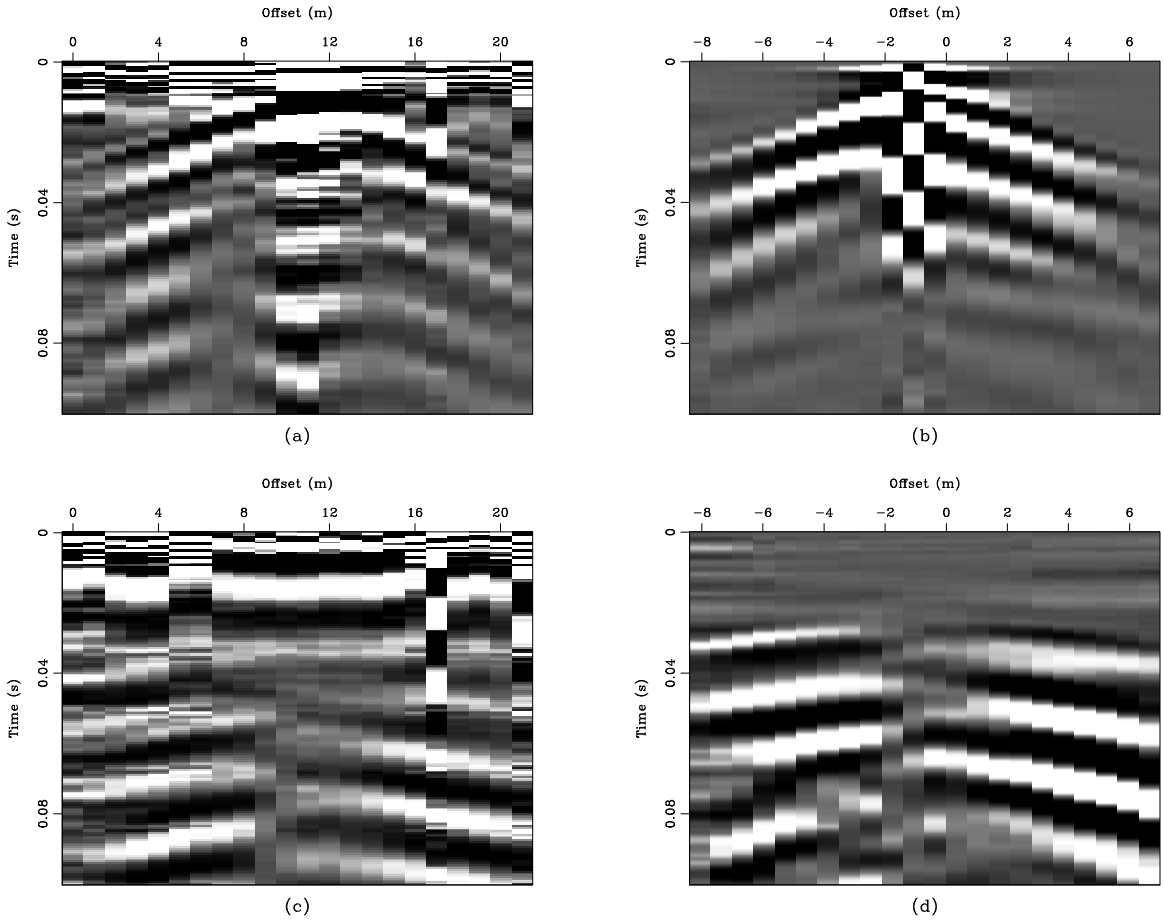

Figure 2.21: Comparison between vibrator data and corresponding hammer data. a) In-line source vibrator data, b) In-line source sledgehammer data, c) fan-profile vibrator data, d) fan-profile sledgehammer data. Note strong electrical noise in the first ∼15 ms of vibrator records, due to recording of the original sweep by all channels (perhaps as cross-talk between recording channels, or perhaps via direct recording of the source EM field) obscuring any seismoelectric signal that might exist in that part of the records. Note: these data are shown with lower frequencies (50 to 500 Hz) than most other data plots in this section, and to a greater travel time in order to show the weak reverberatory energy of the vibrator source. field-vibe_data [ER]

weighted framework, and power it with a 450 watt amplifier. The source signal for the data shown here is a 30-s linear sweep from 1 to 700 Hz, with a half-second taper at each end. The data are cross-correlated with the original pilot sweep before 60 Hz noise removal and bandpass filtering (50 to 500 Hz for the data shown in Figure 2.21). The displayed data were all collected in the month of April with moderately saturated soil conditions at the vineyard site. The electrodes (1.05 m dipoles spaced at 0.7 m) for these gathers were located 1.7 m from the second trench. The pilot sweep and the signal from a vertical geophone located $\sim$10 cm from the source were recorded on auxiliary channels of the seismograph, leaving 22 channels for seismoelectric recording.

Figure 2.21a shows an in-line geometry vibrator gather, and Figure 2.21b shows the corresponding hammer stack gather (25 strikes). Vibrator and hammer fan-profile gathers (source located 2m from the first trench) are shown in Figure 2.21c and d. The hammer clearly provides a greater signal-to-noise ratio, and overall cleaner record. These data displays include lower frequencies than most other displays in this paper because a higher-frequency display of the vibrator data in Figure 2.21a and c would show virtually zero coseismic energy. The other notable feature of the seismoelectric vibrator data is the strong energy at time zero. This is a remnant of the cross-correlation process, a result of the original sweep being recorded by each channel. Whether this is the result of cross-talk in the recording electronics, or direct transmission of the signal from the electromagnetic source to the electrodes is unclear. In either case, the data are rendered unusable by the combined effects of this problem and the previously described lack of sufficient power. A more powerful vibrator should prove useful if care is taken to avoid the cross-talk problem.

Source summary

For our vineyard field site we find sledgehammer stacking to be the best source for short-offset work (a few meters), in terms of repeatability, ease of use, and cost. A plastic hammer plate avoids any unwanted Lorentz fields, while the aluminum cylinder provides slightly improved data quality. Beyond the range of a few meters, we find explosives are needed to provide the power necessary to produce seismoelectric signals that may be observed above the level of

background noise. Both the explosives (when used in a shallow setting) and the sledgehammer create direct field energy which would obscure any interface response energy from very shallow layers (less than ∼5 m). As with seismic work (Miller et al., 1992, 1994), it must be assumed that these findings are site-specific, and will not hold at all locations.

SEISMOELECTRIC DATA ANALYSIS

Data interpretation- observing the direct field and interface response

In order to develop our understanding of the source-related electric fields that may be observed in seismoelectric data, we begin with the simplest possible data-collection scenario, and add complexity one step at a time. In this way we can better identify the effect of each individual element of seismoelectric data collection.

The series of gathers shown in Figure 2.22 was collected at the vineyard field site, but far away from the trenches (∼20 m) so that the trenches should have no effect on the displayed data. The data were collected with a source point in the center of an array of 24 electrode pairs at a spacing of 0.7 m. The distance across each pair of electrodes (the dipole width) is 1.05 m. All gathers are the result of stacking individual impacts of the source (frequently a sledgehammer) on a metal or plastic hammer plate, as noted.

The simplest possible data collection example is carried out by manually triggering the recording seismograph. Figure 2.22a shows data collected by hitting the trigger switch against a stationary object. Thus the data represent electrical background noise and the lack of any coherent energy demonstrates that the trigger mechanism produces no electrical noise. Next we add a level of complexity by putting seismic energy into the ground, but with no moving metal objects. Figure 2.22b shows data collected using the impact of a wooden source (a fence post) on a plastic hammer plate. We now see the expected dipping coseismic energy (with seismic moveout), labeled “CS”. We also observe flat (no moveout) energy in the upper ∼17 ms of the record, labeled “D”. This energy appears to show the amplitude pattern of a dipole and reversed polarity on opposite sides of the shot point. If the site geology included any shallow interfaces, we might conclude that this flat energy was the seismoelectric interface

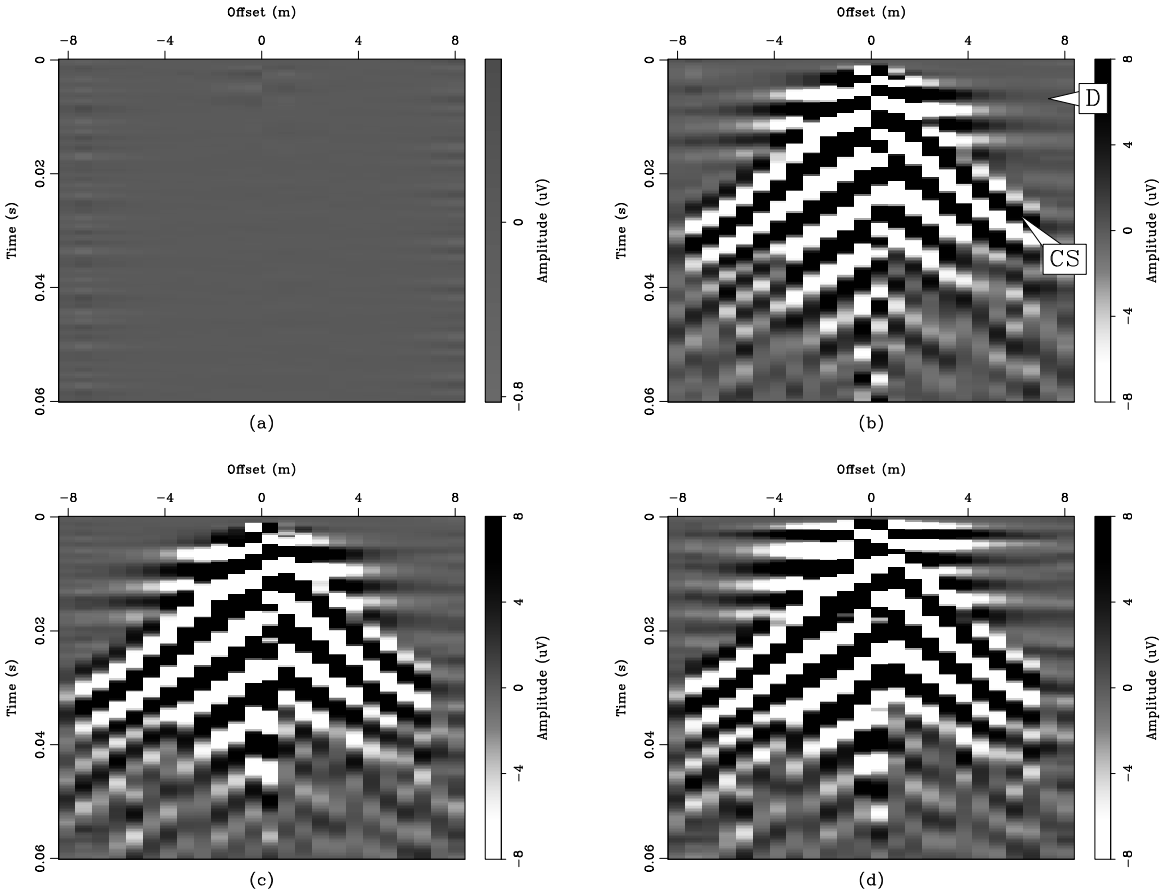

Figure 2.22: Seismoelectric shot gathers collected at the vineyard field site testing various source options. a) stack of manual triggers. Note absence of any coherent arrivals, despite the amplitude scale having one-tenth the range of the other plots. b) Wooden fence post on plastic hammer plate. Note flat direct field arrivals (“D”) and dipping coseismic energy (“CS”). c) Metal sledgehammer on plastic hammer plate. Gather appears very similar to that in b). d) Metal sledge on aluminum hammer plate. Note addition of flat Lorentz field energy in the upper ∼0.01 s (“L”). field-pmv_series [ER,M]

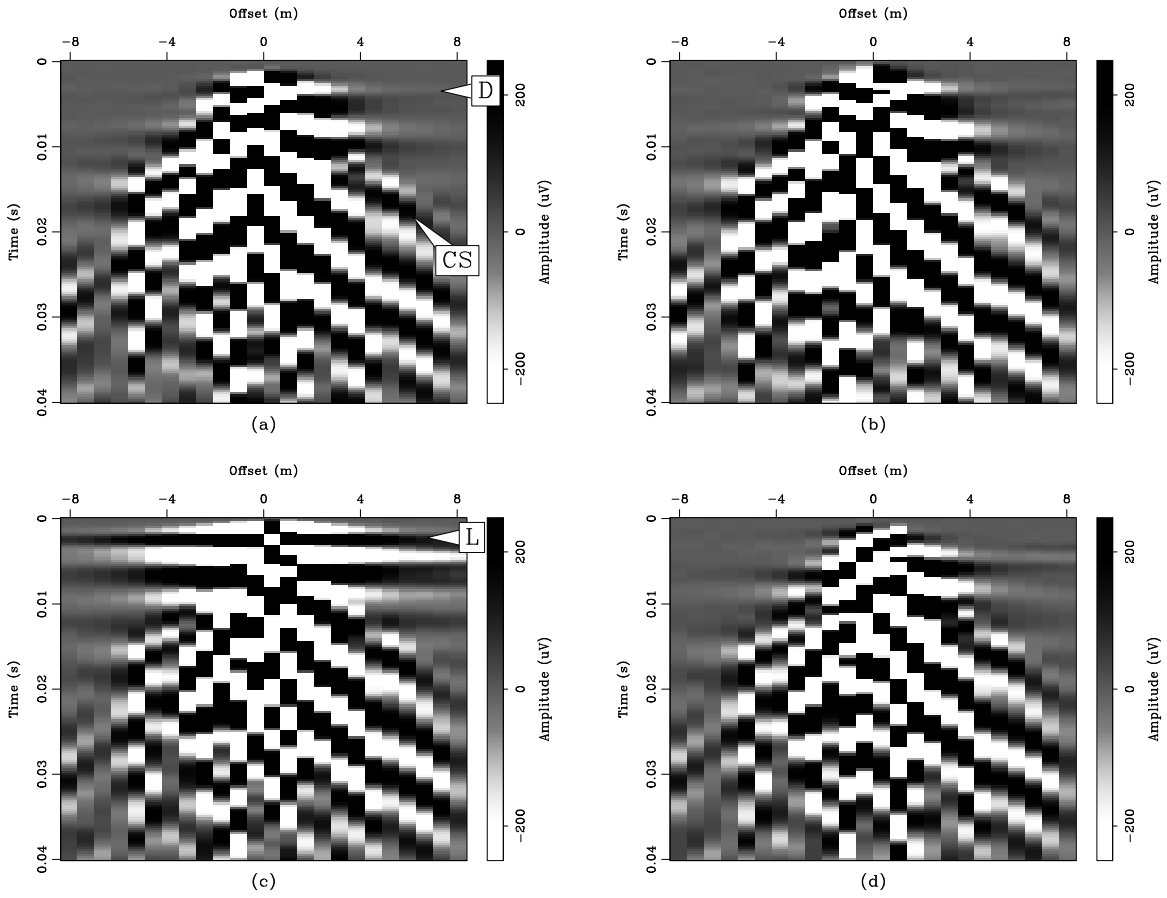

Figure 2.23: Seismoelectric data from the Thompson tree farm with various source types. a) Wooden fence post on plastic hammer plate. Note flat direct field energy ("D")and dipping co-seismic energy ("CS"). b) Metal sledgehammer on plastic plate. c) Metal sledge on aluminum plate. Note addition of flat Lorentz field energy ("L"). d) Metal sledge on aluminum plate BUT plate is insulated from the soil. Note that Lorentz field energy is absent. field-gat_series [ER,M]

response. However, it does not, so we interpret this energy as the seismoelectric direct field. We add another level of complexity by using a metal sledgehammer on the plastic hammer plate (Figure 2.22c) and observe that the result is very similar to that of Figure 2.22b. Thus we can conclude that the moving metal hammer head does not create a noticeable electric field. We move one step further by employing a metal hammer plate (the aluminum cylinder). We now observe (Figure 2.22d) an additional form of flat energy in the upper $\sim$10 ms of the record, labeled "L". It shows no moveout, and an amplitude pattern suggestive of a dipole. But unlike the interface response and the direct field, this energy shows the same polarity on the two sides of the shot point. Thus we conclude that this energy is due to a horizontal electric dipole oriented along the electrode transect line. The Lorentz field (Equation 2.2) offers the most likely explanation for the observed energy. The motion ($\mathbf{v}$) of the conductive hammer plate in the Earth's magnetic field ($\mathbf{B}$) produces an electric field ($\mathbf{E}$) when the conductive object is in electrical contact with the soil. We further examine this field later in this contribution.

In order to gain more certainty in our interpretations, we examine data from a separate field site. The data in Figure 2.23 were collected at the tree farm site. Figure 2.23a shows a gather collected using a wooden source on a plastic hammer plate with dipping coseismic energy and (faint) flat direct field energy visible. The gather in Figure 2.23b looks very similar, and was collected using a metal sledgehammer on the plastic hammer plate. Figure 2.23c shows data collected with a metal hammer on the aluminum hammer plate, and it shows the strong Lorentz electric field as well as the dipping coseismic energy. The gather in Figure 2.23d was also collected with the hammer on the aluminum hammer plate, but in this case the plate was insulated from the soil by a thin layer of wool blanket. The Lorentz field is not observed, demonstrating the need for electrical contact between the metal hammer plate and the soil for observation of this field. We will further discuss this finding in a later section.

Seismoelectric direct field

In order to characterize both the direct field and the Lorentz field, we conducted a series of experiments involving the recording of various sources with electrode pairs deployed in a circular geometry. The electrode array was spaced evenly around a circle of radius 4.3m in a

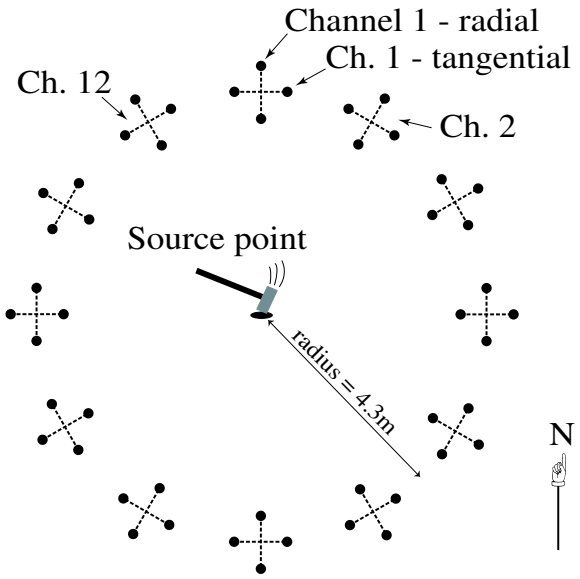

Figure 2.24: Circular electrode array, with 12 radial and 12 tangential channels. Small black circles represent electrodes and dashed lines indicate the pairs across which we measure voltages. field-circle_layout [NR]

homogeneous part of the vineyard meadow, with 12 electrode pairs oriented radially and 12 oriented tangentially. Thus tangential and radial pairs of electrodes were co-located at 30° intervals around the circle. We also collected data with horizontal geophones deployed in the same geometry (radial and tangential phones at 30° intervals around the circle). The source point is in the center of the circle for all shot gathers.

Figure 2.25a shows the radial traces of a seismoelectric shot gather collected with 25 sledgehammer impacts on the plastic plate. Based on arrival times from the data shown in Figure 2.22, we can interpret the strong coherent arrival at 0.02 seconds as the coseismic energy, and the weaker arrival at 0.01 seconds as the direct field. These arrivals do not appear in the tangential part of the same shot gather (Figure 2.25b), as is to be expected for a vertical dipole (the direct field) and radially propagating seismic energy (the coseismic arrival). Further confirmation of our interpretation of the 0.02 second arrival as coseismic energy is provided by the corresponding radial horizontal geophone data shown in Figure 2.25c, where we see that the first seismic arrival closely matches the interpreted coseismic arrival in Figure 2.25b. The lack of any energy at $\sim$0.01 seconds in Figure 2.25c supports our interpretation of the 0.01 second energy in Figure 2.25a as the direct field, or at least as a seismoelectric arrival. As is to be expected, the tangential geophone data (Figure 2.25d) do not show coherent

arrivals.

The fact that the direct field energy in Figure 2.25a shows (approximately) constant amplitudes around the circle is consistent with the interpretation that this energy is due to a vertical dipole. The deviations from constant amplitude are likely caused by imperfect electrode coupling. We can constrain the size and location of this dipole by considering the amplitude pattern of the in-line shot record shown in Figure 2.22c. Figure 2.26a shows the same data, but with a lower-frequency bandpass filter (so as to better represent the full direct field, which can be clearly seen as a single strong arrival at ∼0.005 s). The amplitude of the maximum of this arrival is plotted as dots in Figure 2.26b. Using the Equation 2.1 we model amplitudes corresponding with a disk of dipoles with radius 0.8 m and located at a distance of 0.8 m (z in Equation (2.1)) from the electrode receiver line (offset along the receiver line is x in Equation (2.1)). We approximate the disk of dipoles by simply summing the contributions of 100 dipoles spread along the a region of radius 0.8 m; the modeled amplitude pattern is plotted as a solid line in Figure 2.26b. The fit of this model to the data broadly indicates that the direct field is produced within a volume of soil of radius ∼0.8 m. The absolute magnitude of the modeled dipole is arbitrary; the quantity qd in Equation (2.1) is simply scaled to match the real data. The numerous variables that contribute to the real magnitude are too complex to permit exact modeling.

We have observed the seismoelectric direct field at two different field sites. Although it does not provide any new information about the deeper subsurface, it is of interest as a seismoelectric phenomena. Additionally, it could possibly be employed in a down-hole setting to provide useful new information on permeability or other properties.

Lorentz field of the metal hammer plate

Examples of the Lorentz field are shown in Figures 2.22 and 2.23. One important observation about the Lorentz field is that its polarity can change from one hammer strike to the next, such that for a set of hammer impacts on the aluminum plate, approximately half of the raw gathers show a Lorentz field with one polarity, and the other half show the opposite polarity. This polarity reversal leads us to conclude that the field is created by the horizontal motion of the

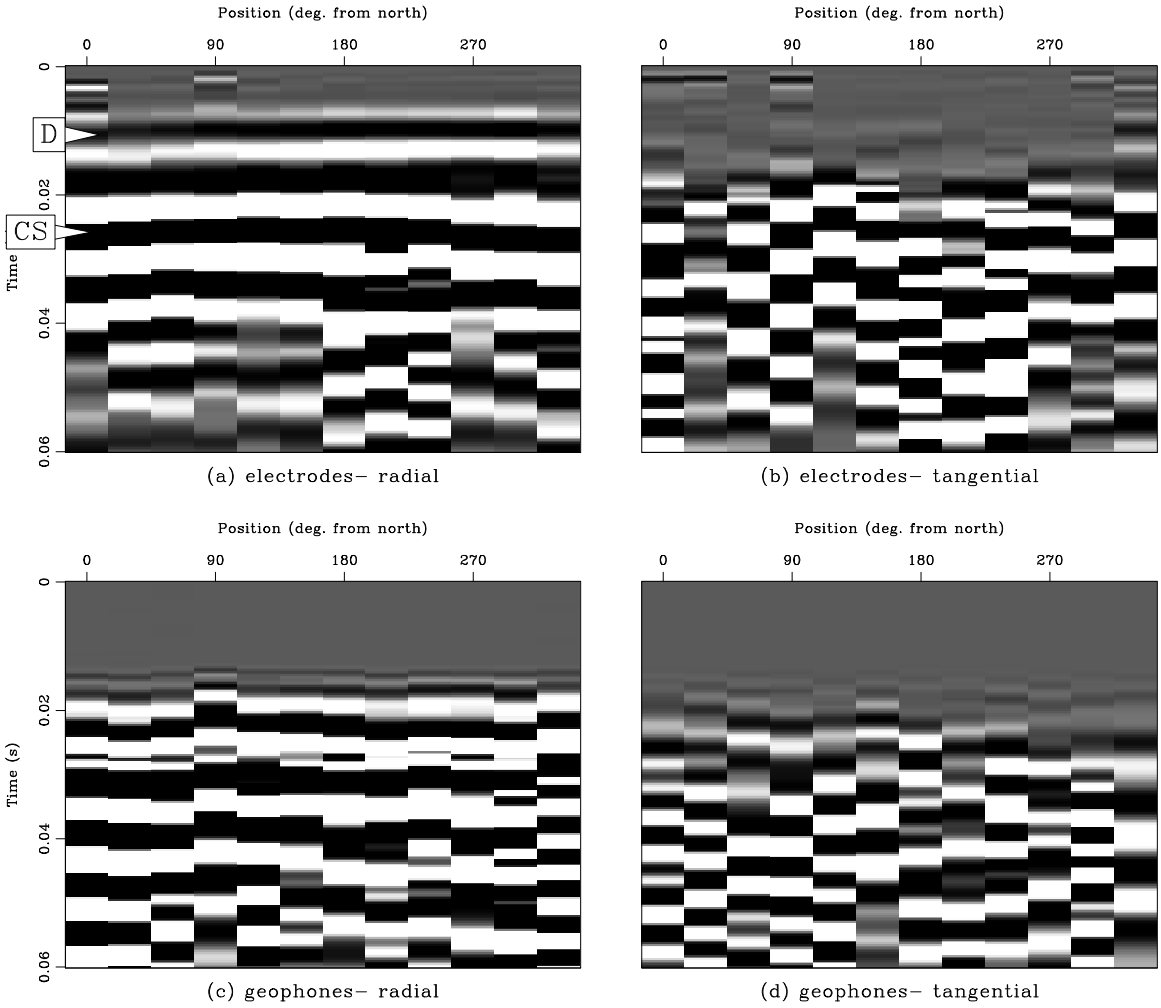

Figure 2.25: Stacked shot gathers recorded by the circular electrode array described in the text. a) Radial component of electric field created by the impact of a sledgehammer on a plastic hammer plate. Note coherent direct field arrival at ∼0.01 sec ("D") and higher-amplitude coseismic arrival at ∼0.02 sec ("CS"). b) Tangential component of the same shot gather (hammer on plastic plate) with no coherent arrivals. c) Radial component of horizontal geophone data, with first seismic arrival at ∼0.02 sec, corresponding with coseismic arrival in a). d) Tangential component of geophone data, with no clear coherent arrivals. field-circle1 [CR,M]

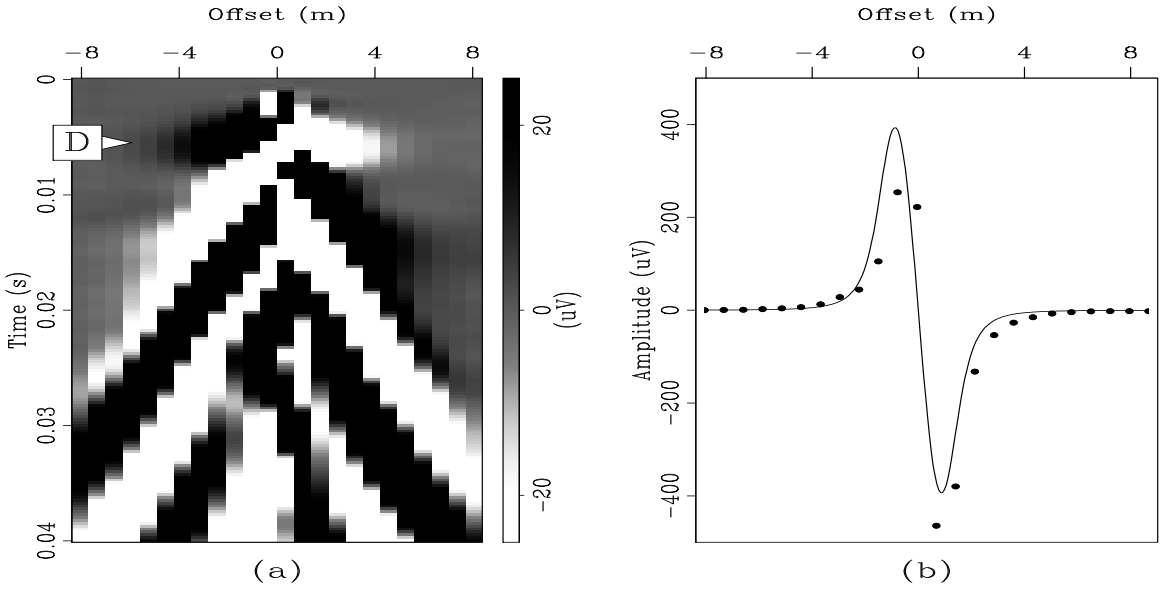

Figure 2.26: Direct field amplitudes. a) Shot gather from Figure 2.22c, shown with bandpass filter 20 to 800 Hz. Direct field energy is labeled "D". b) Amplitude pattern for the direct field arrival in (a) plotted as dots, and modeled amplitudes as a solid line. Modeled amplitudes correspond with a disk of electric dipoles of radius 0.8m centered at 0.8m away from the electrode array. field-direct_amps [ER]

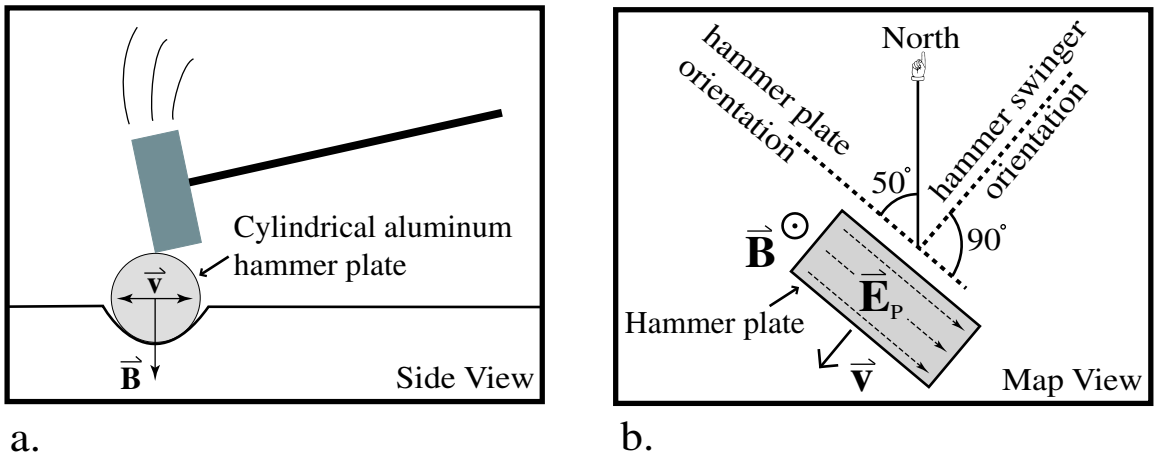

Figure 2.27: Side (a) and map (b) views of the creation of the Lorentz field. The horizontal component of the hammer plate velocity **v** crossed with the vertical component of the Earth's magnetic field **B** creates an electric field **E** in the conductive plate. v_h varies from strike to strike, and may be in either direction. field-lorentz_hammer_both [NR]

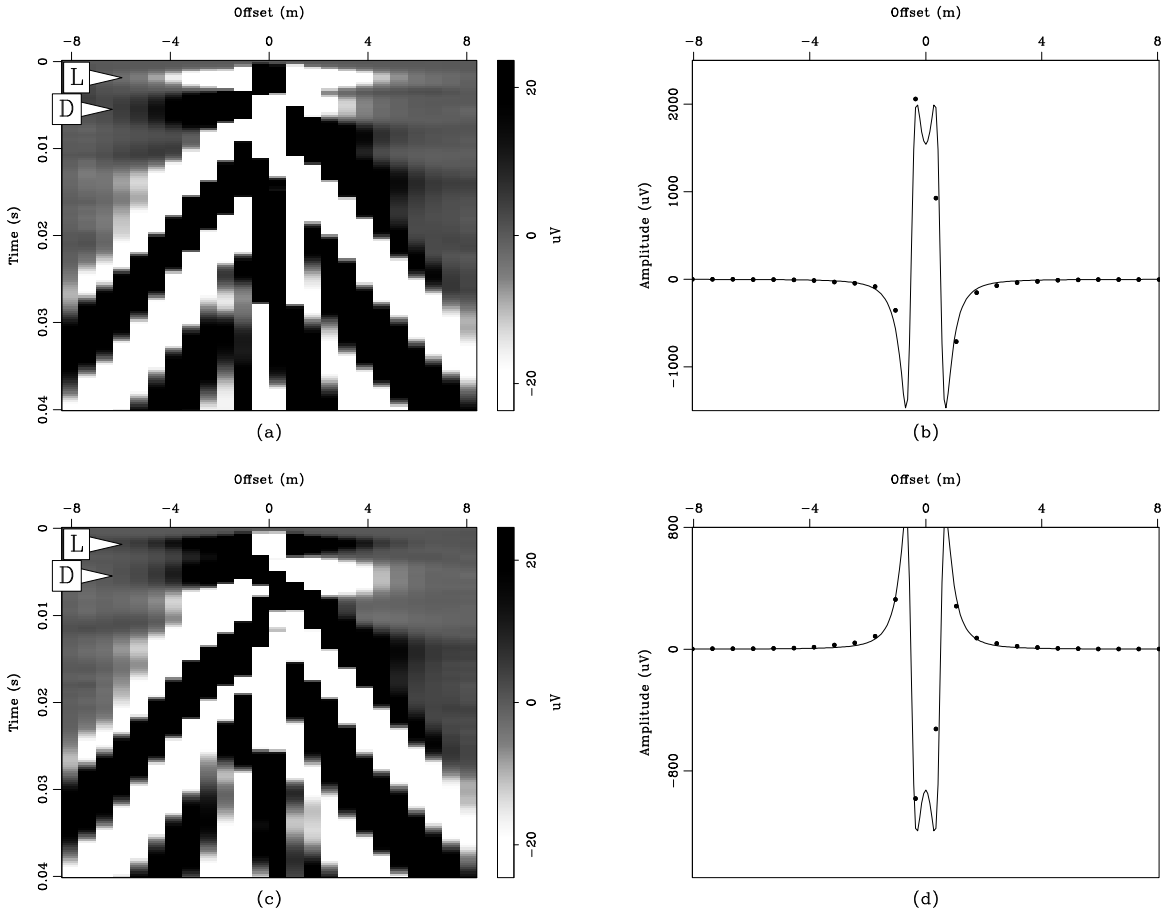

Figure 2.28: In-line data showing the Lorentz field ("L") at ∼0.002 s, the direct field ("D") at ∼0.005 s, and modeled and real amplitudes. a) Stacked data shown in Figure 2.22d, but with lower-frequency bandpass filter (20 to 800 Hz). b) Real amplitudes (dots) of Lorentz field arrival of data in a), and amplitudes modeled with Equation (2.1) (solid line) corresponding with the metal hammer plate acting as an electric dipole oriented along the electrode array. See text for details. c) Stack of other selected shot gathers (those with Lorentz field arrival opposite in polarity to stack in part a). d) Real (dots) and modeled (solid line) amplitudes for metal plate as a horizontal dipole as predicted by the Lorentz equation. field-metal_amps [ER]

hammer plate **v** crossed with the vertical component of the Earth's magnetic field **B**, as shown in Figure 2.27. Support for this conclusion is provided in this section. The stacks shown in Figures 2.22d and 2.23c are made from shot gathers selected on the basis of the polarity of the Lorentz field. The other gathers would produce a stack with a Lorentz field arrival with opposite polarity. A stack of all of the shot gathers shows very little Lorentz energy as it tends to stack out. The data plots in Figure 2.28a and c are stacks of two separate sets of raw gathers, selected on the basis of the Lorentz energy polarity. The strike-to-strike polarity reversals depend on the slight variations between hammer impacts. Data collected when we intentionally strike the plate in a particular horizontal direction show no reversals.

We can improve our knowledge about the Lorentz field by extracting amplitudes from the in-line data (Figure 2.22d). Figure 2.28a and c show stacks of two different sets of impacts collected with the metal hammer plate processed with a broad bandpass filter (20 to 800 Hz); the data in Figure 2.28a is the same stack as in Figure 2.22d. Both of these data plots show a strong flat arrival centered at about 0.002 seconds which we interpret as the Lorentz field, followed by the direct field (vertical dipole) with reversed polarity on opposite sides of the shot point. Amplitudes extracted from these stacks for the Lorentz field are shown in Figure 2.28b and d as dots. Modeled amplitudes for a horizontal electric dipole matching the hammer plate (charge separation of 0.2 m between ends of the dipole, lateral offset of 0.25 m from the receiver line) are plotted as solid lines. Only the magnitude and polarity of the modeled dipole is varied between the two plots. The central two traces show polarity opposite that of the rest of the Lorentz field because they are located along the horizontal dipole and so are measuring the field off of its main axis, where the field is opposite to the direction of the dipole.

Data collected by the circular electrode array using the sledgehammer on the aluminum hammer plate are shown in Figure 2.29. Figure 2.29a and b are the radial and tangential parts of a partial stack of hammer strikes, and 2.29c and d are the radial and tangential parts of a stack of the other hammer strikes. These two sets of impacts were selected from the individual hammer strike gathers based on the presence and polarity of the events that appear at a time of $\sim$0.001 seconds at certain radial positions (90-180° and 270-360°) in the radial component and 90° out of phase (0-90° and 180-270°) in the tangential component. Note that the polarity of these arrivals is reversed between the two stacks (Figure 2.29a and b, versus Figure 2.29c

and d).

The radial pattern of these arrivals suggests that they are due to a horizontal electric dipole oriented a few tens of degrees west of north, with the orientation of the dipole reversed between the two sets of gathers. Because the field occurs only for hammer impacts on a metal plate, we assume that it is caused by the metal plate, and that it is the Lorentz field (Equation 2.2). Because the orientation of the dipole can reverse phase between sequential hammer impacts, we must conclude that it is caused by a component of $\mathbf{v} \times \mathbf{B}$ that can reverse from one strike to the next. The Earth's magnetic field $\mathbf{B}$ is essentially constant (oriented toward magnetic north, and inclined at an angle of $\sim 60^\circ$ from horizontal), so we must look to $\mathbf{v}$ for this reversal. After the first few hammer impacts compact the soil beneath the hammer plate (or cylinder, in this experiment), it has more freedom to move horizontally than vertically. So although the impact is almost entirely vertical, even a small deviation (non-vertical strike, or off-center impact on the rounded top surface of the hammer plate) can produce a briefly-high horizontal velocity $\mathbf{v}$ as shown in Figure 2.32a. For the case of the in-line data (Figure 2.22d and Figure 2.23c), the aluminum cylinder is oriented along the electrode receiver line, and thus the hammer strikes will tend to cause horizontal motion perpendicular to the line. If we take the cross product of this velocity with the vertical component of $\mathbf{B}$, we get a horizontal electric field $\mathbf{E}$ oriented along the electrode line, just as we observe. The orientation of the horizontal component of $\mathbf{v}$ will vary from strike to strike, but will generally be perpendicular to the electrode transect line, in one of two primary polarities. We conclude that the observed electric field is due to the horizontal component of the hammer plate velocity crossed with the vertical component of the Earth's magnetic field.

Next we extract the amplitudes of the observed arrivals and compare them with modeled amplitudes. Figure 2.30a shows the amplitude of the Lorentz field event shown in Figure 2.29a and b, while Figure 2.30b shows the amplitude of the Lorentz in Figure 2.29c and d. The radial component is plotted as a solid line and the tangential component as a dashed line. The amplitude in Figure 2.30a corresponds with the third of the three phases of the Lorentz field arrival in Figure 2.29a (0.0042 to 0.0065 seconds, labeled "L") while the amplitude in Figure 2.30b was extracted from the second of the three main phases of the Lorentz event in Figure 2.29b (0.0025 to 0.0045 seconds, also labeled "L"), hence the two amplitude patterns

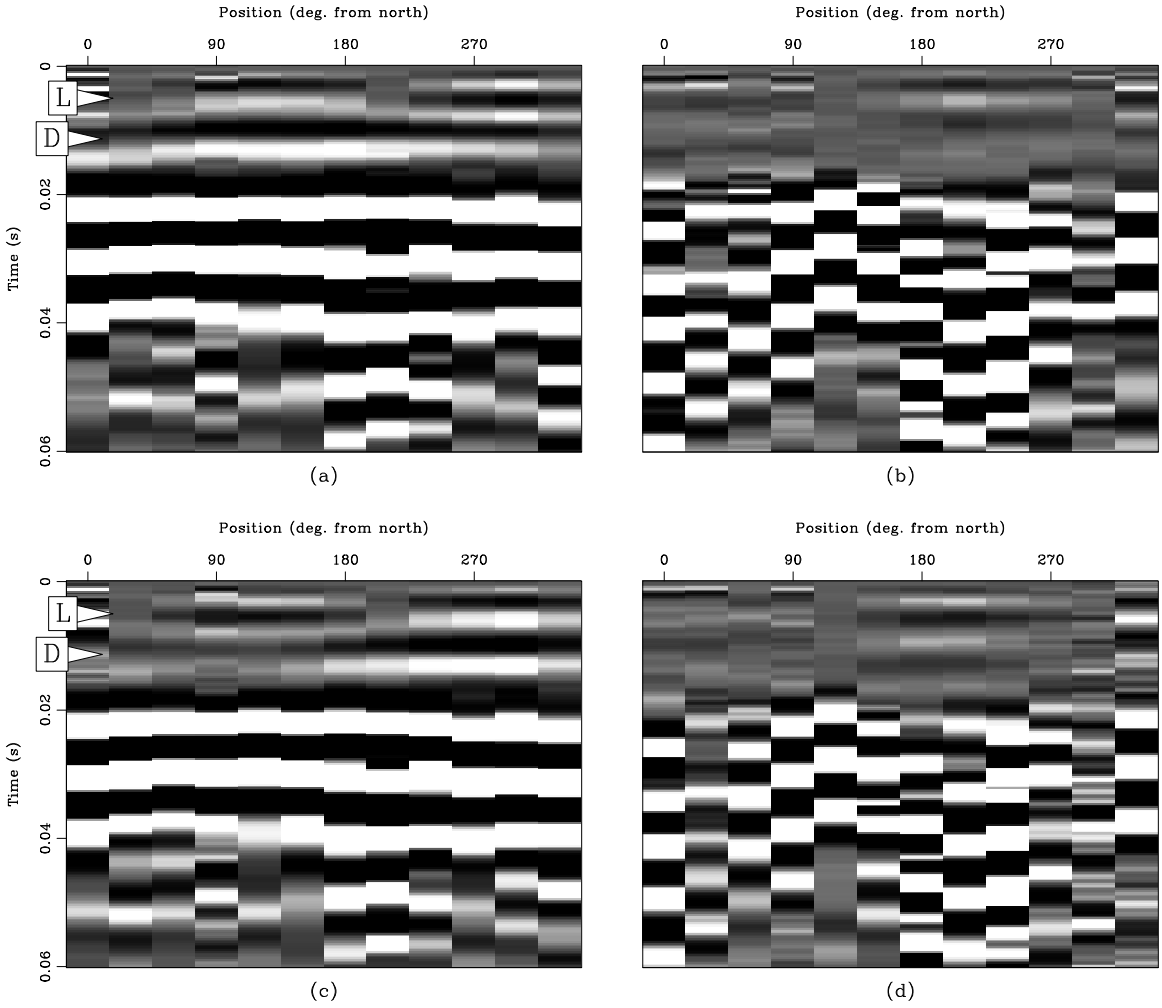

Figure 2.29: Seismoelectric data collected with a sledgehammer on the aluminum hammer plate and recorded by the circular electrode array. Lorentz energy (marked "L") can be seen at ∼0.001 s, above the direct field (D) in each gather. a) Radial component of stack of selected hammer strikes. Note Lorentz energy at ∼0.001 s at 90-180° and 270-360°. b) Tangential component of the same stacked gathers, with faint Lorentz energy at ∼0.001 s at positions orthogonal to the energy in (a). c) Radial component of a stack of other shot gathers, with similar energy at ∼0.001 s but with reversed polarity relative to (a). d) Tangential component of stack of the same gathers as (c), again showing Lorentz energy at positions orthogonal to the energy in (c). field-circle2 [CR,M]

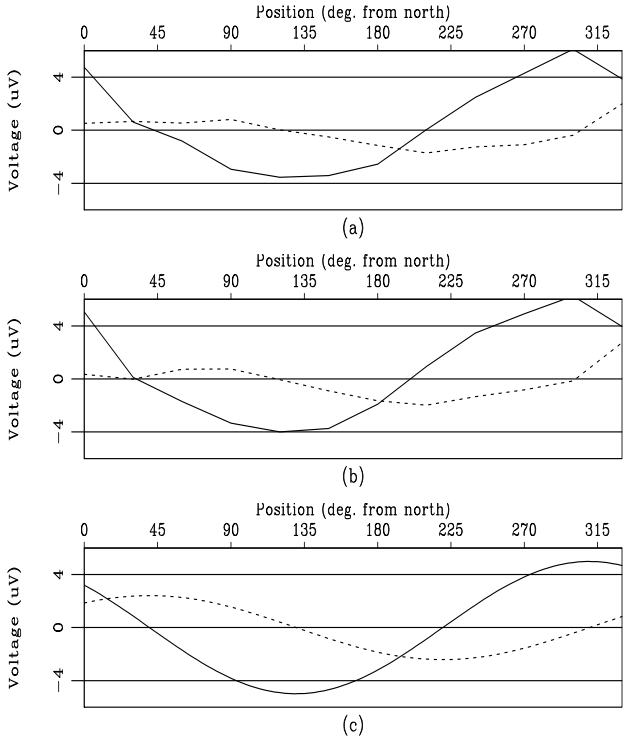

Figure 2.30: Comparison between real and modeled Lorentz energy as a function of radial position. a) Amplitude (solid=radial, dashed=tangential) patterns extracted from the stacks in Figure 2.29a and b. b) Amplitudes extracted from stacks in Figure 2.29c and d. c) Amplitude pattern (theoretical) modeled for a horizontal dipole oriented 50° west of north. field-circ_amps [CR]

are in-phase while the two displayed Lorentz events are 180° out-of-phase. We use Equation (2.1) to model a horizontal dipole at the source point, and find that a best fit is achieved with a dipole oriented ∼50° west of north (Figure 2.30c). This alignment corresponds with the alignment of the hammer plate and the person swinging the hammer (Figure 2.27), not with magnetic north, confirming our interpretation that the horizontal **v** of the hammer plate and the vertical component of the Earth's field **B** are responsible for the Lorentz field. The horizontal component of **B** coupled to the vertical motion of the aluminum cylinder does not seem to play a significant role in the creation of this field.

We look to the radial component of the horizontal geophone data for evidence of horizontal hammer plate motion (Figures 2.25c and 2.31a). If the observed Lorentz field is created by horizontal motion of the hammer plate, then we would expect to see enhanced P-wave energy propagating in the orientation of the horizontal motion, and less energy in the orthogonal directions. Figure 2.31a shows the radial component of horizontal geophone data with the interpreted P-wave arrival noted. This interpretation is based on the fact that this energy is the

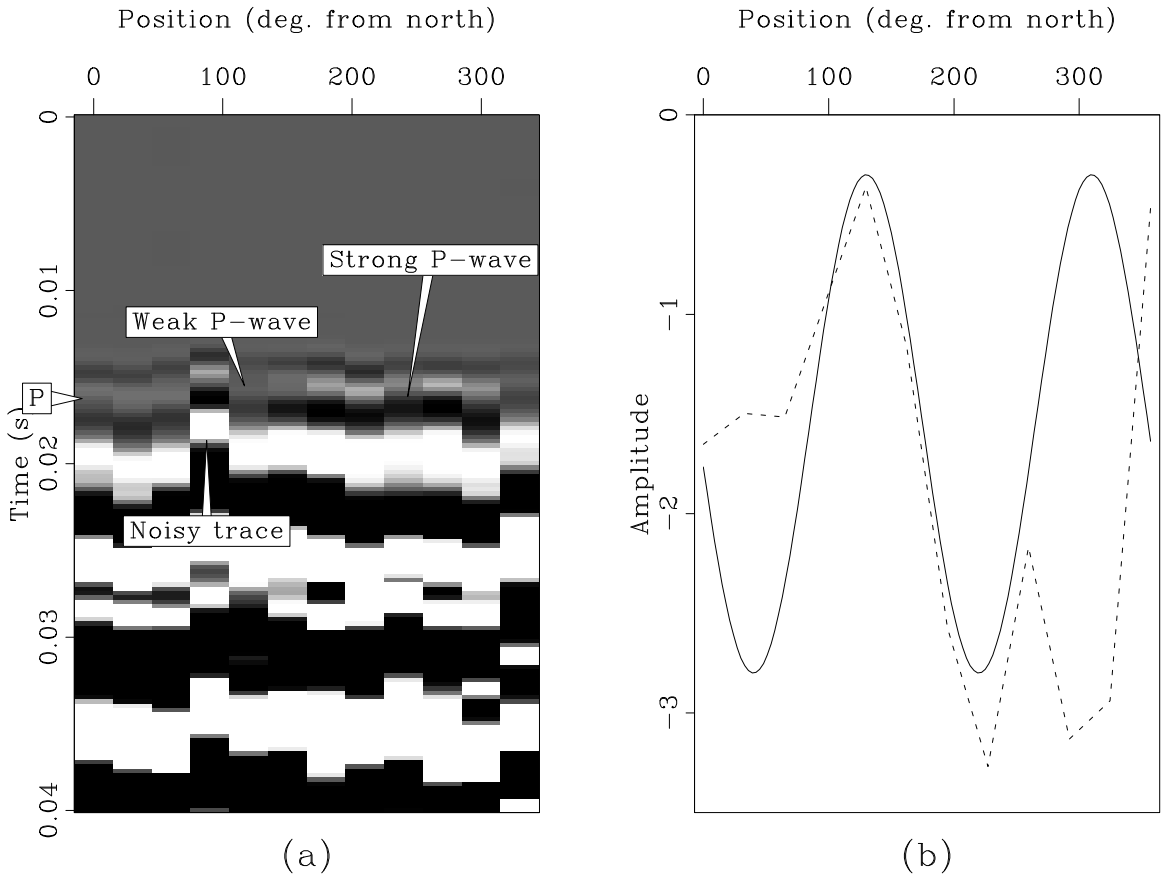

Figure 2.31: a) Radial horizontal geophone data from circular array (same as Figure 2.25c) with interpreted P-wave arrival noted. Data have been trace-balanced to remove effects of coupling variations (surface-wave energy dominates the balancing, so P energy is not artificially balanced). Note azimuthal variation of P-wave amplitude. b) Extracted amplitudes for indicated P-wave arrival, plotted as dashed line. Amplitudes corresponding with a horizontal seismic source (horizontally-moving hammer plate oriented to match orientation of dipole in Figure 2.30c) are plotted as solid line. Though fit is not excellent, the general trends of the two lines are similar. field-p_amps_comp [ER]

first arrival and that it has higher frequency content than the later surface wave energy. It can be seen that the P-wave amplitude varies azimuthally, and is greatest at $\sim 250°$. We extract the maximum amplitude along this arrival, and plot it as the dashed line in Figure 2.31b. The solid line is the amplitude pattern predicted for the distribution of P-wave energy created by a horizontal source oriented 140° west of north, to match the position of the hammer swinger (see Figure 2.27), and corresponding with the orientation of the dipole modeled in Figure 2.30c. Although the fit is far from perfect, the general trends seem to roughly match and we consider this as support for our interpretations. Additionally, it should be noted that the modeled amplitude pattern corresponds with a source creating P-waves equally in two opposite directions. In the real data, we observe stronger P-wave energy in one direction (250°) than in the opposite direction, suggesting that that the hammer plate happened to move in that direction more often than the opposite direction in this particular set of hammer impacts. Therefor, the P-wave energy pattern is fully consistent with our Lorentz field explanation.

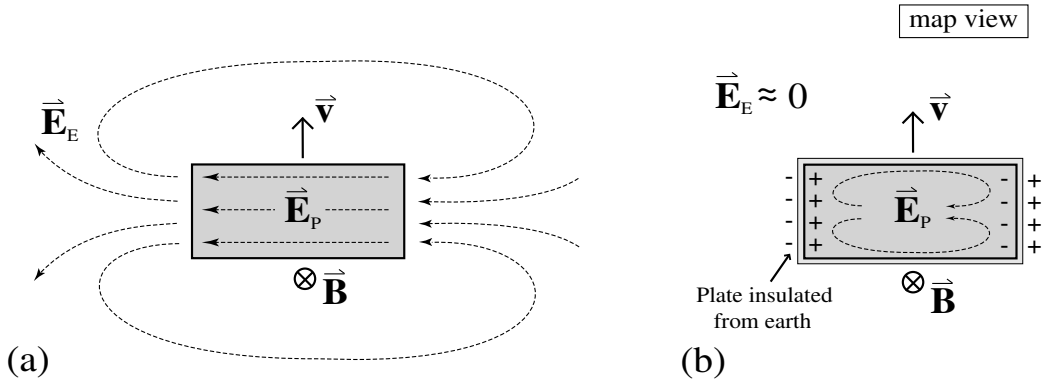

Figure 2.32: Motion of the metal hammer plate $\mathbf{v}$ in the Earth's magnetic field $\mathbf{B}$ creates an electric field $\mathbf{E}_p = \mathbf{v} \times \mathbf{B}$ in the plate. It may or may not cause a noticeable electric field $\mathbf{E}_E$ in the earth, depending on the electrical contact between the plate and the soil. a) When the plate is in contact with the soil, current flows between the two and creates a field $\mathbf{E}_E$ that we measure as the Lorentz field. b) When insulation is present, the currents created by $\mathbf{E}_p$ are restricted to the plate, charge accumulates in the soil to negate the charge accumulations in the plate, $\mathbf{E}_E$ is very small, and we observe no Lorentz field. field-lorentz_both [NR]

The qualitative nature of the electric fields created by a moving metal plate, both with

and without insulation surrounding the plate, is depicted in Figure 2.32. We now attempt to quantify this picture. In what follows, we consider the hammer plate to be the aluminum cylinder that was actually used in our field experiments.

The Lorentz effect (e.g., Landau and Lifshitz, 1984) is responsible for creating an electric current density $\mathbf{J}_p = \sigma_p \mathbf{v} \times \mathbf{B}$ in a conductor of conductivity σ_p that is moving with velocity $\mathbf{v} = v_h \hat{\mathbf{h}} + v_z \hat{\mathbf{z}}$ in a magnetic field $\mathbf{B} = B_h \hat{\mathbf{h}} + B_z \hat{\mathbf{z}}$ (like the earth's magnetic field). In our case of a metal cylinder being hit by a hammer, we take the horizontal unit vector $\hat{\mathbf{h}}$ to be perpendicular to the cylinder's axis and parallel with the earth's surface. It is the horizontal velocity component v_h that varies in sign from one strike to the next and that is dominantly responsible for what we have called the Lorentz field on our seismoelectrograms. There is thus a total current $I_p = \pi a^2 \sigma_p v_h B_z$ being injected into the soil at one end of the metal cylinder (assuming that contact resistance between the plate and the soil is negligible), and the same amount being extracted from the soil at the other end, where a is the radius of the cylinder. For observation distances r that are much greater than the cylinder length d, this situation is well modeled as a horizontal current dipole.

The electric field that is observed in the same plane (the earth's surface) as the horizontal dipole at a position (r, θ) where θ is angle from the cylinder axis, is easily shown to be

$$\mathbf{E}_E = \frac{I_p d}{2\pi \sigma_e r^3} \left(\hat{\mathbf{r}} 2\cos\theta + \hat{\theta} \sin\theta \right) \tag{2.4}$$

where again $I_p = \pi a^2 \sigma_p v_h B_z$ and where σ_e is the earth's (i.e., soil) conductivity. However, if the plate conductivity is taken to be that of aluminum ($\sigma_p = \sigma_{\mathrm{Al}} \approx 4 \times 10^7$ S/m), this formula predicts an electric field in the earth that is much larger than the field actually observed (which is $E_r \approx 10^{-5}$ V/m at a distance of $r = 4$ m).

This problem is easily resolved if we assume that a small lubrication layer of soil having thickness δ moves along with the metal cylinder at the velocity v_h. In this case, the effective "plate conductivity", that includes the aluminum and thin soil layer moving together, can be identified from the series sum (since the same current passes both through the aluminum and attached soil layer)

$$\frac{1}{\sigma_p} = \frac{2\delta}{d\,\sigma_e} + \frac{d - 2\delta}{d\,\sigma_{\mathrm{Al}}}. \tag{2.5}$$

Since $\sigma_e/\sigma_{\mathrm{Al}} \approx 10^{-10}$ for typical soil conductivities, we have the accurate approximation that $\sigma_p \approx \sigma_e d/(2\delta)$. In this case, our estimate of the electric field becomes

$$E_r = \frac{a^2 d^2}{2\delta r^3} v_h B_z \sin\theta. \tag{2.6}$$

Using the experimental values $a = 7$ cm, $d = 20$ cm, $v_h \approx 20$ m/s, $B_z \approx 4 \times 10^{-5}$ T, we find that a lubrication layer thickness of $\delta \approx 10^{-4}$ m is adequate to explain the field observation that $E_r \approx 10^{-5}$ V/m at $r = 4$ m. Note that 10^{-4} m corresponds to the thickness of a couple of sand grains and is thus of reasonable size. We feel these arguments convincingly demonstrate that the fields generated by the aluminum cylinder were indeed generated via the Lorentz effect as postulated.

For the insulated case (Figure 2.32b), charge can not flow to or from the soil. Charge accumulates in the soil at the ends of the plate to counter the accumulations inside the plate, a response that is instantaneous relative to the sampling rate of our recording system, so we measure no field $\mathbf{E}_E$. Dry soil acts as an insulator, so we observe no Lorentz energy under dry conditions or when the plate is intentionally insulated from the soil.

We conclude that horizontal motion of the metal hammer plate in the Earth's magnetic field is responsible for the Lorentz field. This motion is generally parallel to the orientation of the swing of the hammer. The strike-to-strike polarity reversals are due to the random chance governing the slight variations in hammer trajectory which determine the direction of the horizontal plate motion. For data collected while intentionally striking the plate in a particular horizontal direction, we do not observe any polarity reversals. Electrical contact between the metal plate and the soil is necessary for observation of the Lorentz field, so the use of insulation between the plate and the soil eliminates the field, as do soil conditions that are so dry as to prevent adequate contact.

Interface response

Having discussed two unwanted effects (the direct and Lorentz fields), we now focus on the interface response. The interface response is the seismoelectric phenomenon of most interest,

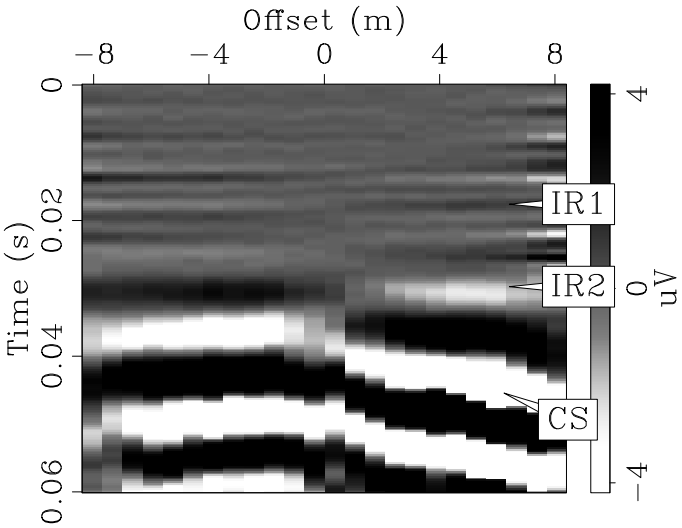

Figure 2.33: Seismoelectric shot gather shown in Figure 2.20c, but including lower frequency energy (to 100 Hz). Source was 0.45 kg of explosive 1.5 m deep, located 6 m from the first trench. Receivers were located 2 m from the second trench. field-fan_boom_plot [ER]

as it can provide useful new information about the subsurface. Many previous experimenters have provided definitive observations of the interface response (Thompson and Gist, 1993; Butler et al., 1996; Garambois and Dietrich, 2001). In this section, we show an example of the interface response from our field experiments, along with an accompanying synthetic model.

Figure 2.34a shows a shot gather collected using the fan geometry at the vineyard site. The source [0.45 kg (1 lb) of explosive buried 1.5 m deep] was located 6 m from the first trench. The receiver array [24 channels of 1.05 m electrode dipoles at 0.7 m intervals] was positioned 2 m from the farther edge of the second trench. In the gather (Figure 2.33) we observe several flat events preceding the arrival of the coseismic energy (labeled CS). Based on travel times, we interpret the flat arrival marked “IR1” as the interface response from the near side of the first trench, and the event marked “IR2” as the interface response from the far side of the second trench.

In order to confirm our interpretations, we compare the amplitude pattern of an observed interface response event with the amplitude pattern that would be predicted for that event. We consider each interface response event to be created by a disk of dipoles spread over the first seismic Fresnel zone, and take the far side of the first trench as the location of the disk associated with IR1. We use Equation (2.1) to model the potential distribution associated with this geometry, and estimate the radius of the first Fresnel zone assuming a frequency of 120

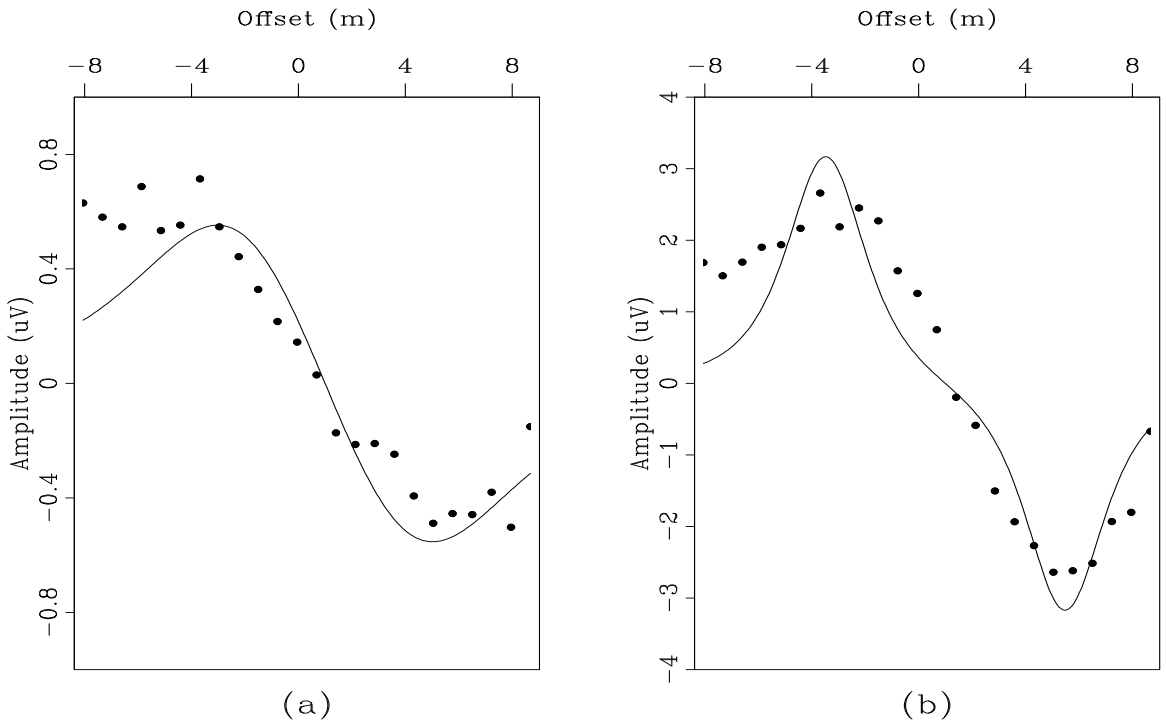

Figure 2.34: Real and modeled amplitudes for the interface response arrivals marked in Figure 2.33. a) Amplitudes for the flat interface response event at 0.019 s (marked "IR1" in the display) are plotted as dots, and the modeled dipole is plotted as the solid line. The model corresponds with an interface response event at the near side of the first trench. b) Amplitudes for the interface response event at ∼30 ms (marked "IR2" are plotted as dots, and modeled dipole representing an interface response occurring at the near side of the second trench is plotted as the solid line. See text for details on modeling. Note that the vertical axis (amplitude scale) is different between the two plots. field-fan_boom_amps [ER]

Table 2.2: Physical properties of materials in modeled gather.

	V_p (m/s)	porosity (%)	saturation (%)	hydraulic perm. (m^2)	elec. cond. (S/m)
clay	341	10	97	10^{-14}	0.05
sand	380	30	97	10^{-11}	0.01

Hz and the simple relation presented by Sheriff and Geldart (1995):

$$r = \left(\frac{\lambda z}{2}\right)^{\frac{1}{2}} \tag{2.7}$$

for a P-wave of wavelength λ encountering an interface at a distance z from the source. To account for the disk of dipoles, we simply sum the potential for a number (100) of electric dipoles spread over the first Fresnel zone. We do not attempt to model the absolute amplitude of this interface response event, and simply assign an arbitrary scale factor (qd in Equation 2.1) to produce the model shown as the solid line in Figure 2.34a. The modeled amplitudes closely match the real amplitudes (plotted as dots in Figure 2.34a), demonstrating that our field data match the seismoelectric theory and helping to confirm our data interpretations. A similar analysis is shown for the interface response event IR2 in Figure 2.34b, which also shows good fit.

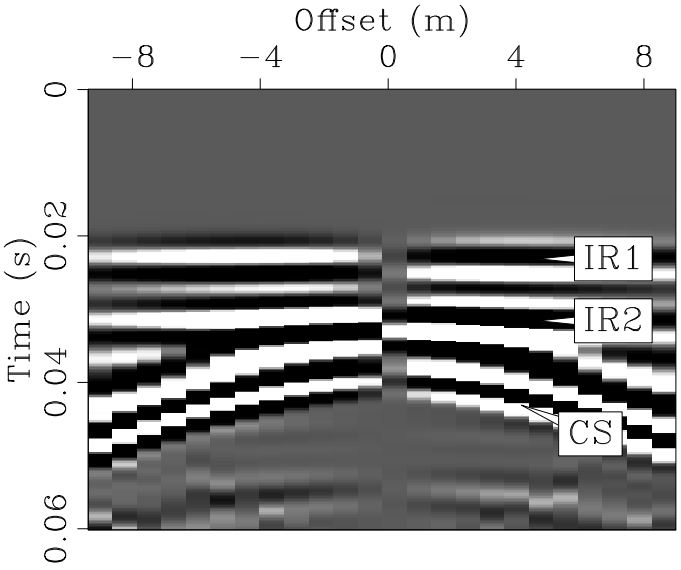

Figure 2.35: Synthetic shot gather, modeling the data shown in Figure 2.33. Geometry is identical (source 6 m from first trench, receivers 2 m from second trench) and material properties are shown in Table 4.1. Interface response events from the trenches are labeled "IR1" and "IR2", and coseismic energy as "CS". field-syn.fan_boom_plot [ER]

We can go a step beyond simple amplitude modeling with synthetic seismoelectrograms.

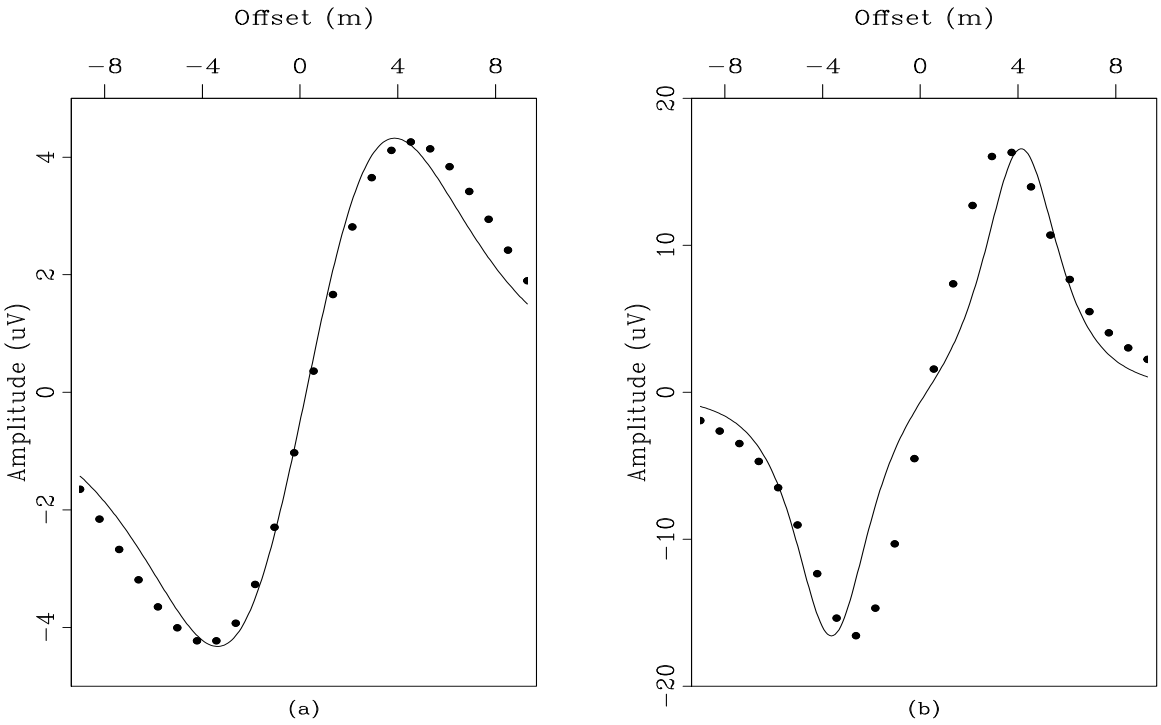

Figure 2.36: Amplitude modeling results for interface response events in Figure 2.35. a) Amplitudes for event IR1 (dots) and amplitudes modeled using Equation (2.1) (solid line). b) Amplitudes for event IR2 (dots) and modeled amplitudes (solid line). Modeled (solid line) amplitudes are calculated the same as those in Figure 2.34. field-syn.fan_boom_amps [ER]

Figure 2.36a shows a synthetic shot gather produced using the finite-difference modeling algorithm described in Appendix A and the same geometry as the real data in Figure 2.33. Material properties for the layers in the model are shown in Table 4.1. The model space is two-dimensional, so the vineyard site is modeled in map-view. Thus the model is unrealistic in that it assumes infinitely-deep trenches and has no free surface. The modeled data (Figure 2.35) closely resemble the real data (Figure 2.33) in the basic trends. The exact arrival times of events (principally the first interface response arrival) do not match exactly, a feature which we attribute to velocity heterogeneities in the real field site that are not included in the highly-simplified synthetic model. For comparison with Figure 2.34, we show comparable plots in Figure 2.36. In this case the dots are amplitudes extracted from the synthetic data (the events labeled IR1 and IR2 in Figure 2.35), and the solid lines are calculated in the same way as those in Figure 2.34. In this case we use a frequency of 200 Hz for calculation of the Fresnel zone radius, as this is the fundamental frequency of the source wavelet for the synthetic. The finite-difference modeling algorithm does not include attenuation, so this fundamental frequency prevails throughout the synthetic data. The fact that the arrivals IR1 and IR2 have similar amplitudes (to each other) in the 2D synthetic, while having different amplitudes in the 3D field data, is at least partly due to the fact that the electric field of a dipole falls off as r^{-2} in 2D but as r^{-3} in 3D.

We have presented examples of interface response arrivals in real field data, along with finite-difference modeling results showing similar arrivals. These results provide further evidence beyond that already existing in the literature of the existence of the seismoelectric interface response, and also confirm that the seismoelectric theory (which produced the synthetic gather) matches the phenomena that we observe in the field.

DATA COLLECTION SUMMARY

In summary of our data collection findings:

- Electric isolation (transformers or pre-amplifiers) between the recording instrument and the electrodes is essential.

- Electrode dipole widths of ∼1 m are preferable to ∼5 m (at least for our sites).
- Geophones within electrode pairs do not contaminate the seismoelectric record.
- The sledgehammer is preferable to the shotgun source (for our sites).
- The Lorentz field can be avoided with a non-metal hammer plate, though our aluminum cylinder produces the best signal of the plates we tested.
- Explosive sources are the only option for producing sufficient energy for offsets greater than (analogous to layers deeper than) ∼8 m, for our vineyard trench geometry.

DISCUSSION AND CONCLUSIONS

We have described a set of experimental methods that enable us to record the seismoelectric interface response separately from the coseismic noise and direct field by placing sources and receivers on opposite sides of a vertical interface. Our two preferred seismic sources are chemical explosions and stacked sledgehammer impacts. We record data using a standard engineering seismograph outfitted with grounded electrode pairs replacing the geophones, and step-up transformers isolating the seismograph from the earth.

Two series of controlled experiments, combined with amplitude modeling and travel-time analysis, permit us to confidently interpret all of the electrical arrivals that we observe in our field data gathers. We observe the seismoelectric direct field predicted by Pride and Haartsen (1996), and establish that it can be approximated as a vertical electric dipole at the location of an asymmetrical seismic source. We provide a physical model for the phenomena producing the Lorentz field associated with the use of a metal hammer plate.

While the seismoelectric method is not yet developed to a point where it may be used "off the shelf" as an exploration method, the seismoelectric method promises to provide useful new information about the subsurface, including information about thin layers and flow property variations. Our work represents important progress toward that goal in terms of developing our understanding of the relation between the well-developed seismoelectric theory and real

field data and in terms of developing experimental methods necessary to reliably collect seismoelectric data.

ACKNOWLEDGMENTS

The data presented here would not exist without the effort of those who swung the hammer: Nick Martin, Jordan Muller, Brian Ebel, Mike Beman, Ashley Griffith, Rob Sanders, Phil Resor, T.J. Kiczenski, Stephan Bergbauer, Antoine Guitton, Morgan Brown, and Jonathan Franklin. Jerry Harris has been an essential source of insight and guidance since the inception of this project. We are very grateful to Jim and Carolyn Pride and to George and Anita Thompson for use of field sites on their property. We offer many thanks to Rufus Catchings and Tom Burdette for help with data collection. Art Thompson graciously provided some essential electronics, along with important input on data collection. Dave Alumbaugh and Adam Pidlisecky provided important input on electric fields in the earth. Acknowledgement is made to the Donors of the American Chemical Society Petroleum Research Fund for support of this research. Additional funding has been provided by the Achievement Rewards for College Scientists Foundation, the Stanford School of Earth Sciences McGee Fund, the AAPG student research grants program, the GSA student research grants program, the Colorado Geological Survey and the Stanford Exploration Project.

Chapter 3

Seismoelectric data processing

INTRODUCTION

The seismoelectric method has the potential to offer useful new subsurface information regarding the location of thin layers and permeability contrasts, complementary to that provided by existing methods and useful in environmental and exploration geophysics. A number of workers in the last decade have observed clear seismoelectric signals (Thompson and Gist, 1993; Butler et al., 1996; Garambois and Dietrich, 2001; Haines et al., 2004), but the utility of the method is limited by the lack of well-established experimental methods. Chapter 2 provides a set of field methods for the collection of seismoelectric data in shallow settings, but these data are generally plagued by strong coherent noise. In this chapter we address the issue of data processing, a key step in developing the utility of the seismoelectric method.

Seismoelectric phenomena produce three forms of energy (as described in Chapter 2): the direct field, the interface response, and the coseismic field. The coseismic field is considered noise in the context of our desire to observe the interface response. We are interested primarily in the interface response, which may be as much as several orders of magnitude weaker than the coseismic noise, as only it can tell us about physical properties at depth. The direct field looks very similar to the interface response (being created by virtually the same physical

mechanism), complicating efforts to separate the two with data processing. However, the direct field is created only at the source point and exists for less than 20 ms, so is not a problem for surface surveys targeting layers deeper than a couple of meters, or for any survey in which the source and receivers are separated by sufficient distance (dependent on the amplitude and arrival times of the events of interest). Thus we primarily concern ourselves with identifying and enhancing the interface response energy in seismoelectric records, and specifically with separating it from the coseismic noise.

Coseismic energy in a seismoelectric record represents the electric field carried in a seismic wave, and thus is very similar to seismic arrivals in terms of waveform and travel time. In particular, the coseismic energy in a P-wave traveling at velocity V_P will show move out along the electrode array, a key difference from interface response energy. Although it is generally very weak, the interface response signal does exhibit several properties which we may exploit in our signal processing efforts. Because it is created by an oscillating electric dipole at depth, it shows opposite polarity on opposite sides of the shot point, and virtually zero move out relative to coseismic energy ($V_{EM} \gg V_P$). The amplitude pattern is the potential field V of a dipole (at a horizontal offset x and depth z):

$$V(x,z) = \frac{qd}{4\pi\epsilon_0} \frac{z}{(x^2+z^2)^{3/2}}, \tag{3.1}$$

where q is the magnitude of the electrical charges, d is the distance between the two separated charges, and ϵ_0 is the electrical permittivity.

The methods presented by Butler and Russell (1993) and Butler and Russell (2003) provide very effective approaches for the removal of power line energy from seismoelectric records, and represent a key first step in seismoelectric data processing. However, these are the only published discussions of seismoelectric data processing (aside from the work of Haines et al. (2003), on which we build), and they do not address the other essential aspects of seismoelectric signal processing. The similarities between seismic and seismoelectric data processing allow us to employ seismic data processing and signal/noise separation techniques as we develop processing flows for seismoelectric data. Pre-processing steps such as amplitude corrections and frequency filtering prepare the data for the separation of the interface response

signal from the coseismic noise.

Waveform transformations into the Fourier (f-k) and radon (τ-p) domains permit the separation of arrivals of different dip or curvature (Yilmaz, 2000). At far offsets, these approaches can therefore separate the dipping coseismic energy from flat interface response events. However, coseismic energy at shorter offsets is very nearly flat and so can not be separated cleanly from interface response energy using transform methods. In addition, the imperfect nature of real seismoelectric data (amplitude variations, spikes, etc) causes further trouble, as these spikes do not transform cleanly, blurring the separation between signal and noise in the transform domain.

Prediction-error filters (Claerbout, 1999) can be used to model the signal and noise separately, and can be used in an iterative inversion scheme to separate the data into estimated signal and noise models (Soubaras, 1994). The approach takes advantage of the amplitude patterns of the signal and noise, as well as the patterns of their arrivals. Prediction-error filters (PEF's) offer an effective alternative to waveform transformations as we compare signal/noise separation techniques for seismoelectric data.

The ultimate goal of seismoelectric data processing is, of course, to produce an image of the subsurface. This is accomplished by stacking individual shot gathers to produce a set of traces that each represent the subsurface beneath that particular shot point. Because the interface response is created only at the first Fresnel zone, a given shot gather provides information only about the subsurface directly beneath that shot point (if we assume horizontal interfaces). A set of shot gathers, with shot points spaced along a linear profile of interest, can thus provide a two-dimensional image of the subsurface beneath. Therefore, it is the goal of the data processing presented here to produce a shot gather that can be stacked to enhance the interface response events of interest, and cancel out any remaining noise energy.

The processing sequence may be divided into two parts: pre-processing, and signal/noise separation. Pre-processing is designed to minimize background electrical noise and to prepare the data for signal/noise separation. Signal/noise separation is intended to separate the coseismic energy from the desired interface response events. We compare results from various pre-processing and signal/noise separation techniques as applied to real and synthetic data.

Table 3.1: Physical properties of materials in synthetic model.

	V_p (m/s)	porosity (%)	hydraulic perm. (m^2)	electrical cond. (S/m)
sand	1859	30	10^{-11}	0.01
clay	2296	10	10^{-14}	0.05

TEST DATA

In order to adequately compare various data processing techniques, we must apply them to the same raw data. For this purpose we chose a synthetic shot gather, and two real data gathers.

Synthetic seismoelectric data

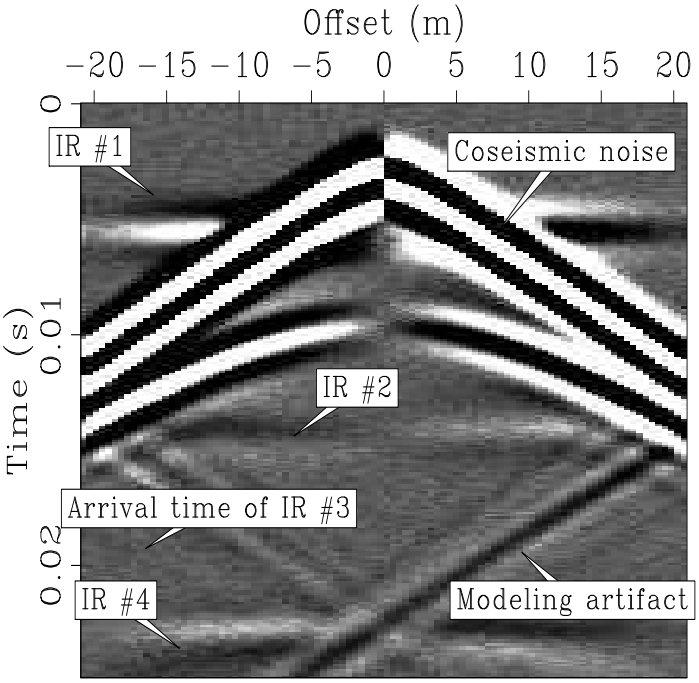

Figure 3.1: Synthetic seismoelectric data for testing signal/noise separation techniques. Arrows and labels identify the seismoelectric arrivals. It is our goal to remove the curved and dipping energy, and to enhance the flat interface response events including the hidden IR #3. Note that the coseismic energy of the reflection from interface 2 arrives later than the window shown. proc-synth [ER]

Testing on synthetic data permits evaluation of the effectiveness of processing techniques while avoiding the complexities of real data. In addition, the use of synthetic data permits us to test processing ideas on data sets that would be prohibitively expensive to collect in the field (large numbers of channels, etc). We use the synthetic seismoelectric shot gather

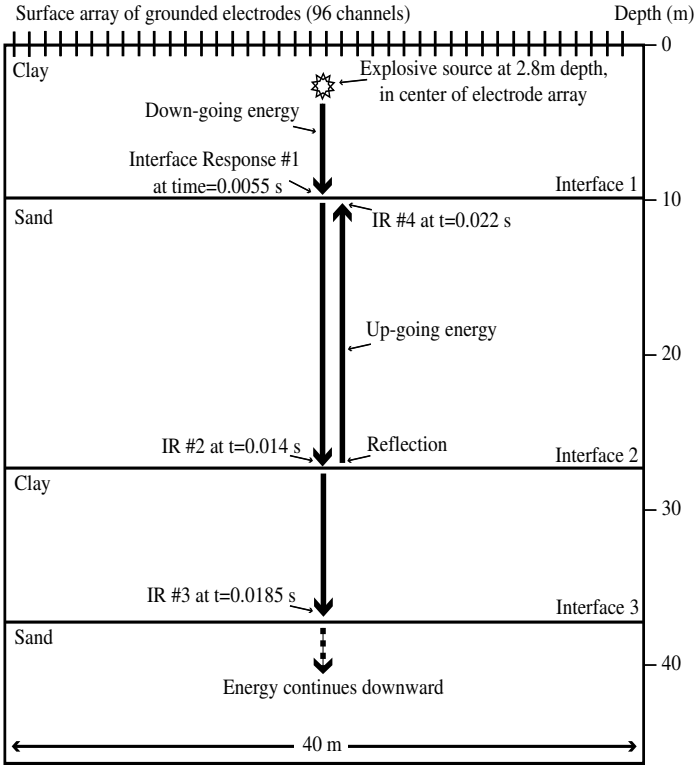

Figure 3.2: Geologic model used for calculation of synthetic data shown in Figure 3.1. Thick arrows indicate ray paths for seismic energy that creates seismoelectric interface response events. In addition to this energy, the direct and reflected seismic arrivals are recorded as coseismic noise (the curved arrivals in Figure 3.1). Seismic reflections of course occur at all interfaces, but only the reflection from the second interface produces an observed interface response event (IR #4) on its path back upward, so only this reflection is represented with a thick arrow. For material properties, see Table 3.1. proc-synth_sketch [NR]

shown in Figure 3.1 as a first test of signal/noise separation options. This 96-channel shot gather was created using the finite-difference modeling approach described in Appendix A. It corresponds with the geologic model shown in Figure 3.2, which consists of alternating clay and sand layers (material properties are shown in Table 3.1). An explosive source at a depth of 2.8 m depth provides the energy that is recorded by 96 pairs of electrodes at the surface of the model. The width of each dipole pair is 1.4 m, and the spacing between the centers of the pairs is 0.44 m. Uniform white noise has been added to the gather for realism.

Within the gather, there are four interface response events which we wish to separate from the curved coseismic energy, the dipping modeling artifacts, and the random noise, as identified in Figure 3.1. The first interface response event (IR #1, in Figure 3.1) was created when the down-going P-wave encountered the first interface. IR #2 corresponds with the second interface, and the unseen IR #3 corresponds with the third interface. This event can not be identified in this shot gather, even with high gains, or low display clipping, as it is below the level of the background noise, and far below the level of the other coherent energy. This event

provides a challenging test for our signal/noise separation techniques. The interface response event labeled IR #4 was created when the reflected P-wave traveling upward from the second interface encountered the first interface. It shows a higher amplitude than IR #3 because the interface is much shallower, but lower amplitude than IR #1, because of energy loss associated with the longer distance traveled (divergence only; this modeling does not include attenuation). Interface response events #1, #2, and #4 are visible in the raw data, but are obscured by coherent noise; these are the main targets for our signal/noise separation comparisons.

Real seismoelectric data

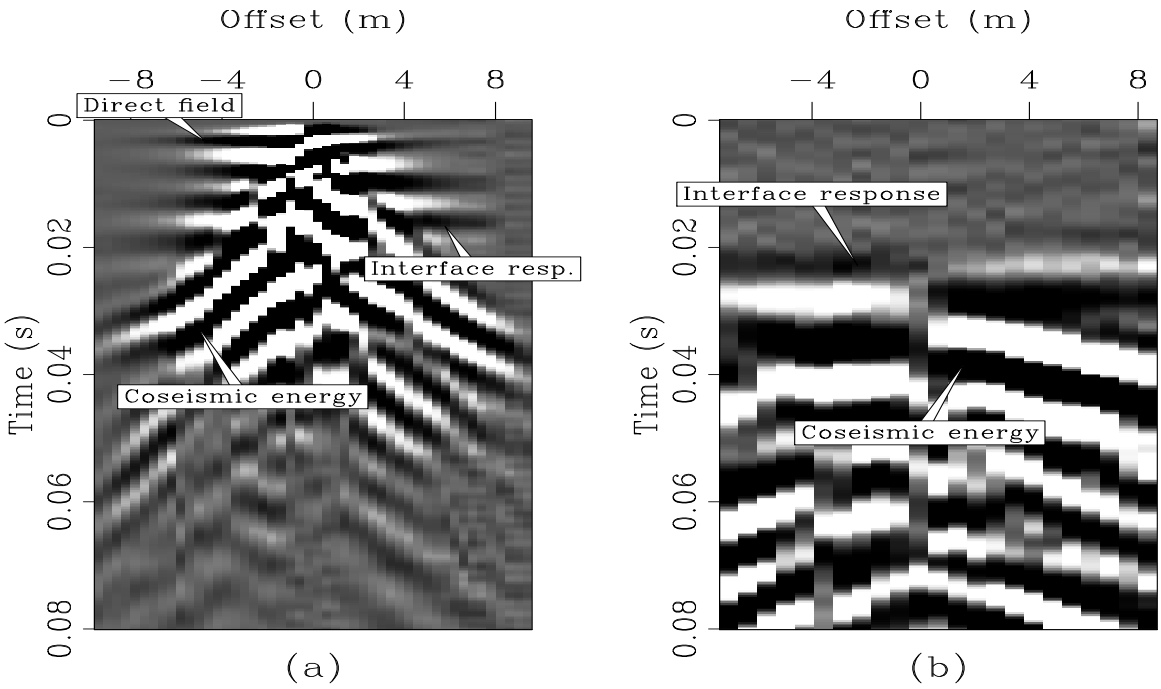

Figure 3.3: Real seismoelectric shot gathers. a) 48-channel in-line geometry gather with seismoelectric arrivals labeled. Display filter: 120 to 500 Hz. b) 24-channel fan-geometry gather with interface response energy arriving before the coseismic energy. Display filter: 110 to 300 Hz. Data specifics are provided in the text. proc-real [ER,M]

While synthetic data provide a valuable test of data processing techniques, they can not replace real data collected in the field. We consider seismoelectric data collected in two different recording geometries (Figure 3.3a and b). First we examine the "in-line" geometry,

in which the source is at the center of a linear array of electrodes. This is comparable to a split-spread seismic survey, and is the geometry most commonly employed in seismoelectric surveys. Figure 3.3a shows an in-line gather, with dipping coseismic energy and flat interface response events labeled. This gather is the result of stacking 25 impacts of a 12-lb sledgehammer on a hammer plate located ∼0.5 m from the center of a 48-channel electrode array with 0.4 m spacing between electrode dipoles that are 1.4 m wide (dipoles overlap). The array was deployed at an angle of 20° to the trenches at the vineyard test site (see Chapter 2), with the center of the line (and the source point) located 3.5 m from the nearer trench.

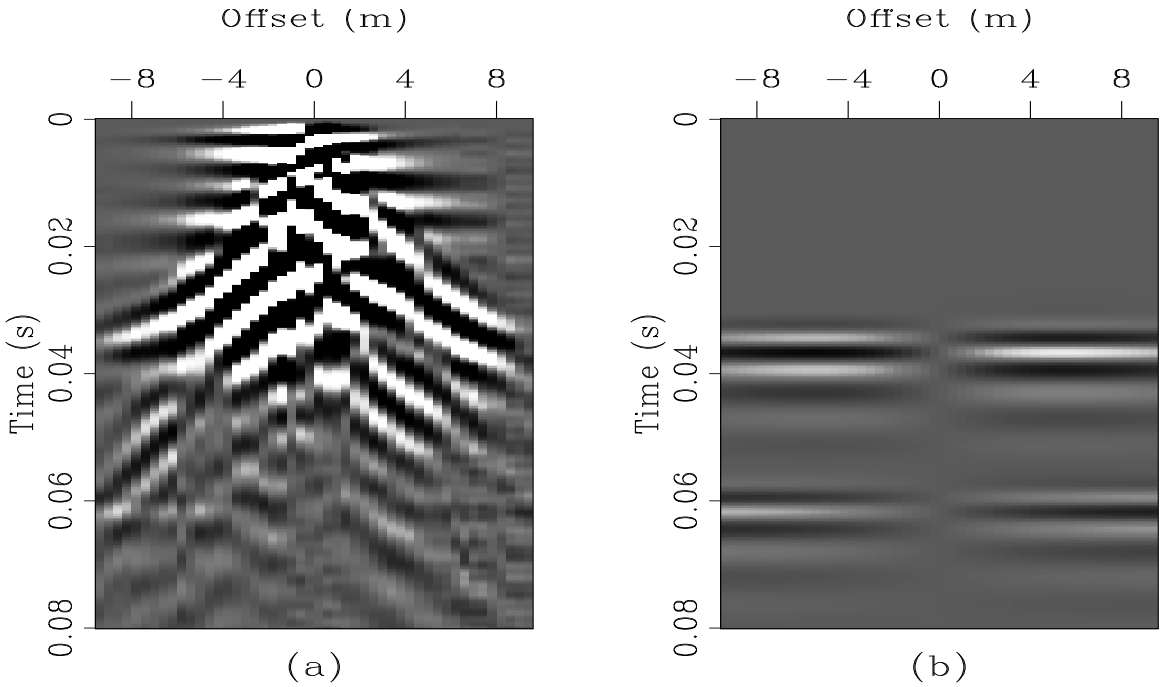

Figure 3.4: a) Real seismoelectric data with added synthetic interface response events. Original gather is the same as that in Figure 3.3a. b) Synthetic events that were added to the data in Figure 3.3a to produce the gather shown in part a. Display filter: 120 to 500 Hz. proc-freal [ER]

Because the in-line geometry is the most-commonly used, we focus our real-data demonstrations on the gather shown in Figure 3.3a. But because of the subsurface geometry, and data acquisition parameters, we do not have any hidden interface response events to try to separate from the coseismic noise. For this reason, we add two synthetic events to the gather shown in Figure 3.3a, with the resulting data shown in Figure 3.4a and the synthetic events shown alone

in Figure 3.4b. These events were created using a Ricker wavelet (dominant frequency 150 Hz) and assuming that the interface response from a particular depth z is the equivalent of the summation of the fields of electric dipoles (potential calculated using Equation (3.1) spread over the first Fresnel zone). We calculate the radius of the first Fresnel zone using the relation presented by Sheriff and Geldart (1995)

$$r = \left(\frac{\lambda z}{2}\right)^{\frac{1}{2}}, \tag{3.2}$$

for a wavelength λ calculated using the dominant frequency of the wavelet and a specified (constant) velocity v =400 m/s. Because we know exactly where these added events are, they provide a good test of signal/noise separation methods. We can also attempt to separate the coseismic noise from the direct field energy in the upper ∼20 ms of the real data gather, as it is very similar to the interface response energy that is our main interest.

We are also interested in a second recording geometry, termed a "fan" deployment, due to its similarity to the seismic fan geometry. The source is positioned at a distance perpendicularly away from the center of electrode receiver line. Figure 3.3b shows such a gather, collected with the source and receivers on opposite sides of two sand-filled trenches (as described in Chapter 2). The fan geometry is useful because it allows the interface response energy to be recorded before the coseismic energy. The source energy strikes the trenches and creates the interface response (traveling at V_{EM}) before the coseismic field (traveling at V_P) reaches the receiver electrodes. The gather in Figure 3.3b is the result of recording the explosion of one-third pound of charge located 3 m from one trench with the electrode receivers located 5 m from the opposite trench. The electrode dipoles were 1.05 m wide, and spaced at 0.7 m. This gather is of particular interest because it was recorded without stacking; it is just one dynamite shot, and so may have stronger and more difficult-to-remove electrical background noise.

DATA PRE-PROCESSING

We consider seismoelectric data $\mathbf{d}$ to be the sum of background noise $\mathbf{n}_{bg}$, coseismic noise $\mathbf{n}_{cs}$ and interface response signal $\mathbf{s}$ (and assume that we are not concerned with the direct field):

$$\mathbf{d} = \mathbf{n}_{bg} + \mathbf{n}_{cs} + \mathbf{s}. \tag{3.3}$$

Our signal/noise separation techniques are designed to separate $\mathbf{s}$ from $\mathbf{n}_{cs}$, so we must first employ some pre-processing steps to remove the background noise $\mathbf{n}_{bg}$. Harmonic noise from the power grid is a major component of $\mathbf{n}_{bg}$, and electrical transients (such as from distant lightning strikes, etc.) are another significant aspect of $\mathbf{n}_{bg}$. This section is a discussion of approaches for removing $\mathbf{n}_{bg}$ and minimizing $\mathbf{n}_{cs}$ in order to prepare the data for the signal/noise separation techniques discussed in the following section.

60 Hz harmonic noise removal

Seismoelectric data contains a great deal of harmonic electrical noise from the power grid and any local sources of AC noise (generators, pumps, etc). Butler and Russell (1993) present a simple and effective approach (which we will refer to as "sinusoidal subtraction") for removing this noise by solving for the amplitude and phase of the dominant frequency and its harmonics in a least-squares sense, using a segment of the shot record that is free of seismoelectric energy such as a pre-trigger recording window. The amplitude and phase information are used to construct a noise sinusoid which is then subtracted from the data. The gather shown in Figure 3.3b has undergone some simple pre-processing; the raw data are shown in Figure 3.5a, and a bandpass-filtered version (100 to 500 Hz) in Figure 3.5b. The 60 Hz energy that dominates the record is clearly visible. Using a pre-trigger window of 0.1 s, we determine the amplitude and phase of all harmonics of 60 Hz up to the Nyquist frequency (2000 Hz) and subtract the resulting sinusoid from the data to produce the result shown in Figure 3.5c and d. A large part of the power line energy has been removed, leaving a much cleaner record. However, a significant amount of harmonic noise remains in the frequency band of interest (shown in Figure 3.5d), making interpretation of flat events difficult.

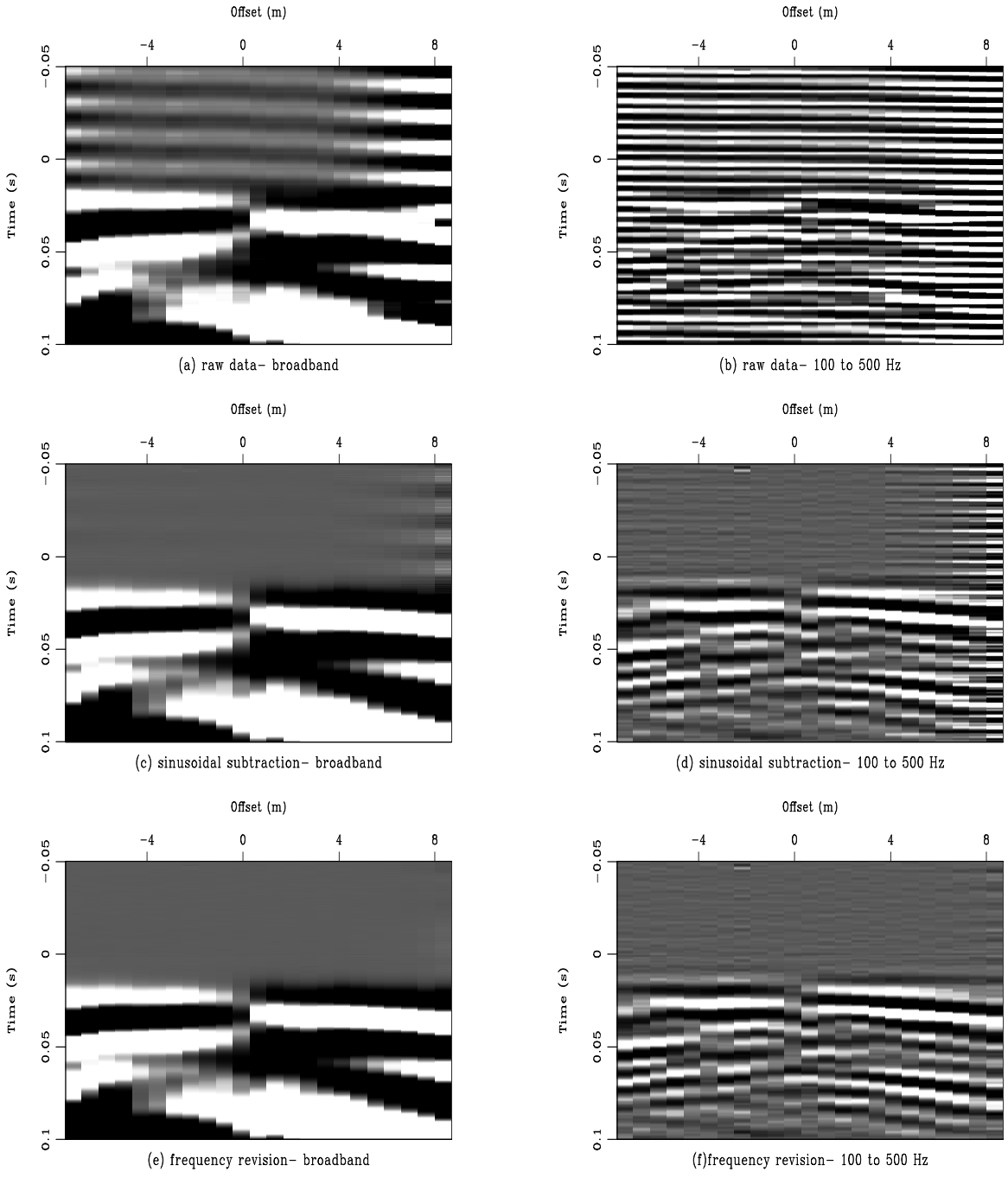

Figure 3.5: Comparison between raw data and results after two different approaches for 60 Hz energy removal. All plots are the data shown in Figure 3.3b, but with different processing applied. The plots on the left are shown with all recorded frequencies, while the plots on the right are shown after application of a 100 to 500 Hz bandpass filter. a) and b) show raw data, c) and d) show data after sinusoidal subtraction technique, and e) and f) show data after the frequency revision technique for removal of power line energy. See text for details. proc-60hzdemo [CR,M]

Butler and Russell (2003) present an improved method for removal of power line energy, which takes into account the slight variations that may exist in the fundamental frequency. Instead of simply assuming that the fundamental frequency of the power line noise is 60.0 Hz (for North America), this "frequency revision" approach employs an inversion for the exact frequency while the phase and amplitude of the fundamental and its harmonics are being simultaneously determined. Another advantage of the approach of Butler and Russell (2003) is that the window used for estimation of the coefficients can be of any length, rather than (as for the sinusoidal subtraction approach) needing to be an integer multiple of the period of the dominant frequency. Using the frequency revision approach, and a noise estimation window from -0.08 to -0.01 s, we produce the result shown in Figure 3.5e and f. In both these displays, the improvement beyond the results shown in Figure 3.5c and d is apparent. The trade-off, however, is that the frequency revision approach is much more computationally intensive than the sinusoidal subtraction. Instead of a simple calculation for the coefficients corresponding with the fundamental frequency, the frequency revision approach requires many inversions for these coefficients as it performs a line search for the best-fitting fundamental frequency.

The difference between results from the sinusoidal subtraction and frequency revision approaches is quite apparent in Figure 3.5. However, this is an extreme case as it is for an unstacked shot record. With sledgehammer stacking, minor deviations of the fundamental frequency from 60 Hz tend to average out over the course of the data collection, resulting in a record whose power line energy is often closer to 60.0 Hz than the individual gathers that went into it. Thus the sinusoidal subtraction technique is generally adequate for sledgehammer data, while the frequency revision approach may be required for explosive-source (or other unstacked) data.

Other pre-processing steps

Many of the standard seismic data processing steps are essential parts of the seismoelectric processing sequence as well. High-frequency noise spikes (from distant electrical storms, etc) and background noise can be minimized with high-cut filters. The signal/noise ratio between the interface response signal and the coseismic noise can often be improved by low-cut filters,

since the coseismic noise generally contains lower-frequency energy due to its longer distance of travel as a seismic wave and the associated attenuation of higher frequencies. (The interface response does not experience any appreciable attenuation because our offsets are far smaller than the wavelength associated with the frequency band employed in seismoelectric studies). We use minimum-phase Butterworth bandpass filters to minimize coseismic and background noise.

Because our ultimate goal is to stack each seismoelectric shot gather to produce a trace that includes only interface response energy, we must be careful that our pre-stack processing does not leave behind any energy that will contaminate the stack. The most difficult-to-remove parts of the coseismic noise are the flat portions of the coseismic hyperbolas which occur at the nearer offsets. One effective option is to simply exclude the near-offset traces from the stack, or to eliminate these traces as part of pre-processing. This can be particularly valuable before waveform transforms since the flat part of a coseismic arrival can be virtually indistinguishable from flat interface response energy in the transform domain.

As with seismic data, seismoelectric data from deeper interfaces will generally show lower amplitudes than shallower interfaces. We adjust for these amplitude variations using standard gain procedures such as automatic gain control (AGC) and also gains corresponding with multiplication of each sample in a trace by a scalar that is the arrival time raised to a certain power (e.g. t^2). In some cases it is beneficial to apply these gains before signal/noise separation, such as to boost the amplitude of deeper events so that they are have equal importance in the residual of inversion schemes. In other cases, the gains are applied after signal/noise separation to produce a desired display. In any case, it is desirable to keep track of the gains applied so that the data can be scaled back to the original amplitudes as needed.

One important characteristic of the interface response is that the polarity of a given even is reversed on opposite sides of the shot point. Thus, before stacking, we must flip the polarity of the traces on one side of the shot point. This can be an important pre-processing step before waveform transformations, so that the events of interest have constant polarity across the gather, and therefore show a simpler pattern in the transform domain.

The pre-processing necessary before a given signal/noise separation technique varies with

the data in question, and the signal/noise separation method to be used. As with seismic data, the specific parameters for a given pre-processing step (e.g. the frequency cut-off's for a bandpass filter) must be determined experimentally for each case.

We show all data as grey-scale variable density plots, with the color white representing the greatest positive values and black representing the greatest negative ones. Variable density plots permit the display of data with greater dynamic range than wiggle plots, and also tend to give the viewer equal appreciation of both positive and negative polarities. The amplitude level that is represented by the color white or black is referred to as the "clip level". That is, a lower clip level will cause lower amplitude positive polarity energy to appear more white, while a higher clip value will cause them to appear more grey.

SIGNAL/NOISE SEPARATION METHODOLOGIES

Assuming that pre-processing has been successful, our data are now the sum of only interface response energy $\mathbf{s}$ and coseismic noise $\mathbf{n}_{cs}$:

$$\mathbf{d} = \mathbf{n}_{cs} + \mathbf{s}. \tag{3.4}$$

It is our goal to separate these two forms of energy, and although coseismic noise may be of much greater magnitude, we can exploit three distinctive attributes of the interface response energy to identify and extract it from a record. The interface response is created by what can be approximated as a disk of oscillating electric dipoles at the first Fresnel zone, and so has (1) the amplitude pattern of a dipole (Equation 3.1) and shows (2) opposite polarity on opposite sides of the shot point. In addition, it shows (3) virtually zero move out because it travels (diffuses) at V_{EM} which is several orders-of-magnitude greater than the velocity of the coseismic energy V_P.

We begin with examples using techniques– filtering in the frequency-wavenumber and radon domains– that exploit the second and third attributes of the interface response. We then present results using non-stationary prediction-error filters that exploit all three of the listed interface response attributes.

Frequency-wavenumber filtering

Waveform transforms allow us to project seismoelectric data into domains where the distinct patterns of the signal and noise may cause them to map separately. Muting in the frequency-wavenumber (f-k) domain is a standard and commonly-used technique for separating seismic events based on dip (c.f. Yilmaz, 2000). In this way, we can readily separate the dipping parts of coseismic energy from flat interface response events. This section is a presentation of results of frequency-wavenumber filtering of seismoelectric data.

Two-dimensional discrete Fourier transforms map data from the time-offset (t-x) domain to the frequency-wavenumber (f-k), or Fourier, domain (c.f. Yilmaz, 2000). Because our signal is composed of events that are approximately flat, they represent a wavenumber of approximately zero (infinite velocity). Thus our signal maps to the wavenumber axis of the f-k domain. All energy that maps off of the wavenumber axis represents arrivals of finite velocity, and may be considered noise. We mute this energy before using inverse Fourier transforms to map the data back into the t-x domain. Our f-k-domain mutes are symmetrical and fan-shaped, bounded by lines that represent a particular velocity. Because we are interested in preserving only energy that maps along the wavenumber axis, we can employ mutes that eliminate all but the highest-velocity events. Sine-squared tapers on the edges of the mutes avoid t-x-domain artifacts that could result from sharp discontinuities in the f-k domain.

Unfortunately, even the most ideal form of our signal is not perfectly flat; the lateral amplitude variation of a given interface response event causes it to map across a range of small wavenumbers. More important, our noise (n_{cs}) is not truly composed of perfectly linear dipping events. Instead, the coseismic noise is hyperbolic, such that the near offsets are essentially horizontal and thus map to the wavenumber axis of the f-k domain along with the interface response signal. As a result, perfect separation of the signal and noise in the f-k domain is not possible without muting the near-offset traces, and is difficult to accomplish even with this muting. Additional difficulty is presented by the fact that real data are far from ideal. Amplitude variations along events can cause signal or noise to smear in the f-k domain, and arrival-time variations that disrupt the hyperbolic shape of coseismic arrivals also cause imperfect mapping to the f-k domain. Through careful pre-processing we can improve the

separation of the signal and noise in the f-k domain, but perfect separation is very difficult to achieve even under the best of circumstances.

Synthetic data f-k results

Our first f-k example employs the synthetic dataset, and is shown in Figure 3.6. The raw data have undergone a polarity flip so that the interface response events have the same polarity on both sides of the shot point. Additionally, we apply a 120 to 500 Hz bandpass filter. In this example, the entire starting shot gather (Figure 3.6a) is processed at once, and Figure 3.6d shows the data after transformation to the f-k domain. The plot is asymmetrical because the original data were asymmetrically zero-padded before Fourier transformation. Energy corresponding with velocities lower than 10^5 m/s is muted before the data are mapped back to the t-x domain, producing the result shown in Figure 3.6b. All that remains is flat energy, but this includes not just the interface response events, but also energy from the flat portions of the coseismic noise. The difference between the starting data and the final result is shown in Figure 3.6c, and clearly shows the removed coseismic energy, as well as evidence that smeared energy from the flat parts of the coseismic arrivals has leaked into the result (the flat event at $\sim$3 ms in Figure 3.6b that does not exist in the original data).

We address the problem of contamination by flat coseismic energy by removing the near-offset traces before transformation. Processing each half of the gather separately, we work with only the offsets greater than 5 m, as shown in Figure 3.7a. The f-k-domain mapping of the positive offset data are shown in Figure 3.7d, and the result after muting energy corresponding with velocities below 10^5 m/s is shown in Figure 3.7b. Smeared near-offset coseismic energy still contaminates the gather, and suggests that although f-k filtering is effective in reducing the coseismic noise, it is unlikely to be the best solution to the seismoelectric signal/noise separation problem.

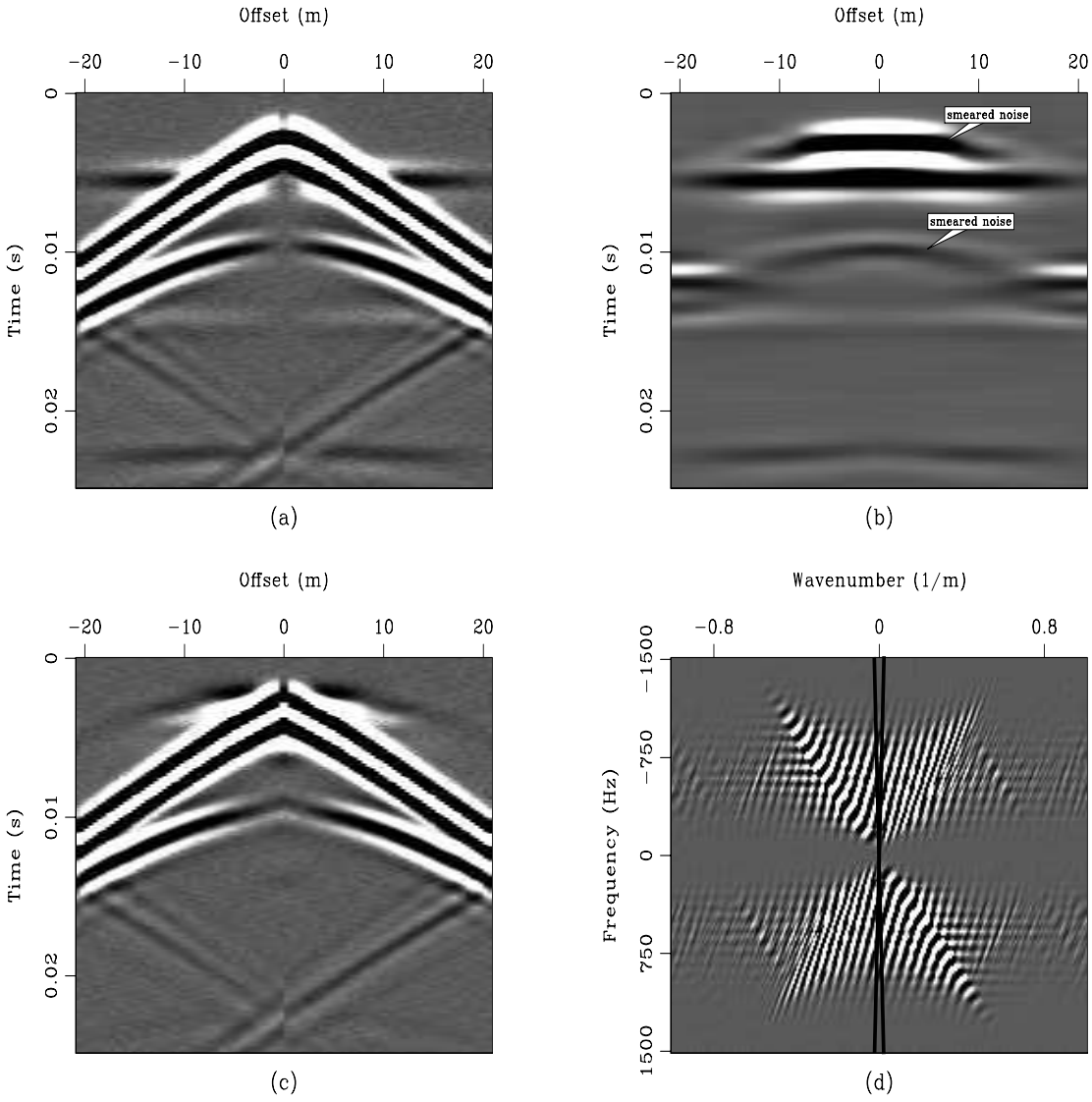

Figure 3.6: f-k filtering results on synthetic data. a) Raw data (polarity-flipped version of the synthetic gather in Figure 3.1, with 100 Hz lowcut filter applied). b) Result after f-k filtering. Note that a significant amount of noise remains. c) Difference between raw data in part (a) and f-k result in part (b). The presence of flat energy indicates that the signal/noise separation was imperfect. d) f-k-domain mapping of the starting data. Energy with velocities below 10^5 m/s (marked by dark lines) is muted before mapping back to the t-x domain. proc-lab_fk_s2 [NR]

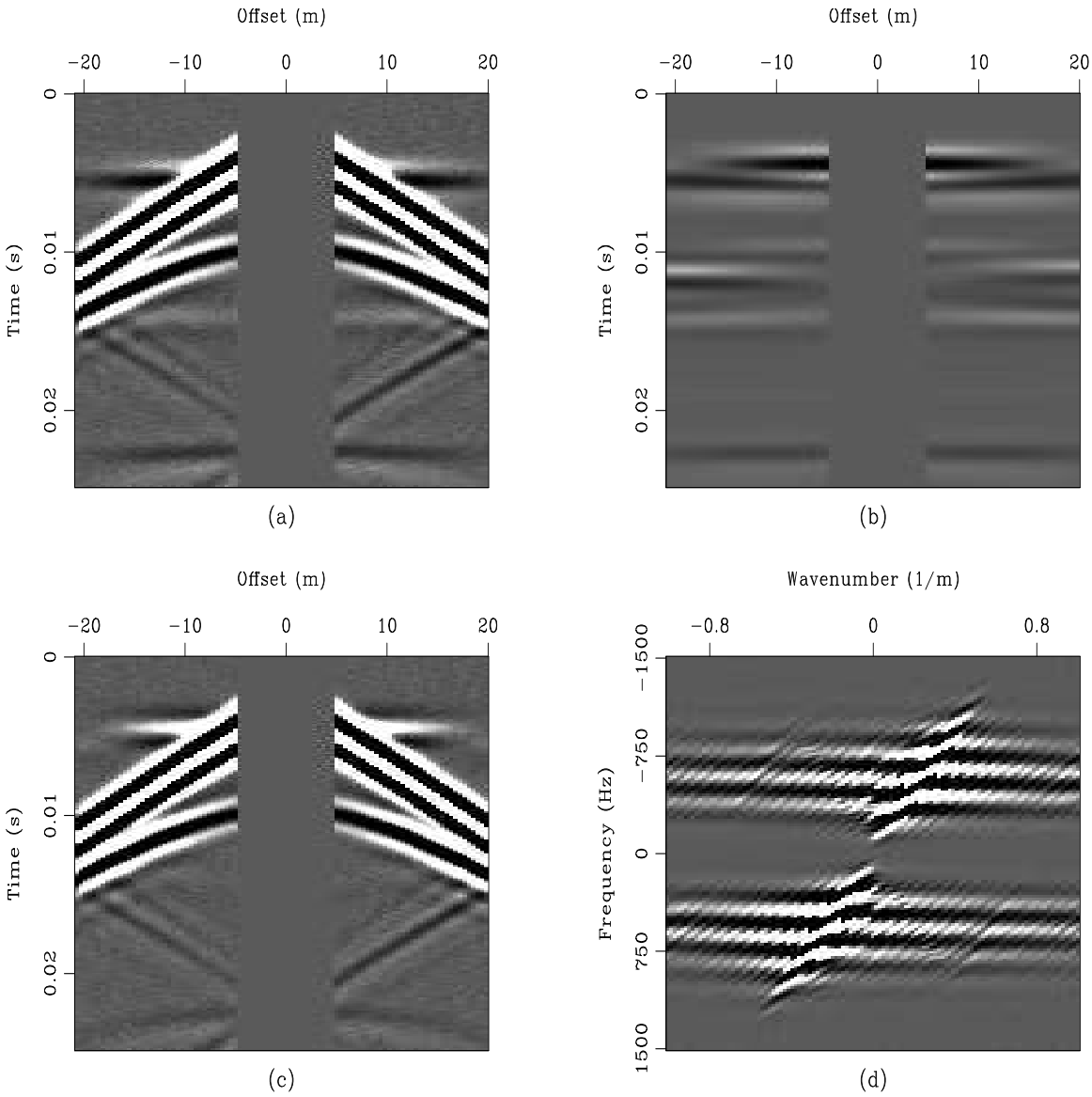

Figure 3.7: f-k filtering results on synthetic data. a) Raw data (polarity-flipped version of the synthetic gather, with near-offset traces removed). The two halves of the gather are processed separately and re-assembled for display purposes. b) Result after f-k filtering. Note that a significant amount of noise remains but that the result is better than that in Figure 3.6. c) Difference between raw data in part (a) and f-k result in part (b). The presence of flat energy indicates that the signal/noise separation was imperfect. d) f-k-domain mapping of the positive-offset part of the starting data. Energy corresponding with velocities below 10^5 m/s is muted before mapping back to the t-x domain (same mute lines as in Figure 3.6). proc-fk.syn2Z [ER,M]

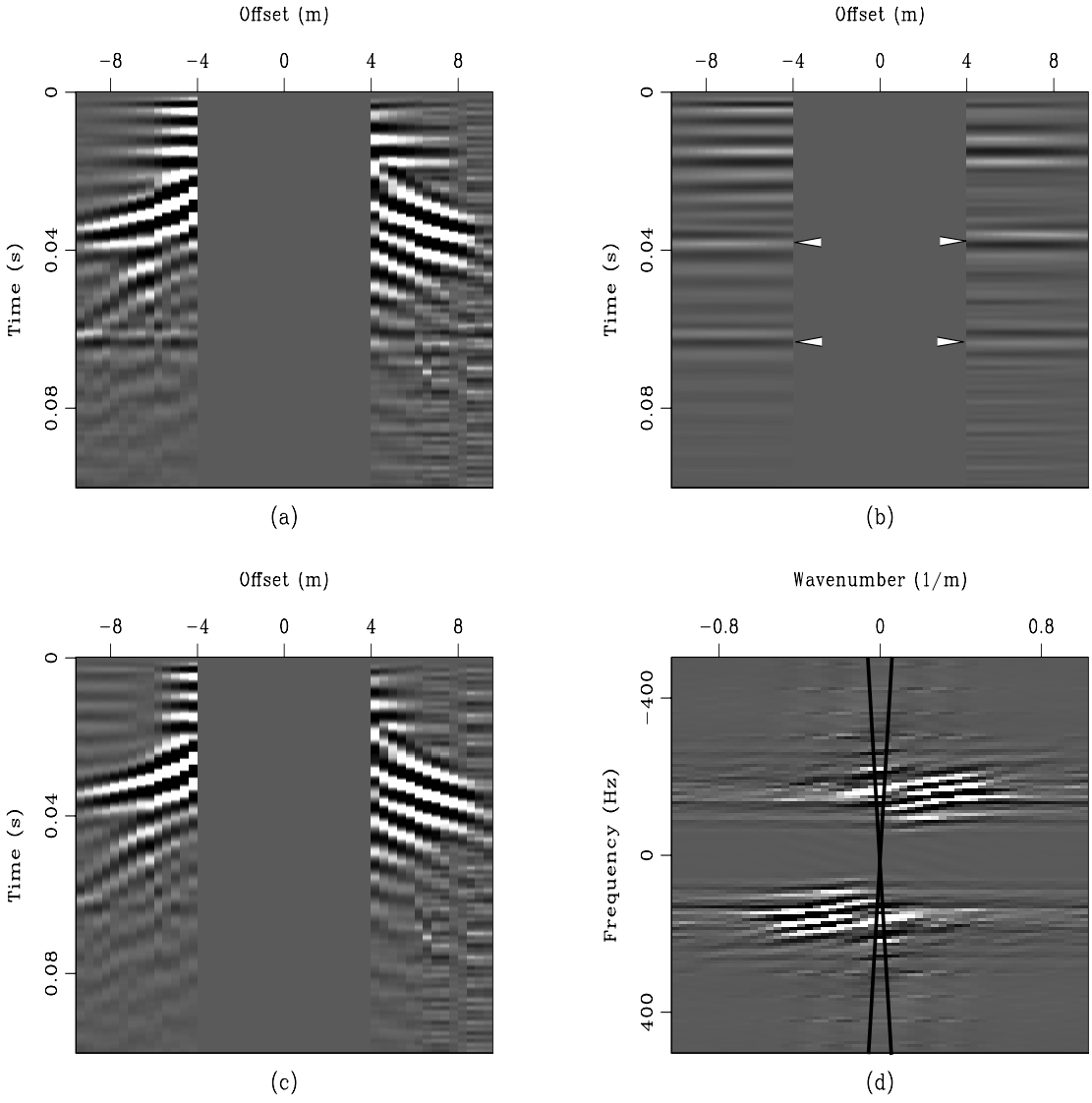

Figure 3.8: f-k filtering results on real data with added synthetic events. a) starting data (polarity-flipped version of data in Figure 3.4a), with central traces removed. b) Result after f-k filtering. Note that most of the coseismic noise has been removed, leaving the direct field and the added events (marked with arrows). c) Difference between the starting data and the f-k result. The presence of flat energy indicates that the signal/noise separation was not perfect. d) f-k-domain mapping of the positive-offset part of the starting data. Energy corresponding with velocities below 8000 m/s (indicated by dark lines) is muted before mapping back to the t-x domain. proc-lab_fk.r1fZ [NR]

Real data f-k results

We turn now to real data, and begin with the polarity-flipped version of the real shot gather with added synthetic events shown in Figure 3.8a. For these real data examples we show only the results performed with the central near-offset traces removed, as they are considerably better than results for the entire shot gather. Figure 3.8d shows the f-k-domain mapping of the positive offset side of the original data, and Figure 3.8b shows the result after muting energy corresponding with velocities below 8000 m/s. The synthetic events are now plainly visible, along with the direct field energy, however there is evidence of amplitude smearing when we look at the difference between the original data and the filtered result (shown in Figure 3.8c). The flat energy at near offsets demonstrates that the amplitude pattern of the coseismic energy has been altered by the narrow mute applied in the f-k domain. For comparison, we show results for the real data without the added synthetic events in Figure 3.9. Here, we see a similar result in Figure 3.9b, but without the synthetic events. This demonstrates that the events in Figure 3.8b are, in fact, the added events and not some product of faulty data processing.

Radon-domain filtering

Radon transforms map from the t-x domain to the τ-p domain (τ is the zero-offset intercept of an event of slowness p), and represent another waveform transformation that may provide a separation of seismoelectric signal from noise. Radon transforms are based on the summation of energy along trajectories of various shapes, with the generic equation often written as

$$\tau = t - p\, g(x), \tag{3.5}$$

where $g(x)$ is a function that describes the curvature of the summation trajectories. Linear radon transforms, or slant-stacks, are accomplished by stacking along linear trajectories ($g(x) = x$) and are often composed of slowness "traces" created by applying a linear move-out (LMO) of a given velocity before stacking the gather. By carrying out this LMO/stack operation over a range of slownesses, a range of slowness traces is created and a slant-stack is

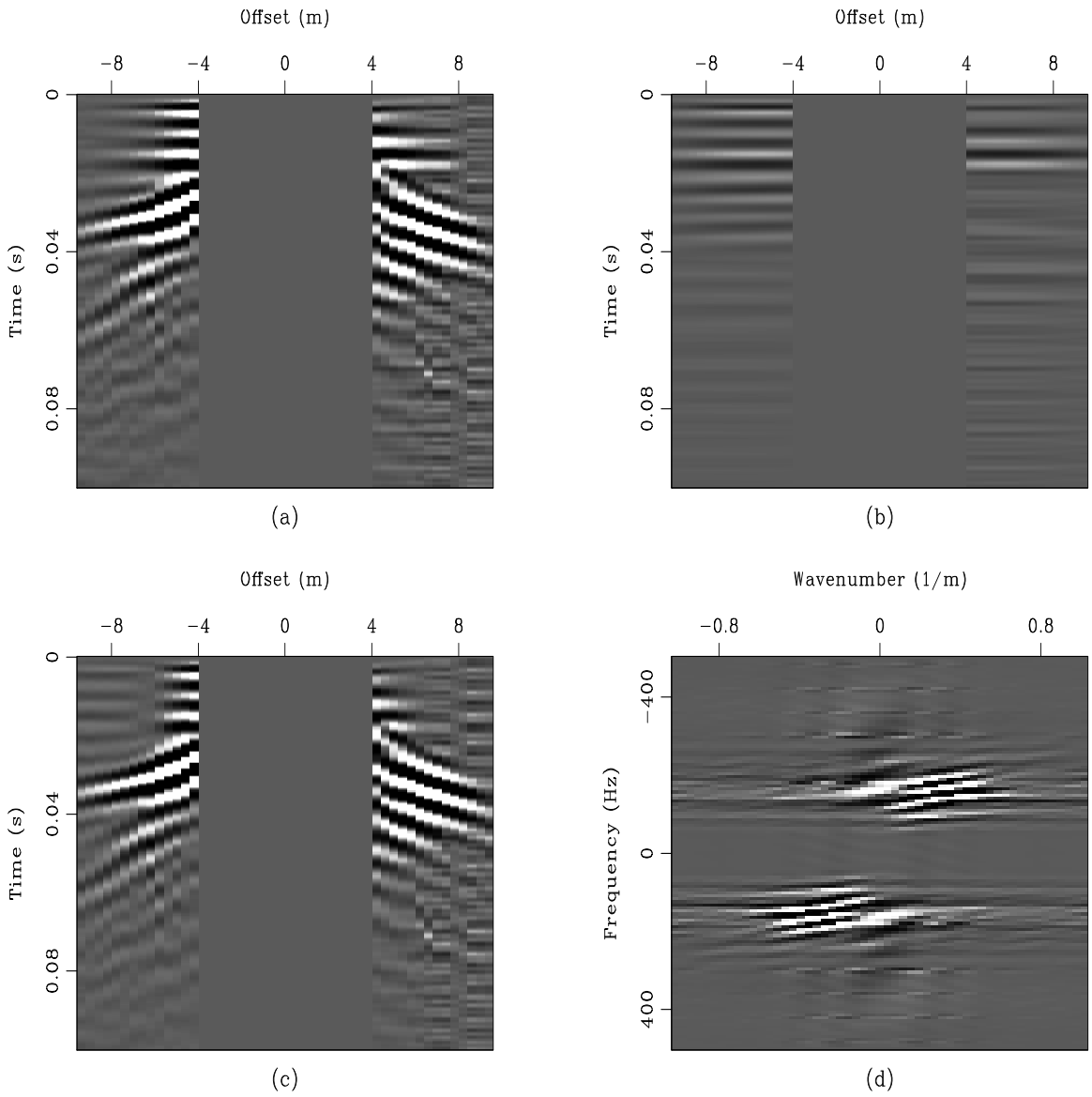

Figure 3.9: f-k filtering results on real data without the added synthetic events. a) starting data. b) final result. Note the absence of the synthetic events, as is expected. c) difference between the original data and the processing result, showing evidence of amplitude smearing. d) f-k-domain mapping of the positive-offset part of the starting data. proc-fk.r1Z [ER,M]

produced. Mapping between the τ-p domain and t-x space is accomplished using the modeling equation/adjoint pair

$$d(t,x) = \sum_{\tau}\sum_{p} m(t - p\,x, p), \tag{3.6}$$

$$m(\tau,p) = \sum_{t}\sum_{x} d(\tau + p\,x, x). \tag{3.7}$$

Similarly, parabolic radon transforms stack along parabolic trajectories ($g(x) = x^2$) representing various slownesses, and hyperbolic radon transforms stack along hyperbolic trajectories. After testing with linear, parabolic, and hyperbolic radon transforms, we find that the linear radon transform (LRT) produces the best separation of seismoelectric data in the τ-p domain. It is the LRT that we focus on in this section.

Unlike the Fourier transform, the inverse LRT does not produce exactly the original input data (that is, the operator is not self-adjoint). Frequently the application of a rho-filter in the τ-p domain is used to account for this feature (Yilmaz, 2000) and provides an essentially exact mapping from the t-x domain to the τ-p domain and back to the t-x domain again. An alternative approach that does not require determination of a suitable rho-filter is to employ an iterative inversion process (Thorson and Claerbout, 1985) to determine the τ-p domain mapping. We re-write Equation (3.6) as

$$\mathbf{d} = \mathbf{L}\mathbf{m}, \tag{3.8}$$

and try to minimize the objective function

$$f(\mathbf{m}) = \|\mathbf{L}\mathbf{m} - \mathbf{d}\|^2. \tag{3.9}$$

We also include a Cauchy regularization term (Sacchi and Ulrych, 1995) to enforce sparseness in the model space (the τ-p domain). This focuses energy in the τ-p domain which provides cleaner separation of signal from noise and permits the minimization of artifacts that

would otherwise exist. Our objective function for a model space of size n is now written:

$$f(\mathbf{m}) = \|\mathbf{Lm} - \mathbf{d}\|^2 + \epsilon^2 \sum_{i=1}^{n} ln(1 + \frac{m_i^2}{b^2}), \tag{3.10}$$

where ϵ and b are two constants that allow us to control the degree of sparseness in the model (ϵ) and the minimum value below which energy in the Radon domain is zeroed (b). This objective function is non-linear (the model m^2 is included in the regularization term) so we use the BFGS quasi-Newton method described by Guitton and Symes (2003) to find the τ-p model that corresponds with the minimum value of $f(\mathbf{m})$.

Once our seismoelectric data are mapped to the τ-p domain, we mute the signal or the noise before mapping back to t-x space. Seismoelectric interface response signals are flat events, and so map to the slowness axis of the τ-p domain ($p \approx 0$) while noise maps elsewhere in the τ-p domain ($|p| > 0$). We mute in the τ-p domain using tapered rectangular mutes centered around the slowness axis. These mutes are generally very narrow since our signal does not extend far beyond the slowness axis. As with the f-k domain, data imperfections cause imperfect mapping in the τ-p domain and hinder our signal/noise separation efforts. In particular, the flat portions of hyperbolic coseismic noise map to the slowness axis along with the signal energy, and amplitude irregularities cause smearing. Additional problems may be caused by the amplitude pattern of the interface response events. Those from shallow interfaces (or the direct field) show a rapid amplitude fall-off with offset, and therefore they map in the τ-p domain as broad bands around the slowness axis rather than as well-focused points. Because of these problems, and because we determine the τ-p model using an inversion scheme which may leave some data energy in the model residual, we generally model the noise, map it back to t-x space and then subtract it from the data, rather than directly modeling the signal. This avoids the problem of leaving un-modeled signal energy in the residual.

Because the radon transform collapses flat events to points in the τ-p domain, it is best to perform a polarity flip on seismoelectric data as part of the pre-processing sequence. Otherwise interface response events will not collapse smoothly to points. We also find it best to apply a gain function to the data so that weaker events later in the record do not get inadvertently removed by the regularization.

Synthetic data radon results

We begin with the synthetic example again, in this case after applying a t^2 gain, as shown in Figure 3.10a. The mapping of the data to τ-p space is shown in Figure 3.10e. We mute the central part of the record, removing the energy with slowness less than 0.00008 s/m, map back to t-x space, and subtract the remaining energy (the estimated noise) from the original data to produce the result shown in Figure 3.10b. Though some artifacts from the dipping coseismic energy remain, they are easily identified and would mostly cancel out of the record if this gather were stacked. The flat interface response events dominate the record, with some contamination of flat energy from coseismic arrivals at the near and far offsets. The modeled noise, produced by muting the noise from the τ-p domain, mapping back to the t-x domain, and subtracting the result from the original data, is shown in Figure 3.10c. It contains very little interface response energy, or other flat energy, and demonstrates that radon transforms are a better option for seismoelectric signal/noise separation than f-k filtering. An alternative approach for creating a signal result is to simply mute the unwanted noise in the τ-p domain (Figure 3.10f), and then transform back to the t-x domain, producing the result shown in Figure 3.10d. This plot is shown with a lower clip level than the other t-x domain plots in order to highlight the fact that it shows event IR #3 more clearly than the result in Figure 3.10b. While it is our objective to "find" this event in the data, we can not rely on this particular approach when working with real data due to the risk of losing amplitude information and/or creating events out of noise.

In order to minimize contamination of the final radon result by flat near-offset coseismic energy, we test the method on the data shown in Figure 3.11a. We process the two halves of the data separately, using only the offsets greater than 5 m. The τ-p mapping of the positive-offset energy is shown in Figure 3.11d. Again we remove energy corresponding with a slowness less than 0.00008 s/m (same mutes as shown in Figure 3.10f) from each τ-p mapping, map back to t-x space, and subtract from the original data, and re-assemble the gather to produce the result in Figure 3.11b. Again we see some contamination from coseismic noise, both dipping and flat, but find the result to be substantially better than the f-k result.

We do not find that removal of the central (near-offset) traces substantially improves the

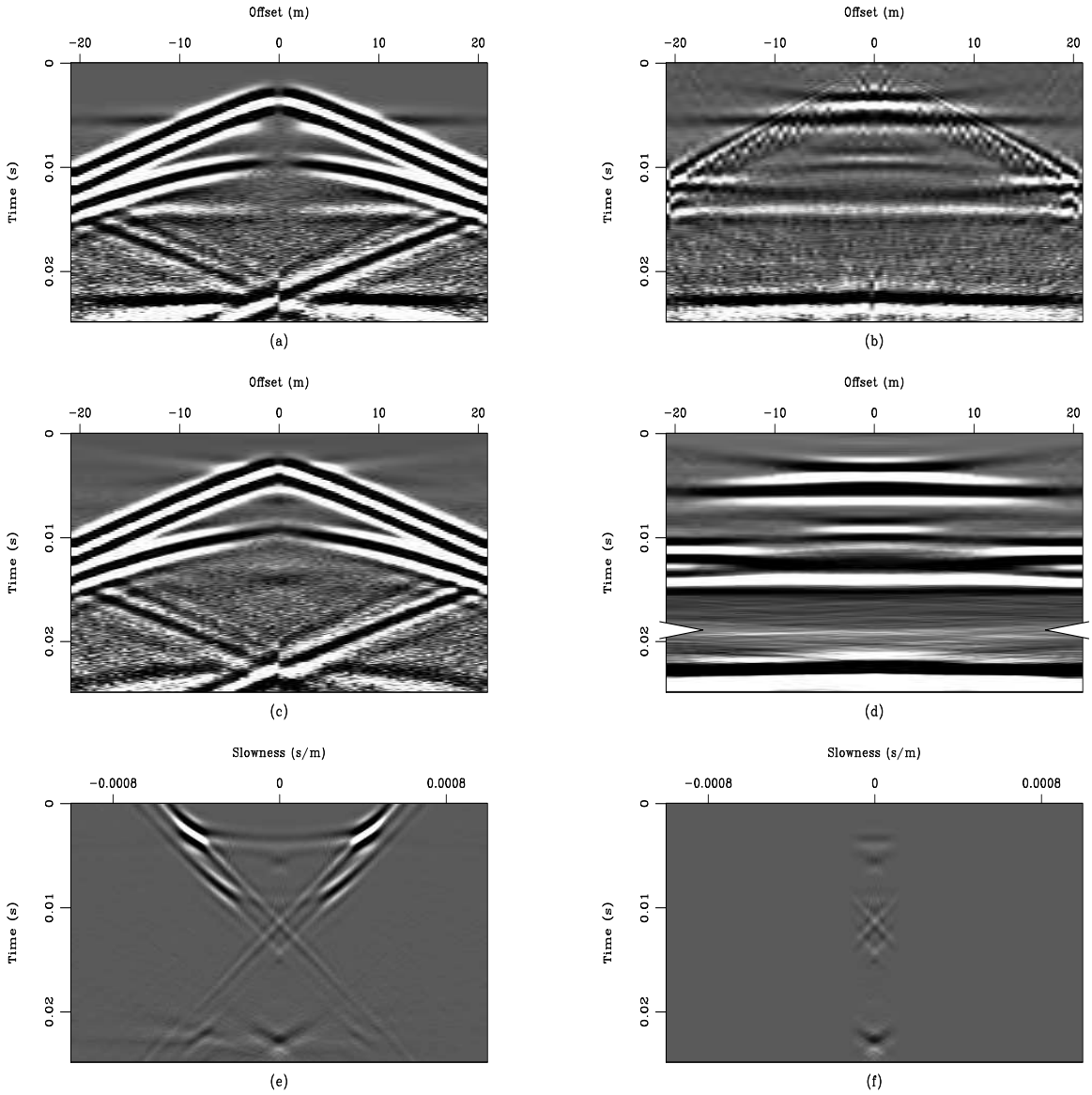

Figure 3.10: Results from radon filtering of synthetic data. a) Starting data– polarity-flipped version of synthetic gather described earlier, with t^2 gain correction applied. b) Signal result obtained by modeling the noise part of the starting data in the LRT domain, and subtracting that model from the starting data. c) Noise result, obtained by modeling the signal part of the starting data in the LRT domain and subtracting that model from the starting data. d) An alternative signal result, produced by mapping the muted result shown in part (f) back to the t-x domain. The previously hidden signal event IR #3 is visible at 0.0185 s and is marked with arrows. This gather is shown with a one-third lower clip level than other plots in this figure. e) τ-p-domain mapping of the original data. f) Muted version of τ-p-domain. proc-6lrt.syn [ER,M]

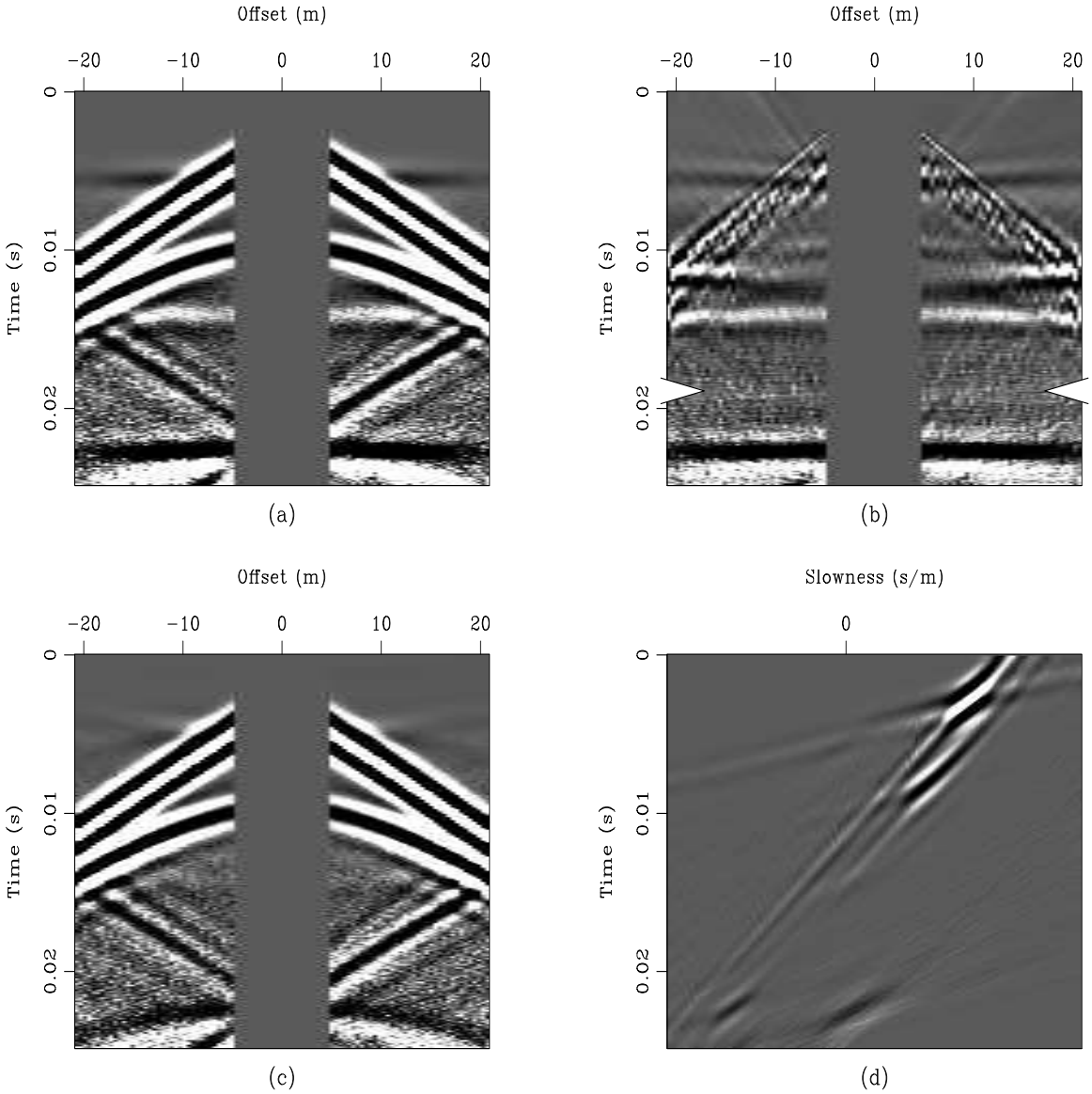

Figure 3.11: Same as Figure 3.10, but the near-offset traces have been removed from the starting data (a) in an effort to minimize the inclusion of the flat coseismic energy in the final result (b), where evidence of the previously hidden event IR #3 is visible at 0.0185 s, shown with arrows. c) The weak flat energy in this plot of the difference between the starting data and the modeled signal energy highlight imperfections in the signal/noise separation. d) τ-p-domain mapping of the positive offset part of the original data. proc-f_lrt.syn [ER,M]

result, so the added work and lost data do not seem to be worthwhile. Overall, however, these radon transform results are encouraging. In particular, we are very pleased to see evidence of the the previously-unseen interface response event #3 at 0.0185 s. These results compare favorably with the f-k results shown in the last section. Although in theory the two approaches should produce similar results, the use of the Cauchy regularization produces a better separation in the radon domain than in the f-k domain, and a better final signal/noise separation result.

Real data radon results

We turn now to the real data, first the gather with the synthetic events added, as shown in Figure 3.12a. We have applied a $t^{1.85}$ gain to balance the amplitude pattern and a 150 to 400 Hz bandpass filter to complete the pre-processing. The τ-p mapping of these data are shown in Figure 3.12d, and the signal result in Figure 3.12b. The added synthetic events are clearly visible, as is the direct field energy. A small amount of flat energy from the near-offset coseismic arrivals remains, as well as a small amount of flat noise energy at 0.085 s, likely source-related (perhaps a second bounce of the hammer on the plate which produces weak energy that we now can observe). The estimated noise (Figure 3.12c) shows very little evidence of flat energy, and encourages our positive assessment of radon methods for seismoelectric data processing.

For comparison, we apply the same processing to the real data without the added events (Figure 3.12), and find that the resulting signal model (Figure 3.12b) is very similar to that in Figure 3.12b, but without the added events, validating our results. We do not show results obtained by removing the central traces, as this approach did not prove worthwhile in the last section, and results with the real data are similarly uninspiring.

As with the synthetic data, we find that our application of the radon transform provides a better signal noise separation result than f-k filtering. We find the linear radon transform to be an effective means for separating seismoelectric signal from noise in both real and synthetic data. The examples shown here have demonstrated that this approach can remove coseismic energy and make visible interface response energy that was previously below the noise level.

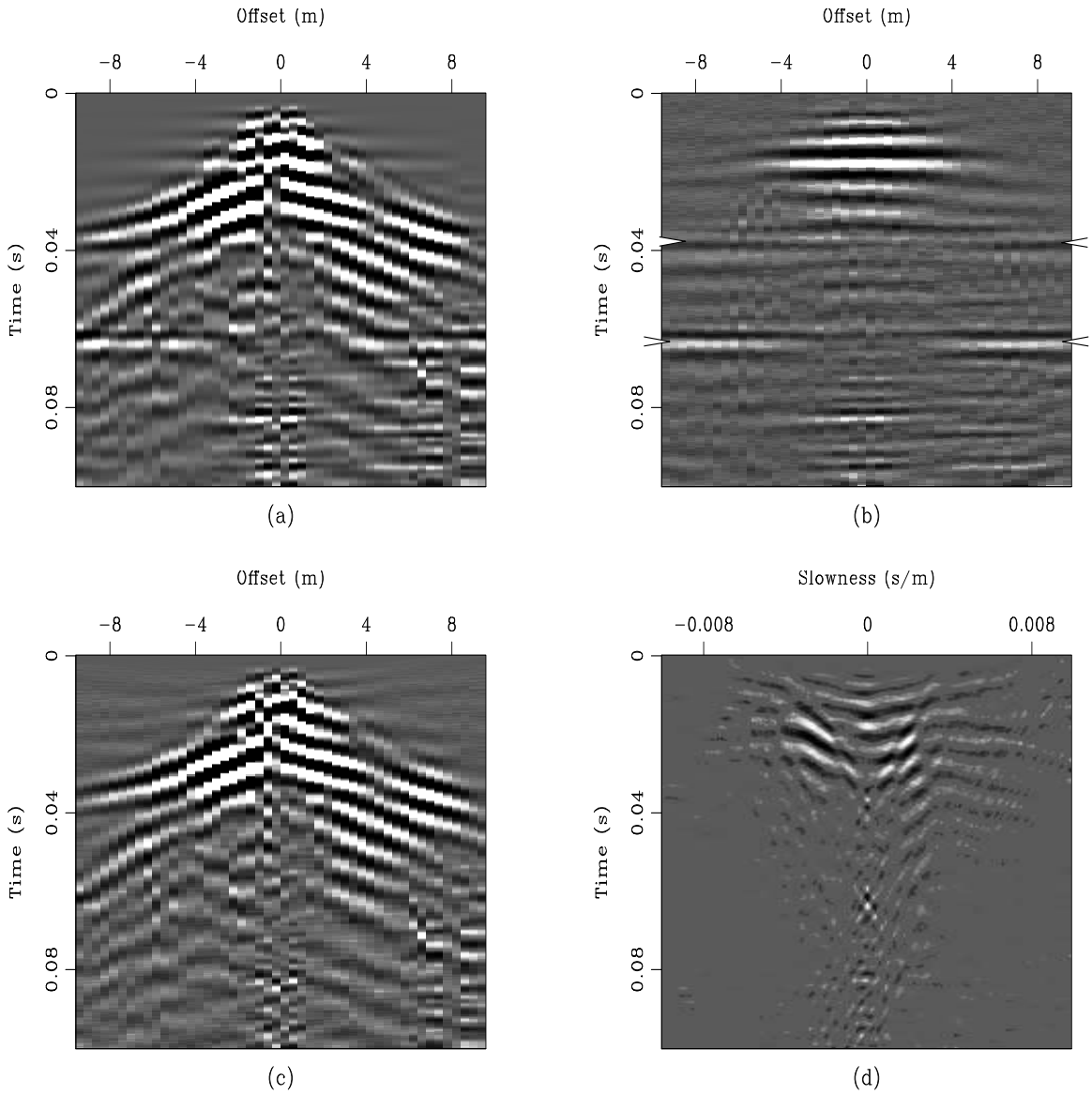

Figure 3.12: Radon results for real data with added synthetic events. a) Starting data– gather shown in Figure 3.4a with 150 to 400 Hz bandpass filter and $t^{1.85}$ amplitude correction applied. b) Signal result, with added events clearly visible along with the direct field, some flat noise, and some faint traces of the dipping coseismic energy. This result was obtained by modeling the noise in the LRT domain and subtracting that result from the starting data. c) Noise result, obtained by modeling the signal in the τ-p domain and subtracting that result from the starting data. The absence of any flat energy indicates that the separation has been largely successful. d)τ-p mapping of the starting data. The impact of the sparseness constraint is obvious, as the energy is largely in distinct clumps with little extraneous noise. proc-lrt.f0 [ER,M]

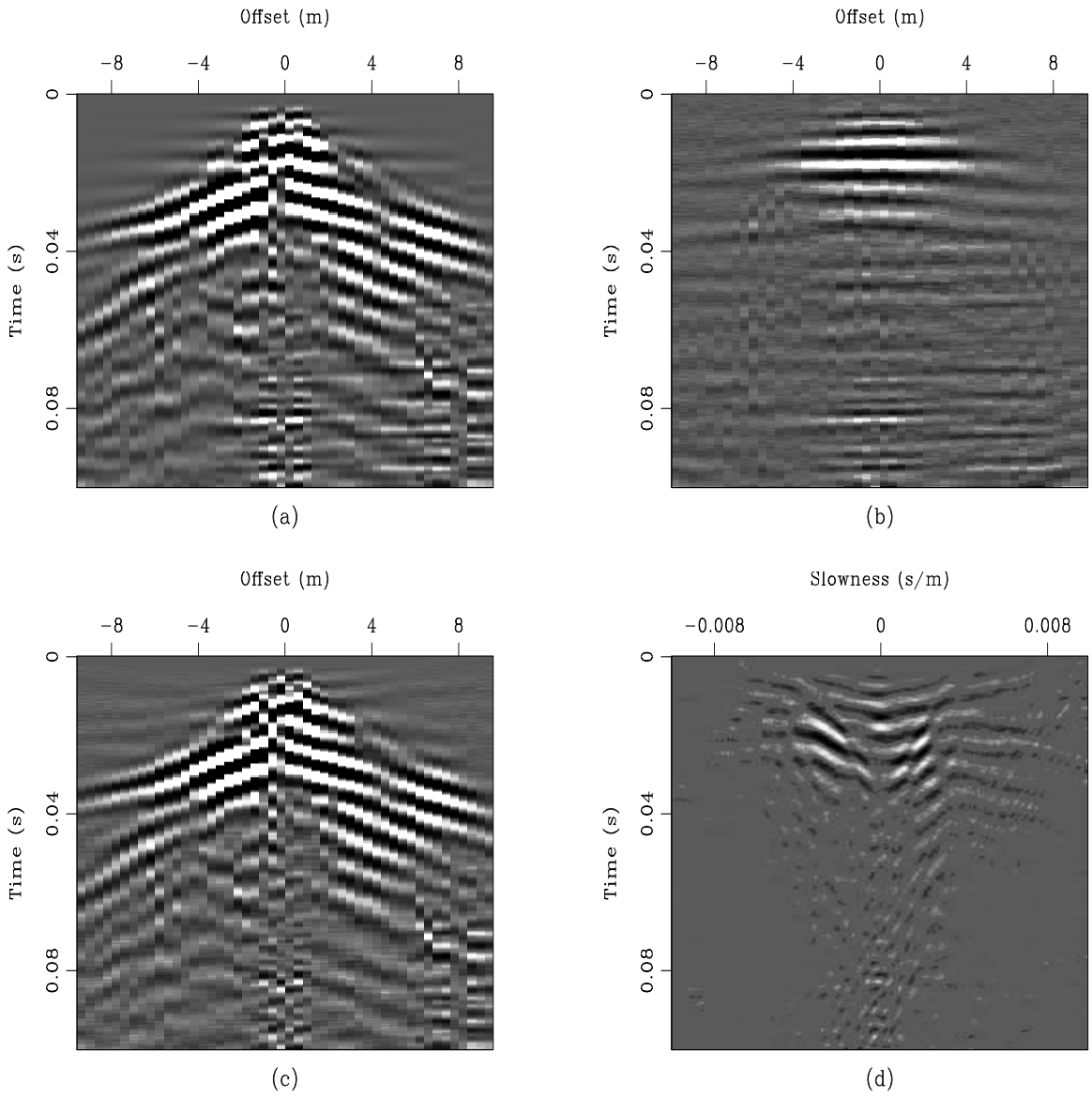

Figure 3.13: Same as Figure 3.12, but starting data (a) is the real gather without synthetic events added. b) Signal result shows flat direct field energy. c) Noise result shows only the dipping coseismic energy. d) τ-p mapping of the starting data is very similar to that in Figure 3.12d, but without the points of energy that correspond with the added events. proc-lrt.0 [ER,M]

Prediction-error filters

We can take advantage of both the amplitude and pattern characteristics of our signal/noise separation problem by implementing a signal-noise separation technique using prediction-error filters (PEF's) (Claerbout, 1999) **S** and **N** to model the signal and noise respectively. By definition, our non-stationary two-dimensional PEF's accomplish

$$\begin{aligned} \mathbf{Nn} &\approx \mathbf{0} \\ \mathbf{Ss} &\approx \mathbf{0}, \end{aligned} \tag{3.11}$$

such that they can be used to separate the data **d** into its signal **s** and noise **n** components.

Our fitting goals (Abma, 1995) are

$$\mathbf{0} \approx \mathbf{N}(\mathbf{s}-\mathbf{d}) \tag{3.12}$$

and

$$\mathbf{0} \approx \epsilon\mathbf{Ss}, \tag{3.13}$$

with a least-squares formulation (Guitton et al., 2001) of

$$\hat{\mathbf{s}} = (\mathbf{N}'\mathbf{N}+\epsilon^2\mathbf{S}'\mathbf{S})^{-1}\mathbf{N}'\mathbf{Nd}. \tag{3.14}$$

We solve for the estimated signal model $\hat{\mathbf{s}}$ iteratively using the conjugate-gradient method.

This method is dependent on the use of PEF's **S** and **N** that accurately convey the essential aspects of the signal and noise. The creation of these PEF's requires both the choice of suitable models for PEF estimation (models that closely resemble the signal and noise) and careful selection of PEF parameters (filter size, patch size for the non-stationary filters, etc). Parameter choice is largely determined through experimentation, though experience and common sense suggest that the flat interface response energy can best be modeled by PEF's that extend farther in the offset direction than in the time direction. The coseismic noise, since its dimensions are more equal in offset and time, is often best modeled by PEF's that have more elements in the time direction than in offset (since the data sample rate is much greater in time than in offset).

PEF estimation models are also often established through experimentation, though the number of options is limited. We can use alterations of the original data, other real data (geophone data as a model for coseismic noise, for instance), or synthetic data, as models. The effectiveness of alterations of the original data is limited, as any alteration that produces a quality signal or noise model would itself be the signal/noise separation technique that we are looking for. However, the noise models estimated through the radon filtering described in the last section do provide useful models for noise PEF estimation. As shown by Garambois and Dietrich (2001), horizontal geophone data can be very similar to the coseismic noise, particularly if the time derivative of the geophone data is calculated. The horizontal ground acceleration should differ from the coseismic noise by only a phase difference and therefore represents an ideal noise model. Unfortunately the quality of the real geophone data collected during out experimentation is not adequate to accomplish this goal (see Chapter 2).

Because we know that the amplitude pattern of interface response events is described by Equation (3.1), we can produce synthetic models for coseismic amplitude patterns as a function of offset. This alone can be an effective model for the estimation of one-dimensional (in offset) signal PEF's. Or, when combined with a generalized waveform this amplitude pattern can provide a model for estimation of two-dimensional signal PEF's. The primary advantage of this approach for signal PEF estimation is that it does not assume any a priori knowledge of the arrival time of interface response events. Because we target events that may not be visible before signal/noise separation, it is important that our methods do not require any a priori knowledge of their existence.

In many cases, the amplitude of the data (and therefore also the amplitude of signal and/or noise models) varies with time or space. While some of this amplitude variation may be an essential identifying characteristic of the signal or noise, large amplitude variations can cause an un-weighted PEF estimation to concentrate only on the high-amplitude parts of the signal or noise model. For this reason, we follow Guitton (2003) and use weighting masks in the PEF estimation as needed.

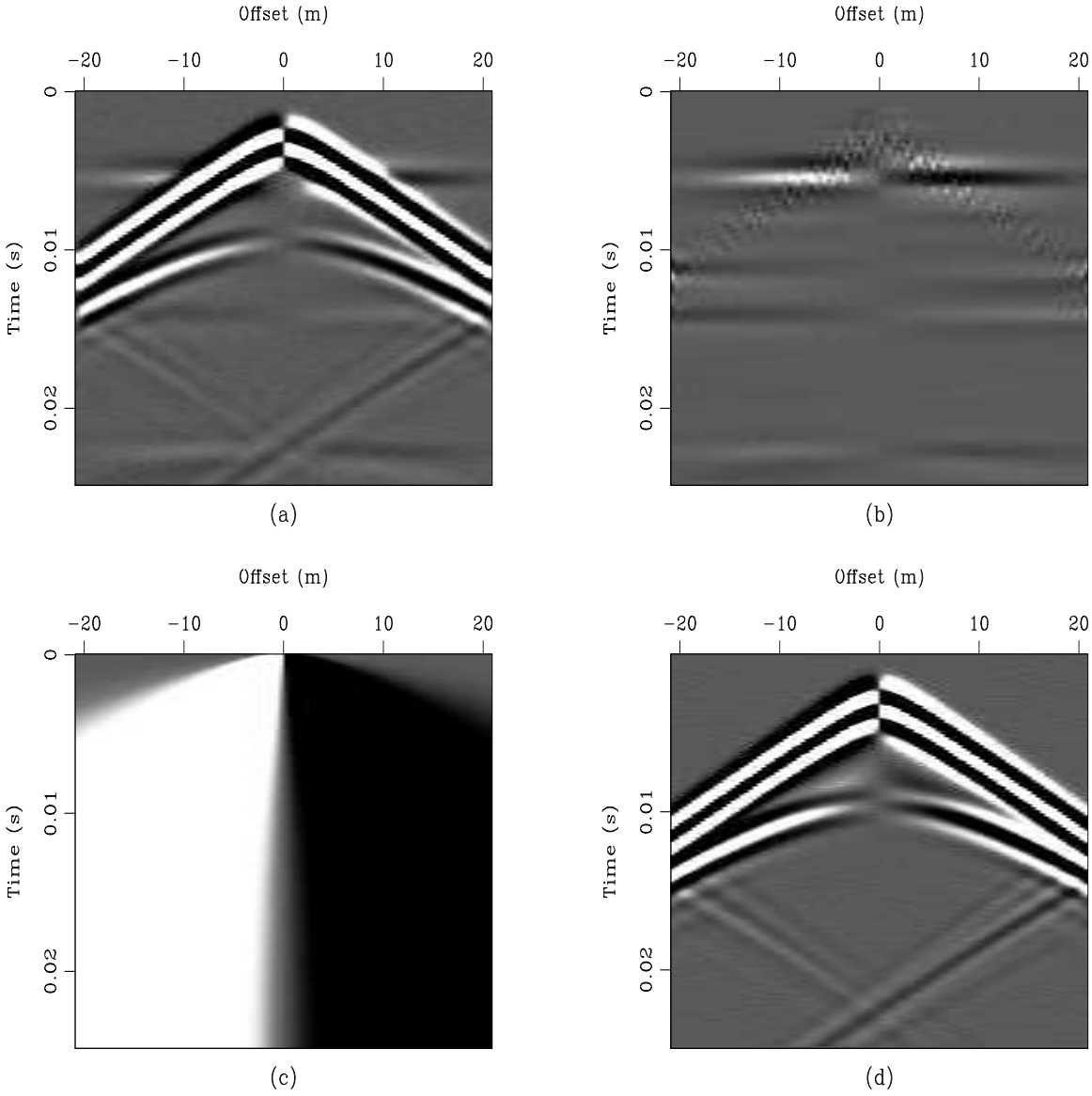

Figure 3.14: PEF-based signal/noise separation results for the synthetic gather. a) Starting data. b) Estimated signal model $\hat{\mathbf{s}}$, with flat signal events remaining and most coseismic noise removed. Some flat smeared energy remains. c) Model used for estimation of one-dimensional signal PEF's, produced using Equation (3.1) and a suitable velocity function. d) Model used for estimation of noise PEF's. This is synthetic horizontal ground-acceleration data, from the same modeling as the seismoelectric data. It represents the time derivative of horizontal geophone data. proc-pef.s2 [ER,M]

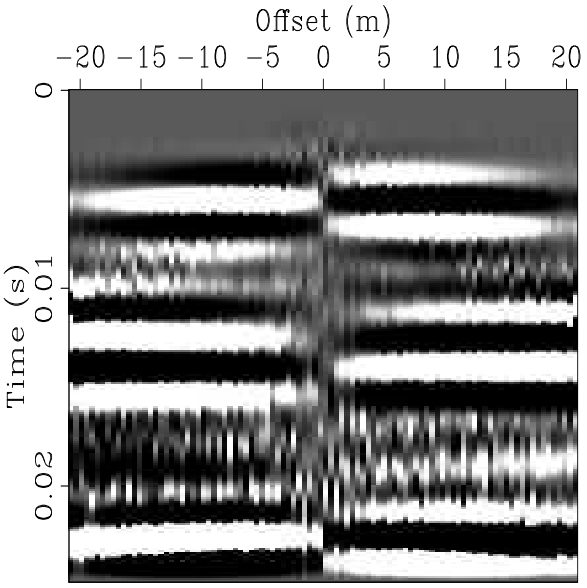

Figure 3.15: Synthetic PEF result, same as shown in Figure 3.14b, but with 500 Hz high-cut filter and $t^{1.8}$ amplitude correction applied after signal/noise separation. Event IR3 is now visible at 0.0185 s. proc-pefIR3 [CR]

Synthetic data PEF results

Again we begin with the synthetic data example (Figure 3.14a). Because the data are synthetic, we have perfect horizontal geophone data available also (simply horizontal particle velocities output from the finite-difference model). We take the time derivative of these data to produce the plot of particle acceleration shown in Figure 3.14d. In this case, we could choose to use the radon signal estimate (Figure 3.10b) as our signal model, but the remaining noise in that gather would cause problems with the PEF signal/noise separation. Instead, we choose the entirely general approach, and use one-dimensional signal PEF's estimated from the amplitude pattern expected for interface response arrivals from any depth (arrival time), shown in Figure 3.14c. Though one-dimensional PEF's aren't generally as effective as two-dimensional PEF's, the final estimated signal result (Figure 3.14b) is our best signal result for this dataset, and shows minimal remaining noise. The dipping random energy that remains from the dipping coseismic events is not a problem for stacking, as it will cancel out. The flat energy remaining at $\sim$0.012 s does represent a problem, however, as it looks just like the interface response event at 0.014 s, and will corrupt any stack of this gather. The previously-unseen interface response event IR #3 is now visible (Figure 3.15), indicating that PEF's are an effective signal/noise separation technique.

Real data PEF results

The real data gather with added events (Figure 3.16a) provides our next test of the PEF-based signal/noise separation. In this case our model for signal PEF estimation (Figure 3.16c) is constructed by convolving the amplitude pattern predicted for interface response events (created using Equation (3.1) and an assumed velocity of 400 m/s) with an estimated waveform. This waveform is created by transposing the axes of the original data (Figure 3.16), applying a low-cut filter (to remove flat energy), transposing back to the original orientation, subtracting the result from the original data, and stacking to produce a single trace with the waveform of the flat elements of the original data. The noise model (Figure 3.16d) is created by muting the parts of the radon transform result in Figure 3.12c that extend above the first seismic arrivals (the faint bit of flat energy that remains in the gather). We also use the arithmetic inverse of an AGC'd version of the noise model as a mask for the noise PEF estimation, so as to force the estimation to equally honor all parts of the noise model.

Using these models for PEF estimation, we obtain the estimated signal result shown in Figure 3.16b. It includes little energy besides the added events, and the original direct field energy. A small amount of flat coseismic energy from the near offsets does remain, but it is very minimal.

We compare results obtained using the same techniques (the same procedures for establishing PEF estimation models, and same parameters) on the real data gather without the added events (Figure 3.17a and find that we obtain a similar result (Figure 3.17b, but without any evidence of the added events, again confirming that their presence in Figure 3.16b is not the result of any processing irregularity.

Based on these results from PEF-based signal/noise separation on synthetic and real data, we conclude that this technique is quite effective for seismoelectric data when adequate PEF estimation models are available.

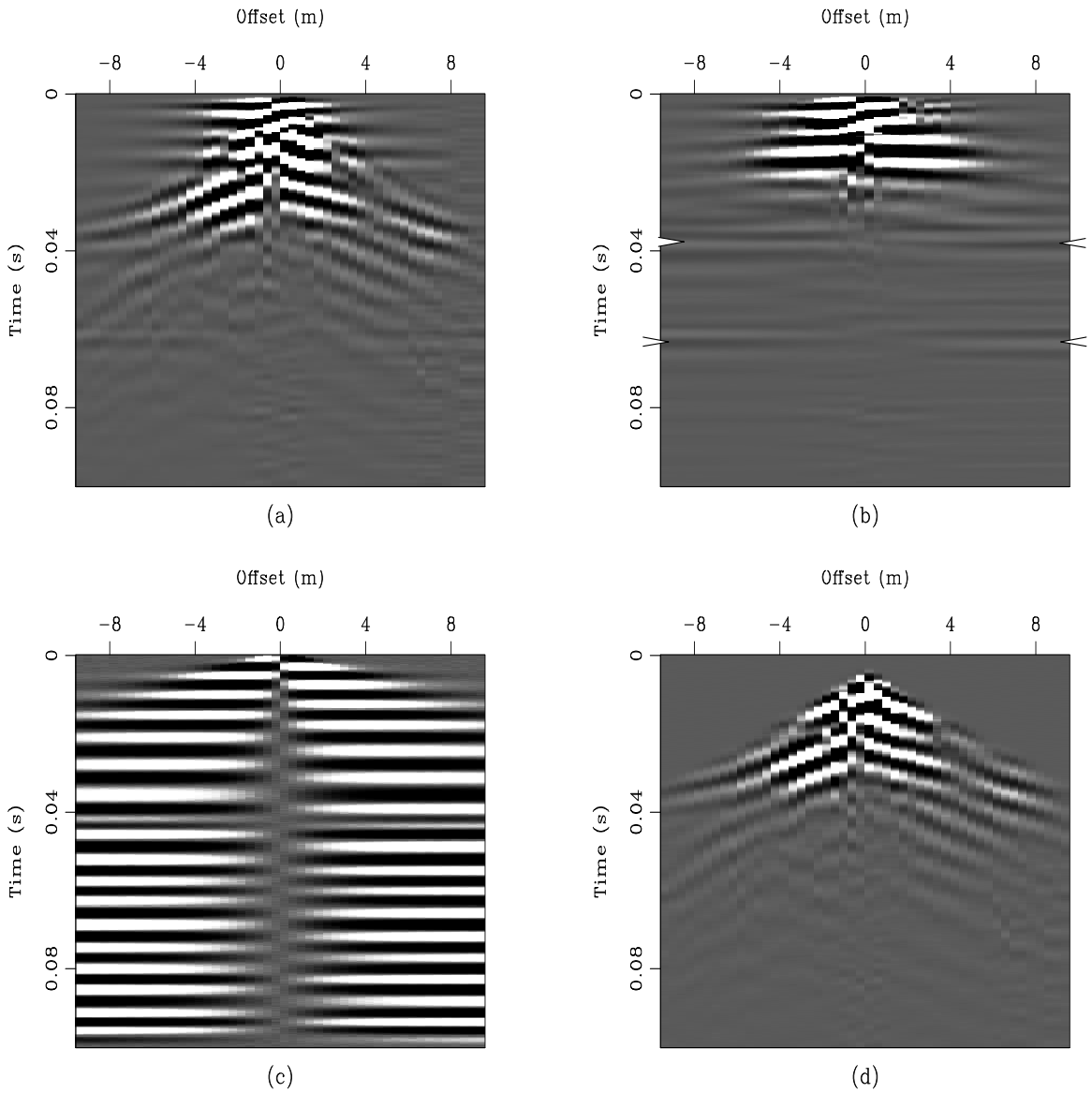

Figure 3.16: PEF results for the real data with added synthetic events. a) Starting data (same as Figure 3.4a, with 150 to 500 Hz bandpass filtering). b) Signal result, with added flat events (with arrows) and direct field energy remaining, and little other energy. c) Signal model used for estimation of signal PEF's, created using Equation (3.1) and waveform information from the real data. d) Noise model used for noise PEF estimation, created by muting the parts of the LRT result in Figure 3.12c above the first coseismic arrivals. proc-pef.freal1 [ER,M]

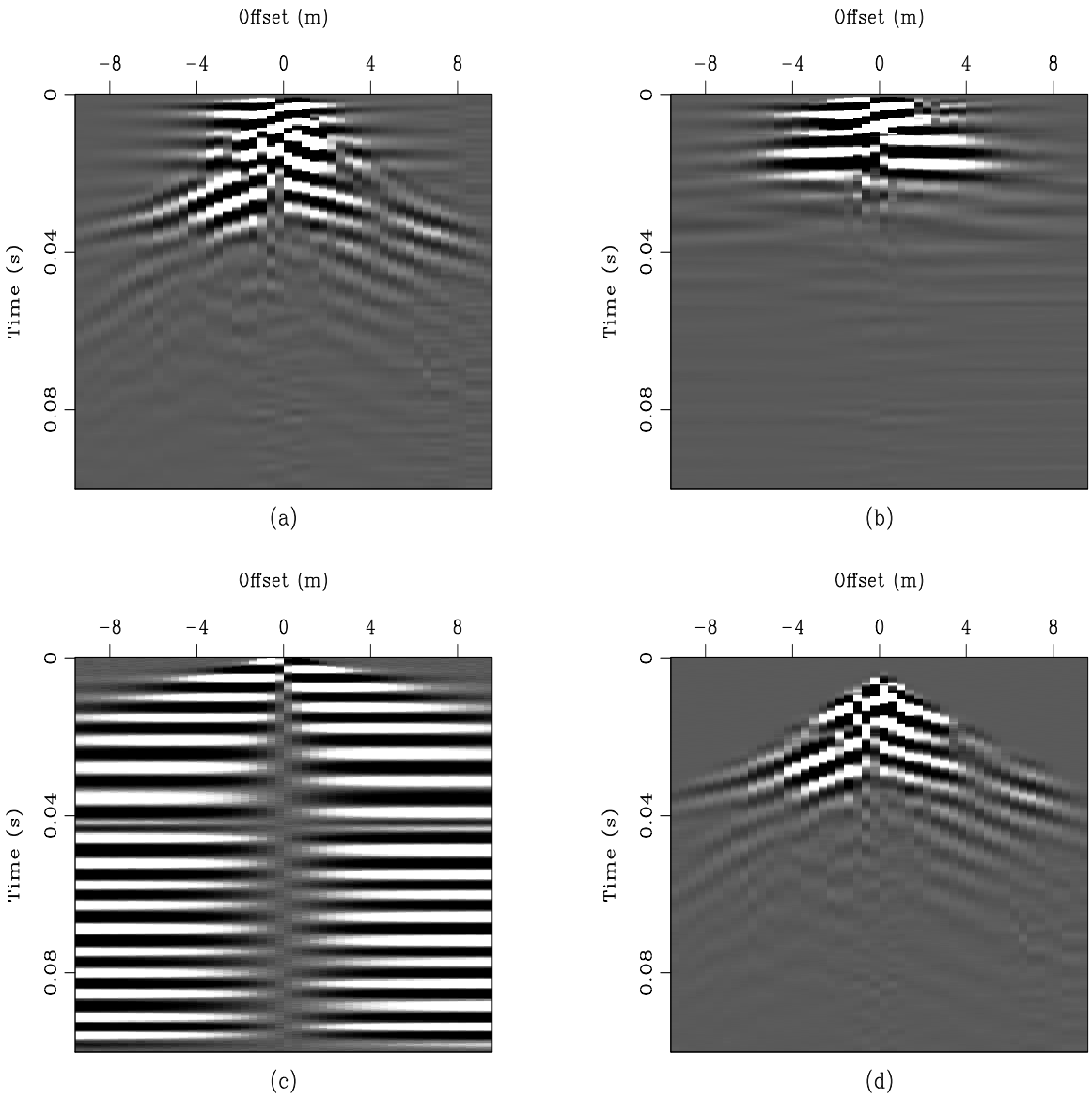

Figure 3.17: Same as Figure 3.16, but using real gather without added synthetic events. a) Starting data. b) Signal result, with little energy besides the direct field. c) Model for estimation of signal PEF's, same as Figure 3.16c. d) Model for estimation of noise PEF's, muted version of LRT result in Figure 3.13c. proc-pef.real1_r [ER,M]

PREFERRED PROCESSING OPTIONS

As with seismic data, the exact processing sequence for a seismoelectric data set must be determined on a case-by-case basis. However, we find the following generalized sequence to be effective.

1. 60 Hz removal using sinusoidal subtraction (Butler and Russell, 1993), or frequency revision (Butler and Russell, 2003) if sinusoidal subtraction proves insufficient.
2. Minimize background noise and coseismic energy with frequency filtering.
3. Signal/noise separation using:
   - Linear radon transform filtering if data quality is good, and if gathers have a sufficient number of traces ($\sim$48)
   - Non-stationary prediction-error filters (PEF's) if computationally feasible, and if adequate PEF estimation models can be obtained.
   - Frequency-wavenumber (f-k) filtering can be helpful, but is the least effective of the methods we tested.
   - Two (or possibly three) of these methods in series could also prove effective.
4. Display processing, such as frequency filtering and gains (AGC or t^x, $x \approx 2$.)

We directly compare the results of the three tested signal/noise separation techniques in Figures 3.18 (synthetic data) and 3.19 (real data with added events). In each of these figures, the starting data are shown in section a, the f-k results in section b, the radon results in section c, and the PEF results in section d. The data are scaled the same in each section (a, b, c, and d), so that accurate comparison may be made. For the case of the synthetic data, the included radon result (Figure 3.18c) is the result of simply muting the noise in the radon domain (same as Figure 3.10d), while for the real data the included radon result (Figure 3.19c) is the result of modeling the noise in the radon domain, and subtracting this from the original data in the t-x domain to produce the displayed signal result (same as Figure 3.12b).

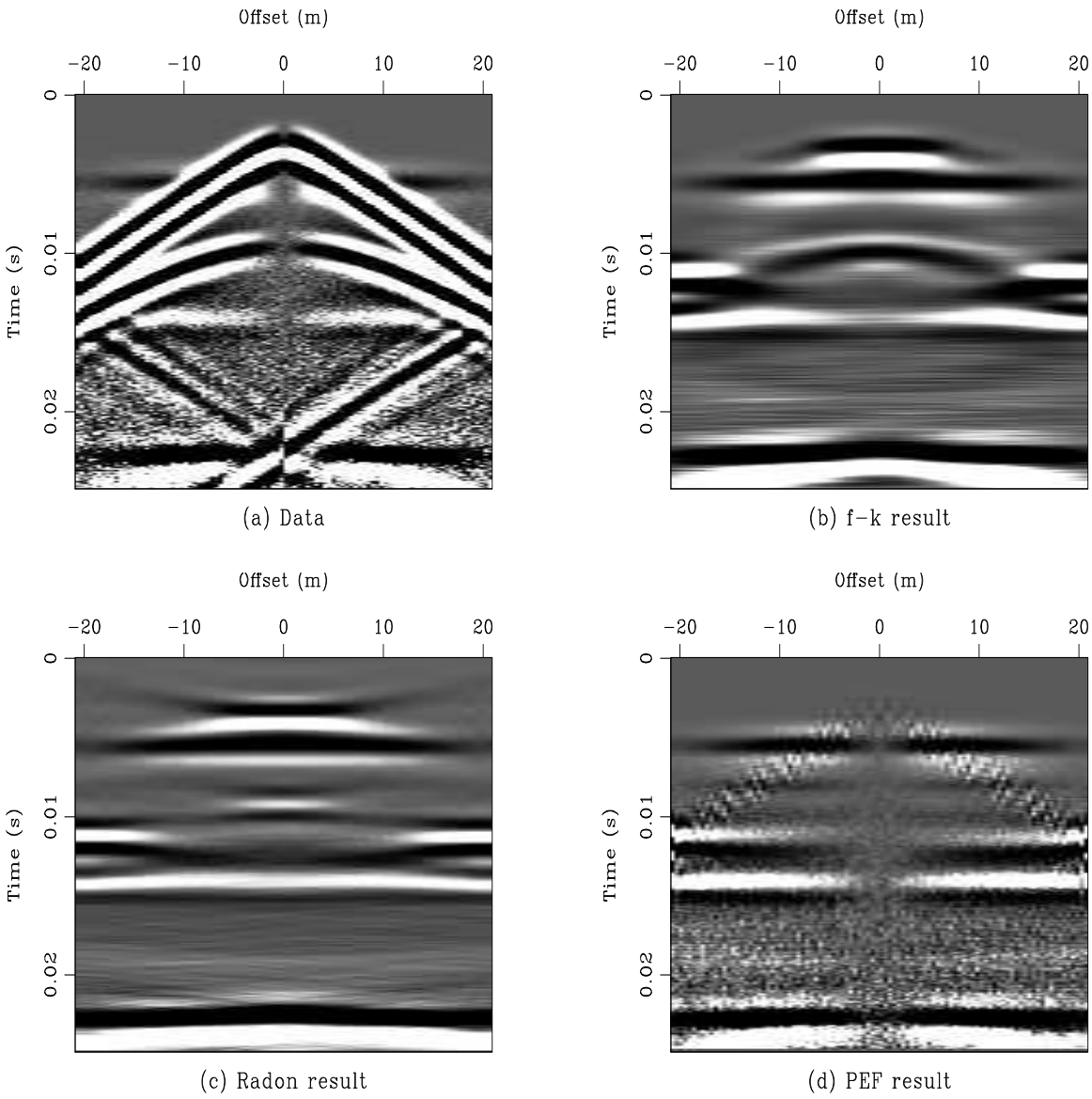

Figure 3.18: Comparison of signal/noise separation results on synthetic data. All are plotted with gain correction of t^2, and at the same scale. a) Starting data. b) f-k result, same as Figure 3.6b. c) Radon result, same as Figure 3.10d. d) PEF result, same as Figure 3.14b. proc-syncomp [ER,M]

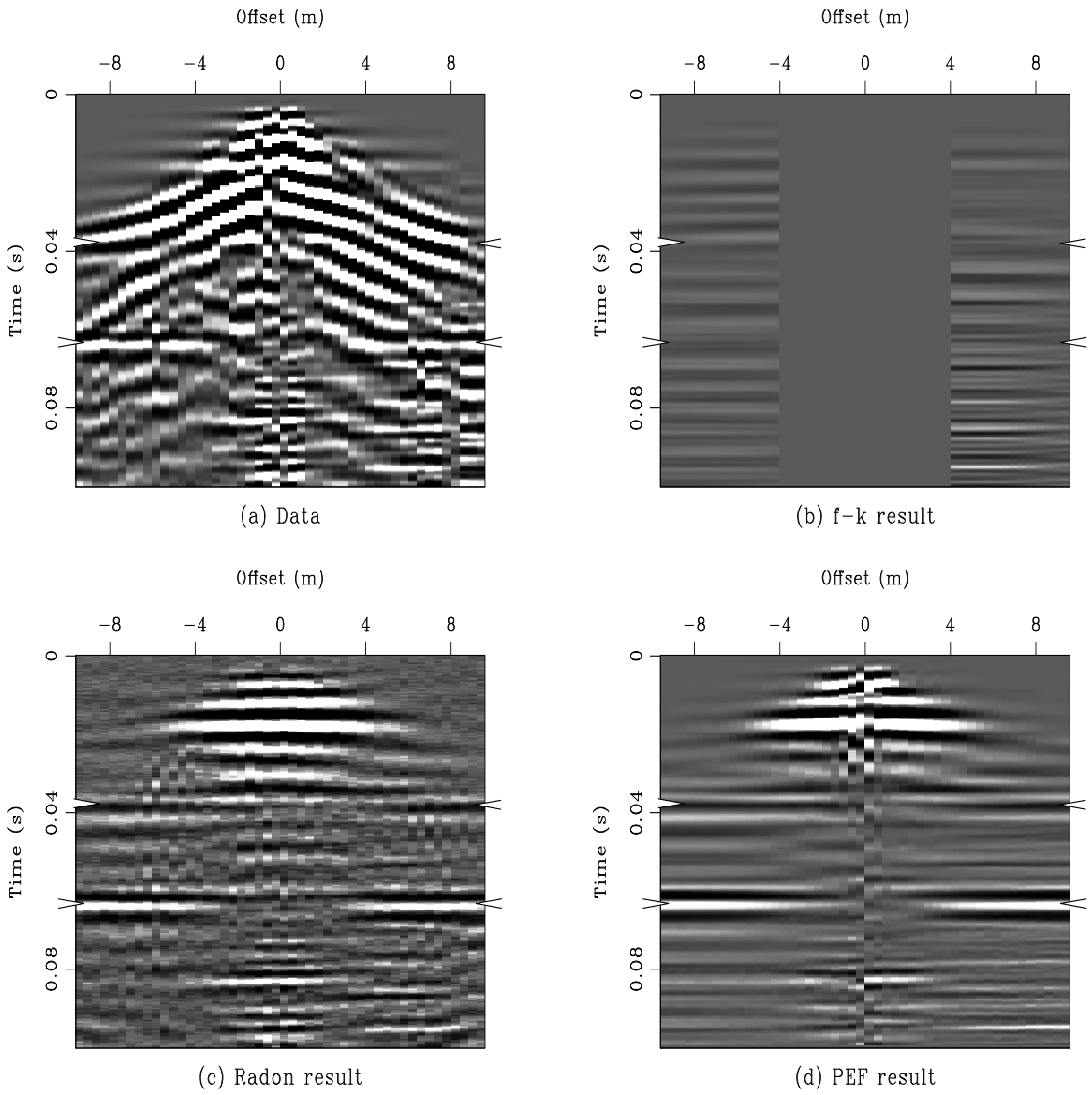

Figure 3.19: Comparison of signal/noise separation results on real data with added events (highlighted with arrows). All are plotted with gain correction of $t^{1.85}$, and at the same scale. a) Starting data. b) f-k result, same as Figure 3.8b. c) Radon result, same as Figure 3.12d. d) PEF result, same as Figure 3.16b. proc-realcomp [ER,M]

In Figures 3.18 and 3.19, we can see that although none of the three signal/noise separation techniques is perfect, they are all effective in removing the bulk of the coseismic energy. Both the f-k and the radon methods have trouble removing the flat central parts of the coseismic hyperbolas, as these methods are based only on patterns, and the flat parts of the coseismic energy show the same (flat) pattern as the interface response signal. Even when the central traces are removed (Figures 3.7, 3.8, 3.11, and 3.19b), a tiny amount of remaining coseismic energy is flat, and is not entirely removed by these methods because they have no means to differentiate between flat signal and flat noise. Similarly, the coseismic energy at the edges of the synthetic data (the larger offsets) presents a challenge to the f-k and radon methods as, like the near-offset energy, these parts of the coseismic arrivals map to the same parts of the transform domains as the signal of interest. In this case the direct and reflected coseismic events arrive at the same time and interfere constructively to produce effectively flat energy that is difficult to remove from the gathers. Another possible disadvantage of the transform-based methods is illustrated by Figure 3.19b – in this case muting in the f-k domain has removed the coseismic energy at the expense of the signal amplitudes. Clearly it is preferable to preserve all amplitude information during data processing, and this application of f-k filtering fails to accomplish this goal. Both comparisons show that the radon method is preferable to the f-k filtering, but the real data (Figure 3.19 c versus d) shows this particularly clearly. Although in theory both results should be similar, the radon result is considerably better in terms of the final signal-to-noise ratio, and in terms of the fact that the result simply looks more realistic. This difference is largely due to our use of the Cauchy regularization, which causes better focusing of energy in the radon domain, and permits a cleaner separation of the signal from the noise.

The PEF results (Figures 3.18d and 3.19d) demonstrate the benefits of using both patterns and amplitude variations. Figure 3.18d shows virtually no evidence of the flat near-offset coseismic energy, and shows much better preservation of the original amplitude patterns of the interface response signal than the f-k and radon results. In the real data (Figure 3.19d), we can see that because the PEF's are "aware" of the amplitude pattern of the interface response events, they can better remove the flat noise events that do not fit this amplitude pattern (the flat events at $\sim$0.05 s).

CONCLUSIONS

Seismoelectric data processing presents a unique challenge, but one that can be addressed using the tools of seismic signal processing. The processing flow must begin with the removal of power-line energy and its harmonics (60 Hz in North America). We find that this is best accomplished using the frequency revision technique of Butler and Russell (2003), but that the large additional computational demand is only necessary for cases where unstacked data (explosion sources, for instance) are contaminated with particularly difficult-to-remove power-line noise. Under most circumstances, the simpler sinusoidal subtraction technique (Butler and Russell, 1993) is sufficient. Once the power-line energy is removed, standard seismic processing steps such as bandpass filtering and gain correction may be applied.

The removal of coseismic energy from seismoelectric data is essential before a shot gather may be stacked. We have presented results on synthetic and real data obtained using f-k filtering, linear radon transform (LRT) domain muting, and signal/noise separation using prediction-error filters (PEF's). f-k filtering proved the least effective method, producing results contaminated by large amounts of coseismic noise. The results presented here show that the LRT and PEF approaches can be almost equally effective. The PEF results are slightly better, but the method is computationally more intensive. For data with fewer traces, and for noisier data, the PEF method produces superior results because the method is more robust in these circumstances. Clean LRT mapping to the τ-p domain requires an adequate number of traces (48 is sufficient, while experience shows that 24 is not), and adequate coherence of signal and noise arrivals (energy from spikes in the t-x domain smears across the τ-p domain). Thus the PEF method is universally effective, while under the best circumstances LRT methods can be almost equally effective at a lesser cost.

This paper represents but a first step in seismoelectric data processing. If the seismoelectric method proves useful in environmental and exploration geophysics, many further advances in data processing will be required. Seismoelectric signals are very weak, so improved signal/noise separation techniques will be needed to permit the observation of signals from deeper layers. In addition, we have assumed that all subsurface interfaces are horizontal, which is obviously a faulty assumption in most settings. Dipping subsurface layers will produce interface

response energy at points that are not directly beneath the shot point, necessitating processing similar to seismic migration to produce CDP-type gathers for stacking. It is the goal of this contribution to present a foundation on which future seismoelectric data processing advances may be built.

ACKNOWLEDGMENTS

We are grateful to Steve Pride, Simon Klemperer, and Jerry Harris for valuable guidance in this project. The field data shown here were collected at the Pride Mountain Vineyards in St. Helena, CA thanks to the generous hospitality of Jim and Carolyn Pride, and with the help of Rufus Catchings, Morgan Brown, Mike Beman, Ashley Griffith, Jesse Lomask, and Rob Sanders. Acknowledgment is made to the Donors of the American Chemical Society Petroleum Research Fund for support of this research. The work would not be possible without the generosity of the Geological Society of America Foundation, the American Association of Petroleum Geologists, the Stanford School of Earth Sciences McGee Fund, the Achievement Rewards for College Scientists Foundation, and the sponsors of the Stanford Exploration Project.

Chapter 4

Applying the seismoelectric method

INTRODUCTION

Observations of seismoelectric phenomena have been reported by many authors in the last seventy years (Thompson, 1936; Martner and Sparks, 1959; Parkhomenko, 1971a). A swell of interest in the past decade (Thompson and Gist, 1993; Butler et al., 1996; Mikhailov et al., 2000; Garambois and Dietrich, 2001) suggests that the seismoelectric method could soon see regular use, but reliable application of the method to geophysical problems remains an elusive goal. Development of data collection (Chapter 2) and processing (Chapter 3) methods represents important progress toward the goal of using the method in real-life situations, but also begs an answer to the question "what can we realistically hope to learn from seismoelectric surveys?" The amassed literature indicates that seismoelectric phenomena can definitely be observed, and encourages continued experimentation. Real progress beyond the current state-of-the-science in seismoelectric prospecting, however, will likely require a significant increase in experimental complexity and bring with it an associated increase in budget. In this contribution we assess the current state of seismoelectric methodology, and address the question of whether the benefits of further method development warrant the necessary increases in experimental complexity.

We begin by presenting a real seismoelectric image of a shallow man-made target, accompanied by a synthetic image of the same target produced with finite-difference modeling. We believe that this is the first numerical modeling-supported seismoelectric image to be presented, and only the second seismoelectric image. We use additional modeling results to examine the effectiveness of the seismoelectric method for imaging targets with various two-dimensional heterogeneities. These results allow us to establish some basic concepts to guide future seismoelectric work.

IMAGING MAN-MADE TRENCHES

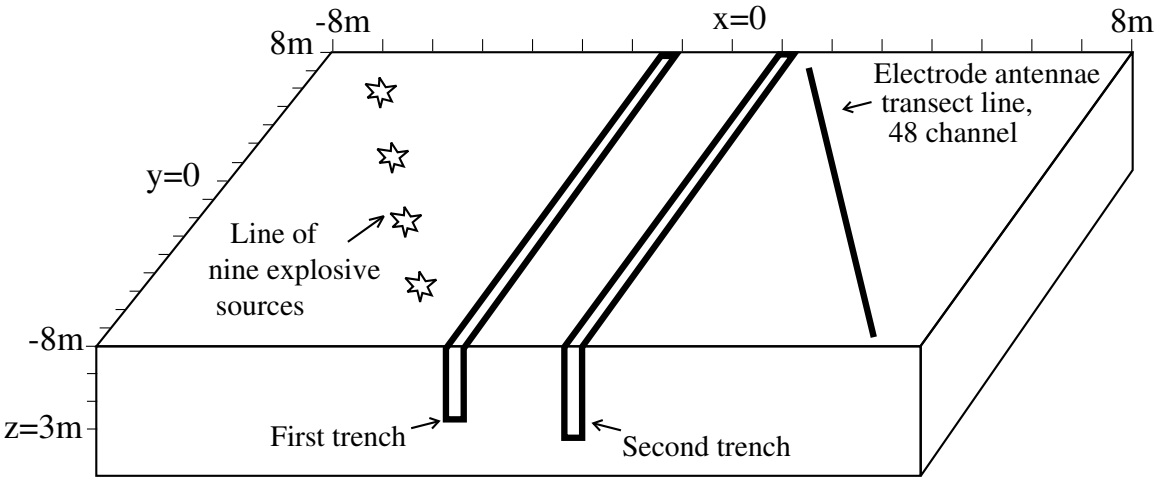

Figure 4.1: Cut-away view of the two-trench geometry at the vineyard field site, showing the receiver line and the shot line. These lines are parallel to each other, and angled 20° to the trenches. Nine shots were fired along the line, and were recorded by 48 channels of electrode receivers. application-new_boom_layout [NR]

In order to test the effectiveness of the seismoelectric method in a controlled setting, we have imaged two sand-filled trenches at the Pride Mountain Vineyards test site, shown in Figure 4.1 and described in detail in Chapter 2. The site consists of a small meadow of predominantly clay-rich soil in which we dug two trenches that are 18 m long, ∼1 m wide, and 2 to 3 m deep. The trenches are filled with sand, and are 2 m apart. By placing seismic sources

and receivers on opposites sides of the trenches (a "fan" geometry), we can record the seismoelectric interface response separately from the coseismic noise. The seismic energy propagates outward from the source, and encounters the trenches and creates the interface response. The interface response is recorded by the receiver electrodes before the coseismic field of the seismic energy reaches the receivers. Because the targets are man-made, data interpretation is relatively simple and method development is facilitated.

In this section we present our seismoelectric image of these trenches, and a complementary synthetic image produced with finite-difference modeling.

Field data collection

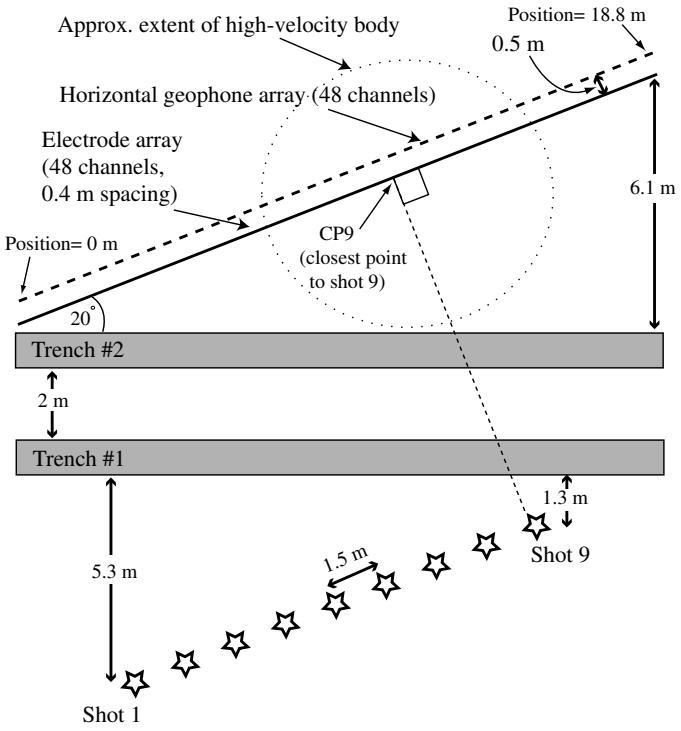

Figure 4.2: Map-view schematic of the dipping trench experimental geometry, including the approximate location of the high-velocity body that is discussed in the text. application-trench_geom [NR]

We collected the data for the trench image using the geometry shown in Figure 4.2. A line of explosive sources is parallel to the line of electrode receivers that is ∼10 m away and on the opposite side of the trenches. These two lines are at an angle of 20° to the trenches, so that we image the trenches as dipping interfaces rather than as flat ones. This geometry was chosen

so that the resulting image would be a convincing example of the seismoelectric method. A flat-layer geometry would cause the signals from the trenches to arrive at the same time for all shots, making these signals more difficult to conclusively distinguish from other flat arrivals such as the seismoelectric direct field.

We chose to use explosive sources because we established in Chapter 2 that they are the best option for the longer offsets used in this experiment. As shown in Figure 4.2, a line of nine chemical explosive sources at 1.5 m intervals provides our seismic energy. These were 0.3 kg (2/3 lb) charges except for the shots at positions 3 and 7 which were 0.45 kg. All shots were $\sim$1.5 m deep in hand-augured holes that were backfilled and tamped with native material. The shots were detonated with blasting caps that were fired by a small battery. Each charge provides one seismoelectric shot gather recorded by the receiver array. We simultaneously recorded each shot with a total of 96 channels – 48 channels of electrode dipoles and 48 horizontal geophones. The electrode array was composed of 1.4 m dipoles spaced at 0.4 m intervals. The geophone array was composed of Mark Products model L-28 horizontal geophones at 0.4 m intervals, aligned along the direction of the receiver line. Although we demonstrated in Chapter 2 that geophones within electrode dipoles do not create noticeable electric noise, the geophone line was positioned a half-meter behind the electrode line to avoid any possible signal contamination.

We used a simple battery-and-blasting-cap firing technique to minimize trigger-related electrical noise, but this approach left the exact shot timing to be determined manually. Comparison with hammer-source data (triggered by a trigger switch accurate to $\sim$0.5 ms) provided a basis for setting time zero for the gathers. Fine adjustments of the relative timing between individual shot gathers we made on the basis of first seismic arrival time on the geophone gathers (geophone and electrical data were recorded simultaneously).

Figure 4.3 shows the seismoelectric record from shot #3, with annotations identifying the arrivals. It should be noted that the interface response arrival from the first trench (labeled “Tr 1”) shows higher frequency energy than the interface response arrival from the second trench (“Tr 2”), likely due to seismic attenuation of the higher frequencies while the seismic wave passed from the first trench to the second. The interface response arrivals are easily identified because they are essentially flat. The coseismic energy (“CS”) shows different arrival times

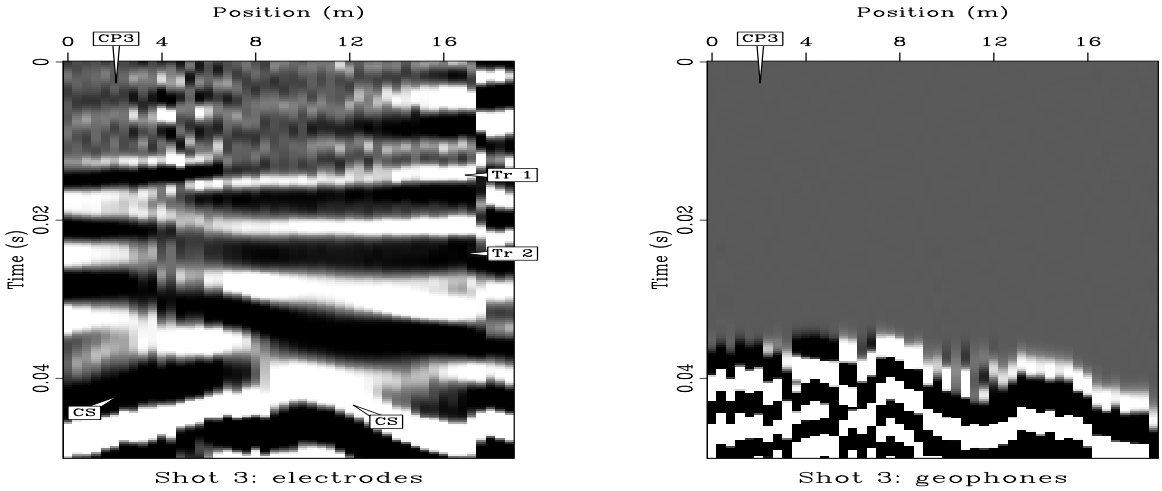

Figure 4.3: Seismoelectric (left) and seismic (right) gathers for shot #3. Annotations identify the interface response arrivals for the two trenches ("Tr 1" and "Tr 2"), and the coseismic energy ("CS") on the elctroseismic data. The lateral position labeled "CP3" is the closest point on the receiver line to the shot point (shot 3), marked for reference. Note that the seismic arrivals correspond with the coseismic energy. application-gather3 [ER]

at different offsets as is expected, however the moveout is far from the hyperbolic shape that would be expected for a fan-profile shot in homogeneous material. In particular, the earliest prominent coseismic first arrival occurs at the receiver position ∼10 m, rather than at ∼2 m which is the point on the receiver line that is closest to the shot point. Thus it is clear that velocity heterogeneity exists at our field site, and that it causes coseismic energy to arrive earlier at receivers around the position ∼10 m than otherwise expected.

Figure 4.4 shows the gathers from shots #1, #2, #4, and #5, and figure 4.5 shows the gathers from shots #6, #7, #8, and #9. The general patterns are the same as the gather for shot #3 (Figure 4.3)– interface response arrivals from the two trenches followed by the curved coseismic energy. The arrival time of the interface response energy becomes earlier as the shots approach the trenches (from shot #1 to shot #9). If seismic velocity at the field site was homogeneous, the coseismic energy would arrive at the same time on all shot gathers (since the distance from the shot to the receiver line is the same for all shots). But because of the site heterogeneity and the fact that the sequential shots approach the ∼10-m offset part of the receiver line (shot #9 is closest to this part of the receiver line), the coseismic energy arrives

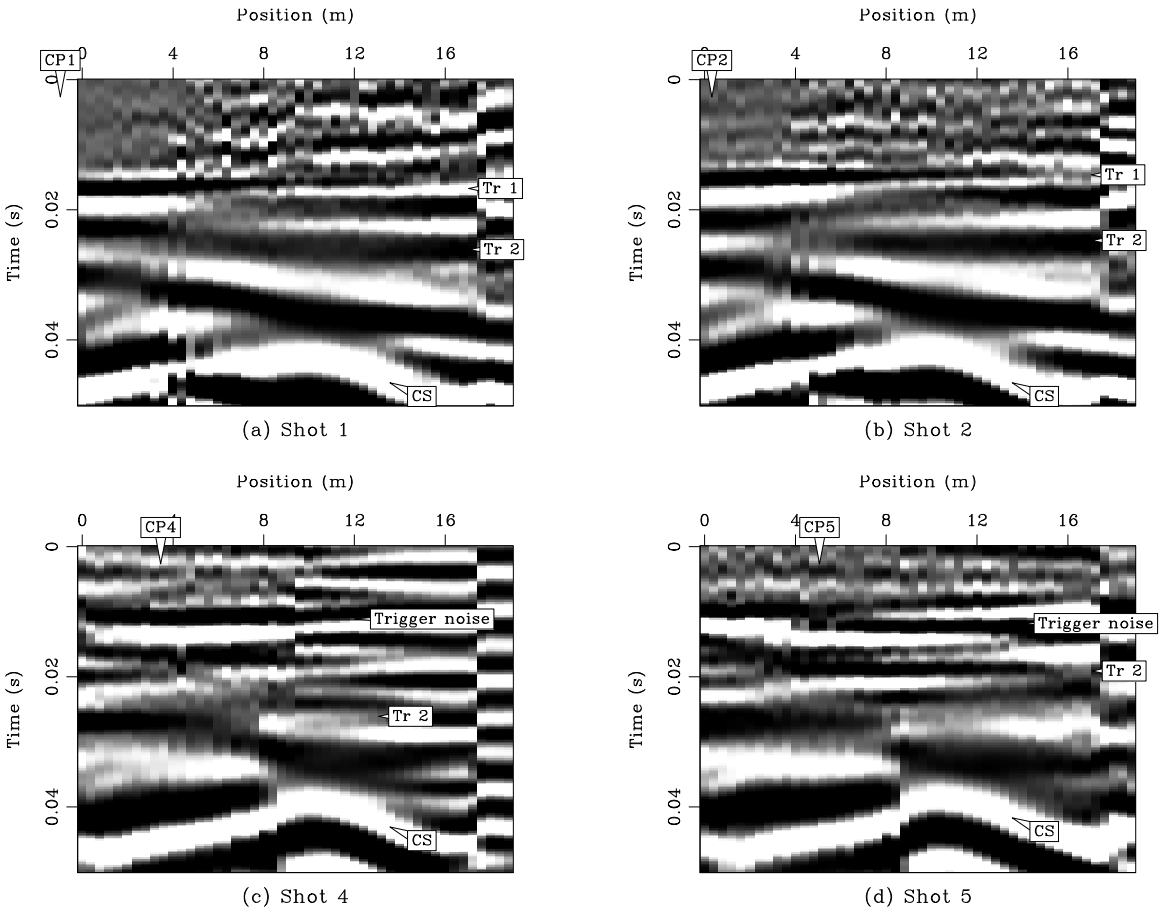

Figure 4.4: Seismoelectric shot gathers for shots #1, 2, 4, and 5. All data have undergone 60 Hz energy removal and are displayed with a 120 to 300 Hz bandpass filter. Note strong 60 Hz energy remaining in gather for shot #4. Also labeled are the closest points to the shot point for each gather, labeled "CPx" where x is the shot number. application-gathers1 [ER,M]

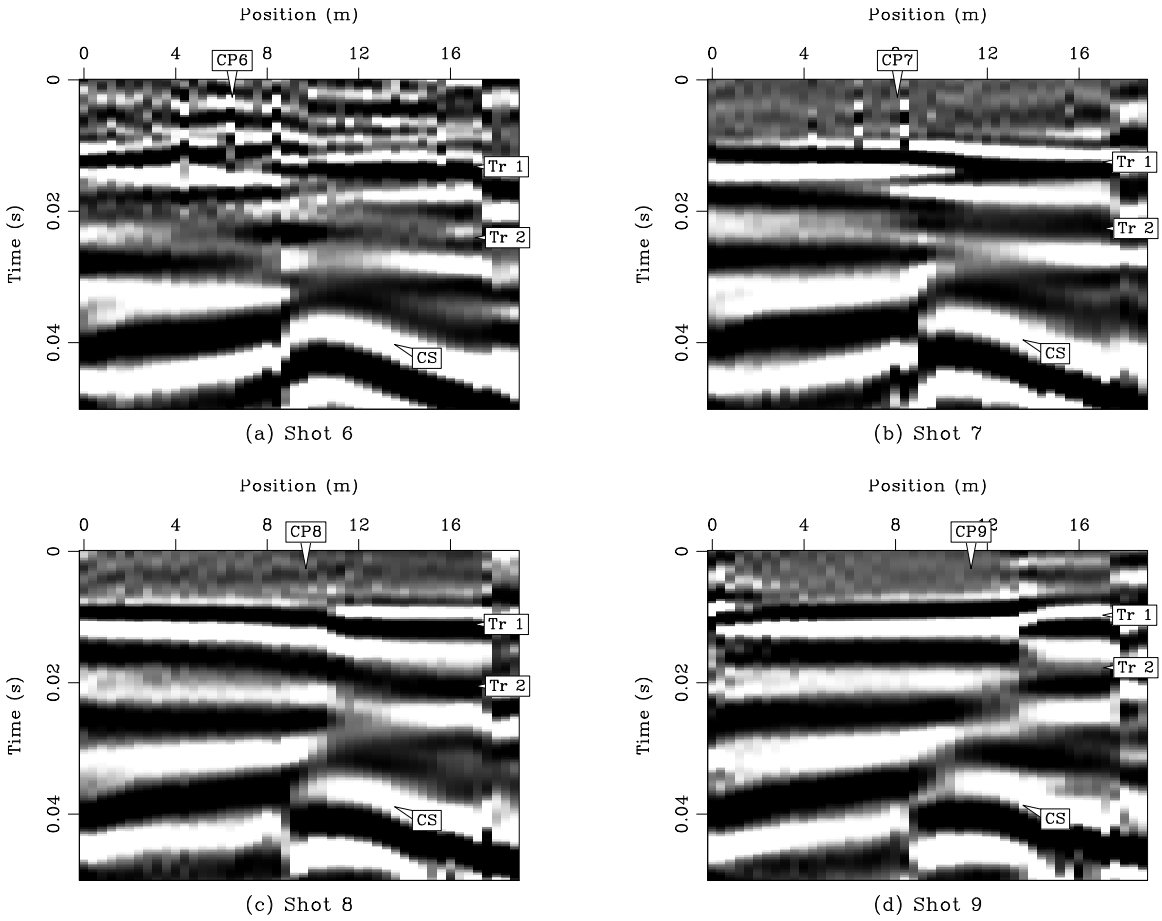

Figure 4.5: Seismoelectric shot gathers for shots #6, 7, 8, and 9. All data have undergone 60 Hz energy removal and are displayed with a 120 to 300 Hz bandpass filter. Also labeled are the closest points to the shot point for each gather, labeled "CPx" where x is the shot number. application-gathers2 [ER,M]

earlier for each sequential shot at this part of the receiver line (position ∼10 m), and earliest for shot #9. So although for our experiment geometry we would expect the coseismic first arrival to occur at the same time for all shots in a homogeneous field site, the heterogeneity at our site causes a slight deviation from this pattern. Note the marked arrivals on the gathers for shots #4 and #5 that are identified as trigger noise. These arrivals occur at nearly the time expected for the first trench interface response, but do not show the correct amplitude pattern, and also arrive earlier than expected. We interpret them as the combination of trigger-related noise and the interface response arrival from the first trench.

Figure 4.6 shows the synthetic shot gather for shot #3 produced by finite-difference modeling. The modeling algorithm is described in detail in Appendix A, and the geometry of the model space is shown in Figure 4.7, with the non-trench material extending ∼4 m beyond the ends of the trenches for the seismic propagation, and ∼20 m beyond the trenches for the electrical simulation. Material property parameters for the model blocks are shown in Table 4.1. The high-velocity body is rectangular, and is made up of 9 strips which provide a gradual transition to the highest velocity, as shown in Figure 4.7. The point source is isotropic and is scaled to represent 0.45 kg of explosive. The source time series is a 200 Hz Ricker wavelet.

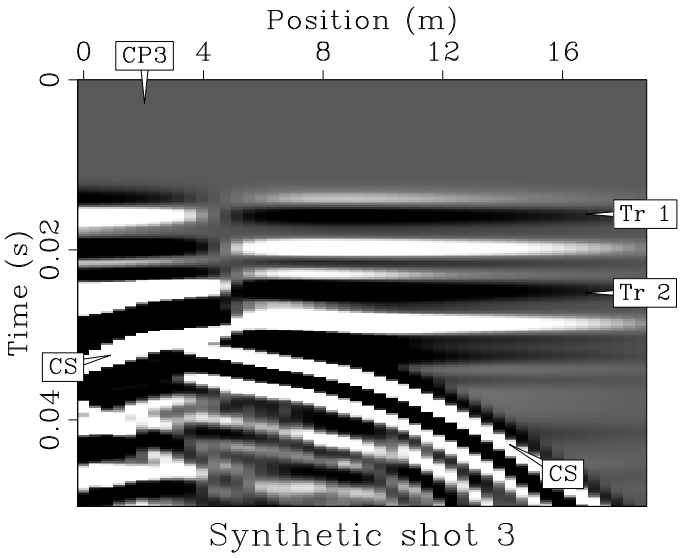

Figure 4.6: Synthetic seismoelectric gather for shot #3, simulating real data shown in Figure 4.3. Trench interface response arrivals ("Tr 1" and "Tr 2") are labeled, along with coseismic energy ("CS"). The closest point on the receiver line to the shot point is labeled "CP3". application-syn_gath3 [ER]

The basic patterns of the seismoelectric arrivals in the gather (Figure 4.6) match the real data gather shown in Figure 4.3 – interface response events from the two trenches (labeled "Tr 1 and Tr 2"), followed by the coseismic energy ("CS"). The arrival times of the events

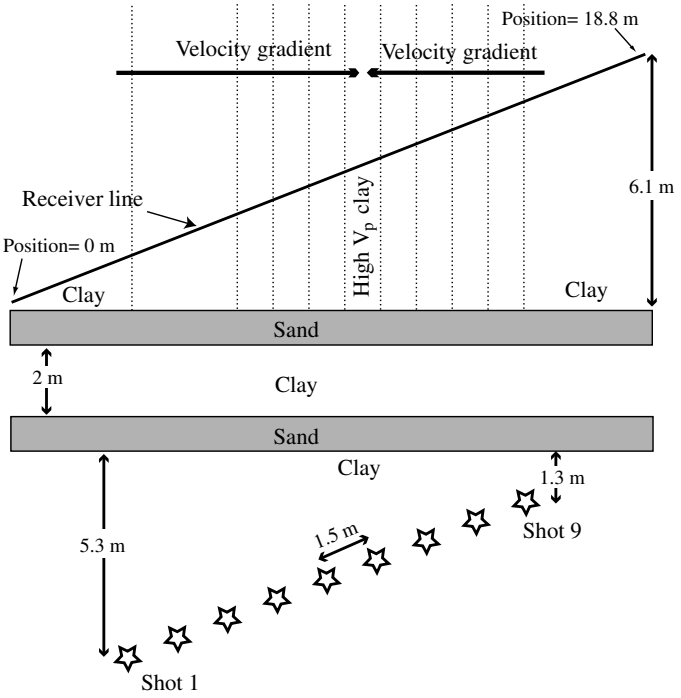

Figure 4.7: Layout of model for trench simulations, showing high velocity body. application-model_geom [NR]

Table 4.1: Physical properties of materials in synthetic trench model.

	V_p (m/s)	porosity (%)	hyd. perm. (m^2)	elec. cond. (S/m)	sat. (%)
Clayey soil	393	10	10^{-14}	0.05	97
High-V_p clay	555	10	10^{-14}	0.05	97
Sand (trenches)	263	30	10^{-11}	0.01	97

are similar, but not exactly the same. The coseismic energy is not hyperbolic, since the model includes the heterogeneity that exists at the real field site.

Figure 4.8 shows synthetic shot gathers for shots #1, #5, #7, and #9. As with Figures 4.4 and 4.5, the interface response events arrive earlier for the higher-numbered shots since they are closer to the trenches. Although the distance between each shot and the closest receivers is constant for all shots (∼10 m), the coseismic energy also arrives earlier for the higher-numbered shots, as in the real data.

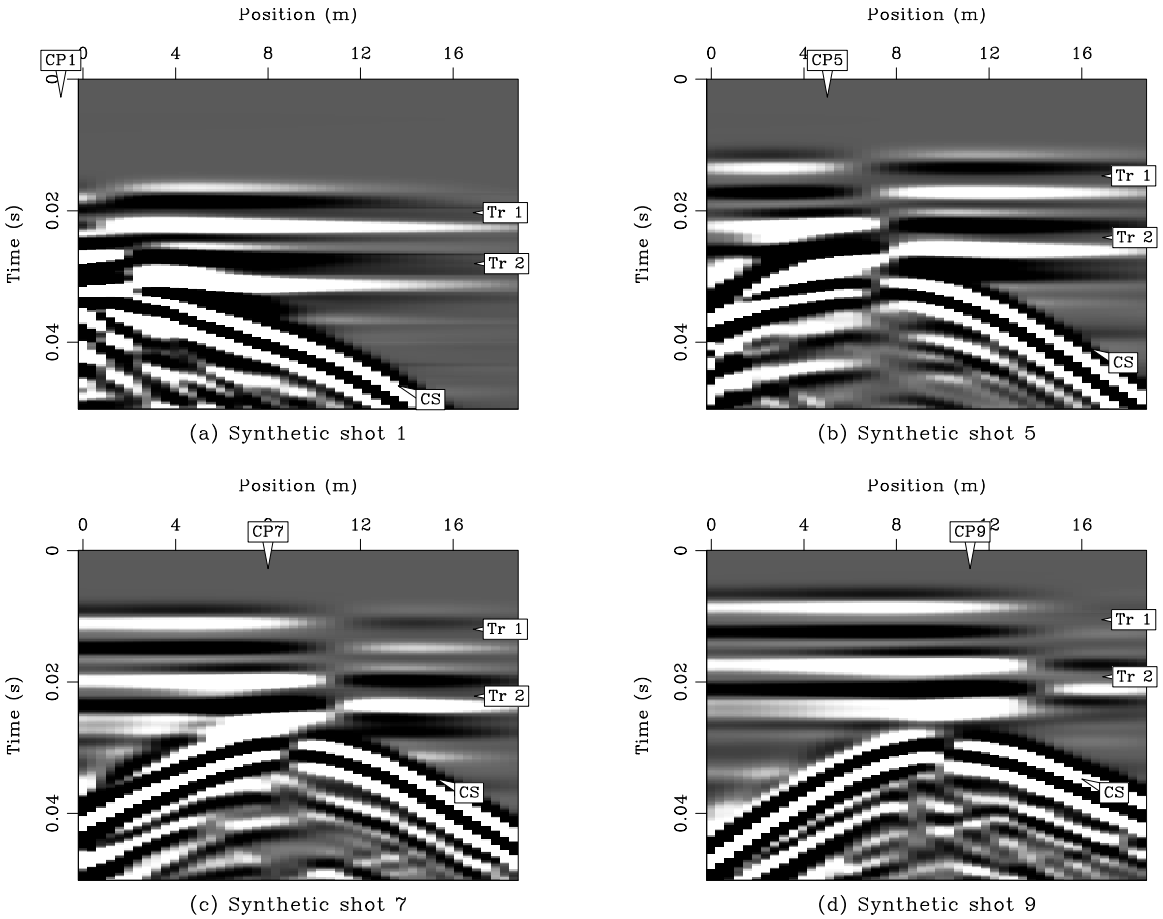

Figure 4.8: Synthetic seismoelectric shot gathers for shots #1, 5, 7, and 9. Note that the curved coseismic energy arrives at approximately the same time for all gathers while the flat trench interface response signals arrive earlier for later (higher-numbered) shots. For reference, the closest points to the receiver line for each shot are labeled "CPx", where x is the shot number. application-syn_gaths [ER,M]

Data processing strategy

Our data processing goal is to enhance the interface response events from the trenches while diminishing or removing all other energy. This "other energy" includes 60 Hz energy from the power grid, the coseismic energy, and background electrical noise. In Chapter 3 we established that the "frequency revision" approach for removing 60 Hz energy (Butler and Russell, 2003) is the most effective option for that form of noise, particularly for un-stacked shot gathers. We begin the data processing by employing this approach for all shots other than shot #4. This shot gather is particularly troublesome, and the best 60 Hz removal results are obtained by using the simpler sinusoidal subtraction technique presented by Butler and Russell (1993). After 60 Hz removal, we use a 120 to 300 Hz bandpass filter to minimize background electrical noise as well as the coseismic energy.

Each seismoelectric shot gather contains information about only a small region of the subsurface. For a surface survey layout with the source in the center of the electrode receivers and flat layers in the subsurface, the interface response events in each shot gather contain information coming from the first seismic Fresnel zones of the layers directly beneath the shot point. The polarity of the interface response events is reversed on opposite sides of the shot point. A subsurface image would in that case be made by reversing the polarity of either the positive or the negative offsets of each shot gather, stacking those gathers, and displaying the resulting traces side-by-side. The interface response energy in each shot gather comes from points directly beneath the source, so it all "belongs" in one trace in the final image. Note that in this seismoelectric geometry, we stack shot gathers, in constrast to typical seismic prospecting in which one stacks common-midpoint gathers.

Because our cross-trench geometry is more complex, with the sources and receivers on opposite sides of dipping interfaces (Figure 4.2), the assignment of seismoelectric energy to specific locations is not as simple. As can be seen in the synthetic shot gathers (Figures 4.6 and 4.8), the interface response polarity reversals do not occur at the same point for the two interface response events in each gather. And neither of these polarity reversal points is the same as the center of the coseismic event. As shown in Figure 4.9, the center (top of the hyperbola, and point where the polarity reverses) for the coseismic arrivals is found at the

location along the receiver line that is closest to the shot point. The location of the centers of the interface response events is determined by the location of the point on the corresponding interface that is nearest the shot point (that is, the location of the first seismic Fresnel zone) and its orientation with respect to the receiver line. These interface response polarity reversal points are not necessarily the closest points to the location of the interface response dipole. The polarity reversal points for the real and synthetic gathers for shot #3 are marked with thick white lines in Figure 4.10.

We reverse the polarity of approximately half of the traces of each shot gather before stacking. In the case of a simple horizontally layered subsurface survey, the point where the center point of this polarity flipping would be the shot point, with positive and negative offsets being of opposite polarity. For our dipping geometry, we manually define a line within each shot gather that defines the line around which the polarity is reversed. This approach allows us to honor the patterns visible in the data and to produce the best possible stack. Figure 4.10 shows the polarity-flipped versions of the real and synthetic gathers for shot #3. We flip the polarity of the other shot gathers in a similar manner.

Applying the signal/noise separation methods developed in Chapter 3, we can attempt to remove the unwanted coseismic energy. Lacking an adequate model for noise PEF estimation, we apply the radon filtering approach to the polarity-flipped versions of the gathers (as shown in Figure 4.14). Figure 4.11a shows the radon-filtered version of the gather from shot #3, with the complementary synthetic result shown in Figure 4.11b. We have muted the signal from τ-p domain, and subtracted the resulting noise estimate from the starting data. For the real data, the mute is for slowness less than 0.0006 s/m, while for the synthetic data the mute removes energy with slowness less than 0.0004 s/m. Both mutes are tapered, as described in Chapter 3. For the synthetic data, where the coseismic arrivals are close to being well-rounded hyperbolas, the radon filtering is effective (Figure 4.11b shows very little remaining coseismic energy), while for the real data the method is not as effective. In this case, the fan geometry and earth heterogeneity result in coseismic arrivals that are irregular in shape and difficult to remove with radon filtering. The result (Figure 4.11a) shows that the dipping parts of the coseismic arrivals have been removed, but that a large amount of flat energy remains, labeled "CS".

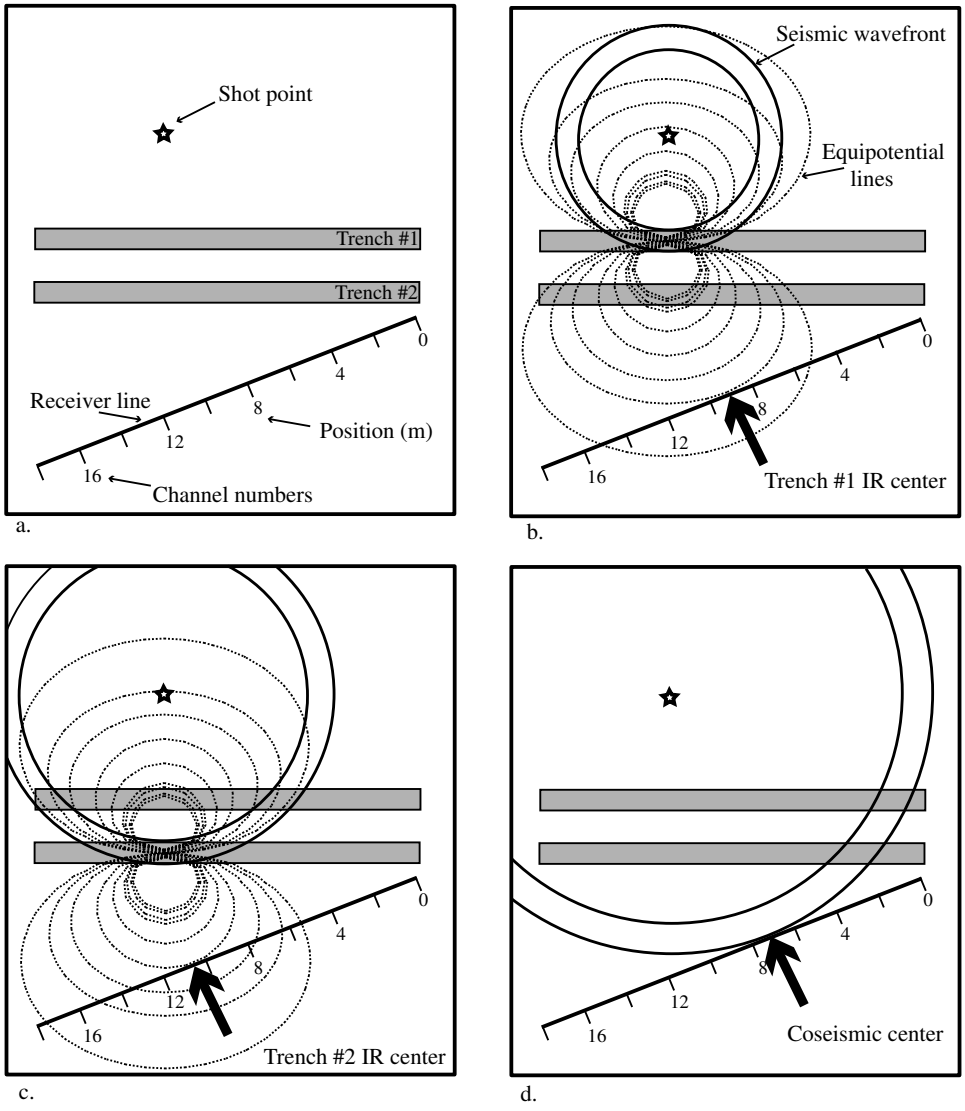

Figure 4.9: Schematic diagram showing propagating compressional seismic wavefront for a homogeneous medium (two concentric dark circles) and the potential field (dashed lines) of the resulting interface response events created at the trenches. The four plots are the same site at four different points in time. Note that the observed "centers" of the three recorded events are different. a) Starting time, b) the time of the interface response event at the first trench (IR 1), c) time of the interface response event at the second trench (IR 2), and d) the time of the arrival of the coseismic field at the receivers. The coseismic center is at the point on the receiver line that is closest to the shot point. Because of the dipping geometry, the three centers are at three different points along the receiver line. application-dip_centers [NR]

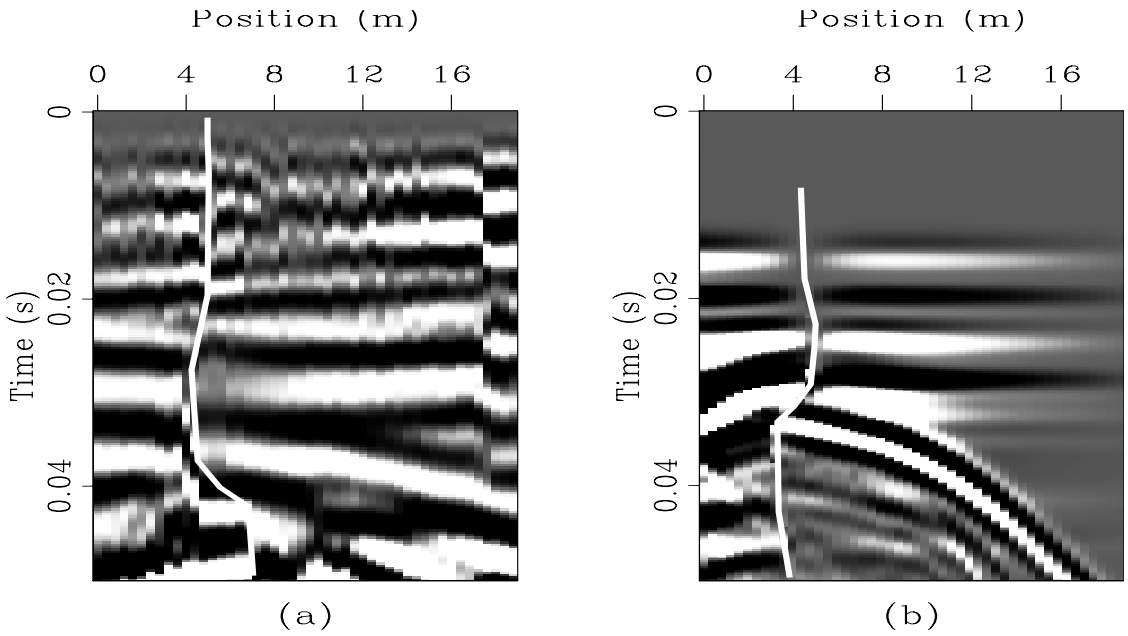

Figure 4.10: Real (a) and synthetic (b) seismoelectric shot gathers for shot #3 (compare with Figures 4.3 and 4.6), after polarity flipping. The location of the polarity flip has been manually picked and is indicated by the white line. application-lab_flip3 [NR]

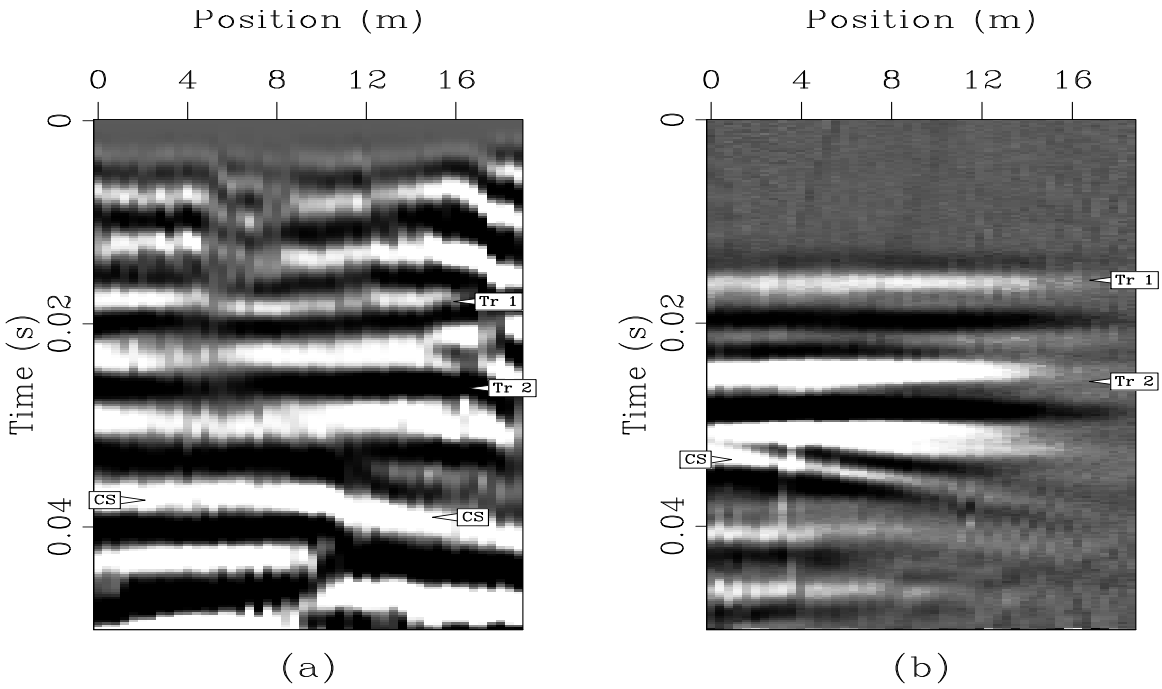

Figure 4.11: Real (a) and synthetic (b) seismoelectric shot gathers for shot #3, after radon filtering. Considerable coseismic energy ("CS") remains. application-lrt3 [ER]

Trench images

Once the polarity of the seismoelectric shot gathers has been flipped, it is a simple matter to stack each one to produce a single trace that (ideally) represents a single region of the subsurface. By placing these traces side-by-side, we create the images of the two trenches shown in Figure 4.12a (real data) and b (synthetic data). These are stacks of the gathers after the polarity flip, but without having applied the radon filtering. The plots clearly show the two dipping trenches, and also strong coseismic energy, all labeled. Although nominally hyperbolic, the coseismic arrivals stack to produce strong energy at the apex of the curve.

Figure 4.13 shows images created by stacking the radon-filtered versions of the gathers (as in Figure 4.11). The images are virtually indistinguishable from the un-filtered images in Figure 4.12. In both cases this is disappointing, but not surprising given that the coseismic energy left behind by the radon approach is the flat part; this is the same part of the coseismic energy that stacks coherently into the images.

These images clearly show the two dipping trenches, but they also show additional, unwanted, energy. The real image (Figure 4.12a) shows strong coseismic energy in the lower part of the record and also shows some coherent trigger-related noise in the upper part of the traces from shots #4 and 5. This energy is also visible at $\sim$10 ms in the unstacked gathers (Figure 4.4 c and d). It looks similar to the interface response arrivals from the first trench, but arrives too early and does not show a polarity flip at the expected location. Following the example of standard seismic processing technique, we employ front mutes to remove the offending energy from these two shot gathers. We also apply tail mutes to all shot gathers to remove the coseismic energy (a reasonable choice, since we do not expect any interface response arrivals within the coseismic noise). For the case of shot #3, the resulting muted gathers (real and synthetic) are shown in Figure 4.14a and b. After applying similar mutes to the other gathers, we stack and produce the images shown in Figure 4.15.

We now have produced a seismoelectric image of the two dipping trenches, and a complementary synthetic image. While these images each contain only nine traces, they clearly show the targets and also show a good similarity to each other. This similarity is comforting in terms of supporting our interpretations of the real data, and also is scientifically significant as

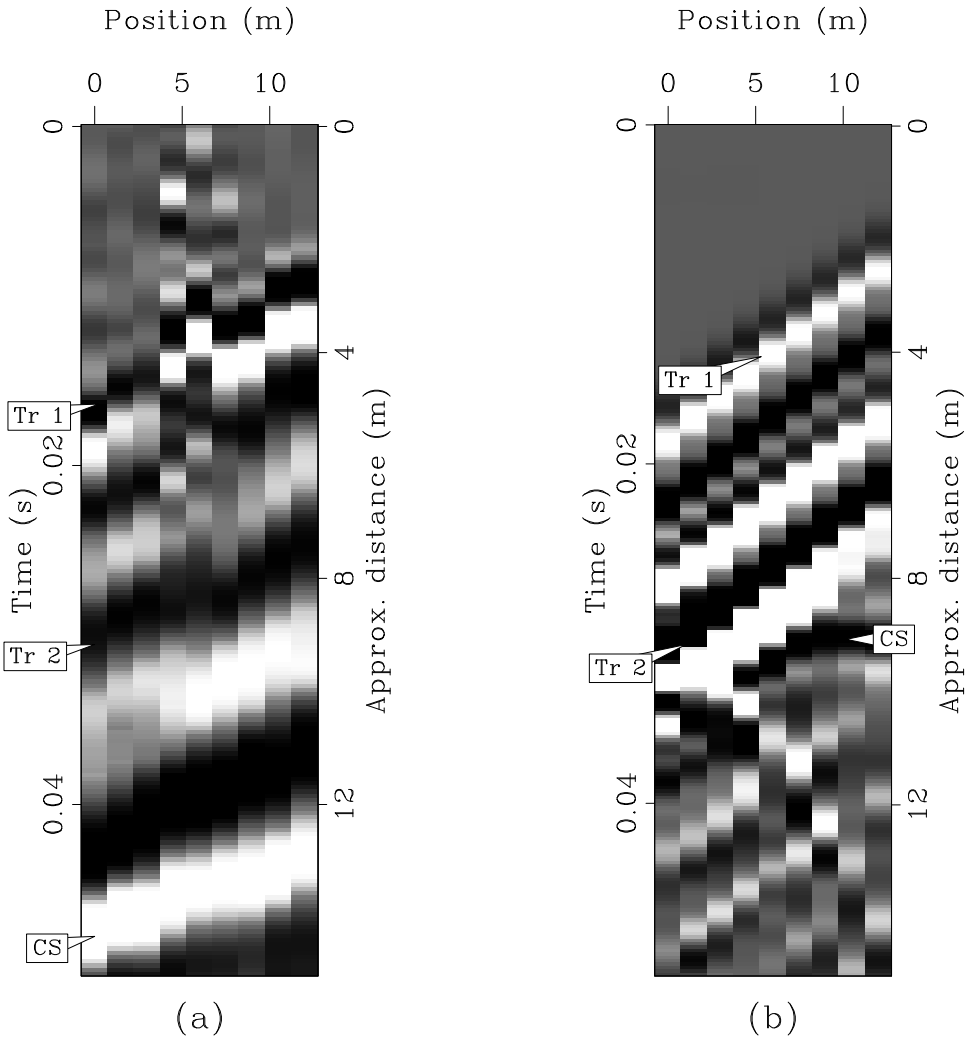

Figure 4.12: Real (a) and synthetic (b) images of the two dipping trenches, created by stacking the flipped versions of the gathers shown in Figures 4.3, 4.4, 4.5, and 4.6 and 4.8, respectively. Arrivals are annotated, and an approximate distance scale is noted, based on V_p=300 m/s. application-images [ER]

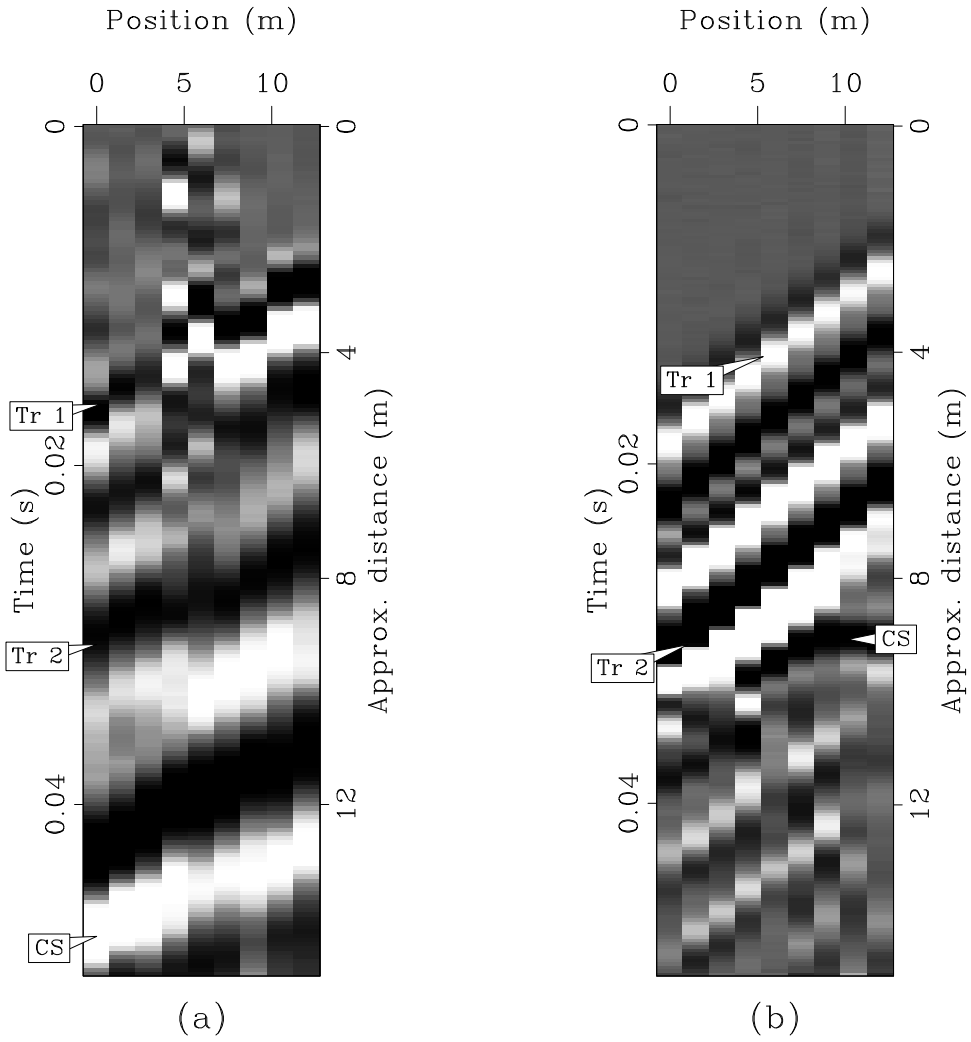

Figure 4.13: Real (a) and synthetic (b) images of the two dipping trenches, created by stacking the radon-filtered versions of the shot gathers. Arrivals are annotated, and an approximate distance scale is noted, based on V_p=300 m/s. Note that strong coseismic energy remains. application-lrt_images [ER]

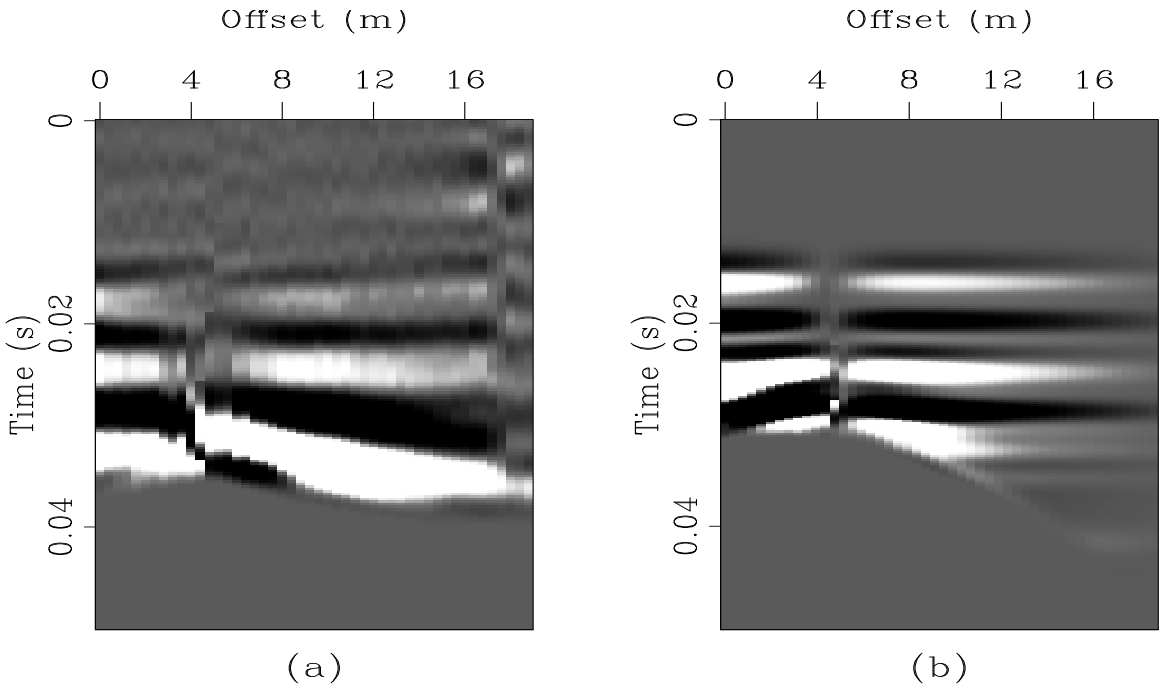

Figure 4.14: Gathers for shot #3, after applying tail mutes to remove coseismic energy. application-mute3 [ER]

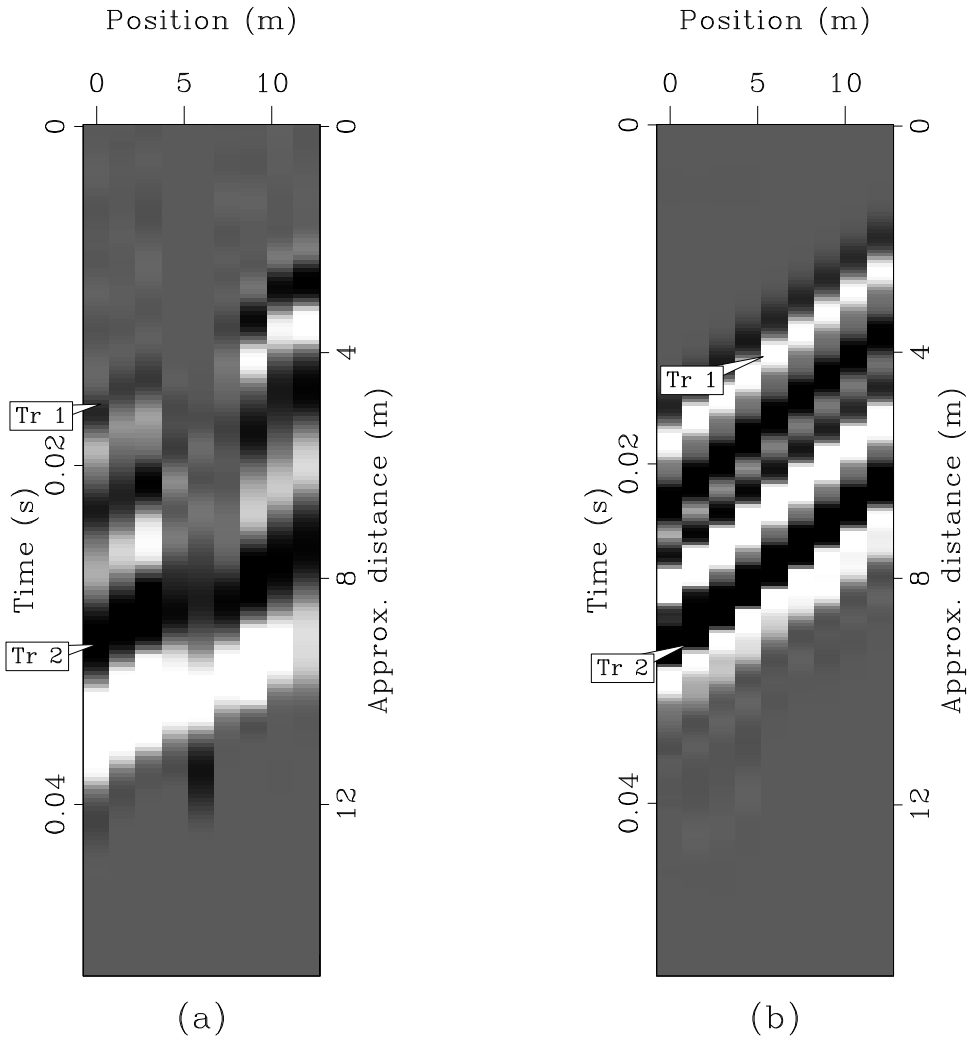

Figure 4.15: Real (a) and synthetic (b) images of the two trenches, produced by stacking shot gathers after muting the unwanted noise. Arrivals are annotated, and an approximate distance scale is noted, based on V_p=300 m/s. Note that strong coseismic energy remains. application-mute_images [ER]

it provides a confirmation that the seismoelectric theory (as represented by the finite difference modeling algorithm) can predict the phenomena observed in the field. The small number of traces can be easily improved by carrying out more complex experiments with greater budgets. Another limitation demonstrated by this trench experiment is the need for interpreter input in assigning the points at which to flip the data. For a homogeneous one-dimensional earth, assignment of the flip point is trivial (flip at the shot point). But for more complicated geometries it is necessary to manually choose the flip point, or to design processing algorithms that can automate the assignment.

We have demonstrated that the seismoelectric method can be used to image shallow structures, and so now must establish the basic parameters that control the effectiveness of the method in various circumstances. In this way, we can establish whether it is worthwhile to increase experimental complexity and cost.

SYNTHETIC DATA: MODELED APPLICATIONS

Having established that the seismoelectric method can be used in one highly-controlled setting, we must now establish a basic understanding of the sorts of applications to which the method can be successfully applied. Can we image deep crustal structures at tens of kilometers depth? Can we characterize fracture patterns within the few centimeters of thickness of the asphalt of a roadway or airport runway? The answer to both these questions is most likely “no”, but it is not clear which applications between these two extremes of scale are best-suited to the seismoelectric method. It is the goal of this section to provide some insight into the applications that are well-suited to the seismoelectric method.

Previously-published seismoelectric simulations (Garambois and Dietrich, 2002; Haartsen and Pride, 1997) include full three-dimensional wave propagation, but are limited to one-dimensional geologic models. We use a different approach that permits us to model two-dimensional structures, but is limited to two-dimensional wave propagation and two-dimensional electric field simulation. Thus we can simulate seismoelectric surveys of targets with arbitrary two-dimensional heterogeneity, allowing us to test a variety of geometric situations. Accurate amplitude modeling is difficult due to the uncertainties in seismic source

Table 4.2: Physical properties of materials in layer thickness models.

	V_p (m/s)	porosity (%)	hydraulic perm. (m^2)	electrical cond. (S/m)
Sand	1859	30	10^{-11}	0.01
Clay	2296	10	10^{-16}	0.05

scaling and the amplitudes shown for synthetic seismoelectrograms represent perfect electrode coupling, a very unlikely scenario. Thus the modeled amplitudes are best considered on a relative basis, rather than absolute. The modeling algorithm is described in detail in Appendix A.

Thickness and lateral extent of an aquitard

We begin with basic geometric variations of a simple case, illustrated in Figure 4.16. The simple case is an interface at 30 m depth between a sand layer and a clay layer. Material properties for these layers are shown in Table 4.2. We are interested in the ability of the seismoelectric method to image thin subsurface layers (thinner than those that may be imaged seismically), so we have run seismoelectric simulations with various thicknesses of the clay layer, ranging from a half-space (extending from 30 m depth to the base of the model at 51 m) to 0.5 m thickness. These layers are represented by the dashed lines in Figure 4.16, and a sample synthetic seismoelectrogram is shown in Figure 4.17a, for the case of a 2-m thick clay aquitard. This shot gather has 96 channels of data, extracted from a depth of 0.5 m in the finite-difference model. The source wavelet is a Ricker wavelet centered at 200 Hz. This shot gather represents the data that would be recorded by surface electrodes, as shown in Figure 4.16. The gather shows the strong dipping coseismic arrivals (labeled "coseismic"), as well as the flat interface response event from the aquitard ("IR"). It also shows the coseismic arrival associated with the reflected P-wave ("reflection CS").

We also extract a seismoelectrogram from a depth of 50 m, representing a "fan" geometry, shown in Figure 4.17b. Although not very realistic for this surface survey, it represents the data that would be collected if the model space were rotated 90 degrees, such that Figure 4.16 would represent a map view. In this case, the clay layer would be a vertical layer intersecting

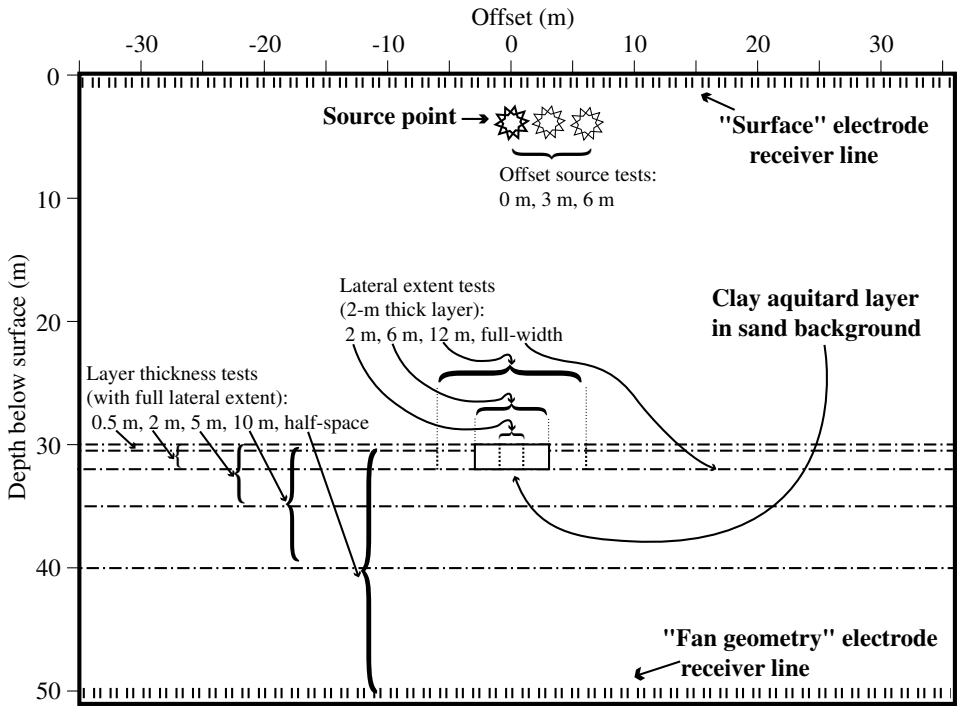

Figure 4.16: Schematic diagram showing geometry used for synthetic models in this section. These models feature a clay aquitard layer at 30 m depth in a sand background. The layer thickness varies, as does its lateral extent. And for the case of a 2 m thick by 6 m wide layer, the shot position is varied. Data shown are for electrode receiver lines at the ground surface ("surface" geometry) and at depth in the model ("fan" geometry). application-tard_schem [NR]

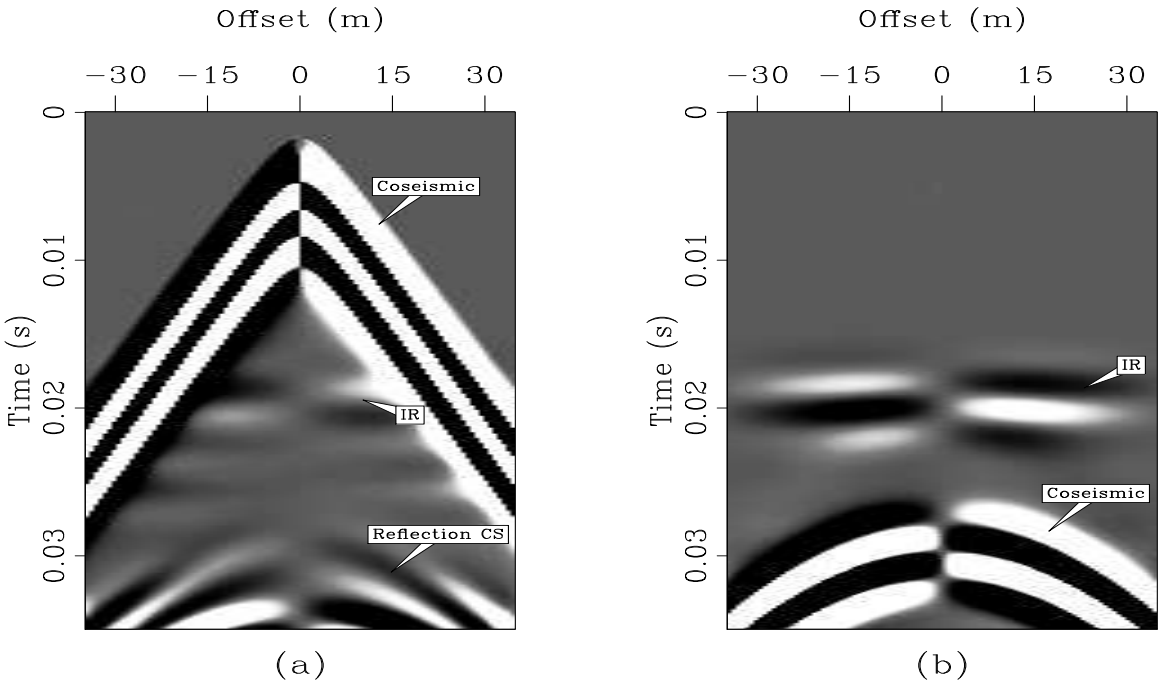

Figure 4.17: Synthetic seismoelectrograms for the case of a 2-m thick clay layer at 30 m depth. a) surface geometry shot gather, with coseismic energy recorded at the same time as the interface response ("IR"). The coseismic field of the reflected P-wave is also labeled. b) fan geometry gather, with coseismic field arriving after the interface response. application-t2_syn [ER]

the ground surface. As illustrated earlier in this contribution, the fan geometry provides a separation between the interface response and coseismic fields.

We can easily extract interface response arrival amplitude from the fan profile synthetic seismoelectrograms, without interference from the strong coseismic arrivals. Figure 4.18 shows the absolute value of the amplitude of the maximum of the interface response arrivals for various layer thicknesses, each labeled. Note that for these synthetics, the amplitude of the coseismic fields ranges from ∼4 to ∼16 mV. We can observe the dependence of amplitude on layer thickness, and note that the observed amplitude is least for the half-space. For the layer with thickness similar to the wavelength of the P-wave (∼10 m in this case), the two interface response events from the two sides of the layer constructively interfere, increasing the amplitude of the strongest phase. The two events are of opposite polarity, but the timing of the two events causes them to constructively interfere. For layers thinner than the wavelength, the two interface response events from the two sides of the layer are no longer separate events; instead a single interface response event occurs, with the layer resulting in a one separation of charge (into one dipole). For the 5, 2, and 0.5 m-thick layers, we can see that the amplitude decreases with layer thickness, corresponding with the decreasing distance between the regions of electrical charge build-up. Even for the thinnest case (thickness = 0.5 m), the interface response arrival is stronger than for the half-space model, demonstrating the effectiveness of the seismoelectric method in imaging thin layers.

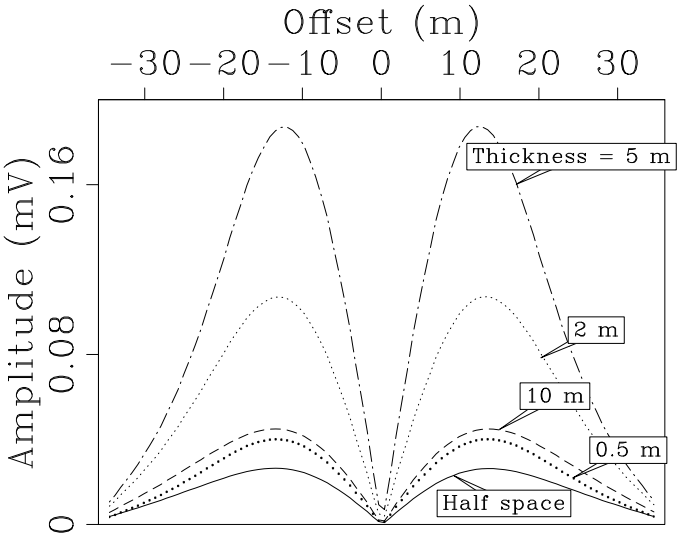

Figure 4.18: Graph of amplitude versus offset for the peak of the interface response as measured by the "fan" receiver array, for layers of various thickness from a half-space to a half meter. Even a very thin layer produces an interface response arrival with greater amplitude than the case of a half-space. These amplitudes are roughly two orders of magnitude less than those of the modeled coseismic fields. application-t_graph [ER]

We are also interested in the lateral resolution of the seismoelectric method, and so we have conducted a series of models with a 2-m thick clay aquitard of variable lateral extent, ranging from 2 m to the full width of the model space. For all of these cases, the shot point is centered above the layer in question. Figure 4.19 shows amplitudes for the interface response from this layer, showing that as the layer becomes more laterally restricted, the resulting interface response decreases in magnitude. This result is unsurprising, but provides a confirmation that we can image narrow subsurface bodies, including those that are significantly narrower than the diameter of the first seismic Fresnel zone (which is ∼24 m, in this case).

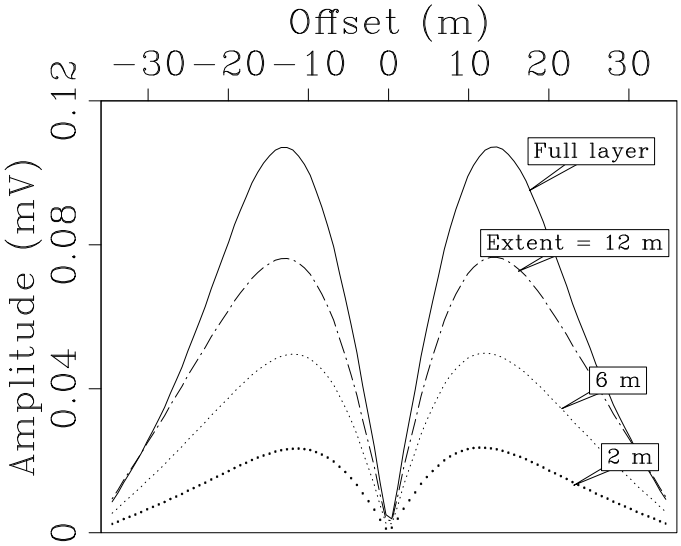

Figure 4.19: Graph of amplitude versus offset for the peak of the interface response arrival from a 2-m thick clay layer of varying lateral extent. The full-width layer produces the greatest amplitude, as is expected. But even very laterally restricted layers produce a response. These amplitudes are roughly two orders of magnitude lower than those of the modeled coseismic fields. application-e_graph [ER]

The amplitudes in Figure 4.19 are all for the case of a shot point centered above the layer of interest. This represents, of course, a fortuitous shot placement and is not the only geometry that will occur in a seismoelectric survey. For this reason we investigate the effect of moving the survey laterally along the model space, as shown with the "offset shot tests" in Figure 4.16. Figure 4.20 shows amplitudes for the offset shots. Rather than the amplitude simply decreasing for shots that are not directly above the target, we see that the pattern is more complex. Because the target is not directly beneath the shot, the expanding seismic wavefront that encounters the target at an oblique angle rather than perfectly vertically. Thus the resulting interface response dipole is oriented at an oblique angle rather than being vertical. The pattern that we observe (asymmetrical amplitude pattern that is not centered at the source point) corresponds with the angle at which the interface response dipole is aligned. Unfortunately for the interpreter, this pattern is the same as for a dipping layer (as we observed with the dipping

trench experiment described earlier). A series of shots along the surface would resolve this ambiguity, however.

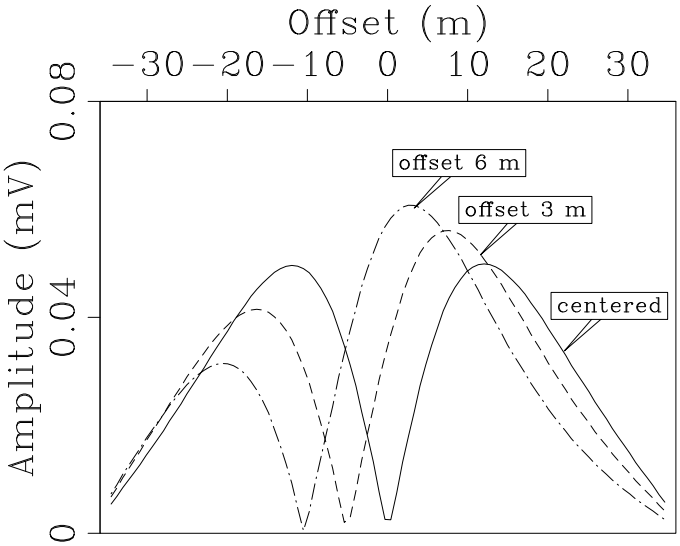

Figure 4.20: Graph of amplitude versus offset for the peak of the interface response arrival from a 2 m-thick by 6 m-wide clay layer, with shot position varied from centered above the clay layer, to offset 6 m from the center. application-o_graph [ER]

The finite-difference modeling results just described provide a demonstration that the seismoelectric method can image subsurface layers that are very small relative to the seismic wavelength. They also demonstrate the advantage of recording geometries that mechanically separate the coseismic arrivals from the interface response events. By placing sources and receivers on opposite sides of a target (fan geometry), we can record the interface response without interference from the coseismic fields, a great advantage as we attempt to measure very small interface response fields. Additionally, if we can record the fields near the targeted layers then the observed amplitudes will be greater. Geometries resembling the vertical seismic profile (VSP) geometry (see e.g., Sheriff and Geldart, 1995) offer a practical approach to accomplish this.

Time-lapse sand channel study

Having established some basic relations between subsurface geometry and seismoelectric interface response, and having established that survey geometry plays an important role in determining the success of a survey, we now apply these ideas and present one possible application of the seismoelectric method to a problem of interest. Figure 4.21 shows the basic survey layout. We are targeting a sand channel at 30 m depth, within a clayey soil background. Material

Table 4.3: Physical properties of materials in time-lapse models.

	V_p (m/s)	porosity (%)	hyd. perm. (m^2)	elec. cond. (S/m)	salinity (mol/L)
Sand t0	1859	30	10^{-11}	0.01	0.001
Sand t1	1859	30	10^{-11}	0.02	0.002
Sand t2	1859	30	10^{-11}	1.0	0.1
Clay	2296	10	10^{-16}	0.05	0.001

properties are shown in Table 4.3. The channel is 2 m thick, and 6 m wide (the same geometry as one of the cases in the last section, but with the materials swapped). A well is located 5 m away from the edge of the channel, and allows us to employ a vertical data-collection geometry, as shown in Figure 4.21. Data collected at one point in time (t0) are shown in Figure 4.22a, plotted in the usual way as for vertical seismic profiling (VSP) data, with the depth axis vertical, and the time axis horizontal. We can see the coseismic arrival (labeled "Coseismic"), and the coseismic field of the reflected P-wave ("reflection CS"). Also we can see the interface response created at the channel ("IR"). Coseismic field amplitude ranges from $\sim$0.2 to $\sim$2 mV, considerably lower than the coseismic fields in the previous section. This difference is due largely to the higher conductivity of the material in which the field is being measured, and also is due to the distance between the seismic source and the electrode receivers.

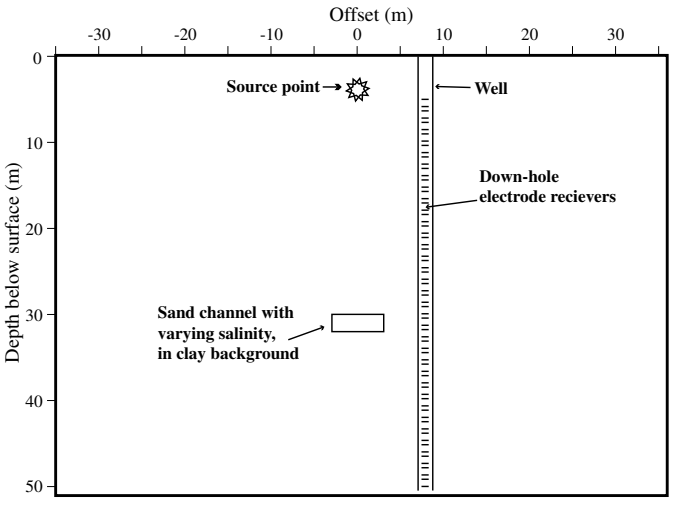

Figure 4.21: Schematic diagram of the model for the time-lapse synthetics. A sand channel (2 m thick and 6 m wide) lies at a depth of 30 m in a predominantly clay area. A well is 5 m away from the edge of the layer, and we use a down-hole electrode array to record shot gathers at three different points in time. The mechanical properties remain the same, but we simulate contamination by increasing the salinity of the pore water in the channel from 0.001 to 0.002 to 0.1 mol/L. application-vsp_schem [NR]

The down-hole survey affords the opportunity to conduct a time-lapse survey with very

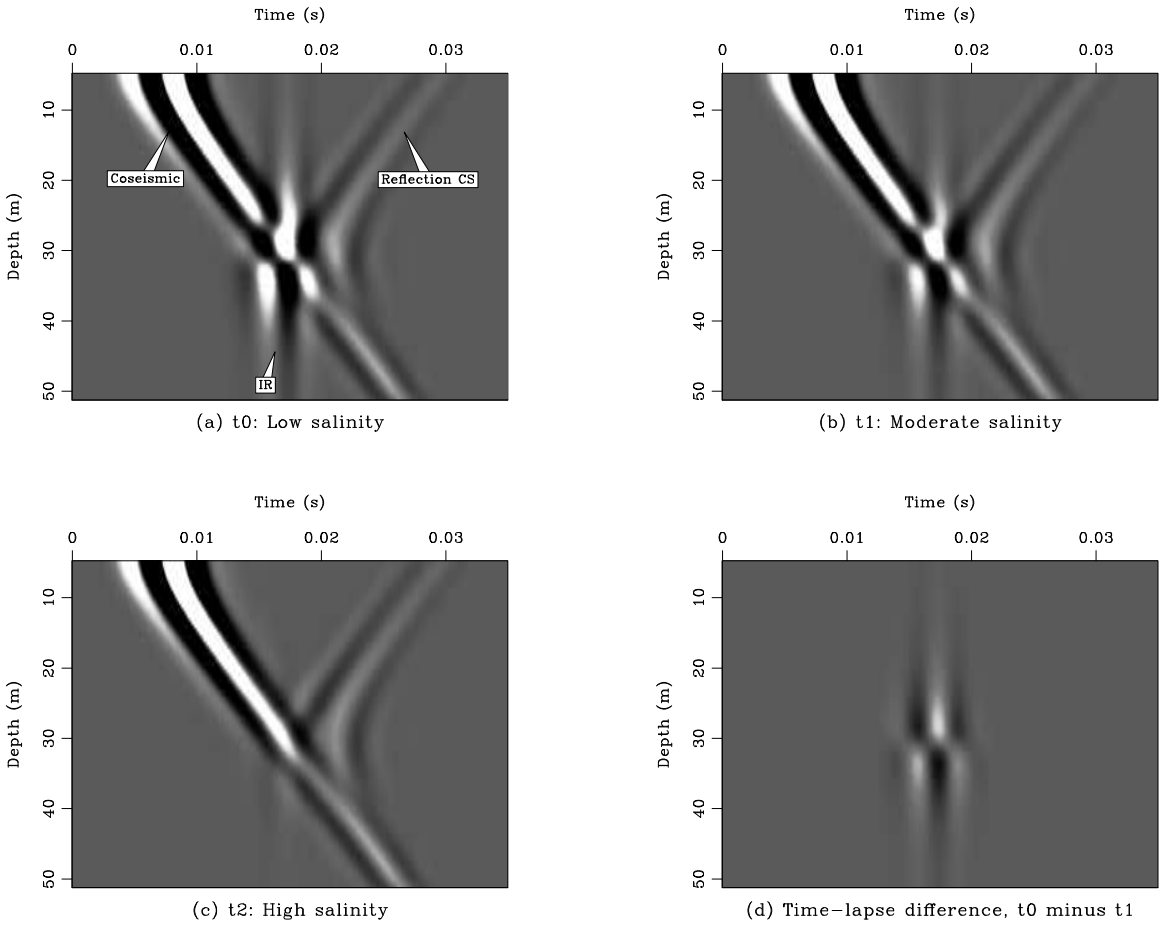

Figure 4.22: Synthetic seismoelectrograms for the time-lapse downhole study. a) Starting case (time t0) with salinity of the pore water in the sand channel 0.001 mol/L. b) At t1 the salinity has risen to 0.002, a small change that produces a noticeable change in the interface response. c) At t2 the salinity is much higher (major contamination), and the interface response has nearly disappeared. d) The time-lapse difference between t0 and t1, showing that the coseismic energy has subtracted out, leaving just the difference between the interface response arrivals. application-tl_vsp [ER,M]

similar recording conditions from one time to the next. A time-lapse survey offers the possibility of simply differencing two shot gathers from different times to remove the coseismic energy (assuming that it is the same between the two time steps). Figure 4.22b shows data representing a later time (t1), when the pore fluid in the sand channel has become somewhat contaminated (the salinity has risen from 0.001 to 0.002 mol/L). The interface response amplitude has fallen considerably, a change that is easily seen in the difference between the data collected at t0 (Figure 4.22a) and t1 (Figure 4.22b), plotted in Figure 4.22d. At a later point in time (t2), the contamination has worsened considerably, and the salinity of the channel pore water is now 0.1 mol/L. The shot gather shown in Figure 4.22c shows that the interface response amplitude is significantly decreased. These changes can be seen also in the plots of the interface response amplitude differences between t0 and t1 and t2 in Figure 4.23. The amplitude change between t0 and t2 is similar in scale to the coseismic fields, meaning that it would likely be easy to observe in field data. The amplitude change between t0 and t1 is smaller, but still within an order of magnitude of the coseismic amplitude.

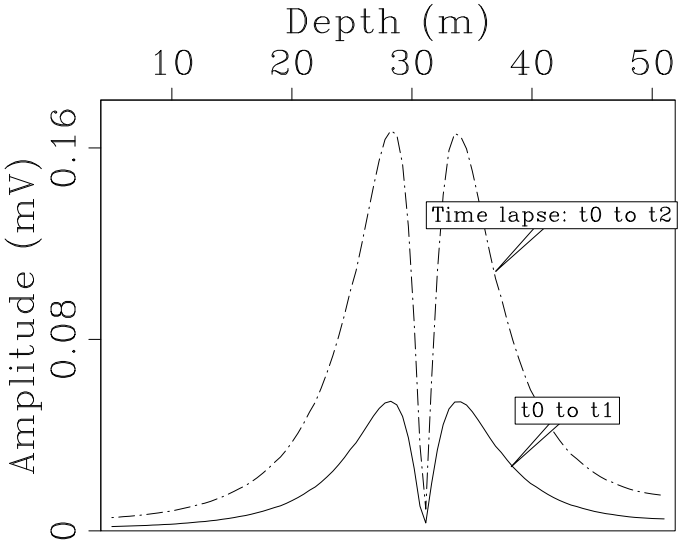

Figure 4.23: Graph of amplitude versus depth for the the interface response arrival in the time-lapse survey simulation. Note that these amplitude changes are within one order of magnitude of the absolute amplitude of the coseismic fields, meaning that they should be easily observed. application-vsp_amps [ER]

This example demonstrates two important points about the application of the seismoelectric method to real problems. First, the use of a down-hole recording geometry has allowed us to record the interface response energy closer to its source (the interface), resulting in a stronger signal and also providing some separation between the coseismic fields and the interface response. Additionally, the down-hole recording would likely provide quieter recording conditions, since the electrodes would be removed from electric fields at the earth's surface.

Second, the time-lapse study has allowed us to capitalize on the unique powers of the seismoelectric method. The salinity change has virtually zero effect on seismic wave propagation, so the coseismic energy subtracts out of the gathers. The target of this study (the 2 m by 6 m sand channel at 30 m depth in a clay background) would be difficult to image seismically, and nearly impossible to image with ground-penetrating radar (GPR) (e.g. Davis and Annan, 1989). The change in salinity is totally invisible seismically, and would likely be difficult to characterize even with a resistivity survey using the borehole for single-well electrical resistivity tomography (e.g. Oldenburg and Li, 1999).

This example also demonstrates an important limitation of the seismoelectric method. If we had only the data from the single shot and the down-hole electrodes, it would be very difficult to determine the lateral position and extent of the sand channel. The same is true for other geophysical surveys (e.g. a single-shot VSP survey), a limitation that can be addressed with a more thorough survey layout (more shots, and perhaps also surface electrode receivers).

DISCUSSION AND CONCLUSIONS

We have presented a real seismoelectric image of two dipping trenches, along with a complementary image produced through numerical simulation. These images confirm that the seismoelectric method can be used to image shallow thin layers, and that the observations agree with theoretical predictions. Our numerical algorithm permits us to simulate surveys of targets with arbitrary two-dimensional heterogeneity. We exploit this capability and establish that the seismoelectric method can image layers that are thin (much thinner than the one-quarter seismic wavelength that is typically taken as the limit of seismic resolution) and narrow (lateral extent much smaller than that of the first Fresnel zone).

Thus we claim that the seismoelectric method can provide useful new information about the subsurface. But we also must keep in mind that like all techniques, this method has its own limitations. The method will not work in all cases. In surface surveys of layers that are too shallow (a couple of meters) the interface response arrival will likely be obscured by the strong coseismic field, while for layers that are too deep the amplitude fall-off of a dipole with depth will make the interface response too weak to record. We can address these limitations

by adhering to certain guidelines, however:

- The seismoelectric method will not work in all cases, and will not surpass existing methods in many cases. It can be used to image small thin layers (aquitards, faults, fracture zones, etc.), and can "see" fluid-chemistry changes that are invisible to other methods (e.g. salinity contrasts, pH changes). It is not the best approach to, for example, determine the depth to bedrock or the water table in a shallow basin.

- It is essential to use sufficient channels that data can be interpreted unambiguously, covering a sufficient offset range on each side of the source point. We find that 24 channels is sometimes adequate, 48 is preferable, and more would certainly be desirable.

- It is essential to use a sufficient number of source points, because (unlike seismic reflection) each seismoelectric shot gather contains information about only one location on a given interface. For a simple in-line geometry survey of a horizontally-layered subsurface, each shot gather contains information only about the locations directly beneath the source point. The relation is more complex for other subsurface geometries, but the need for many shot points holds.

- The use of creative survey geometries (beyond simple surface surveys) can mechanically separate signal from noise and can lead to a stronger recorded interface response signal. This will likely prove more valuable than simply adding more recording channels to a surface survey.

- As with most other methods, we must be sure to collect enough information to address the non-uniqueness of the data.

- As with most methods, time-lapse studies offer many advantages, including the possibility of subtracting out the strong coseismic noise.

In our synthetic examples, we have entirely neglected background electrical noise, and instead have discussed amplitudes only relative to the coseismic energy. While it would be much more valuable to be able to speak in quantitative terms, our results do not permit such interpretations. The amplitude of background noise can vary by an order-of-magnitude or more from

site to site. Electrode coupling has a huge impact on the recorded signal-to-noise ratio, but is difficult to quantify in a meaningful way. The parameters used to scale the modeled seismic sources are uncertain at best, and could vary by as much as a few orders-of-magnitude. The amplitudes can be compared to each other, but should not be thought of as absolute amplitudes. Thus our results serve to illustrate various qualitative concepts, but can not be taken as definite indications that the seismoelectric method is effective to a particular depth at every location. As with all other methods, the absolute depth of resolution will be found to vary greatly between field sites. Future field experimentation will provide better answers to these questions than numerical modeling can hope to.

ACKNOWLEDGMENTS

We are very grateful to those who made possible the field experiments carried out as part of this project: Jim and Carolyn Pride for the use of their property, Tom Burdette and Rufus Catchings for help with explosives, and Ashley Griffith and Rob Sanders for field assistance. In addition, we are greatly indebted to Chunling Wu (Stanford Tomography Project) for the use of her poroelastic modeling code. We are also very grateful to those whose advice and guidance made possible the finite-difference modeling presented: Jim Berryman, Adam Pidlisecky, Morgan Brown, Antoine Guitton, and Dave Alumbaugh. Biondo Biondi and Jerry Harris have provided valuable guidance throughout this project. Acknowledgment is made to the Donors of the American Chemical Society Petroleum Research Fund for support of this research. Additional funding has been provided by the Achievement Rewards for College Scientists Foundation, the Stanford School of Earth Sciences McGee Fund, the Geological Society of America Foundation, the American Association of Petroleum Geologists Grants-in-Aid program, and the sponsors of the Stanford Exploration Project.

Chapter 5

Conclusions and Discussion

RESEARCH CONCLUSIONS

This dissertation includes findings in many different areas of seismoelectric work. Some of these (e.g. analysis of the direct field and the Lorentz field in Chapter 2) are interesting from a scientific point of view, but are not of immediate value to a person setting out to conduct a seismoelectric survey. The goal of this research was to develop a protocol that one could follow to collect, process, and interpret seismoelectric data in a reliable and useful manner. Though it will surely change as further research provides new information, I present the following set of steps, and of points to be kept in mind, as my preferred protocol.

1. Consider the target carefully – if another method will work, then perhaps that other method should be used.
2. Design the survey with the following points in mind:
    - If at all possible, use a survey geometry with the sources away from the receivers (fan geometry, down-hole, etc).
    - The number of recording channels and receiver spacing must be such that co-seismic energy is not aliased, and that signal/noise separation may be effectively carried out. I consider 48 channels to be a minimum, though 24 can be sufficient.

- The number of shots, and shot spacing, must be such that the target is adequately illuminated. In contrast to multi-channel seismic, each shot illuminates only one location (the first Fresnel zone) on a given interface.
- Be sure to collect enough information that the seismoelectric data may be interpreted unambiguously.

3. If using a standard seismograph to record data, be sure to electrically isolate the instrument from the electrodes with transformers or pre-amplifiers. I used transformers, but pre-amps would most likely be superior as they can amplify signals while also accounting for the input impedance of the seismograph.

4. Source choice is, of course, very important and is also site- and survey-dependent. I found best results with sledgehammer for near offsets and with explosives for offsets longer than a few meters.

5. Apply pre-processing steps such as 60 Hz removal [following Butler and Russel (1993 and 2003)], and frequency filtering, to minimize noise.

6. Employ an appropriate signal/noise separation technique:

   - Prediction-error filters offer the most effective, but most difficult, option.
   - The linear radon transform provides a simpler, and sometimes equally effective, option.

7. The polarity of interface response events must be flipped such that the polarity of a given event is constant across each shot gather. For in-line geometry surveys of horizontal layers the polarity should be flipped at the source point; for other cases it is not so simple. This topic is explored in more detail in the next section.

8. (Optional) Mute remaining noise from each gather.

9. Each shot gather is stacked to produce one trace.

10. These traces are placed side-by-side to produce a seismoelectric image.

DIRECTIONS FOR FUTURE ELECTROKINETIC WORK

The task of developing the seismoelectric method for regular use is not complete. This dissertation represents important progress, but is only a first step. We can look at the development of seismic reflection surveys as an example. Exploration seismic surveys have been carried out over the last century, and the reflection method has seen regular use over the last seven decades. The method has advanced considerably throughout those 70 years, to the point where examples of data recorded during the early years appear so crude as to be nearly useless by our present-day standards. Advances in seismic sources, data recording equipment, and data processing methods have all played essential roles in this progress. In this section I speculate about the importance of developments in each of those three areas of seismoelectric work.

Source development will clearly play a role in seismoelectric method development. In particular, a vibrator source that does not create any electric fields would be a great benefit. Such a device would have to be mechanical, rather than electromagnetic. The use of metal parts might be unavoidable, but would have to be done such that the Lorentz field is avoided. (Simply insulating the vibrator from the soil might be sufficient; in addition the low velocity of vibrator parts might avoid such an effect altogether.)

Seismoelectric data recording is an area with great potential for improvement, both in terms of ease (or cost, in a production setting) and in terms of data quality. I have used transformers between each pair of electrodes and the seismograph. A data quality improvement would likely be achieved with pre-amplifiers. And further improvement could be gained with dedicated equipment, either a device similar to a seismograph but with the pre-amps built in, or an box containing the pre-amps that would be placed between the seismograph and the recording cable. In either case, the sometimes high impedance across each pair of electrodes would be reduced to a level better-suited to the recording device, leading to better data quality. Also, the use of dedicated hardware represents one possible simplification of data acquisition, leading to easier, quicker, surveys. Another major data acquisition advance would be the development of methods to measure electric fields in the earth without the need for grounded electrodes. Capacitive coupling offers one possibility that could lead toward this goal, but requires considerable technological development before it is a viable option for seismoelectric

surveys.

Data processing is perhaps the area of seismoelectrics most ripe for development. If the method is to be used in a production setting, data processing needs require considerably less user intervention than the approach that I used in making my images. In particular, the determination of the "flip line" (the line around which the polarity of the data is flipped) is probably the weakest part of my processing flow. Unfortunately, the determination of this line is not trivial in a case with unknown 2- or 3-dimensional subsurface heterogeneity. The interface response is created at the first Fresnel zone, and is approximately the field of an electric dipole located at the center of that Fresnel zone and oriented perpendicular to the interface. Thus without knowing the approximate geometry and/or visually identifying the flip points for each event, we can not manually define the flip lines for seismoelectric shot gathers, except for the simple case of an in-line survey (Figure 5.1a and b). Since we have established that it is best to avoid the in-line geometry, it is important to note that other geometries will lead to greater difficulty in assigning the flip point (Figure 5.1c and d). Even if we could manually define these flip lines, however, the approach would still be based on the faulty assumption that all of the energy in a given shot gather represents the a particular linear (perhaps vertical) swath of the subsurface, which is clearly not the case in Figure 5.1c and d. So we will need to consider a seismoelectric analog to seismic migration. Ideally this algorithm would, similar to wave-equation migration methods, possess the ability to migrate even previously-unseen energy throughout the image without user intervention and also take into account the issue of the polarity reversals of events. So rather than first assigning a flip line, then flipping polarity, and then stacking shot gathers, we would use an algorithm that would more accurately take into account all of these issues in the shot domain, and produce an image that correctly places all of the interface response energy. The development of this algorithm would be a major contribution to seismoelectric work.

This thesis has dealt entirely with seismic-to-electric conversions. However, the physics of the conversion is entirely reciprocal, so we can also consider the use of electric-to-seismic conversions as an survey method. In this case we would put an electric field into the earth, and record the resulting mechanical response with geophones. Electric fields in the earth cause fluid flow, which creates propagating seismic waves at interfaces. One clear advantage of this

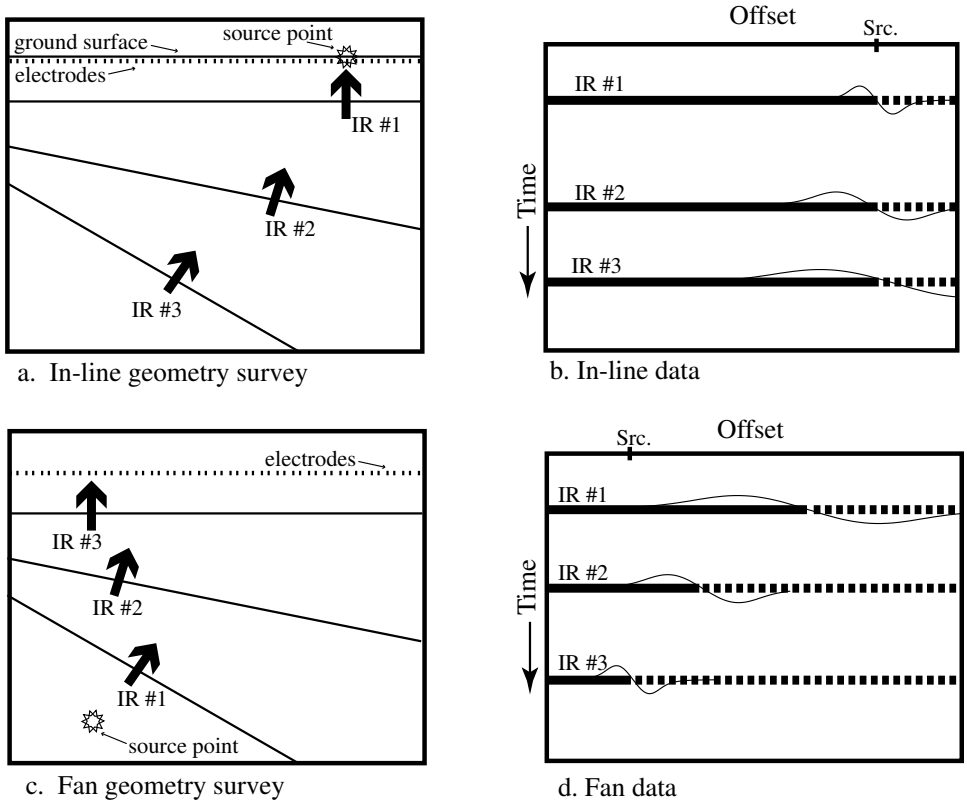

Figure 5.1: Schematic diagram illustrating the position of the polarity reversal (flip) point for in-line- and fan- geometry surveys of a region with three interfaces with various dips. a) In-line survey geometry, with source and receivers positioned along the ground surface. Bold arrows depict interface response dipoles. b) Seismoelectrogram for in-line survey, with arrivals from the three interfaces labeled. Thick solid lines are positive amplitude and thick dashed lines are negative amplitude. The very thin lines show the amplitude pattern for each arrival. Note that the amplitude pattern is wider for layers farther from the receivers. c) Fan-geometry survey of the same geometry. d) Seismoelectrogram, showing that the flip points do not line up with the source position in this case. All cartoons are drawn for uniform seismic velocity; lateral variations would introduce additional artifaces (c.f. Figures 4.4, 4.5, and 4.7). conclusion-migration [NR]

approach is that we can use any desired time series as the electrical source, so can overcome noise by using a very long time series (much like seismic vibrators). One possible problem with the electric-to-seismic method is that the geophones could record the source electric field, which could be stronger than the seismic waves created at interfaces, obscuring signal. Solid-state geophones (e.g. www.hydrophones.com/Design.pages/solid.state.html) offer a simple solution to this problem.

This dissertation represents progress toward the reliable use of the seismoelectric method. The many branches of seismoelectric work require further development, and hopefully this section will in time prove to have correctly identified some of the areas most ripe for this development.

Appendix A

Finite-difference modeling algorithm

Pride (1994) obtains a general set of equations that govern the coupled seismic and electromagnetic response of a porous material when electrokinetics is responsible for the coupling. Assuming an $e^{-i\omega t}$ time dependence of all fields and displacements, these equations are

$$-\omega^2\rho\mathbf{u} = -\nabla P_c + \nabla\cdot\tau^D + \omega^2\rho_f\mathbf{w} \tag{A.1}$$

$$\tau^D = G\left(\nabla\mathbf{u} + \nabla\mathbf{u}^T - \frac{2}{3}\nabla\cdot\mathbf{u}\,\mathbf{I}\right) \tag{A.2}$$

$$-\begin{bmatrix} P_c \\ p_f \end{bmatrix} = K_U\begin{bmatrix} 1 & B \\ B & B/\alpha \end{bmatrix}\begin{bmatrix} \nabla\cdot\mathbf{u} \\ \nabla\cdot\mathbf{w} \end{bmatrix} \tag{A.3}$$

$$\begin{bmatrix} -i\omega\mathbf{w} \\ \mathbf{J} \end{bmatrix} = \begin{bmatrix} k(\omega)/\eta_f & L(\omega) \\ L(\omega) & \sigma(\omega) \end{bmatrix}\begin{bmatrix} -\nabla p_f + \omega^2\rho_f\mathbf{u} \\ \mathbf{E} \end{bmatrix} \tag{A.4}$$

$$\nabla\times\mathbf{H} = -i\omega\epsilon\mathbf{E} + \mathbf{J} \tag{A.5}$$

$$\nabla\times\mathbf{E} = i\omega\mu\mathbf{H} \tag{A.6}$$

and are simply Biot's (1962) equations for the solid displacements $\mathbf{u}$ and filtration displacements $\mathbf{w}$ (the relative fluid-grain displacement), along with Maxwell's equations for the electric and magnetic fields $\mathbf{E}$ and $\mathbf{H}$. The seismoelectric coupling occurs in the transport laws of equation (A.4) where $\mathbf{J}$ is the electric-current density and $-i\omega\mathbf{w}$ the Darcy filtration velocity.

Table A.1: Variables and parameters used in equations.

symbol	meaning	units	symbol	meaning	units
$\mathbf{E}$	electric field	V/m	ω	frequency	Hz
$\mathbf{H}$	magnetic field	A/m	ρ	bulk density	kg/m^3
$\mathbf{u}$	grain displacement	m	ρ_f	fluid density	kg/m^3
$\mathbf{w}$	grain/fluid rel. disp.	m	σ	elec. cond.	S/m
P_C	confining pressure	Pa	p_f	fluid partial press.	Pa
τ^D	deviatoric stress tensor	Pa	ϵ	elec. permittivity	C^2/Nm^2
$\mathbf{J}$	current density	A/m^2	μ	mag. permeability	N/A^2
G	shear modulus	Pa	η_f	fluid viscosity	Pa s
K_U	undrained bulk modulus	Pa	k	hydraulic perm.	m^2
L	coupling coeff.	(C m)/(N s)	α	Biot Willis const.	–
$\mathbf{I}$	identity matrix	–	B	Skempton's coeff.	–
Φ	elect. potential	V	F	formation factor	–
ζ	zeta potential	V	ϕ	porosity	–

If the coupling coefficient L were set to zero then there would be complete decoupling between the poroelastic and electromagnetic response fields. Other terms include the confining pressure P_C, the shear modulus G, the electrical permittivity ϵ, the magnetic permeability μ, and the identity matrix $\mathbf{I}$. The deviatoric stress tensor τ^D is defined as $\tau^D = \tau + P_C\mathbf{I}$. Skempton's (1954) coefficient B represents the ratio of the fluid partial pressure p_f to the confining pressure P_C, under the condition that no fluid leaves the region of interest ($\nabla \cdot \mathbf{w} = 0$). The undrained bulk modulus K_U, also referred to as Gassmann's (1951) modulus, represents the bulk modulus of the closed system of the fluid-saturated grain matrix. These two variables, along with the Biot and Willis (1957) coefficient α, can be expressed as

$$\alpha = 1 - \frac{K}{K_s}, \tag{A.7}$$

$$B = \frac{\alpha}{\alpha + \phi(K/K_f - K/K_s)}, \tag{A.8}$$

$$K_U = \frac{K}{1 - B\alpha}. \tag{A.9}$$

All of the parameters and variables, along with their respective units of measurement, are shown in Table A.1.

Two types of seismoelectric coupling are present in equation (A.4). Seismic waves generate a force $-\nabla p_f + \omega^2 \rho_f \mathbf{u}$ that, in addition to driving a Darcy fluid filtration $(k/\eta_f)(-\nabla p_f + \omega^2 \rho_f \mathbf{u})$, also transports the diffuse charge of the double layer relative to the bound charge on the grain surfaces resulting in a "streaming" electric current $L(-\nabla p_f + \omega^2 \rho_f \mathbf{u})$. Such generation of an electric current from an applied fluid-pressure gradient is known as "electrofiltration". Conversely, when an applied electric field $\mathbf{E}$ acts on a porous material, in addition to driving a conduction current given by $\sigma \mathbf{E}$, it also acts as a body force on the excess charge of the diffuse double layer resulting in a net fluid filtration given by $L\mathbf{E}$. Such generation of a fluid filtration from an electric field is known as "electro-osmosis".

Pride (1994) obtains analytic expressions for the frequency dependence of the three porous-media transport coefficients: permeability $k(\omega)$, electrokinetic-coupling coefficient $L(\omega)$, and electric conductivity $\sigma(\omega)$. The important relaxation in these coefficients is associated with the onset of viscous boundary layers in the pores; i.e., above a certain transition frequency ω_t, inertial forces in the pores begin to dominate the viscous shearing except in a small boundary layer near the grain surfaces. The creation of such viscous boundary layers changes the amplitude and phase of the induced transport. The transition frequency is given by $\omega_t = \eta_f/(\rho_f F k_o)$ where η_f is the fluid viscosity, ρ_f is the fluid density, F is the electrical formation factor and k_o is steady flow permeability (Pride, 1994). For typical rocks and soils, one has $\omega_t/(2\pi) > 10^5$ Hz which lies far above the seismic bandwidth of interest. As such, we neglect all relaxation in the transport coefficients, which allows Pride's (1994) results to be written $k(\omega) = k_o$, $L(\omega) = \varepsilon_f \zeta/(\eta_f F)$ and $\sigma(\omega) = \sigma_f/F$. The zeta potential ζ describes the strength of the electric double layer at the grain fluid boundary. In this case ($\omega \ll \omega_t$), only two pore-space topology parameters k_o and F must be specified to model the seismoelectric transport. Relaxation in the elastic moduli associated with fine-scale fluid flow (e.g., as modeled by Pride et al., 2004) will also be neglected.

Not every term within the governing equations (A.1)–(A.6) need be included in the numerical modeling. For example, the dielectric-displacement current $-i\omega\varepsilon\mathbf{E}$ can be neglected relative to the conduction current $\sigma\mathbf{E}$ since, throughout the seismic band and for materials of interest, $\omega\varepsilon/\sigma < 10^{-4}$.

Further, for our applications in which seismic waves are generating electric fields, one can

neglect the electro-osmotic feedback by which the generated electric field acts on the electric double layers in the pores retarding fluid flow. The amplitude of this feedback effect can be estimated by considering the electric field generated in a compressional wave propagating through a homogeneous material. In this case, the charge accumulating in the peaks and troughs of the wave generates a conduction current that just balances the streaming current so that $\mathbf{J} = 0$. As such, equation (A.4) gives that $\mathbf{E} = -(L/\sigma)(-\nabla p_f + \omega^2 \rho_f \mathbf{u})$ which allows the Darcy law to be written

$$-i\omega\mathbf{w} = \frac{k}{\eta_f}\left(1 - \frac{\eta_f L^2}{k\sigma}\right)(-\nabla p_f + \omega^2 \rho_f \mathbf{u}).$$

The dimensionless correction term in the parentheses represents the electro-osmotic feedback and for the materials of interest will typically satisfy $\eta_f L^2/(k\sigma) < 10^{-5}$. So the term $L\mathbf{E}$ can safely be neglected from the Darcy law.

Last, our modeled region will typically be far smaller than a kilometer; indeed, smaller than even 100 m. The electromagnetic skin depth δ associated with the inductive electromagnetic diffusion is found to be $\delta = 1/\sqrt{\omega\mu\sigma}$ by combining equations (A.5) and (A.6) after neglecting the dielectric displacement (Landau and Lifshitz, 1984). Across the seismic band, and for the materials of interest to us, one obtains that $\delta > 1$ km. As such, our modeled regions are contained within the electrostatic nearfield of the electromagnetic disturbances so that the effects of induction can be entirely neglected. This means that $\nabla \times \mathbf{E} = 0$ throughout the modeled region, and thus $\mathbf{E} = -\nabla\Phi$, where Φ is the electric potential.

We are finally in a position to write the governing equations in the manner that they will be numerically solved. Using $\mathbf{q} = -i\omega\mathbf{w}$ to represent the Darcy filtration velocity, $\mathbf{v} = -i\omega\mathbf{u}$ to represent the solid's particle velocity, and $\tau = \tau^D - P_c\mathbf{I}$ to represent the total bulk stress tensor, we have the time-domain poroelastic laws

$$\rho\frac{\partial \mathbf{v}}{\partial t} + \rho_f\frac{\partial \mathbf{q}}{\partial t} = \nabla\cdot\tau \tag{A.10}$$

$$\rho_f\frac{\partial \mathbf{v}}{\partial t} = -\frac{\eta_f}{k_o}\mathbf{q} - \nabla p_f \tag{A.11}$$

$$\frac{\partial \tau}{\partial t} = \left[\lambda_U \nabla\cdot\mathbf{v} + K_U B\nabla\cdot\mathbf{q}\right]\mathbf{I} + G\left[\nabla\mathbf{v} + (\nabla\mathbf{v})^T\right] \tag{A.12}$$

$$\frac{\partial p_f}{\partial t} = -K_U \left[B\nabla\cdot\mathbf{v} + \frac{B}{\alpha}\nabla\cdot\mathbf{q} \right] \tag{A.13}$$

that are completely decoupled from the electrical response. Here, $\lambda_U = K_U - 2G/3$ is the undrained Lamé modulus. A numerical solution of these equations is obtained using explicit time-stepping finite-difference approximations. We use a 2D code written by Chunling Wu (pers. comm., 2003), following Zhang (1999), that makes 2nd-order updates in time, and that determines the space derivatives using the Fourier transform (the so-called "pseudo-spectral" technique). At the limits of the zone being studied, absorbing boundary conditions are applied.

To model the effect of an explosion at the source point $\mathbf{r}_s$, we add to the above stress tensor an additional isotropic stress tensor τ_s having the form

$$\tau_s(\mathbf{r},t) = m(t)\mathbf{I}\,\delta(\mathbf{r}-\mathbf{r}_s). \tag{A.14}$$

The scalar moment $m(t)$ of such an explosion has been modeled by Haartsen and Pride (1997) as $m(t) = M_o s(t)$ where $s(t)$ is any preferred dimensionless source wavelet function, and the seismic moment release M_o (units of energy) is modeled as

$$M_o = \sqrt{\epsilon m_o^4 \mathcal{E} V_o K_U}. \tag{A.15}$$

Here, ϵ is a dimensionless number characterizing what fraction of the chemical energy $m_o\mathcal{E}$ is actually converted into seismic wave energy where m_o is mass (kg) of dynamite exploded and $\mathcal{E} \approx 10^6$ J/kg is a common handbook value for chemical explosive. Estimating ϵ is difficult, but taking $\epsilon \approx 10^{-6}$ seems to produce reasonable results. The source volume V_o contains the zone in which the deformation was non-linear. For our sources in which $m_o = 0.45$ kg of explosive was detonated in an unsaturated near-surface sand having $K_U = 2\times 10^8$ Pa, with a source region having a radius of 0.10 m, one obtains $M_o \approx 200$ J. In modeling a Dirac delta function on a finite-difference grid having discretization lengths Δ_i in each of the i directions, one has, in 2D, $\delta(\mathbf{r}-\mathbf{r}_s) = \delta(x-x_s)\delta(z-z_s) \approx 1/(\Delta_x\Delta_z)$ at the point where the source is detonated, and zero elsewhere. In 3D, one has $\delta(\mathbf{r}-\mathbf{r}_s) = \delta(x-x_s)\delta(y-y_s)\delta(z-z_s) \approx 1/(\Delta_x\Delta_y\Delta_z)$ at the source point, and zero elsewhere.

To model the effect of a hammer hitting a metal plate on the surface, we impose a plate

(particle) velocity v_z at the point of impact. For a hammer of mass M_h impacting a metal plate of mass M_p, conservation of momentum requires that the imposed plate velocity v_z is related to the hammer velocity v_h as $v_z = (M_h/(M_p + M_h)v_h$. A hammer accelerated at $3g$ from a height h achieves a velocity of $v_h = \sqrt{6gh}$. For $M_h/M_p \approx 1$ and $h \approx 3$ m, one obtains that the imposed plate velocity is $v_z \approx 13$ m/s. We multiply this amplitude by the dimensionless order-one wavelet $s(t)$ to model the effect of a hammer source.

To obtain the electric fields generated by the mechanical response, we take the divergence of equation (A.5), and use the simplifications discussed above, to obtain the Poisson problem

$$\nabla \cdot (\sigma \nabla \Phi) = \nabla \cdot \left(\frac{\eta_f L}{k_o} \mathbf{q} \right). \tag{A.16}$$

Using the Darcy velocity $\mathbf{q}$ known at each time step after solution of the above poroelastic laws, the Poisson problem is solved using 2nd-order finite-difference approximations. Following Claerbout (1999), we can express Equation (A.16) as the pair of fitting goals

$$\mathbf{L}\Phi - \mathbf{d} \approx \mathbf{0} \tag{A.17}$$

$$\mathbf{A}\Phi \approx \mathbf{0} \tag{A.18}$$

where $\mathbf{L}$ is the operator $\nabla \cdot \sigma \nabla$, $\mathbf{d}$ is the "data", in this case the product $\nabla \cdot \left(\frac{\eta_f L}{k_o} \mathbf{q} \right)$. We solve this equation using the conjugate-direction method. Because the problem is very poorly conditioned, we use the helix derivative ($\mathbf{A}^{-1}$) as a pre-conditioning operator, and also as a weighting operator. Thus we actually try to minimize the fitting goals

$$\mathbf{A}^{-1}\mathbf{L}\mathbf{A}^{-1}\mathbf{p} - \mathbf{A}^{-1}\mathbf{d} \approx \mathbf{0} \tag{A.19}$$

$$\mathbf{I}\mathbf{p} \approx \mathbf{0} \tag{A.20}$$

where $\mathbf{p} = \mathbf{A}^{-1}\Phi$. The helix derivative is well-suited to this case, because it is similar to the Laplacian operator $\nabla^2 = \nabla \cdot \nabla$. We find that this pre-conditioning reduces the necessary number of iterations by at least one order-of-magnitude.

We solve this system of equations independently for each time step in the poroelastic solution. The electric fields are then determined using 2nd-order finite-difference approximations

of $\mathbf{E} = -\nabla\Phi$. On the free surface, we require the normal (vertical) component of the electric field to be zero $\partial\Phi/\partial z(z=0) = 0$ (Neumann conditions). On the other three sides of the model, we add an additional layer of at least 50 pixels with a variable grid spacing, in order to push those boundaries far from the modeled region. Following Anderson and Woessner (1992), we increase the grid spacing by a factor of 1.3 from one pixel to the next, up to a maximum factor of 20 times the original grid spacing. The result is that the boundaries are at least as far from the modeled region as the modeled region is wide. As is commonly done in such cases (e.g. Haber and Ascher, 2001), we apply Neumann conditions to these far-removed boundaries.

We test the code that numerically solves Poisson's equation (Equation (A.16)) by comparing results for a simple dipole with the analytical solution for the same case. We numerically model a vertical dipole current source located at r_s by adding to the current density $\mathbf{J}$ a directed point source current $J_z = Id\delta(r - r_s)$ where I is the current, d is the dipole length, and δ is the Dirac delta function. We distribute the Dirac delta function over a 5 by 5 pixel area, and so use $\delta(r - r_s) = \delta(z - z_s)\delta(x - x_s) = 1/(25dxdz)$, where dx and dz are the grid spacings in the x and z directions respectively. The corresponding 2D analytical solution is

$$\Phi(x,z) \;=\; \frac{Id}{2\pi\sigma}\left[\frac{z-z_s}{(x-x_s)^2+(z-z_s)^2} - \frac{z+z_s}{(x-x_s)^2+(z+z_s)^2}\right], \tag{A.21}$$

including the free surface at the top of the model space (at $z = 0$). The model space is 512 by 512 pixels, with a pixel width of 0.1 m. A layer of 50 pixels with variable grid spacing pads the sides and bottom of the model space. Figure A.1 shows a comparison between the two solutions along several slices across the model space. The fit is good for slices near to the dipole, but worse near the edges of the model space. Thus we concentrate on the relative amplitudes calculated from modeling results. The exact amplitudes are not meaningful, as demonstrated by this test. Our modeling approach was not designed to produce exactly correct amplitudes, as numerical modeling can never hope to include the myriad of factors (principally variable source and receiver coupling) that impact signal strength measured in the field. Our goal was rather to produce a modeling algorithm in a reasonable period of time that would help us to understand some basic phenomena and basic patterns, and in that we have succeeded.

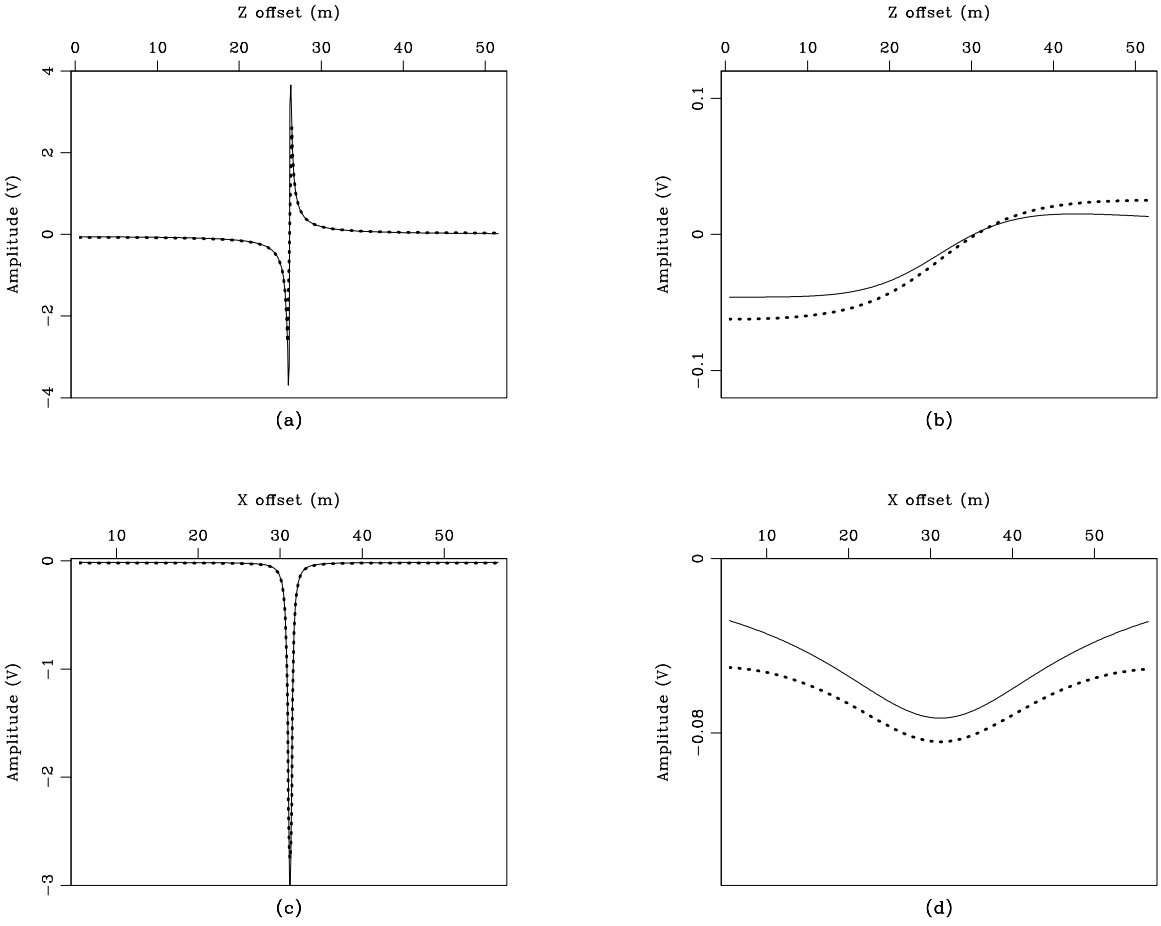

Figure A.1: Plots of the analytical solution (solid line) and the numerical solution (dotted line) along several tracks across the model space. a) A slice along the axis of the dipole shows good fit. b) A slice parallel to the axis of the dipole, but 15 m away from it, shows that the numerical model produces the correct trends, but not the exact amplitude, of the analytical solution. c) A slice perpendicular to the dipole axis, one pixel from it, showing good fit. d) A slice perpendicular to the dipole axis 15 m above it (toward the free surface) shows the correct trends, but some error in the exact amplitude. Note that the vertical scale varies between plots, and that this algorithm test is a worst-case situation. model_app-testplot [CR]

This test must be taken as a worst-case-scenario for the accuracy of the Poisson solving algorithm, because the current distribution is made up of just two isolated points, rather than the more smoothly distributed currents that we solve for in the seismoelectric simulations. In this test case the residual ($\mathbf{L}\Phi - \mathbf{d}$) is dominated by the very strong energy at the dipole itself. The edge regions are neglected because the energy is several orders of magnitude lower there. For this test case, the problem just described could easily be resolved by using a weighting mask on the residual, but we do not use one in our modeling algorithm since the seismoelectric simulations do not warrant such a mask.

The calculations required for each seismoelectric simulation are very costly. For the case of a 1024 by 1024 pixel grid (as is used for most of the simulations presented here), solution of the poroelastic equations for 3000 time steps, with a time increment of 0.01 s (as required for stability), requires roughly 8 hours of computation on one processor. While the poroelastic calculation is difficult to parallelize, the Poisson calculation can simply be split into different time blocks as needed. Because we neglect electro-osmotic feedback, we can independently solve for the electric potential at each time step, and we no longer need to be concerned with stability as we choose the time increment. Using a time increment of 0.1 ms (300 time steps for the case mentioned above), we can solve the Poisson problem in about five hours on 32 processors, using 500 conjugate-direction iterations to solve each Poisson step.

Appendix B

The EMvibe seismic source

INTRODUCTION

The choice of an appropriate seismic source is vital for any seismic or seismoelectric survey, but budgetary constraints frequently limit one's options. For shallow surveys, a sledgehammer is often the preferred option. It is effective and economical, but the repeatability from one strike to the next can be far from perfect. And while hammer stacking improves the signal-to-noise ratio, it degrades the resulting waveform because strike-to-strike variations lead to the partial cancellation of the higher frequencies. Moreover, successive hammer impacts deform the area of impact, precluding exact source repeatability and possibly damaging the subject of study (asphalt, etc). Vibrator sources (Anstey, 1991) address many of these shortcomings, but are generally too expensive to consider for shallow seismic surveys. I have developed an inexpensive electromagnetic vibrator source, called the EMvibe, that can produce any desired seismic time series. Sweeps or pulses may be stacked cleanly, resulting in a high-frequency source wavelet. The EMvibe can be used without damaging the site, and with little or no permanent plastic deformation of the study area. It does not replace the sledgehammer, but offers an alternative that is well-suited to certain applications such as high-resolution reflection, or Continuous Surface Wave (CSW) method (Matthews et al., 1996). Field experimentation demonstrates that the EMvibe is not well-suited to seismoelectric work since it produces a significant electric field of its own.

The EMvibe is a highly-repeatable seismic source that can be built for only about $1000. In order to create an effective and economical vibratory source in a timely manner, I utilized a combination of off-the-shelf electronics and simple-to-machine mechanical parts. Field data demonstrate the utility of the source, and allow comparison with sledgehammer stacking results.

VIBRATOR DESIGN

The EMvibe consists of an electromagnetic transducer mounted in a rigid framework that transfers vibrations to the earth. The first two parts of this section describe these two principal parts of the EMvibe, and the third part describes the signal generation and production electronics.

Transducer

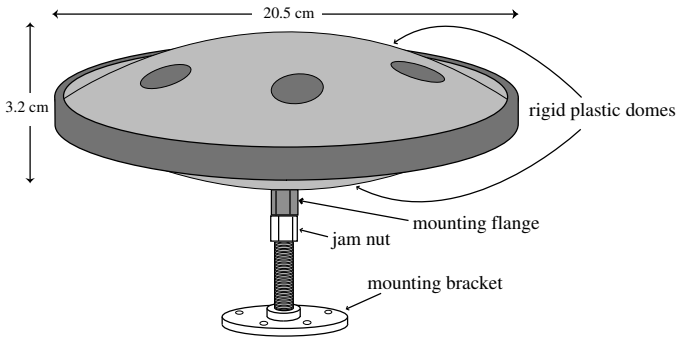

Figure B.1: Diagram of transducer used in the EMvibe. A magnet and an electric coil are attached to the inside of the two plastic domes, such that a current in the coil causes relative motion between the domes (similar to a standard audio speaker). vibe-vibe_transducer [NR]

The heart of the EMvibe is an off-the-shelf audio device produced by Clark Synthesis of Littleton, CO (www.clarksynthesis.com). It is termed a "tactile transducer" and is used to shake physical objects with a desired broadband, time-domain, signal. Vibration is produced by a coil of wire and a strong magnet, much like a standard audio speaker, but instead of a paper cone designed for the impedance of air, the device has two stiff plastic domes which are designed to match the impedance of solid objects. With the magnet attached inside one dome, and the coil attached inside the other, the tactile transducer vibrates when an alternating current is applied. Because the magnet is sufficiently strong and massive, the device vibrates

objects to which it is bolted. It is designed for use in home theater seating, theme park rides, and military vehicle simulators, and it offers the power necessary to produce a vibratory signal in the earth.

The Clark Synthesis model TST-429 tactile transducer employs a 567 g (20 oz) neodymium magnet, and offers an even frequency response over the range 5 to 800 Hz according to the product specifications, although a response curve is not provided. It is designed to be powered at a continuous level of 135 watts, and a peak power of 400 W. The device measures 20.5 cm in diameter, and is 3.2 cm thick (see Figure B.1). It is mounted to objects by way of the mounting flange which is affixed to one of the domes. Because the flange is part of the dome that is attached to the coil, the 567 g magnet on the opposite dome acts as the reaction mass for the vibrator device. Although this is not a very large mass relative to other seismic vibrators, I find it to be adequate for producing a seismic signal measurable at 10 or 20 m offset.

Framework

Figure B.2 shows the framework which houses the tactile transducer and conducts its vibrations to the soil. It is a rigid structure of machined aluminum and Delrin plastic (made from an acetal homopolymer resin produced by DuPont). These materials are both very rigid, and they can be readily obtained and are easy to work with. Starting with raw stock and very minimal machine shop experience, I produced the needed parts with about a half-week of work. The transducer is designed to be hung beneath its mounting surface, so it is attached to the 4.6 cm-thick Delrin top plate as shown in Figure B.2. The top plate is supported by six 2.3 cm-diameter, 13 cm-long, aluminum posts. These posts transfer the energy to the 2.3 cm-thick Delrin base plate, which is resting on the soil. The parts are bolted together with standard 6.3 cm-long steel bolts which pass through the top and base plates and thread into the ends of the aluminum posts. A magnetically-shielded vertical 40-Hz geophone on the baseplate provides data on the actual vibrator motion.

In order to improve coupling, six 7.5 cm spikes (removed from unwanted geophones) extend from the bottom of the baseplate. These spikes are easily removed for vibrator use on rock or other hard surfaces. In addition, a 2.5 cm-diameter pipe extends upward from a flange

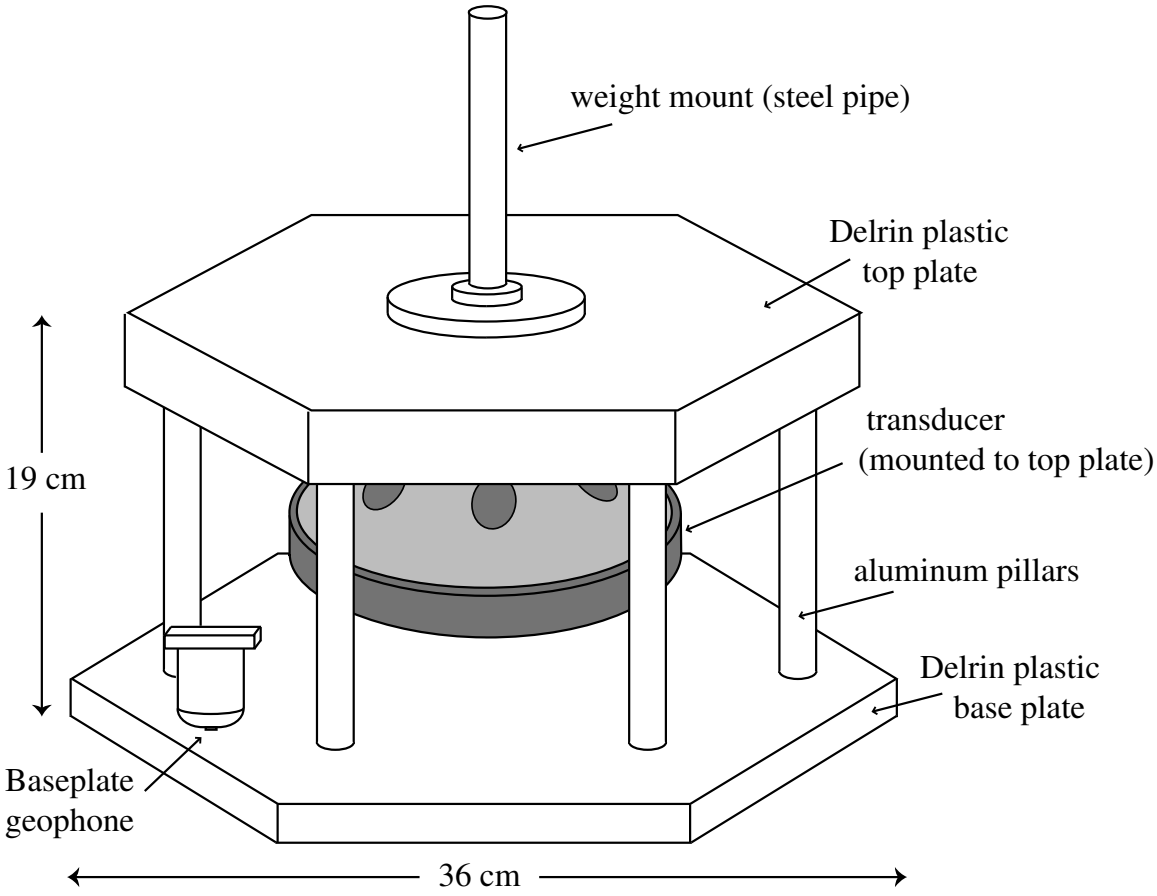

Figure B.2: Sketch of vibrator framework, with essential structural parts labeled. The transducer vibrations are conducted to the earth by the rigid assembly. vibe-vibe_unit [NR]

on the top plate, allowing weights to be stacked on top of the EMvibe. I use buckets of cement, with holes in the center to permit the weight support pipe to pass through, though any weight that fits snugly over the pipe is equally functional.

Signal generation and amplification

I create the source signal (described in the next section) on a field laptop computer, and output it via a Sonica (brand) M-audio 24-bit USB sound device (www.m-audio.com), though any higher-quality sound device would suffice. The device produces a high-quality but low-power signal which passes through a small pre-amplifier and then to a 450 watt-per-channel rack-mount two-channel power amplifier, intended for musical performances. The amplifier is designed for transportable durability, and so is well suited to field use. It offers high power and good signal quality, but requires 120-volt AC power. Car stereo amplifiers offer a 12-volt battery alternative, but large amps require enough power that auxiliary AC power would be required to keep the battery charged during a day of use. Though a limitation, the need for AC power can be easily accommodated with a generator or extension cords at most field sites.

FIELD DATA COMPARISON

I employ two different types of source waveform with the EMvibe. Because vibratory sources permit the use of long time series, it is common and sensible to use frequency sweeps (Anstey, 1991). Frequency sweeps (and other input time series) offer signal-to-noise improvements proportional to $T^{1/2}$, where T is the duration of the time series. Because small vibratory sources also offer near-perfect repeatability (the small-magnitude vibrations do not deform the local soil properties, and the device can reliably produce the same exact signal again and again), the use of stacked pulse signals is also an effective option. In this case, the signal-to-noise ratio improves as $N^{1/2}$, where N is the number of stacked pulses. While each pulse is not very strong, N can be very large with minimal effort. In this section I present a comparison between results from sweeps and pulses and sledgehammer stacking.

Linear sweep signals

The linear sweep is the simplest vibrator sweep and is generally quite effective. A linear sweep from frequency f_{min} to f_{max} is easily produced with the simple algorithm

$$f(t) = f_{min} + \frac{(f_{max} - f_{min})\, t}{2} \tag{B.1}$$

where $f(t)$ is frequency as a function of time t. The primary disadvantage of the linear sweep is that it does not take into account the vibrator or earth responses, and so it may result in an uneven spectrum and survey inefficiency (Pritchett, 1994). I record data with a 24-channel Geometrics Geode seismograph offering 64,000 samples per record, and so can record for as long as 32 s with a 0.5 ms sample interval and can therefore use up to a 30-second sweep. Because the device is intended for academic rather than exploration use, the slight inefficiency of the long linear sweep (the long sweep leads to slower data collection) does not present a major problem and I can simply stack more sweeps to enhance any weaker frequencies. After testing various sweeps, I find that 30-second sweeps from 50 to 650 Hz, with a half-second taper at each end, are quite effective.

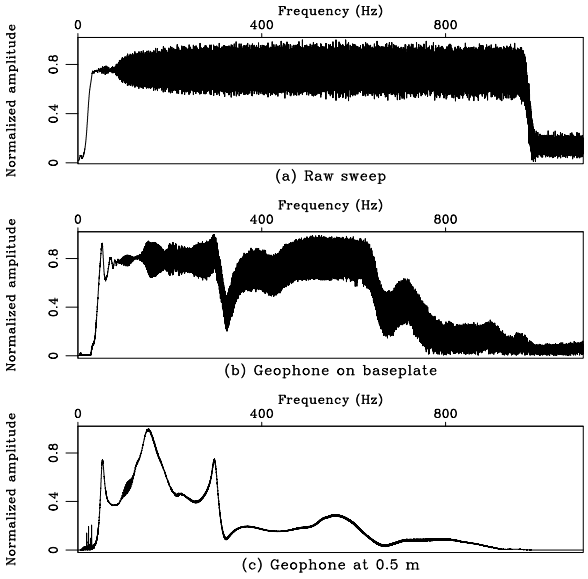

Figure B.3: Comparison of normalized frequency spectra for a) the raw sweep, b) vertical base plate velocity, as measured by the 40-Hz vertical geophone on the plate, and c) vertical particle velocity at 0.5 m, as recorded by a geophone at that position. vibe-plate_spec [ER,M]

Figure B.3a shows the frequency spectrum of a raw sweep (1 to 1000 Hz), essentially flat from about 25 to 975 Hz (the half-second taper at each end of the sweep accounts for the

bulk of the “missing” 25 Hz at each end of the sweep). The actual frequency spectrum of the resulting vibrations (as recorded by the geophone on the baseplate) is shown in Figure B.3b. This is the frequency response of the EMvibe, and shows a fairly flat response from 50 to 625 Hz, with the exception of the obvious notch at 325 Hz. Another notch at 675 Hz is within the down-slope of the frequency response and marks the high end of the useful frequencies. A geophone located ∼0.5 m from the EMvibe (Figure B.3c) shows that the higher frequencies do not efficiently couple into the earth and/or that they attenuate quickly. Figure B.3 clearly shows that the EMvibe is most effective in the range 50 to 650 Hz, so I employ that frequency band for field surveys.

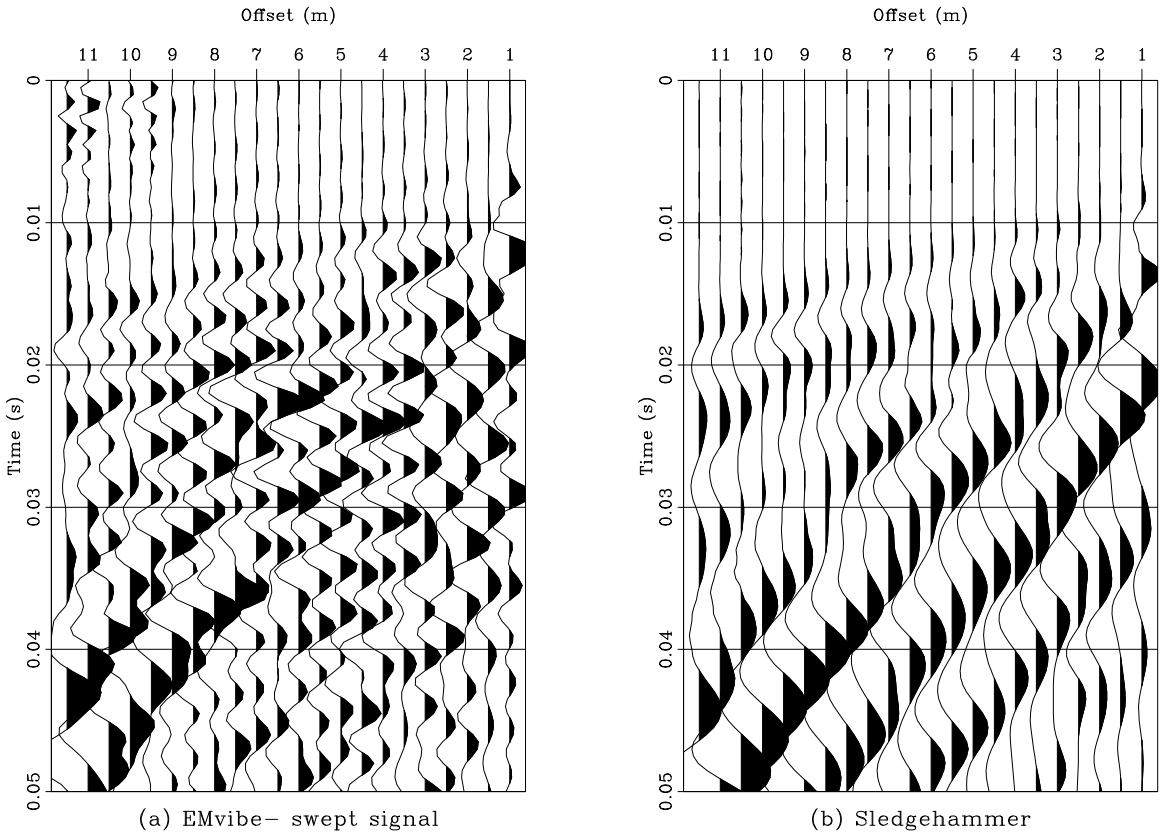

Figure B.4: Comparison between a) EMvibe results from stacking ten 30-second sweeps (5 to 650 Hz) and b) stacking ten hammer strikes. Data were recorded with 40-Hz vertical geophones spaced at half-meter intervals. Data are displayed with a 100 to 600 Hz bandpass filter, and automatic gain control (centered 75-sample window). vibe-new_wig_sweep_comp [CR,M]

Vibrator data resulting from sweeps must be cross-correlated with a pilot trace to compress the source time series to (ideally) a spike before the data can be interpreted. Comparison of correlation results using, respectively, the raw sweep, the baseplate motion data, and data from the geophone at 0.5 m, as the pilot trace show that the original sweep produces gathers that are the clearest and least reverberatory. Data are correlated using the raw sweep, and then stacked to produce each shot gather. Slight triggering variations are addressed with an auto-shift algorithm that uses cross-correlation to calculate shifts that are applied to each gather before stacking.

Figure B.4a shows a gather created by stacking ten vibrator sweeps (5 to 650 Hz), and Figure B.4b shows data collected by the same geophone array but with ten sledgehammer impacts as the source. Both are displayed after application of a minimum-phase 100 to 600 Hz bandpass filter, and automatic gain control (AGC) using a centered window of length 75 ms. The data were recorded by a 24-channel seismograph deployed with 40-Hz vertical geophones at half-meter intervals and the source 1 m from one end of the geophone line. The site is located in Redwood City, CA, on a small beach area adjacent to the San Francisco Bay. The subsurface geology consists of layers of sand, clay, and sea shell shoals. The data plots in Figure B.4 a and b show similar features, including ground roll and a refracted first arrival. The vibrator data show more high-frequency energy than the hammer data, and shows the first breaks more clearly as well. The sledgehammer data show more low-frequency groundroll energy. No clear reflections are visible in the data, nor have any been observed in other seismic data collected at this site.

Pulse signals

Short seismic pulses exploit the repeatability of the EMvibe and do not require long record lengths or correlation with a pilot trace. They can include any frequencies desired, and many copies can be stacked with little effort. Pulses are made up of a small number (one, two, five, etc.) of cycles of a sine wave of a given frequency (in this case, between 100 and 800 Hz). After testing various numbers of cycles of various frequencies, a pulse composed of two cycles of a 300 Hz sine wave was deemed to be the best option for the EMvibe in the chosen

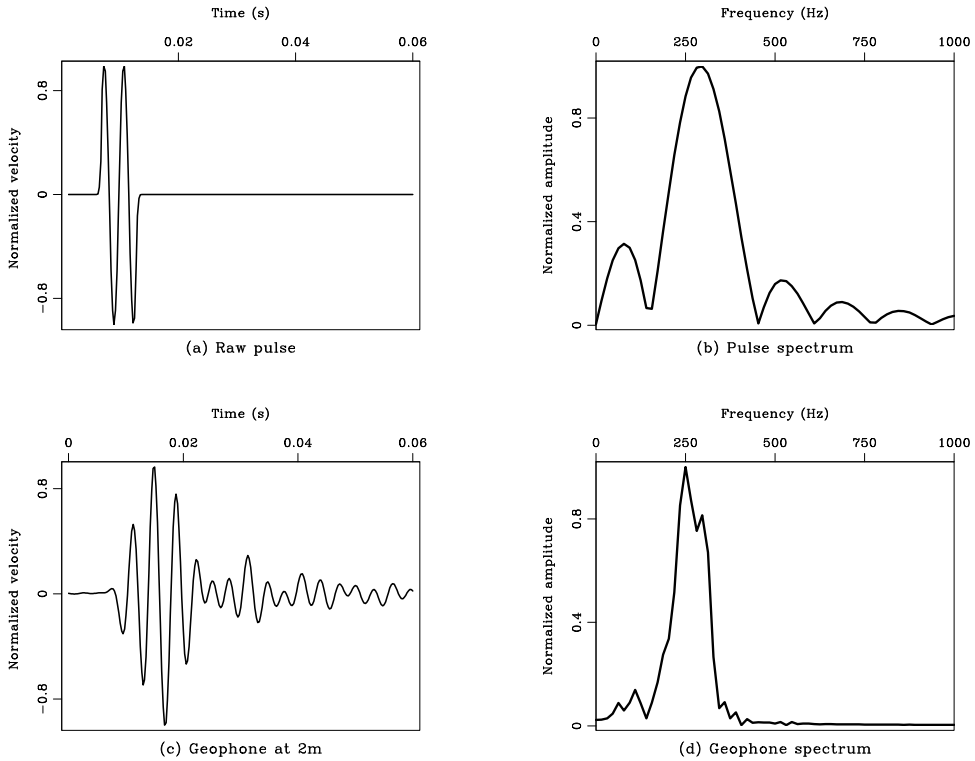

Figure B.5: a) Raw pulse used for data shown in Figure B.6a (2 cycles of a 300 Hz sine wave, tapered at the ends). b) Spectrum of the raw pulse. c) Data from vertical geophone at 2 m, result of stacking 100 pulses. d) Frequency spectrum of 0.0 to 0.04 s portion of trace shown in part c). Note that higher frequency portion of the original pulse has been lost, but that the main lobe remains. vibe-pulse [ER,M]

test setting. Figure B.5a shows this pulse, with the frequency spectrum in Figure B.5b. The ends of the pulse are tapered with an exponential function to avoid a sharp-onset signal going to the amplifier and vibrator.

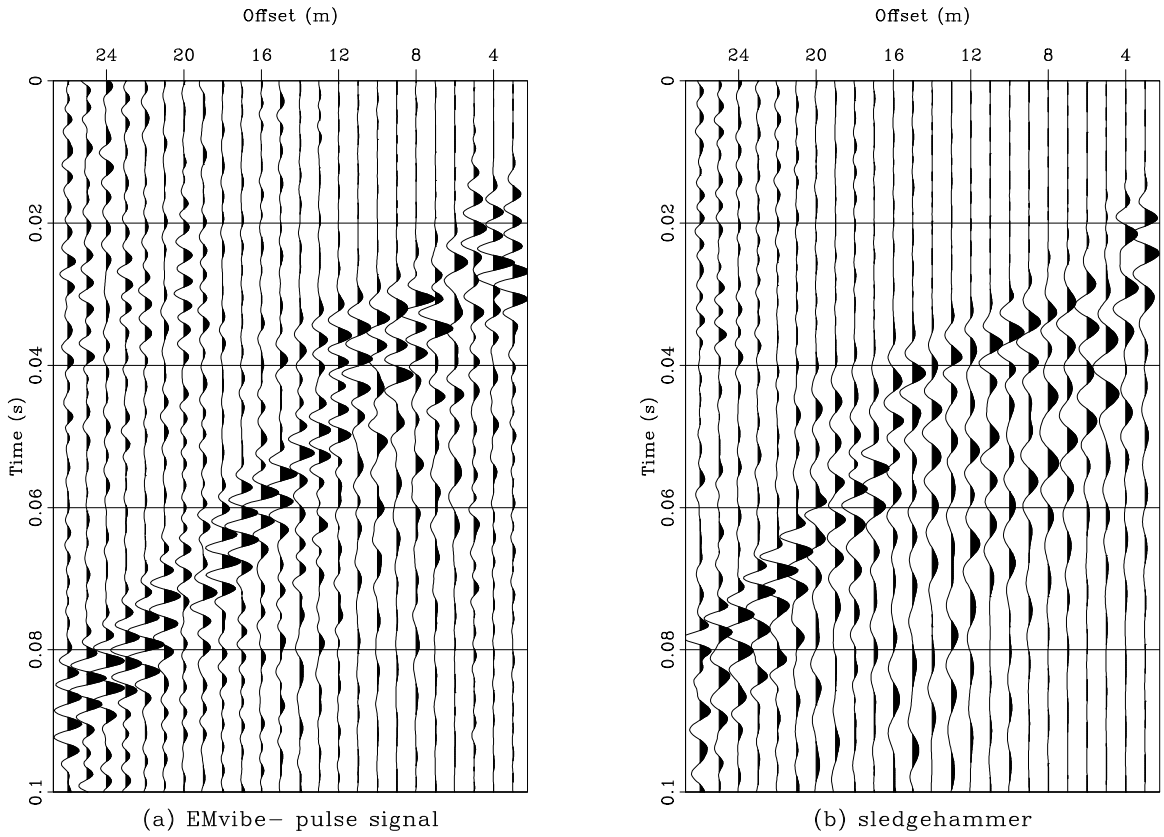

Figure B.6: Comparison between a) EMvibe results from stacking 900 pulses (described in the text) and b) stacking five hammer strikes. Data were recorded with 40-Hz vertical geophones spaced at 1-m intervals. Display filter: 140 to 650 Hz bandpass filter. vibe-wig_pulse_comp [CR,M]

The gather shown in Figure B.6a is a stack of 900 individual pulses (2 cycles of a 300 Hz sine wave) as recorded by 40-Hz vertical geophones at 1-m spacing. The source was 3 m from the nearest phone, and the site is a grassy lawn on the Stanford University campus, with mixed sediments in the upper few tens of meters. Hammer-source data collected during the same deployment as the pulse vibrator data are shown in Figure B.6b. Both are displayed with a 140 to 350 Hz minimum-phase bandpass filter and AGC with a window of 75 ms. They show the same basic features (refracted first arrival, air wave, and some ground roll energy).

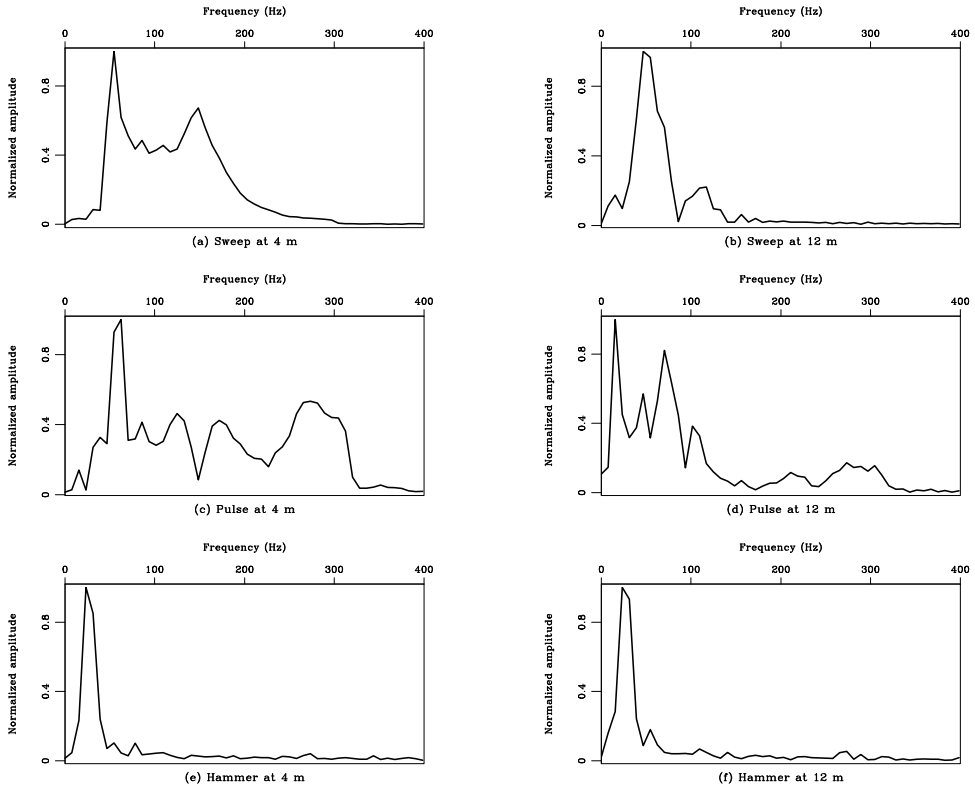

Figure B.7: Frequency spectra from geophones at 4 and 12 meters offset. Sweep-signal EMvibe data (14-second sweep 1 to 1000 Hz, as shown in Figure B.3) at a) 4 m, and b) 12 m. Pulse-signal EMvibe data (same as data shown in Figure B.6) at c) 4 m, and d) 12 m. Hammer-source data at e) 4 m, and f) 12 m. Note that at 4 m, the EM vibe data show a much broader frequency spectrum than the hammer data, and that at 12 m, the sources are more comparable. All data were collected at the same site on the Stanford campus. vibe-vibe_spec_comp [ER,M]

Direct comparisons of EMvibe data with sledgehammer-source data (Figures B.4 and B.6) show that the vibrator device is effective, but that for these particular experiments the hammer is at least as effective in terms of getting sufficient energy to geophones at 20 m of offset with a minimum of effort and time. However, the frequency content of the sledgehammer data is much narrower than that of the vibrator data, particularly at shorter offsets, as shown in Figure B.7. This figure shows data collected at a site on the Stanford campus at the same location where the data shown in Figure B.6 were collected. Data collected by the geophone

at 4 m (Figure B.7 a, c, and e) shows a much broader-band signal for both the pulse and the sweep data than for the hammer. Energy reaching the geophone at 12 m (Figure B.7 b, d, and f) shows that much of the higher-frequency energy has attenuated at this offset, and that the vibrator and hammer offer similar frequency energy. Visual inspection of the data in Figures B.4 and B.6 shows that the hammer is preferable at longer offsets with its greater total energy. Although the spectra shown in Figure B.7 suggest that the pulse is a better source signal than the sweep, visual inspection of Figures B.4 and B.6 indicates that the sweep is more effective at offsets beyond a couple of meters.

The data shown here were collected at two test sites with few subsurface layers and no strong reflectors. They show that the EMvibe offers a highly-repeatable broadband signal at offsets less than $\sim$10 m. Testing of the device at a test site with many shallow layers would would likely offer a better comparison with the sledgehammer, and demonstrate its effectiveness in high-resolution reflection work. The device does not replace the sledgehammer, but it does offer an alternative for use in cases where a non-destructive, highly-repeatable, source is required (asphalt evaluations, teaching demonstrations, etc). Increased numbers of stacks of both pulses and sweeps would extend these advantages to greater offsets, though it is unlikely that the EMvibe will be effective beyond a few tens of meters at sites with mainly unconsolidated sediments. The EMvibe shows particular promise for applications such as the Continuous Surface Wave method (Matthews et al., 1996), where a very precise seismic sources is desired to produce surface waves with desired frequency content.

Simple changes such as the use of non-linear sweeps would likely offer significant improvement in the post-correlation wavelet (flatter frequency spectrum leads to a higher-frequency wavelet). A more powerful amplifier would likely produce more energy, though the transducer may not be able to withstand a great deal more input power. The development of more powerful transducers would obviously lead to improvements in data quality. Other areas for improvement include the sweep correlation procedure; an accelerometer on the EMvibe baseplate would likely provide a better sense of the exact baseplate motion than the raw sweep or the baseplate geophone. Many authors have discussed the use of feedback mechanisms to ensure optimal vibrator/soil coupling (e.g. Sallas, 1984, Schrodt, 1987), but I have neglected this complicated issue and simply attempted to overcome coupling response problems with

Table B.1: EMvibe components

Item	Manufacturer	Part	Specs	Approx. cost ($)
Transducer	Clark Synthesis	TST 429	5-800 Hz	500
Amplifier	Crest Audio	FAV900	450 W/chan	500
Sound card	M-Audio	Sonica	24-bit	60
Base plate	self	2.3-cm Delrin sheet	43-cm hexagon	30
Top plate	self	2 x 2.3-cm Delrin	35-cm hexagon	55
Alum. posts	self	2.3-cm Al. rod	12 cm long	8
Total				$1153

brute force. Better results would almost certainly be obtained if the EMvibe were equipped with a feedback mechanism.

SPECIFICATIONS

Table B.1 shows the major parts of the EMvibe, along with source, basic specifications, and approximate cost at the time of construction (March 2003). The amplifier was purchased used from a music store. The plastic plates and aluminum rods were machined from scrap stock purchased from local industrial supply stores, so the cost includes only the purchase price of the raw materials. Many other types of plastic offer the rigidity and easy workability of Delrin; any of these would be equally effective. The manufacturer's price for the transducer has been reduced to ∼$350 since the time of purchase. Thus the total cost was just over $1000, but would likely be different for another construction.

ACKNOWLEDGMENTS

Essential guidance and supervision for this project were provided by Simon Klemperer and Jerry Harris. The framework of EMvibe was designed and constructed with a great deal of help from the knowledgeable and good-natured staff of the Stanford University Department of Mechanical Engineering Product Realization Lab, to whom the author is very grateful. Valuable design advice was also provided by Adam Pidlisecky and Andrea Les. Thanks also are

due to the many people who helped with data collection. Data processing was conducted using the computational resources of the Stanford Exploration Project. Funding for the EMvibe was provided by the Colorado Scientific Society and the Stanford School of Earth Science McGee Fund.

Bibliography

Abma, R., 1995, Least-squares separation of signal and noise with multidimensional filters: Ph.D. thesis, Stanford University, 158 pp.

Anderson, M., and Woessner, W., 1992, Applied groundwater modeling: Academic Press, San Diego, 381 pp.

Anstey, N., 1991, Vibroseis: Prentice Hall, Englewood Cliffs, 171 pp.

Beamish, D., and Peart, R., 1998, Electrokinetic geophysics– a review: Terra Nova, **10**, no. 1, 48–55.

Berryman, J., 2003, Electrokinetic effects and fluid permeability: Physica B, **338**, 270–273.

Biot, M. A., and Willis, D. G., 1957, The elastic coefficients of the theory of consolidation: J. Appl. Mech., **24**, 594–601.

Biot, M., 1956a, Theory of propagation of elastic waves in a fluid-saturated porous solid, I. Low-frequency range: J. Acoust. Soc. Am., **28**, 168–178.

Biot, M., 1956b, Theory of propagation of elastic waves in a fluid-saturated porous solid, II. Higher-frequency range: J. Acoust. Soc. Am., **28**, 178–191.

Broding, R., Buchanan, S., and Hearn, D., 1963, Field experiments on the electroseismic effect: IEEE Trans. Geosci. Electronics, **GE-1**, 23–31.

Butler, K. E., and Russell, R. D., 1993, Subtraction of powerline harmonics from geophysical records (short note): Geophysics, **58**, no. 06, 898–903.

Butler, K. E., and Russell, R. D., 2003, Cancellation of multiple harmonic noise series in geophysical records: Geophysics, **68**, no. 3, 1083–1090.

Butler, K. E., Russell, R. D., Kepic, A. W., and Maxwell, M., 1996, Measurement of the seismoelectric response from a shallow boundary: Geophysics, **61**, no. 06, 1769–1778.

Claerbout, J., 1999, Geophysical estimation by example: Environmental soundings image enhancement: Stanford Exploration Project, `http://sepwww.stanford.edu/sep/prof/`.

Davis, J., and Annan, A., 1989, Ground-penetrating radar for high-resolution mapping of soil and rock stratigraphy: Geophys. Prosp., **37**, no. 5, 531–551.

Deresiewicz, H., and Skalak, R., 1963, On uniqueness in dynamic poroelasticity: Bull. Seismol. Soc. Am., **53**, 783–788.

Frenkel, J., 1944, On the theory of seismic and seismoelectric phenomena in a moist soil: J. Physics (Soviet), **8**, no. 4, 230–241.

Garambois, S., and Dietrich, M., 2001, Seismoelectric wave conversions in porous media: Field measurements and transfer function analysis: Geophysics, **66**, no. 5, 1417–1430.

Garambois, S., and Dietrich, M., 2002, Full waveform numerical simulations of seismoelectromagnetic wave conversions in fluid-saturated stratified porous media: J. Geophys. Res., **107**, no. B7, 10.1029/2001JB000316.

Gassmann, F., 1951, Über die Elastizität poröser Medien: Vierteljahrsschrift der Naturforschenden Gesellschaft in Zürich, **96**, 1–23.

Gershenzon, N., and Bambakidis, G., 2001, Modeling of seismo-electromagnetic phenomena: Russian Journal of Earth Sciences, **3**, no. 4, 247–275.

Guitton, A., and Symes, W., 2003, Robust inversion of seismic data using the Huber norm: Geophysics, **68**, no. 4, 1310–1319.

Guitton, A., Brown, M., Rickett, J., and Clapp, R., 2001, Multiple attenuation using a t-x pattern-based subtraction method: Soc. of Expl. Geophys., 71st Ann. Internat. Mtg, 1305–1308.

Guitton, A., 2003, Multiple attenuation with multidimensional prediction-error filters: 73rd Ann. Internat. Mtg., Soc. of Expl. Geophys., Expanded Abstracts, 1945–1948.

Haartsen, M. W., and Pride, S. R., 1997, Electroseismic waves from point sources in layered media: J. Geophys. Res., **102**, no. B11, 24745–24769.

Haartsen, M., Dong, W., and Toksoz, M. N., 1998, Dynamic streaming currents from seismic point sources in homogeneous poroelastic media: Geophys. J. Int., **132**, 256–274.

Haber, E., and Ascher, U., 2001, Fast finite volume simulation of 3d electromagnetic problems with highly discontinuous coefficients: SIAM J. Sci. Comput., **22**, no. 6, 1943–1961.

Haines, S., Pride, S., and Klemperer, S., 2001, Development of experimental methods in electroseismic research, with application to aquifer characterization: Eos Trans. AGU, **82**, no. 47, Abstract GP22A–0268.

Haines, S., Guitton, A., Biondi, B., and Pride, S., 2003, Development of experimental methods in electroseismics: 73rd Ann. Internat. Mtg., Soc. of Expl. Geophys., Expanded Abstracts, 560–563.

Haines, S., Pride, S., Klemperer, S., and Biondi, B., 2004, Development of electroseismic experimental methods: Symposium on the Application of Geophysics to Engineering and Environmental Problems, Environmental and Engineering Geophysical Society, Proceedings, 1490–1503.

Ivanov, A., 1939, Effect of electrization of earth layers by elastic waves passing through them: Dokl. Adad. Nauk SSSR, **24**, no. 1, 41–45.

Kepic, A. W., Maxwell, M., and Russell, R. D., 1995, Field trials of a seismoelectric method for detecting massive sulfides: Geophysics, **60**, no. 02, 365–373.

Landau, L., and Lifshitz, E., 1984, Electrodynamics of continuous media: Pergamon, New York, 460 pp, 2nd edition.

Long, L. T., and Rivers, W. K., 1975, Field measurement of the electroseismic response: Geophysics, **40**, no. 02, 233–245.

Martner, S. T., and Sparks, N. R., 1959, The electroseismic effect: Geophysics, **24**, no. 02, 297–308.

Matthews, M., Hope, V., and Clayton, C., 1996, The use of surface waves in the determination of ground stiffness profiles: Proc. Instn. Civ. Engrs. Geotech. Engng., **119**, 84–95.

Mavko, G., Mukerji, T., and Dvorkin, J., 1998, The rock physics handbook tools for seismic analysis in porous media: Cambridge University Press, Cambridge, 329 pp.

Maxwell, M., Russell, R. D., Butler, K. E., and Kepic, A. W., 1992, Field tests of piezoelectric exploration for quartz: Soc. of Expl. Geophys., 62nd Ann. Internat. Mtg, 443–445.

Migunov, N., and Kokorev, A., 1977, Dynamic properties of the seismoelectric effect of water-saturated rocks: Izvestiya, Earth Physics, **13**, no. 6, 443–446.

Mikhailov, O. V., Haartsen, M. W., and Toksoz, M. N., 1997, Electroseismic investigation of the shallow subsurface: Field measurements and numerical modeling: Geophysics, **62**, no. 01, 97–105.

Mikhailov, O. V., Queen, J., and Toksooz, M., 2000, Using borehole electroseismic measurements to detect and characterize fractured (permeable) zones: Geophysics, **65**, no. 4, 1098–1112.

Miller, R. D., Pullan, S. F., Steeples, D. W., and Hunter, J. A., 1992, Field comparison of shallow seismic sources near Chino, California: Geophysics, **57**, no. 05, 693–709.

Miller, R. D., Pullan, S. E., Steeples, D. W., and Hunter, J. A., 1994, Field comparison of shallow P-wave seismic sources near Houston, Texas: Geophysics, **59**, no. 11, 1713–1728.

Murty, Y., 1985, First results on the direct detection of groundwater by seismoelectric effect-a field experiment: Bull. Aust. Soc. Expl. Geophys., **16**, 254–255.

Neev, J., and Yeatts, F., 1989, Electrokinetic effects in fluid-saturated poroeleastic media: Physical Review B, **40**, no. 13, 9135–9141.

Oldenburg, D. W., and Li, Y., 1999, Estimating depth of investigation in dc resistivity and IP surveys: Geophysics, **64**, no. 2, 403–416.

Parkhomenko, E., 1971a, Borehole and laboratory studies of the seismoelectric effect of the second kind in rocks: Izvestiya, Earth Physics, **9**, 663–666.

Parkhomenko, E., 1971b, Electrification phenomena in rocks: Plenum Press, New York, 285 pp.

Pride, S. R., and Garambois, S., 2002, The role of Biot slow waves in electroseismic wave phenomena: J. Acoust. Soc. Am., **111**, 697–706.

Pride, S. R., and Haartsen, M. W., 1996, Electroseismic wave properties: J. Acoust. Soc. Am., **100**, no. 3, 1301–1315.

Pride, S., and Morgan, D., 1991, Electrokinetic dissipation induced by seismic waves: Geophysics, **56**, no. 7, 914–925.

Pride, S. R., Tromeur, E., and Berryman, J. G., 2002, Biot slow-wave effects in stratified rock: Geophysics, **67**, 271–281.

Pride, S. R., Harris, J. M., Johnson, D. L., Mateeva, A., Nihei, K. T., Nowack, R. L., Rector, J. W., Spetzler, H., Wu, R., Yamomoto, T., Berryman, J. G., and Fehler, M., 2003, Permeability dependence of seismic amplitudes: The Leading Edge, **22**, 518–525.

Pride, S. R., Berryman, J. G., and Harris, J. M., 2004a, Seismic attenuation due to wave-induced flow: J. Geophys. Res., **109**, B01201,doi10.1029/2003JB002639.

Pride, S. R., Moreau, F., and Gavrilenko, P., 2004b, Mechanical and electrical response due to fluid-pressure equilibration following an earthquake: J. Geophys. Res., **109**, B03302,doi10.1029/2003JB002639.

Pride, S., 1994, Governing equations for the coupled electromagnetics and acoustics of porous media: Physical Review B, **50**, no. 21, 15678–15696.

Pritchett, W. C., 1994, Why waste money with linear sweeps?: The Leading Edge, **13**, no. 09, 943–949.

Russell, R. D., Butler, K. E., Kepic, A. W., and Maxwell, M., 1997, Seismoelectric exploration: The Leading Edge, **16**, no. 11, 1611–1615.

Sacchi, M. D., and Ulrych, T. J., 1995, High-resolution velocity gathers and offset space reconstruction: Geophysics, **60**, no. 04, 1169–1177.

Sallas, J. J., 1984, Seismic vibrator control and the downgoing P-wave: Geophysics, **49**, no. 06, 732–740.

Schrodt, J. K., 1987, Techniques for improving Vibroseis data: Geophysics, **52**, no. 04, 469–482.

Shaw, D., 1992, Introduction to colloid and surface chemistry: Butterworths, London, 306 pp, 4th edition.

Sheriff, R., and Geldart, L., 1995, Exploration seismology: Cambridge University Press, Cambridge, 592 pp, 2nd edition.

Skempton, A. W., 1954, The pore-pressure coefficients A and B: Geotechnique, **4**, 143–147.

Soubaras, R., 1994, Signal-preserving random noise attenuation by the F-X projection: Soc. of Expl. Geophys., 64th Ann. Internat. Mtg, 1576–1579.

Strachan, E., and Wolfe, P., 2001, Seismoelectric investigations at clean and contaminated sites: Symposium on the Application of Geophysics to Engineering and Environmental Problems, Environmental and Engineering Geophysical Society, procedings.

Thompson, A. H., and Gist, G. A., 1991, Electroseismic prospecting: Soc. of Expl. Geophys., 61st Ann. Internat. Mtg, 425–427.

Thompson, A. H., and Gist, G. A., 1993, Geophysical applications of electrokinetic conversion: The Leading Edge, **12**, no. 12, 1169–1173.

Thompson, R. R., 1936, The seismic electric effect: Geophysics, **01**, no. 03, 327–335.

Thompson, R. R., 1939, A note on the seismic-electric effect: Geophysics, **04**, no. 02, 102–105.

Thorson, J. R., and Claerbout, J. F., 1985, Velocity stack and slant stochastic inversion: Geophysics, **50**, no. 12, 2727–2741.

Wolfe, P., Yu, J., and Gershenzon, N., 1996, Seismoelectric studies in an outwash plain: Symposium on the Application of Geophysics to Engineering and Environmental Problems, Environmental and Engineering Geophysical Society, procedings, 21–31.

Yilmaz, O., 2000, Seismic Data Analysis Vol. 1: Soc. of Expl. Geophys., Tulsa, 1000 pp.

Zhang, J., 1999, Quadrangle-grid velocity-stress finite difference method for poroelastic wave equations: Geophys. J. Int., **139**, 171–182.

Zhu, Z., and Toksoz, M., 2003, Crosshole seismoelectric measurements in borehole models: Geophysics, **68**, no. 5, 1519–1524.

Zhu, Z., Haartsen, M. W., and Toksoz, M. N., 1999, Experimental studies of electrokinetic conversions in fluid-saturated borehole models: Geophysics, **64**, no. 5, 1349–1356.